ON-AXIS ROTATION PIN-ON-DISC TRIBOMETRY & METAL CUTTING

AN ANALYSIS OF ON-AXIS ROTATION PIN-ON-DISC TRIBOMETRY AND ITS CORRELATION TO FRICTION IN METAL CUTTING

BY JEREMY BOYD, B. ENG., M.A.SC.

A Thesis Submitted to the School of Graduate Studies in Partial Fulfilment of the

Requirements for the Degree Doctor of Philosophy

McMaster University DOCTOR OF PHILOSOPHY (2021) Hamilton, Ontario (Mechanical Engineering)

TITLE: An Analysis of On-Axis Rotation Pin-on-Disc Tribometry and its Correlation to Friction in Metal Cutting

AUTHOR: Jeremy Boyd, B.Eng., M.A.Sc. (McMaster University)

SUPERVISOR: Professor S.C. Veldhuis NUMBER OF PAGES: xxvii, 233

LAY ABSTRACT

This dissertation further develops the concept of a pin-on-disc apparatus for evaluating the friction coefficient between materials under temperature and stress conditions similar to those experienced in metal cutting.

Firstly, characteristics of the imprint formed by the pin in the disc during tests with the apparatus are studied. Specific focus is given to the growth of the imprint during the rotating stage of the test and different zones of contact at the imprint surface.

Secondly, the importance of estimating the actual temperature at the pin-disc interface, inaccessible for direct measurement, is raised and a numerical model developed to aid in its estimation.

Finally, coefficient of friction results generated on the apparatus are correlated to the magnitude of forces measured and other observations made during metal cutting trials involving the same material pairs.

ABSTRACT

In metal cutting applications, development of coatings to reduce friction between tool and chip and also enhance wear resistance of the tool is an important objective. The effectiveness of such coatings is ultimately evaluated through metal cutting trials; however, bench-scale tests can play a role in predicting some aspects of a candidate coating's performance. This dissertation further develops the concept of an on-axis rotation pin-on-disc tribometer for the evaluation of friction coefficient between tool and work material pairs under temperature and stress conditions similar to those experienced between tool and chip in metal cutting.

Firstly, the characteristics of the imprint formed by the spherical-tipped pin in the disc during tribometer tests are studied. Specific focus is given to the growth of the imprint during the rotating stage of the test; the severity of pile-up of work material around the periphery of the imprint; different zones of contact at the imprint surface; and evidence of (or lack thereof) of bulk shear in the surrounding work material below the surface of the disc.

The importance of estimating the actual temperature at the pin-disc interface (inaccessible for direct measurement) is also raised. Evidence is presented that suggests the pin-disc interface is higher for tests involving coatings with higher electrical resistivity, despite exhibiting similar temperatures 2 mm above the interface (accessible for direct measurement). A numerical model is developed in an effort to estimate the pin-disc interface during stationary specimen tests for specific pin and disc materials under

controlled conditions. An empirical relationship is also established to express the variation of electrical resistivity with temperature for cemented tungsten carbide (6% cobalt content).

Finally, coefficient of friction results for coated and uncoated cemented carbide pins in contact with AISI 1045 steel discs are related to short duration turning trials involving the same material pairs. Coatings exhibiting low friction coefficient result in appreciably lower cutting forces, reduced built-up edge intensity and more tightly curled chips. The possibility that the low thermal conductivity of such coatings could be producing similar effects by forcing more heat into the chips is also explored.

ACKNOWLEDGEMENTS

To my wife, Karen, and daughter, August – you have both made many sacrifices to allow me to pursue and complete my PhD studies. I love you, and I thank you for your patience with me.

To my mom and dad – thanks for investing in me and believing in me. You laid the ground work for me to pursue and succeed in these postgrad studies.

To my sister – yes, I am finally finished my PhD! While these studies have taught me a thing or two about perseverance, you have endured more numerous and greater challenges in this life than I have. Your resilience is inspiring.

To my supervisor, Dr. Stephen Veldhuis – you took a chance on me as an undergraduate research intern in Summer 2008. I do not think either of us envisioned at the time that you would go on to supervise my Masters and now my Doctoral studies. Thank you for your mentorship and entrusting me with various leadership opportunities within the MMRI. I am glad this dissertation is *finally* done, and I suspect you are as well.

To my committee members, Dr. Eu-Gene Ng & Dr. Igor Zhitomirsky – thank you for reading through five (or six?) progress reports as well as this dissertation, sharing your critiques and feedback and entertaining multiple shifts in research direction over the last nine years.

To Dr. Abul Arif – thank you for your invaluable feedback during the process of writing this dissertation, identifying gaps and weaknesses that needed addressing and helping me to structure it more effectively.

Thanks to Dr. German Fox-Rabinovich for the countless and informative discussions we had regarding metal cutting and tribology.

Thanks to Dr. Julia Dosbaeva for support with various scanning electron microscopy analyses that were required in my research.

Thanks to Dr. Danielle Covelli for support with x-ray photoelectron spectroscopy analyses and extended e-mail discourses regarding interpretation of results.

Thanks to Maneesh Khanna for design and engineering support with regards to the development of hardware improvements for the MMRI Tribometer.

Thanks to Terry Wagg for technical guidance in the machining of hardware for the MMRI Tribometer and countless refreshers on how to run the CNC machines in the Machining Systems Lab.

Thanks to Joe Verhaege for support at various times troubleshooting electrical problems with the MMRI Tribometer and offering innovative solutions. Likewise, thanks to the staff in the Mechanical Engineering machine Shop for technical advice and assistance along the way.

Thanks to Doug Culley from the Materials Engineering department for training on the Nikon Microscope and technical guidance and support with lapping, polishing and etching of samples.

Thanks to Matt Li for designing and fabricating the slip ring concept – it definitely made testing much easier.

Thanks to Terrance Leung for translating my very manual algorithm for data analysis in Microsoft Excel and implementing it in Matlab – you saved me hundreds of hours.

Thanks to Ali Khoei and Maximiliano Miranda for performing ‘just one more test’ for me on multiple occasions during the latter years of my studies. You both have done excellent work with the MMRI Tribometer to further advance our knowledge base and practice in tribology.

Thanks to the various other students and staff who worked alongside me in the MMRI during my years of full-time study, encouraging and supporting me along the way – notably but not exhaustively: Mohammed Tauhiduzzaman, Simon Oomen-Hurst, Brady Semple, Steve Remilli, Junfeng (Jerome) Yuan, Mohammad Shariful (Sharif) Chowdhury, Shahareen Chowdhury, Taib Arif, William Long, Emma Badowski, Travis Taylor, Jonathan Bunting, Kevin Tanaka and Salomon Gabriel.

Thanks to the Government of Canada for financial support of this research through the NSERC CANRIMT initiative.

Thanks to Adrian Burke and Anita Ramroop – Director of Operations and Operations Engineering Manager, respectively, at L3Harris Wescam (Don Mills location) – for checking in on the status of my PhD and encouraging me to finish.

Lastly, thanks to God the Father, the Lord Jesus Christ and the Holy Spirit – for giving me strength to persevere in this work and finally finish what I started; for providing me with a rich pool of support and resources in the above individuals; and for teaching me things far more valuable than metal cutting and tribology on this long but finite journey.

CONTENTS

Lay Abstract iii

Abstract iv

Acknowledgements vi

List of Figures xvi

List of Tables xx

List of all Abbreviations and Symbols xxi

Declaration of Academic Achievement xxv

1. Introduction 1

    1.1 Context and Motivation 1

    1.2 Research Objectives 5

    1.3 Structure of the Dissertation 5

2. Basic Concepts & Literature Review 8

    2.1 Fundamentals of Friction 8

        2.1.1 Classical Friction 8

        2.1.2 Friction under Heavy Load 9

    2.2. Fundamentals of Cutting 11

        2.2.1 Orthogonal Cutting 11

        2.2.2 The Primary Shear Zone 11

2.2.3 The Secondary Shear Zone 18

2.2.4 Stress Distribution on the Cutting Tool 21

2.2.5 Heat Generation during Cutting 22

2.3 Control of Friction and Forces in Cutting Operations 24

2.3.1 Motivation 24

2.3.2 The Effect of Cutting Speed 25

2.3.3 The Effect of Tool Geometry 27

2.3.4 The Effect of Tool Material 28

2.3.5 The Effect of Work Material 32

2.3.6 The Effect of Cutting Fluids 33

2.3.7 Summary 35

2.4 Evaluation of Friction under Load and Temperature Typical of Cutting 35

2.4.1 A General Overview of Tribometers Aimed at Characterizing Friction in Cutting Processes 35

2.4.2 The Adhesiometer Developed by Shuster 36

2.4.3 The MMRI Tribometer – Mark I 42

2.4.4 The MMRI Tribometer – Mark II 44

2.4.5 The MMRI Tribometer – Mark III 47

2.5 Gaps in Knowledge in the Literature to be Bridged in this Dissertation 50

3. Imprint Growth Analysis at Elevated Temperatures 53

3.1 Opening Remarks 53

3.2 Changes Implemented in the MMRI Tribometer (Mark III) 53

3.3 General Overview of the Test Methodology and Sample Preparation 55

3.3.1 General Overview 55

3.3.2 Sample Preparation 57

3.4 Stages of the Automated Test 58

3.4.1 Applying Load to the Specimens 59

3.4.2 Heating the Specimens 61

3.4.3 Rotating the Disc about the Pin 67

3.4.4 Test End 70

3.5 Experimental Work – Imprint Growth during Elevated Temperature Tests 72

3.5.1 Correlating growth in imprint diameter with reaction torque and observations of adhesion at and work material distortion surrounding the imprint 72

3.5.2 Establishing the rate at which the imprint diameter grows during on-axis rotation pin-on-disc tribometer tests 78

3.5.3 The influence of pile-up on imprint diameter measurements and COF evaluation 84

3.6 Concluding Remarks 90

4. Shear Patterns in the Imprint Microstructure 92
4.1 Opening Remarks 92
4.2 Materials and Methods 92
4.2.1 Materials 92
4.2.2 Methods 94
4.3 Results and Discussion 96
4.3.1 Quantitative Results from Tribometer Tests 96
4.3.2 Analysis of Friction Surfaces 99
4.3.3 Proposed Mechanism for Low Friction between Tungsten Carbide and Ductile Iron 112
4.4 Concluding Remarks 115
5. Insights into the Test Temperature from the Imprint 118
5.1 Opening Remarks 118
5.2 Results and Analyses 118
5.2.1 Examination of Command Signal vs. Temperature and Imprint Diameter vs. Temperature from Tribometer Tests 118
5.2.2 Analysis of Imprints 121
5.2.3 Examination of Temperature-Time Profiles 125
5.2.4 Examination of Coating Electrical Resistivity 126

5.3 Concluding Remarks 128

6. Modeling the Temperature Distribution in the Pin and Disc 130

6.1 Opening Remarks 130

6.2 Initial Model Formulation 130

6.2.1 Formulating A One-Dimensional Thermal Model of the Pin subject to Internal Heat Generation via Electric Current 130

6.2.2 Formulating a Two-Dimensional Thermal Model of the Disc including Convective Heat Transfer at the Top and Sides but Neglecting Internal Heat Generation 135

6.2.3 Modeling Contact Resistance at the Pin-Disc Interface 141

6.3 Initial Model Implementation 142

6.3.1 Solution Technique 142

6.3.2 Assumptions regarding Model Parameters and Conditions 143

6.3.3 Empirical Measurements of Electrical Potential Drop along Pin and Disc 147

6.3.4 Tuning Model Parameters to Achieve Agreement with Empirical Values of R_1 and R_2 149

6.3.5 Simulation Results: Coated and Uncoated Pins, Low Electric Current 150

6.3.6 Simulation Results: Coated and Uncoated Pins, Moderate Electric Current 152

6.3.7 Discussion of Results from the Initial Model Implementation 155

6.4 Revised Model Implementation 157

6.4.1 Motivation for a Revised Model 157

6.4.2 Revised Assumptions regarding Model Parameters and Conditions 157

6.4.3 Solution Technique 168

6.4.4 Simulation Results: Uncoated Pin, Varying Levels of Electric Current 170

6.4.5 Discussion of Results from the Revised Model Implementation 176

6.5 Concluding Remarks 179

7. Comparison of Tribometer Tests with Cutting Trials 181

7.1 Opening Remarks 181

7.2 Materials and Methods 181

7.2.1 Materials 181

7.2.2 Machining Conditions 183

7.2.3 Machining Outputs 183

7.3 Results 185

7.3.1 Tool Forces 185

7.3.2 Built-Up Edge Intensity 188

7.3.3 Chip Characteristics 189

7.4 Discussion 191

7.5 X-ray Photoelectron Spectroscopic Analysis of Coated Pin and Cutting Inserts 197

7.6 Conclusion....204

8. Conclusions and Recommendations....206

8.1 Restatement of Objectives....206

8.2 Summary of Contributions in Fulfillment of Research Objectives....206

8.2.1 Key Findings with regards to Objective 1....206

8.2.2 Key Findings with regards to Objective 2....208

8.2.3 Key Findings with regards to Objective 3....210

8.3 Recommendations for Further Work....211

8.3.1 Refinement of the Thermal Model, Experimental Methods to Support it, and Implementation in More Efficient Software....211

8.3.2 Studies on the Oxide Thickness on the Chip Undersurface and Evaluation of the Colour of Chip Undersurface as a function of Cutting Speed....212

8.3.3 Comparative Tribofilm Studies on the Pin Tip and Cutting Insert....213

Appendix A: Summary of Coefficients for All Types of Nodes used in the Two-Dimensional Thermal Model of the Disc....223

Appendix B: Reproduction of the First Six Paragraphs in the Discussion Section of an Article written by the Author....227

Appendix C: Permission to Reproduce/Adapt Content from Article by Author....231

LIST OF FIGURES

Figure 1	Schematic of (a) an on-axis rotation pin-on-disc tribometer vs. (b) a conventional pin-on-disc tribometer	**4**
Figure 2	Depiction of Normal Force F_n and Friction Force F_f acting on a Moving Body as it slides in contact with a Stationary Body	**8**
Figure 3	Variation in Shear Stress with Increasing Normal Stress at the Interface between Two Sliding Bodies (adapted frrom)	**11**
Figure 4	Basic Schematic of Orthogonal Cutting	**13**
Figure 5	More Detailed Schematic of Orthogonal Cutting	**13**
Figure 6	Velocity and Force Diagrams for Orthogonal Cutting	**14**
Figure 7	Chip Thickness Ratio, r, as a function of Shear Plane Angle, as per Eq. 2.2.2.8	**17**
Figure 8	Shear Strain along the Shear Plane as a function of Shear Plane Angle, as per Eq. 2.2.2.9	**17**
Figure 9	Stress Distribution and Sticking vs. Sliding Zones on the Tool Rake Face	**21**
Figure 10	The relationship between imprint radius and imprint depth, per Eq. 2.4.2.3	**41**
Figure 11	The relationship between imprint radius and penetration ratio, per Eq 2.4.2.4	**41**
Figure 12	New collet designed for the MMRI Tribometer (Mark III)	**54**
Figure 13	(a) New mounting location for the collet; (b) new copper plate with spring-loaded graphite slipring	**54**
Figure 14	Snapshot of the new hardware elements of the Mark III Tribometer	**54**
Figure 15	Normal stress achieved vs. normal load applied (first stage of the test)	**60**
Figure 16	Illustrative data from a tribometer test between an AlTiN-coated WC-Co pin and AISI 4150 Steel disc under 200 N load and 93 A of current	**64**
Figure 17	Illustrative data from a tribometer test between an AlTiN-coated WC-Co pin and AISI 4150 Steel disc under 200 N load and 113 A of current	**65**
Figure 18	Torque vs. imprint diameter under 200 N and ambient temperature	**74**
Figure 19	Torque vs. imprint diameter under 200 N and 200 °C	**74**
Figure 20	Torque vs. imprint diameter under 200 N and 400 °C	**74**

Figure 21	Torque vs. imprint diameter under 2000 N and ambient temperature	**75**
Figure 22	Torque vs. imprint diameter under 2000 N and 200 °C	**75**
Figure 23	Torque vs. imprint diameter under 2000 N and 400 °C	**75**
Figure 24	Torque vs. time curve highlighting peak vs. end torque	**76**
Figure 25	Torque curves from select tests presented in Figure 21	**76**
Figure 26	Torque curves from select tests presented in Figure 23	**76**
Figure 27	Imprints corresponding to tests presented in Figure 25 and Figure 26	**77**
Figure 28	Imprint diameter vs. rotation duration for the AISI 1045 steel disc	**79**
Figure 29	(a) Torque vs. Time profiles and (b) Temperature vs. Time profiles for elevated temperature tests with the AISI 1045 steel disc	**80**
Figure 30	Imprint diameter vs. rotation duration for the aluminum disc	**80**
Figure 31	(a) Torque vs. Time profiles and (b) Temperature vs. Time profiles for elevated temperature tests with the aluminum disc	**81**
Figure 32	Imprint diameter vs. temperature during stationary specimen tests with AISI 1045 steel	**83**
Figure 33	Cross-sectional profile obtained from a white light interferometer measurement of an imprint	**85**
Figure 34	Comparison of $d_{pile\text{-}up}$, d_{plane} and d_{opt}	**85**
Figure 35	The ratio of d_{opt}/d_{plane} increases linearly with respect to d_{opt}	**87**
Figure 36	Schematic depicting A1 and A2 relative to d_{plane} and $d_{pile\ up}$	**87**
Figure 37	Microstructure of (a) AISI 1045 steel discs and (b) SAE J434 D5506 ductile iron discs	**94**
Figure 38	Imprint profiles from white light interferometry scans	**96**
Figure 39	τ/σ vs. temperature for tests involving (a) AISI 1045 steel discs and (b) SAE J434 D5506 ductile iron discs	**98**
Figure 40	h/r vs. temperature for tests involving (a) AISI 1045 steel discs and (b) SAE J434 D5506 ductile iron discs	**98**
Figure 41	$h/r + \tau/\sigma$ vs. temperature for tests involving (a) AISI 1045 steel discs and (b) SAE J434 D5506 ductile iron discs	**98**
Figure 42	SE images of uncoated pins after tribometer tests at 550 °C in contact with (a) AISI 1045 steel and (b) SAE J434 D5506 ductile iron	**100**
Figure 43	Optical micrographs of select imprints in SAE J434 D5506 after tribometer tests with an uncoated carbide pin	**102**

Figure 44	Torque curves from tests corresponding to the imprints shown in Figure 43	**103**
Figure 45	Optical micrographs of select imprints in AISI 1045 steel after tribometer tests with an uncoated carbide pin: (a) at 300 °C; (b) at 525 °C; and (c) at 660 °C	**105**
Figure 46	SE images of imprints from select trials	**107**
Figure 47	Circular striations and adhered work material present on the tip of the TiAlN-coated pin	**108**
Figure 48	SIMS data obtained from (a) uncoated pin and (b) TiAlN-coated pin	**112**
Figure 49	Results from rotating specimen (a - c) and stationary specimen (d) tribometer tests with AISI 1045 carbon steel	**119**
Figure 50	Select imprints from tests involving TiN-coated pins	**122**
Figure 51	Select imprints from tests involving TiAlCrSiYN/TiAlCrN-coated pins	**123**
Figure 52	Temperature-time profiles from various tests against an AISI 1045 steel disc	**125**
Figure 53	Illustration of ohmmeter measurements	**128**
Figure 54	Defining nodes and spacing for a one-dimensional model of heat transfer in a generalized radially symmetric object (e.g., the pin)	**131**
Figure 55	(Top) simplified schematic of the actual pin-disc interface. (Bottom) approximate representation of the pin-disc interface used in the thermal model	**134**
Figure 56	Overview of nodes and control volumes used to model heat transfer in the disc	**136**
Figure 57	General depiction of a Category f Node	**137**
Figure 58	Location of Voltage Measurements Obtained during Stationary Disc Tests for Initial Model Calibration	**148**
Figure 59	Predicted distribution of temperature in the pin and disc for Scenarios 4 and 10: (a) the pin; (b) the centermost nodes of the disc; (c) the topmost nodes of the disc	**154**
Figure 60	Test Temperature vs. Command Signal corresponding to the Stationary Specimen Tests presented in Figure 49(d)	**156**
Figure 61	Location of Voltage Measurements and Temperature Measurements Obtained during Stationary Disc Tests for Refined Model Calibration	**160**
Figure 62	Temperature (Test, Mid and Top) vs. Electrical Current for Second Round of Stationary Specimen Tests	**164**

Figure 63	Distribution of Temperature along the Cylindrical Body of the Pin as measured during Second Round of Stationary Specimen Tests	**165**
Figure 64	Electrical Resistivity vs. Temperature	**165**
Figure 65	Temperature distribution along the length of the pin for various scenario	**173**
Figure 66	Axial temperature distribution along the centermost nodes of the disc for various scenarios	**174**
Figure 67	Radial temperature distribution along the topmost nodes of the disc for various scenarios	**175**
Figure 68	SE image obtained from a Triumph TNMA 332 Grade C2 carbide insert	**182**
Figure 69	Cutting force components	**184**
Figure 70	Example force measurement	**184**
Figure 71	Distinguishing the 'free surface' and 'sliding surface' of the chip (not to scale)	**185**
Figure 72	Average cutting force components at 50 m/min (left) and 100 m/min (right)	**186**
Figure 73	Fluctuation in cutting forces at 50 m/min (left) and 100 m/min (right)	**187**
Figure 74	Average BUE height observed on inserts after tests at (a) 50 m/min and (b) 100 m/min	**188**
Figure 75	Differences in built-up edge intensity at 50 m/min cutting speed, as viewed from the rake face and the flank face	**189**
Figure 76	High-resolution XPS spectra obtained at the Al2p peak on different TiAlCrSiYN/TiAlCrN coated samples	**200**
Figure 77	High-resolution XPS spectra obtained at the Al2s peak on different TiAlCrSiYN/TiAlCrN coated samples	**201**
Figure 78	High-resolution XPS spectra obtained at the Cr2p 1/2 and 3/2 peaks on different TiAlCrSiYN/TiAlCrN coated samples	**202**

LIST OF TABLES

Table 1	The effect of using dpileup vs. dplane in the evaluation of COF and (h/r)	**89**
Table 2	Summary of friction test conditions and yields from EDX spectroscopy analyses in the outer region of imprints shown in Figure 46	**107**
Table 3	Comparison of electrical resistance measurements	**128**
Table 4	Description of Model Parameters and Notation as well as Values Used in the Initial Model Implementation	**144**
Table 5	Radial position of disc nodes with subscript m, as a function of modeled imprint diameter	**145**
Table 6	Vertical position of disc nodes with subscript j	**145**
Table 7	Temperature measurements at different positions along the length of the pin	**145**
Table 8	Summary of Voltage and Imprint Diameter Measurements from select Stationary Disc Tests, as well as Corresponding Resistance Calculations	**148**
Table 9	Model Parameters and Simulation Results for Low Current Simulations	**151**
Table 10	Model Parameters and Simulation Results for High Current Scenarios	**153**
Table 11	Temperature, Voltage and Imprint Diameter Measurements from Second Round of Stationary Specimen Tests	**161**
Table 12	Calculated Electrical Resistance, Electrical Resistivity and Mean Temperature based on Measurements in Table 11	**162**
Table 13	Model Inputs, Outputs and Errors for Scenarios Explored using the Revised Thermal Model	**171**
Table 14	Nominal composition of AISI 1045 steel	**183**
Table 15	Observations of chips collected after short duration tests at 50 m/min	**190**
Table 16	Observations of long, continuous chips collected after short duration tests at 100 m/min	**190**
Table 17	Reported thermal conductivity values for select tool materials	**193**
Table 18	Binding energies and assignments reported in the NIST X-Ray Photoelectron Spectroscopy Database	**203**

LIST OF ALL ABBREVIATIONS AND SYMBOLS

$\boldsymbol{A}$	Area
A	Ampere *(unit of electrical current)*
$\boldsymbol{A_a}$	Apparent area of contact
AISI	American Iron and Steel Institute
$\boldsymbol{A_r}$	Real area of contact
$\boldsymbol{A_s}$	Area of the shear plane
$\boldsymbol{B}$	Ratio of $\boldsymbol{d_{pile\text{-}up}}$ to $\boldsymbol{d_{plane}}$
BUE	Built up edge
$\boldsymbol{COF}$	Coefficient of friction
$\boldsymbol{COF_{opt}}$	Coefficient of friction evaluated on the MMRI tribometer based on the imprint diameter evaluated by means of an optical microscope
$\boldsymbol{COF_{pile\text{-}up}}$	Coefficient of friction evaluated on the MMRI tribometer based on the imprint diameter evaluated at the top of the pile-up
$\boldsymbol{COF_{plane}}$	Coefficient of friction evaluated on the MMRI tribometer based on the imprint diameter evaluated at the plane surface of the disc
$\boldsymbol{CR}$	Contact ratio, the ratio between real area of contact and apparent area of contact
CVD	Chemical Vapour Deposition
$\boldsymbol{D}$	Imprint diameter
$\boldsymbol{d_{opt}}$	Imprint diameter evaluated by means of an optical microscope
$\boldsymbol{d_{pile\text{-}up}}$	Imprint diameter evaluated at the top of the pile-up
$\boldsymbol{d_{plane}}$	Imprint diameter evaluated at the plane surface of the disc
EDX	Energy dispersive x-ray (spectroscopy)
$\boldsymbol{F}$	Cutting force component resolved tangential to the rake face of the tool
$\boldsymbol{F_c}$	Cutting force component resolved along the direction of cut
$\boldsymbol{F_{exp}}$	Force required to rotate the sleeve and pin in Shuster's adhesiometer
$\boldsymbol{F_f}$	Friction force, in a general free body diagram
$\boldsymbol{F_n}$	Normal force, in a general free body diagram
$\boldsymbol{F_N}$	Normal force in Shuster's adhesiometer and the MMRI tribometer; also, the cutting force component resolved normal to the shear plane
$\boldsymbol{F_s}$	Cutting force component resolved along the shear plane

F_t	Cutting force component resolved along the direction of feed
H	Imprint depth; also, convective heat transfer coefficient
h_{side}	Convective heat transfer coefficient at the side of the disc
h_{top}	Convective heat transfer coefficient at the top of the disc
H	Hardness
HRB	Rockwell B Hardness
I	Electrical current
K	Thermal conductivity
k_{contam}	Thermal conductivity of the contaminant layer at the contact between pin and disc
k_{disc}	Thermal conductivity of the disc
k_{pin}	Thermal conductivity of the pin
k_s	Work material shear stress
K	Kelvin *(unit of temperature)*
L	Length
l_c	Tool-chip contact length
M	Moment or torque measured during an on-axis pin-on-disc tribometer test
Ms	Millisecond *(unit of time)*
N	Cutting force component resolved normal to the rake face of the tool
N	Newton *(unit of force)*
N_x	Scalar multiplier used in thermal mode in Chapter 6, where x = 1, 2, 3, 4
Nm	Newton meter *(unit of torque)*
PID	Proportional Integral Differential
PVD	Physical Vapour Deposition
MMRI	McMaster Manufacturing Research Institute
MPa	Megapascal *(unit of stress)*
Q	Heat flow
q_{gen}	Rate of heat generation
R	Radius of the imprint; also, chip thickness ratio
r_{ind}	Radius of the indentation (imprint)
$r_{pile\text{-}up}$	Radius of the imprint evaluated at the top of the pile-up

r_{plane}	Radius of the imprint evaluated at the plane surface of the disc
R	Radius of the spherical tip/indenter; also, electrical resistance
Ra	Average roughness
RPM	Revolutions per minute *(unit of angular speed)*
S	Second *(unit of time)*
SAE	Society of Automotive Engineers
SE	Secondary electron
SEM	Scanning electron microscopy
SIMS	Secondary ion mass spectroscopy
T	Temperature
T_{bot}	Temperature at the bottom of the disc
T_{int}	Temperature at the pin-disc interface
T_{mid}	Temperature at the mid-point of the exposed length of the pin
T_{top}	Temperature at the top of the exposed length of the pin
T_{test}	Temperature of the pin at a location approximately 2 mm above the pin-disc interface
T_{∞}	Ambient temperature some distance away from the pin and disc
t_1	Uncut chip thickness (or feed)
t_2	Chip thickness
V	Cutting velocity; also electrical voltage or potential
V_c	Chip velocity
V_x	Electrical voltage between different locations along the pin and disc, as defined in more detail in Chapter 6 (x = 1, 2, 3, etc.)
W	Uncut chip width (or depth of cut)
XPS	X-ray photoelectron spectroscopy
°C	Degrees Celcius *(unit of temperature)*
A	Tool rake angle
Γ	Shear strain
M	Coefficient of friction
P	Electrical resistivity

ρ_{contam}	Electrical resistivity of the contaminant layer at the contact between pin and disc
ρ_{disc}	Electrical resistivity of the disc
ρ_{pin}	Electrical resistivity of the pin
Σ	Normal stress
T	Shear stress
Φ	Shear plane angle
Ω	Ohm *(unit of electrical resistance)*

DECLARATION OF ACADEMIC ACHIEVEMENT

The content described herein, in particular **Chapters 3** through **7**, is the original work of the author, with the exception of the following contributions:

- The spring-loaded graphite slipring method of electrical contact, referenced in **Section 3.2**, was designed and implemented by Matthew Li, under the direction of the author;
- The Matlab script referenced in **Section 3.4.4** was developed and implemented by Terrance Lau, based on the general approach devised by the author;
- Tribometer tests in Section **3.5.2** and stationary specimen tests in Section **6.3.2** were performed by Mr. Ali Khoei, under the direction of the author;
- SEM analysis (SE imaging and EDX spectroscopy) of pin tips and imprints in **Section 4.3.2** and the carbide insert in **Section 7.2.1** was conducted by Dr. Julia Dosbaeva, under the direction of the author;
- SIMS analysis of pin tips in **Section 4.3.2** was conducted by Winnats Scientific Services, under the technical direction of Dr. Robin West, with input from the author in terms of the regions of samples to inspect;
- XPS analysis of the pin tips in **Section 7.5** was conducted by Dr. Danielle Covelli, with input from the author in terms of the general nature of analyses and regions of the samples to inspect;
- Stationary specimen tests in Section **6.4.2.2** were performed by the author in collaboration with Mr. Ali Khoei and Mr. Maximiliano Miranda.

Furthermore, it should be clarified that the contents of **Chapter 7** are largely adapted from the previously published, original work of the author entitled "Manifestations of Reduced Tool-Chip Friction during Turning of AISI 1045 Steel with PVD-Coated Carbide Inserts", as published in *The International Journal of Advanced Manufacturing Technology* (Boyd & Veldhuis, 2016). More specifically:

- **Section 7.2** borrows from the *Experiments and Analysis* section of the above article, specifically from the *Short Duration Turning Tests* sub-section. The wording and flow of content in **Section 7.2** differs slightly from the article, but the content is otherwise equivalent, except that details regarding the ZrN/NbN coating have been omitted.
- **Section 7.3** is adapted from *Results and Discussion* section of the above article, specifically from the Short Duration Turning Tests sub-section. Similar to **Section 7.2**, the wording of content in **Section 7.3** differs slightly from the article, but the content is otherwise equivalent, the only exception that results and discussion regarding the performance of the ZrN/NbN coating have been omitted.
- **Section 7.4** is in part adapted from the first six paragraphs in the *Discussion* section of the above article, but expands significantly beyond the content in the article and presents a slightly different interpretation of results pertaining to chip colours for cutting tests performed at 100 m/min. It is difficult via words alone to cleanly decouple the content adapted from the article with the new concepts presented in **Section 7.4**; thus, the first six paragraphs of the *Discussion* section

of the article have been reproduced in **Appendix B**, for the sake of comparison and transparency.

- Note that the concepts in paragraph two of the *Discussion* section of the article have been incorporated into **Section 2.3.2** paragraph 2 and **Section 2.3.4** paragraphs 1 and 3, as they are a discussion on existing concepts in the literature.

It should be further clarified that the aforementioned article (Boyd & Veldhuis, 2016) presents results and discussion regarding long duration turning tests involving the subject coating and work materials; however, as these portions of the article do not directly align with the stated objectives of this dissertation, they were intentionally excluded.

Lastly, the results of friction tests reported in the article are presented briefly in **Section 4.3.1**, specifically, in **Figure 39 (a)**.

Permission to adapt the article in the above-described manner for use in this dissertation was obtained from Springer Nature. Permission to reproduce content of the article (as in **Appendix B**) was obtained from the Copyright Clearance Center. See **Appendix C** for details regarding both permissions.

1. INTRODUCTION

1.1 Context and Motivation

For well over a century, metal cutting has played an important role in diverse industries, particularly automotive and aerospace, whether applied directly in fabricating components used in end-products or indirectly in making the tools and dies used to support their production. Despite advances in new manufacturing technologies in recent years, notably additive manufacturing, metal cutting technology remains a strong contributor to the global economy. In 2018, the global market for machine tools, which encompasses both metal cutting and metal forming technologies, was valued at USD 108 Billion (Machine Tools Market: Global Industry Trends, Share, Size, Growth, Opportunity and Forecast 2019-2024, 2019). Likewise, in 2016, the global metal cutting tool market was valued at USD 36 Billion and estimated to reach USD 54.5 by the end of 2021 (Global Metal Cutting Tools Market 2017-2021, 2017).

Since its inception, metal cutting technology has advanced tremendously, not only in terms of the cutting tools employed, the work materials processed, and the material removal rates achievable; but also, in the robustness and level of automation featured in the machines governing the kinematics and dynamics of the cutting operation. However, the fundamental physics of metal cutting operations remains largely unchanged: a wedge-shaped tool feeds into a layer of work material, resulting in the shearing of that work material and its flow over the face of the tool in the form of a chip.

The flow of the chip over the face of the tool occurs under extremely high levels of mechanical stress, temperature, strain and strain rate. Coupled with the fact that the

contacting surface of work material in contact with the tool is chemically fresh or 'virgin', the tribological conditions present in metal cutting are among the most demanding in engineering practice and unique among manufacturing processes. The severity of friction between the tool and chip is known to have a direct effect on the ease and efficiency of chip formation, corresponding to the magnitude of force and thereby energy and machine power required in the process. As well, friction occurring between tool and chip contributes significantly to the temperature rise on the rake face of the tool, which in turn impacts the rate of tool wear and the quality of surfaces produced by the operation.

The application of thin, hard, protective coatings to the surface of cutting tools has resulted in tremendous gains in both tool life as well as material removal rates. Supported by a substrate material with good mechanical properties (e.g., hardness, toughness), the deposition of protective coatings by means of Chemical Vapour Deposition (CVD), Physical Vapour Deposition (PVD) and other techniques has allowed tailoring of the surfaces, where friction occurs, to possess properties different from and often superior to the substrate. Many of these coatings have evolved from simple monolayer binary types (e.g., TiN, TiC, ZrN) to multilayered and multi-component compositions wherein the variation of chemical ratios and layer thickness can begin to have significant influence on the wear resistance of the coating.

While the ultimate test of a coating performance remains cutting of work material, such tool wear tests are time-consuming and expensive. Though not trivial, it is of great economic interest to develop a bench-scale test to evaluate the potential effectiveness of one coating, or variant of coating, versus another in terms of its resistance to a particular

mechanism of wear inherent in the process of cutting a given work material. Such a bench-scale test should replicate as many of the tribological conditions present during a metal cutting process as is reasonably possible in order that the results of the bench-scale test stand the best chance of representing the performance of the coating subject to actual tool wear tests.

Of equal interest is the ability to quantify the coefficient of friction between a tool (or coating) and work material pair under levels of stress and temperature representative of the cutting process. While the coefficient of friction can itself be an indicator of coating performance in metal cutting, its incorporation into numerical models of metal cutting operations can be of value to both the academic community in its pursuit of improved models for scientific understanding of the metal cutting process; as well as to manufacturers using such models in an effort to predict cutting forces and machine power requirements, not to mention deleterious phenomena such as regenerative chatter, for greater success and efficiency in their operations.

The McMaster Manufacturing Research Institute (MMRI) has been engaged in cutting tool research for more than two decades now. In partnership with research associates in Japan, Russia and the United Kingdom, the MMRI has published numerous papers highlighting advanced PVD coatings with the ability to significantly improve tool life and/or material removal rates. Many of the advantages gained by using these coatings has been tied to the reduction in friction resulting from the formation of beneficial tribofilms on the surface of the cutting tool during the early-stages of tool wear.

To date, much of the fundamental evaluation of friction coefficient of these novel coatings has been performed by Professor Lev S. Shuster, from the Ufa State Aviation University in Moscow, Russia, who some time ago pioneered a novel adhesiometer for the characterization of friction between materials under heavy load and high temperature. Shuster's adhesiometer is a special class of pin-on-disc tribometers, herein referred to as on-axis rotation pin-on-disc tribometers: the contact zone is hemispherical, formed by loading a hard spherical-tipped pin against a soft, flat disc and imparting relative motion between the specimens about the axis of the pin. This is fundamentally different from conventional pin-on-disc tribometers, which feature a pin loaded against the disc some distance away from the axis of rotation of the disc, resulting in a circular or possibly a spiral wear track depending on the exact kinematics involved. These differences are depicted in **Figure 1** for clarity.

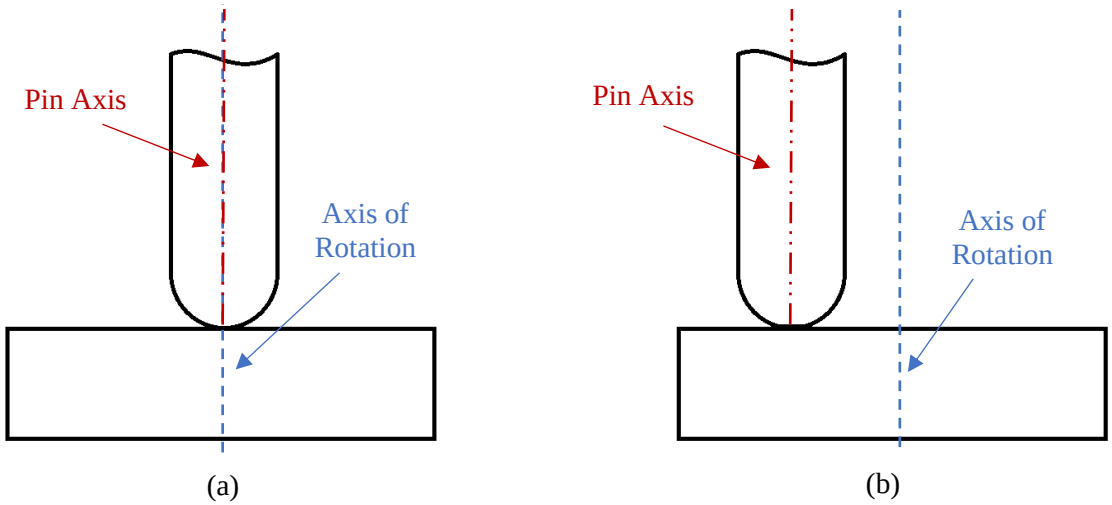

Figure 1: Schematic of (a) an on-axis rotation pin-on-disc tribometer vs. (b) a conventional pin-on-disc tribometer

Since 2008, the MMRI has been developing its own on-axis rotation pin-on-disc tribometer, gaining an understanding of the testing methodology needed to produce repeatable results that correlate well with metal cutting. The initial efforts were detailed by Biska (2010), expanded upon by Boyd (2012) and later by Khoei (2019).

1.2 Research Objectives

The objectives of the research outlined in this dissertation are three-fold:

i) Increase the understanding of the evolution of the contact zone between pin and disc, both macroscopically and microstructurally, during on-axis rotation pin-on-disc tribometer tests under varying operating conditions;

ii) Establish a means of more accurate estimation of the temperature at the contact zone during an on-axis rotation pin-on-disc tribometer test, which is physically inaccessible for direct measurement; and

iii) Study the correlations between the outputs of on-axis rotation pin-on-disc tribometer tests with those of metal cutting processes featuring the same tool (substrate + coating) and work material pair.

1.3 Structure of the Dissertation

The dissertation is divided into eight chapters, the first chapter being the present introduction. The content of the other chapters is summarized in the following paragraphs.

Chapter 2 presents a review of literature, touching on relevant topics in metal cutting theory and application, with a focus on the effects of tool-chip friction on the fundamentals

of the cutting process. Additionally, an overview of Shuster's adhesiometer is presented, along with details of the separate works of Biksa (2010) and Boyd (2012) in developing a heavy-load, high-temperature on-axis rotation pin-on-disc tribometer inspired by this original design. Lastly, gaps in the academic literature are identified.

Chapters 3 and **4** address the first objective. **Chapter 3** presents an overview of the experimental procedures and methodology developed, followed by a series of studies focused on understanding the growth of the imprint formed in the disc of work material during on-axis rotation pin-on-disc tribometer tests, particularly at elevated temperatures. **Chapter 4** presents experimental work between uncoated and PVD-coated cemented tungsten carbide pins in contact with discs of different work materials, SAE J434 D5506 Ductile Iron and as AISI 1045 Steel, with a focus on microstructural analysis of the imprints and the surrounding work material in the disc coupled with analyses of the chemical species present on select pin tips.

Chapter 5 transitions between the first two objectives: important observations regarding the imprint microstructure and diameter as a function of temperature are highlighted for some of the experimental results with AISI 1045 Steel presented in the previous chapter, raising questions as to the real temperature at the pin-disc interface. **Chapter 6** builds on this, developing and implementing a numerical model for the temperature distribution at and in the vicinity of the pin disc interface, in support of the second objective.

Chapter 7 addresses the third and final objective, presenting the results of short duration turning tests involving AISI 1045 Steel and the same tool/coating materials that

were explored in on-axis rotation pin-on-disc tribometer tests presented in **Chapter 4**. Empirical evidence of reduced friction in characteristic outputs of the turning process are correlated with friction coefficient results from the tribometer tests. An attempt is also made at relating tribofilm formation on the rake surface of the cutting tools to those observed on the pin tip during elevated temperature on-axis rotation pin-on-disc tribometer tests.

Finally, **Chapter 8** summarizes the major findings and contributions detailed in the previous chapters and outlines potential improvements and directions for further exploration.

2. BASIC CONCEPTS & LITERATURE REVIEW

2.1 Fundamentals of Friction

2.1.1 Classical Friction

In its most general sense, friction can be understood as the resistance to tangential motion experienced at the interface between two adjacent bodies as one moves relative to the other. Referring to **Figure 2**, the resistive or friction force $\boldsymbol{F_f}$ acting tangential to the interface between the two bodies is well known to be proportional to the normal force $\boldsymbol{F_n}$ acting in the normal direction, or perpendicular, to that same interface. For many practical applications, the proportionality is constant and referred to as the coefficient of friction $\boldsymbol{\mu}$, which is expressed as in **Eq. 2.1.1.1**, commonly known as Amonton's law.

$$\boldsymbol{\mu = \frac{F_f}{F_n}} \qquad \textbf{Eq. 2.1.1.1}$$

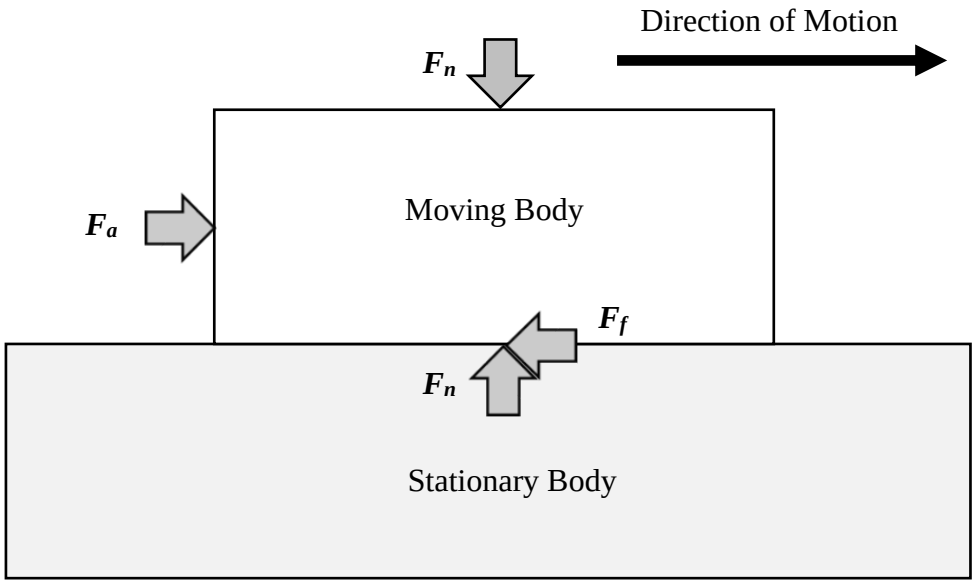

Figure 2: Depiction of Normal Force F_n and Friction Force F_f acting on a Moving Body as it slides in contact with a Stationary Body

When the friction force and normal force are normalized by the apparent area $\boldsymbol{A_a}$ over which the two bodies are in contact, the coefficient of friction can also be expressed in terms of shear stress $\boldsymbol{\tau}$ and normal stress $\boldsymbol{\sigma}$ acting at the interface between those bodies, as per **Eq. 2.1.1.2**.

$$\boldsymbol{\mu = \frac{\tau}{\sigma}} \qquad \textbf{Eq. 2.1.1.2}$$

In reality, under most practical applications, the real area of contact $\boldsymbol{A_r}$ between two bodies is confined to local asperities (irregularities in the surface of either body at the microscopic level) and is considerably smaller than the apparent area $\boldsymbol{A_a}$. Under sufficiently low loads, the real area of contact can be estimated as per **Eq. 2.1.1.3**

$$\boldsymbol{A_r = \frac{F_n}{H}} \qquad \textbf{Eq. 2.1.1.3}$$

where $\boldsymbol{H}$ is the hardness of the asperities (Shaw M. C., Friction, 1984). As the normal force increases, the original contacting asperities further deform and flatten out, enabling new asperities to contact and contribute to supporting the load. In effect, the number and size of contacting asperities between each body, i.e., the real area of contact, increases as the normal force between those bodies increases. The real area of contact will also tend to increase when sliding is initiated, and this effect is known as junction growth (Shaw M. C., Friction, 1984).

2.1.2 Friction under Heavy Load

When the normal force is sufficiently large, the zones of plastic deformation supporting contacting asperities can begin to overlap, with the result that subsurface flow will begin

and the rate of growth of asperities and the real area of contact with increasing normal load will diminish. Shaw (Friction, 1984) argued that this should occur around $\boldsymbol{A_r / A_a}$ = 1/3 and cites other studies that confirmed this empirically. Shaw, Ber and Mamin (1960) demonstrated that as the normal load (and normal stress) increases sufficiently, the relationship between shear stress and normal stress becomes nonlinear, as depicted in **Figure 3**.

When the applied load is such that the stress conditions at the interface between two sliding bodies fall within Regime II of **Figure 3**, the term "coefficient of friction" should not be thought of in the same way as in Regime I. As Shaw points out, the "coefficient of friction" decreases as the normal load increases within Regime II, even though the effective shear stress over the apparent area of contact continues to increase. Likewise, in Regime III, the shear stress is completely independent of the normal stress, but the "coefficient of friction" will appear to decrease with further increases in normal load (Friction, 1984).

It follows from the discussion above that when comparing the "coefficient of friction" for two different material pairs (or "tribopairs") operating under conditions similar to Regime II in **Figure 3**, where subsurface plastic flow begins to come into play, examination of the normal stress acting between the tribopairs should be considered. That one tribopair exhibits a lower "coefficient of friction" than another may simply reflect that it was subject to a higher level of normal stress.

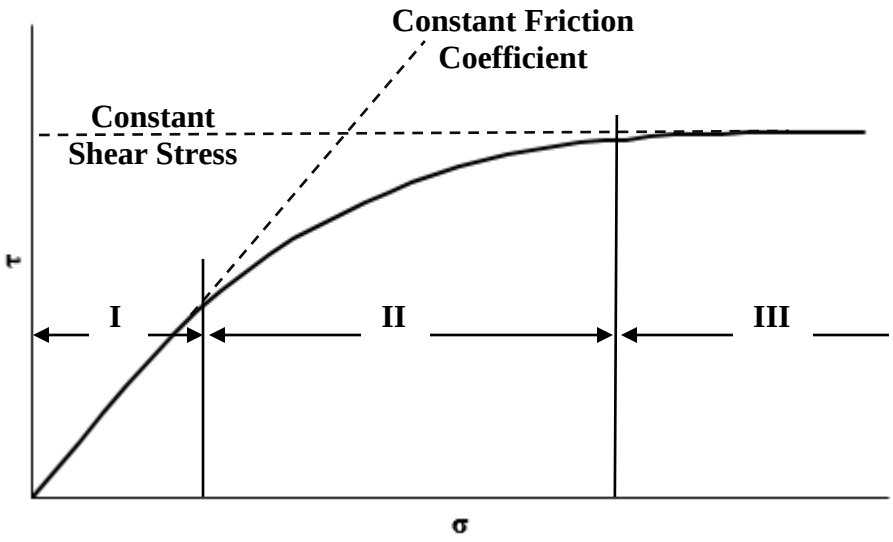

Figure 3: Variation in Shear Stress with Increasing Normal Stress at the Interface between Two Sliding Bodies (adapted frrom (Shaw, Ber, & Mamin, 1960))

2.2. Fundamentals of Cutting

2.2.1 Orthogonal Cutting

While virtually all cutting operations have more complex geometric and kinematic configurations, a great deal of theoretical understanding has been gained by focusing on the simpler configuration of orthogonal cutting, in which the tool edge is straight, normal to both the cutting direction and feed direction (Trent & Wright, The Essential Features of Metal Cutting, 2000), as depicted in **Figure 4**.

2.2.2 The Primary Shear Zone

As the wedge-shaped tool advances through the workpiece, material ahead of the cutting edge of the tool undergoes shear and transitions into a chip that flows over the rake

face of the tool and eventually separates. For simplicity, in the absence of a built-up edge on the tool rake face and under conditions leading to a continuous chip (Trent & Wright, Forces and Stresses in Metal Cutting, 2000), such shear can be thought of as occurring along a plane ***AB*** extending from the cutting edge of the tool (***A***) to the transition point between the free surface of the uncut work material and the chip (***B***). This plane is referred to as the shear plane, which forms an angle $\boldsymbol{\varphi}$ with the direction of tool motion through the work material, as shown in **Figure 5**. In more sophisticated models, it is recognized that shear ahead of the tool occurs within a finite volume, often referred to as the primary shear zone, but the concept of a shear plane is a simple starting point for discussion.

Assuming that the cutting tool is sharp (i.e., negligibly small cutting edge radius and no wear on the flank face of the tool), the force $\boldsymbol{F_s}$ involved in shearing work material along the shear plane can be calculated as per **Eq. 2.2.2.1** (Trent & Wright, Forces and Stresses in Metal Cutting, 2000) based on evaluation of force components $\boldsymbol{F_c}$ and $\boldsymbol{F_t}$, which act on the tool in the cutting direction and feed direction, respectively, as well as the shear plane angle $\boldsymbol{\varphi}$, as depicted in **Figure 6**.

$$\boldsymbol{F_s = F_c \cos\varphi - F_t \sin\varphi} \qquad \textbf{Eq. 2.2.2.1}$$

Force components $\boldsymbol{F_c}$ and $\boldsymbol{F_t}$ can be measured by means of a suitable tool dynamometer. The shear plane angle $\boldsymbol{\varphi}$ is most reliably obtained by means of metallographic analysis of cross-sections of the chip and work piece obtained from experiments employing quick-stop devices. Such devices rapidly disengage the cutting tool from the work material so that the shear deformation patterns present in the chip and work material reflect those present during actual cutting.

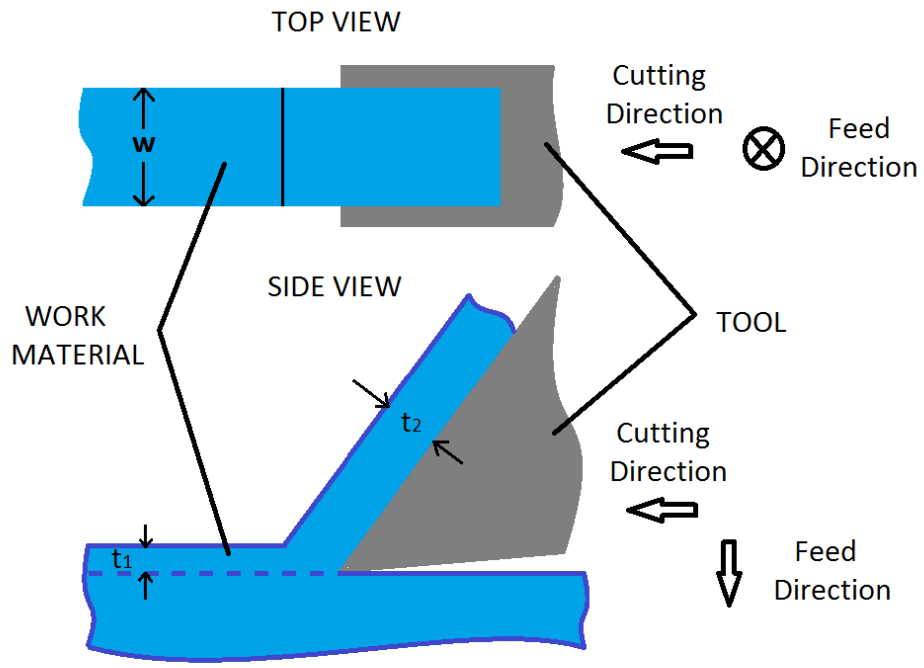

Figure 4: Basic Schematic of Orthogonal Cutting

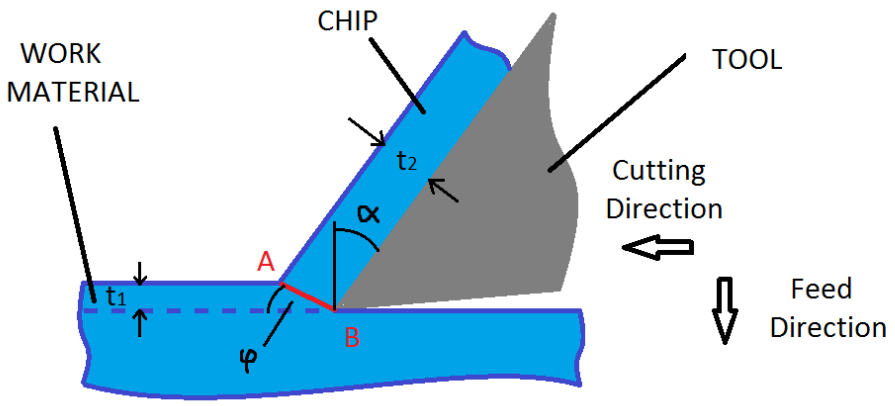

Figure 5: More Detailed Schematic of Orthogonal Cutting

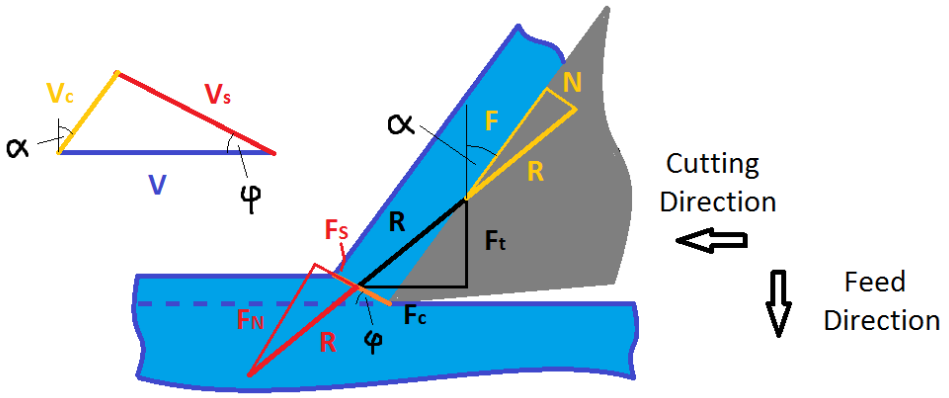

Figure 6: Velocity and Force Diagrams for Orthogonal Cutting

The area of the shear plane A_s can be calculated as per **Eq. 2.2.2.2** (Trent & Wright, Forces and Stresses in Metal Cutting, 2000), with knowledge of the uncut chip thickness t_1, uncut chip width w and the shear plane angle.

$$A_s = \frac{t_1 w}{\sin \varphi} \qquad \textbf{Eq. 2.2.2.2}$$

Naturally, it follows that the shear stress k_s required to shear work material along the shear plane, and thus form the chip, is given by **Eq. 2.2.2.3** (Trent & Wright, Forces and Stresses in Metal Cutting, 2000), shown below.

$$k_s = \frac{F_s}{A_s} \qquad \textbf{Eq. 2.2.2.3}$$

Trent and Wright (Forces and Stresses in Metal Cutting, 2000) note that, for a given metal or alloy, the shear stress k_s acting along the shear plane is relatively insensitive to the cutting speed and feed rate (the latter being equivalent to the uncut chip thickness t_1). This implies that, for a given metal or alloy, the force F_s acting along the shear plane is dependent on the area of the shear plane A_s. It follows then that, for a given metal or alloy as well as constant uncut chip thickness t_1 and uncut chip width w, the force F_s acting along

the shear plane depends only on the shear plane angle $\boldsymbol{\varphi}$. Thus, any changes in the cutting setup that have the effect of increasing the shear angle will effectively reduce the force required for chip formation. Examples of such changes could include a different cutting fluid, a different tool material, or a different tool geometry (notably rake angle).

Other implications of a larger shear plane angle include a higher velocity of the chip $\boldsymbol{V_c}$ flowing over the rake face of the tool (see **Eq. 2.2.2.4**, where $\boldsymbol{V}$ is the velocity of work material flowing toward the tool edge and $\boldsymbol{\alpha}$ is the rake angle of the tool) as well as a reduced chip thickness $\boldsymbol{t_2}$ (see **Eq. 2.2.2.5**) (Trent & Wright, The Essential Features of Metal Cutting, 2000). It should be clarified that both **Eq. 2.2.2.4** and **Eq. 2.2.2.5** assume a perfectly rectangular profile of the chip and neglect the small increase in chip width relative to the uncut chip width that typically occurs in actual cutting (Trent & Wright, The Essential Features of Metal Cutting, 2000).

$$\boldsymbol{V_c = \frac{\sin \varphi}{\cos(\varphi - \alpha)} V} \qquad \textbf{Eq. 2.2.2.4}$$

$$\boldsymbol{t_2 = \frac{\cos(\varphi - \alpha)}{\sin \varphi} t_1} \qquad \textbf{Eq. 2.2.2.5}$$

As an alternative to quick stop devices, the shear plane angle can also be estimated as per **Eq. 2.2.2.6** (Trent & Wright, The Essential Features of Metal Cutting, 2000) based on careful evaluation of the mean chip thickness $\boldsymbol{t_2}$ and knowledge of the uncut chip thickness $\boldsymbol{t_1}$ and tool rake angle $\boldsymbol{\alpha}$. For simplicity, **Eq. 2.2.2.6** uses the term $\boldsymbol{r}$, known as the ***chip thickness ratio***, which is the ratio of the uncut chip thickness to the mean chip thickness, as expressed in **Eq. 2.2.2.7** (Trent & Wright, The Essential Features of Metal Cutting, 2000).

$$\tan \varphi = \frac{r \cos \alpha}{1 - r \sin \alpha} \qquad \textbf{Eq. 2.2.2.6}$$

$$r = \frac{t_1}{t_2} \qquad \textbf{Eq. 2.2.2.7}$$

Eq. 2.2.2.5 can be rearranged and substituted into **Eq. 2.2.2.7** to express the chip thickness ratio as a function of the shear plane angle and rake angle, as expressed in **Eq. 2.2.2.8** (Trent & Wright, The Essential Features of Metal Cutting, 2000).

$$r = \frac{\sin \varphi}{\cos(\varphi - \alpha)} \qquad \textbf{Eq. 2.2.2.8}$$

The shear strain occurring along the shear plane can be expressed as in **Eq. 2.2.2.9** (Trent & Wright, The Essential Features of Metal Cutting, 2000).

$$\gamma = \frac{\cos \alpha}{\sin \varphi \cos(\varphi - \alpha)} \qquad \textbf{Eq. 2.2.2.9}$$

Figure 7 and **Figure 8** graphically display **Eq. 2.2.2.8** and **Eq. 2.2.2.9**, respectively, for tools of different rake angle **φ**. A few observations are noteworthy:

- As the tool rake angle increases, the shear strain along the shear plane (at a given shear plane angle) decreases.
- As the tool rake angle increases, the minimum shear strain occurs at an increasingly higher shear plane angle.
- For a given tool rake angle, the minimum shear strain coincides with a chip thickness ratio ***r = 1***.
- For a given tool rake angle, the chip thickness ratio increases with increasing shear plane angle.

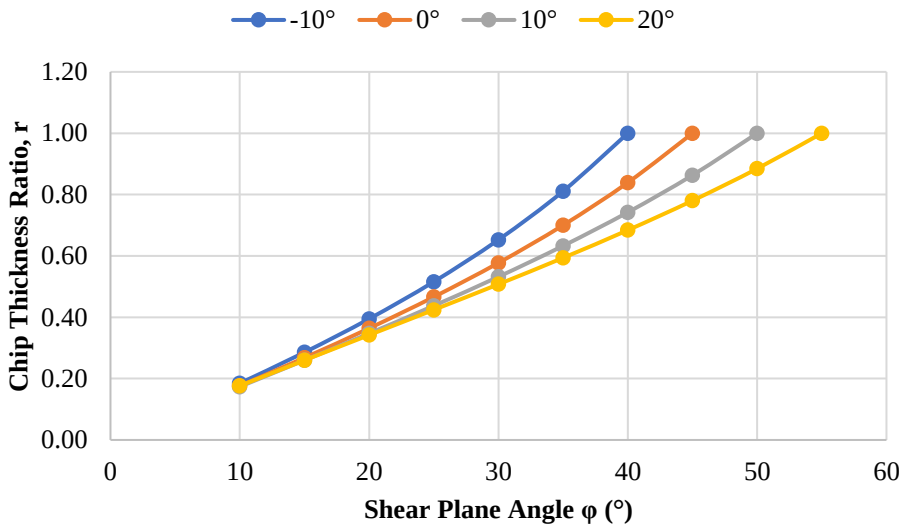

Figure 7: Chip Thickness Ratio, r, as a function of Shear Plane Angle, as per Eq. 2.2.2.8

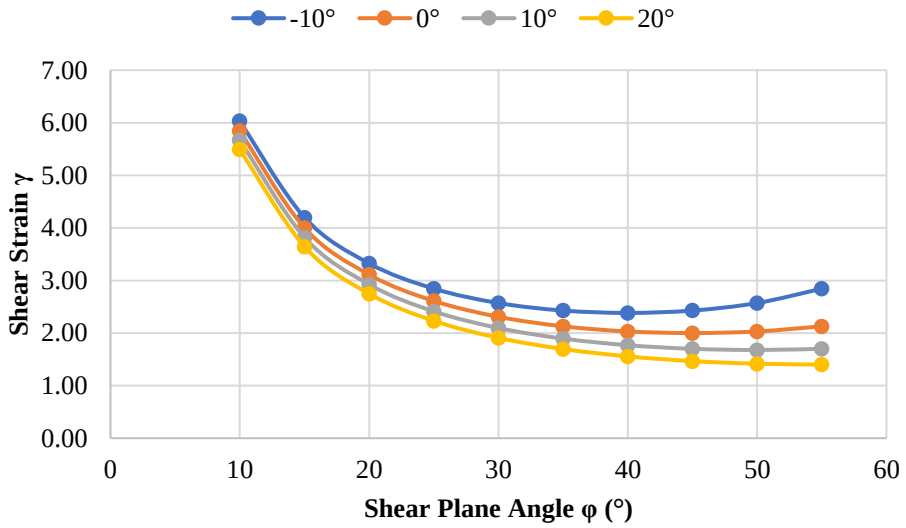

Figure 8: Shear Strain along the Shear Plane as a function of Shear Plane Angle, as per Eq. 2.2.2.9

In practice, the chip thickness ratio is always less than unity ($\boldsymbol{r < 1}$) (Trent & Wright, The Essential Features of Metal Cutting, 2000), which means that the mean chip thickness will always be greater than the uncut chip thickness, and the chip velocity $\boldsymbol{V_c}$ will always be less than the work material velocity $\boldsymbol{V}$.

2.2.3 The Secondary Shear Zone

In early analyses, such as the model proposed by Merchant (1945), the flow of the chip across the rake face of the tool was assumed to occur under conditions of sliding friction (i.e., Amonton's law, or **Eq. 2.1.1**, holds true). In this case, the friction coefficient $\boldsymbol{\mu}$ acting at the interface between the chip and the rake face of the cutting tool can be calculated as per **Eq. 2.2.3.1**.

$$\boldsymbol{\mu = \frac{F}{N} = \frac{F_c \sin\alpha + F_t \cos\alpha}{F_c \cos\alpha + F_t \sin\alpha}} \qquad \textbf{Eq. 2.2.3.1}$$

Per **Figure 6**, $\boldsymbol{F}$ and $\boldsymbol{N}$ are the force components resolved tangential and normal to the tool rake face, while $\boldsymbol{F_c}$ and $\boldsymbol{F_t}$ are the force components acting in the cutting and feed directions, respectively. Shaw (Friction, 1984) points out that the "coefficient of friction", evaluated per **Eq. 2.2.3.1**, is typically quite high ($\boldsymbol{\mu} > 1$) and is dependent upon the rake angle of the cutting tool used (in fact, $\boldsymbol{\mu}$ increases as the rake angle becomes increasingly positive), all other cutting conditions held constant. The latter observation is in conflict with Amonton's law (**Eq. 2.1.1.1**) but can be understood in terms of **Figure 3** when one recognizes that the stress conditions acting on the rake face of the cutting tool are largely those of Regime II and III (Shaw M. C., Friction, 1984) and that changes in the rake angle will have an influence on the mean normal stress acting on the tool.

In contrast to Merchant's assumption of sliding conditions between tool and chip, Trent has written extensively on the phenomenon of seizure dominating the tool-chip interface (Metal cutting and the tribology of seizure: I Seizure in metal cutting, 1988), (Metal cutting and the tribology of seizure: II Movement of work material over the tool in metal cutting,

1988), (Metal cutting and the tribology of seizure: III Temperatures in metal cutting, 1988). In short, evidence points to the tool and chip being in such intimate contact and so strongly bonded that sliding at the tool-chip interface does not occur, except under very limited conditions (e.g., at very low cutting speeds and with the aid of lubricants) (Trent & Wright, The Essential Features of Metal Cutting, 2000).

Under conditions of seizure, the relative motion or 'friction' actually occurs within a finite thickness of the chip immediately adjacent to the tool-chip interface, known as a flow zone or secondary shear zone. Typically, on the order of 25 – 50 μm in thickness (Trent & Wright, The Essential Features of Metal Cutting, 2000), the flow zone is characterized by steep velocity gradients, approaching $\boldsymbol{V_c}$ towards the bulk of the chip and zero towards the tool-chip interface. Shear strain within the flow zone is exceptionally high, much more so than along the shear plane, and inversely proportional to the distance from the tool-chip interface. Trent and Wright report that typical shear strains $\boldsymbol{\gamma}$ along the shear plane range from about 2 to 4, whereas in the flow zone they can vary from 20 to >600 (Heat in Metal Cutting, 2000). The deformation within the flow zone, especially adjacent to the tool-chip interface, is so severe that grains and other structural features are typically unresolvable by optical microscopy, likely reflecting recrystallization (Trent & Wright, The Essential Features of Metal Cutting, 2000).

Though only occurring in certain alloys and typically at lower, more modest cutting speeds (Trent & Wright, The Essential Features of Metal Cutting, 2000), the formation of a built-up edge (BUE) is another common manifestation of seizure at the tool-chip interface. As its name implies, the BUE is a build up of layers of severely strain-hardened

work material on the cutting edge and adjacent portions of the rake face. Due to the intensive strain-hardening it has undergone, the BUE functions as an extension of the tool: work material shears along the shear plane ahead of the BUE and the chip flows/shears over the upper regions of BUE, only contacting the tool rake face some distance away from the cutting edge beyond the limits of the BUE. Similarly, the formation of the machined surface occurs at the leading edge of the BUE instead of at the cutting edge and flank face of the tool.

Unfortunately, the BUE is dynamic and unstable, growing over time and often fully or partially collapsing, with fragments dragging across the rake face or flank face of the tool with the chip or machined surface, and then building itself up again as additional work material flows over it and strain hardens. Due to its dynamic structure, machining under conditions involving a BUE typically lead to poorer surface finish (Trent & Wright, Machinability, 2000) and is thus usually undesirable. As the cutting speed or feed rate is increased, the BUE gradually decreases in intensity and is replaced by a flow zone (Trent & Wright, Heat in Metal Cutting, 2000).

Because the BUE functions as an extension of the tool, possessing an effective rake angle $\boldsymbol{\alpha}$ different from that of the tool, use of **Eq. 2.2.3.1** for quantifying changes in tribological conditions at the tool-chip interface under conditions when a BUE is present should be exercised with caution.

2.2.4 Stress Distribution on the Cutting Tool

Various researchers have identified that the approximate distribution of normal stress and shear stress acting on the rake face of the tool resembles that shown in **Figure 9**, where $\boldsymbol{l_c}$ denotes the tool-chip contact length. In effect, the coefficient of friction is not at all constant over the tool-chip contact length, such that $\boldsymbol{\mu}$ expressed in **Eq. 2.3.1** is more appropriately referred to as the "average coefficient of friction".

The contact length is commonly divided into "sticking" and "sliding" portions. The "sticking" portion of the contact length extends from the tool tip to approximately one half the contact length and is characterized by a generally constant shear stress despite significant decay of the normal stress moving away from the tool tip, corresponding to Regime III of **Figure 3**. It is worth noting that the shear stress has often been observed to decrease toward zero close to the cutting edge of the tool (Trent & Wright, Forces and Stresses in Metal Cutting, 2001).

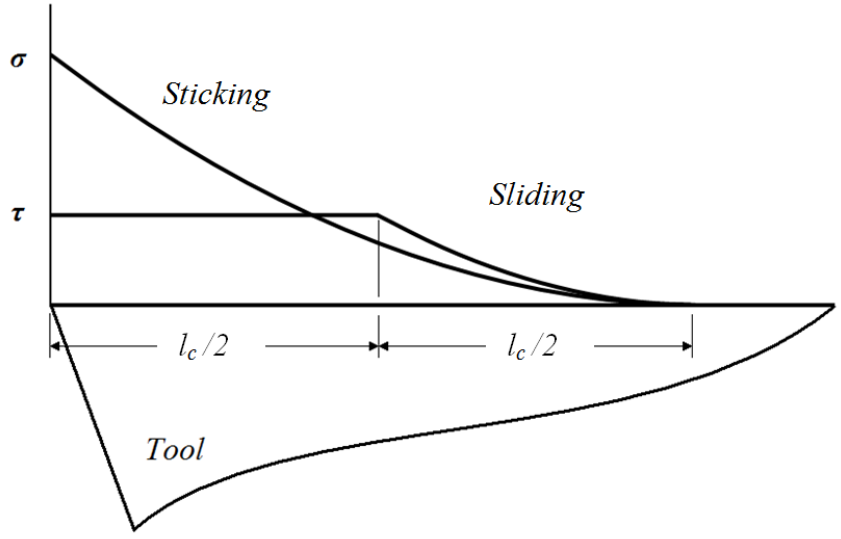

Figure 9: Stress Distribution and Sticking vs. Sliding Zones on the Tool Rake Face

In the "sliding" portion, Amonton's law is assumed to hold; however, in reality, some portion of the tool-chip contact length should transition between "sticking" and "sliding" and would correspond to Regime II in **Figure 3**.

The magnitude of stress experienced by the cutting tool will depend on the strength of the work material being cut. Trent and Wright (Trent & Wright, Forces and Stresses in Metal Cutting, 2001) list a typical mean compressive stress of 770 MPa acting on the tool when cutting medium carbon steel. Based on the approximate variation in normal stress acting along the tool-chip contact length shown in **Figure 9**, the peak compressive stress at the tool tip can be expected to be approximately 2 times higher.

2.2.5 Heat Generation during Cutting

The by-product of plastic deformation is heat. Most metal cutting operations involve a considerable amount of plastic deformation, concentrated in the primary shear zone and secondary shear zone (or 'flow' zone). As wear of the cutting tool edge progresses and a wear land develops, an increasing amount of plastic deformation can also occur in this so-called tertiary shear zone. The amount of heat generated in each of these zones depends on a) the mechanical properties of the work material, b) the rate of shear strain in each zone, being largely dependant on the cutting speed of the tool edge advancing through the work material, and c) the length of the zone over which shear deformation occurs, being largely dependent on both the tool feed as well as the tool geometry, specifically the rake angle. The depth/width of cut also affects the area over which plastic deformation occurs, and

thereby the amount of heat generation, but this is neglected in orthogonal cutting which considers only a slice of the tool engaged with the work material.

While heat generation can be thought to have a beneficial effect on the ease of cutting a material, insomuch as the mechanical properties of a material governing its resistance to plastic deformation (i.e., its strength) decrease as its temperature increases, the heat generated must flow somewhere – whether into the body of the chip, into the volume of uncut work material, or into the tool – and this can lead to adverse effects in some instances. Flow of heat into the chip is generally preferable: the heat is carried away with great speed as the chip leaves the cutting zone and the tool. Flow of heat into the work material is also not a large concern, although too much heat flow can begin to influence residual stresses in the work surface and lead to dimensional changes in the part that must be accounted for in production. Flow of heat into the tool is the greater concern in most situations, since the strength of the tool will eventually weaken and wear processes generally accelerate as the tool temperature increases.

As noted by Trent and Wright (Heat in Metal Cutting, 2000), at lower cutting speeds, where plastic deformation in the chip is characterized by dislocation movement and strain hardening leads to built-up edge formation, temperature rises rapidly with increases in temperature and the peak temperature in the tool occurs at the cutting edge. However, when cutting speed and likewise temperatures increase sufficiently, strain hardening and built-up edge formation ceases and is replaced by a flow zone or thermoplastic shear band, with shear strain governed by crystal recovery. Past this critical point, further increases in cutting speed see more gradual increases in cutting temperature and peak temperature

occurs some distance away from the cutting edge, at approximately the mid-point along the tool-chip contact length. For steels, this critical temperature is approximately 600 – 675 °C. In general, peak temperatures in the range of 500 – 1000 °C are typical for a wide range of cutting materials and cutting conditions.

As the length of wear land on the flank face of the tool increases, an increasing amount of heat is generated there (Trent & Wright, Heat in Metal Cutting, 2000), which may cause the peak temperature in the tool to advance towards the cutting edge, often leading to catastrophic tool failure shortly thereafter.

2.3 Control of Friction and Forces in Cutting Operations

2.3.1 Motivation

Generally speaking, the reduction of friction in cutting operations is desirable from an efficiency standpoint. Removal of material from a workpiece via chip formation is the goal of a cutting operation. As tool-chip friction impedes the flow of the chip over the rake face of the cutting tool, reducing this friction implies that cutting will occur more efficiently. Furthermore, tool-chip friction in the secondary shear zone is the dominant source of heat flowing into the cutting tool and raising its temperature. Most wear mechanisms intensify with increases in temperature, and likewise forces tend to increase with tool wear (particularly flank wear, causing increased deformation in the tertiary shear zone), thus providing further motivation to reduce friction in cutting.

To be clear, the term "tool-chip friction" is herein used synonymously with the "friction force", i.e., the component of force acting tangentially along the rake face of a cutting tool,

when cutting a given work material under a given feed rate and depth of cut. Accordingly, a reduction in tool-chip friction does not imply an equivalent reduction in the so-called "coefficient of friction" detailed earlier in the Merchant model. Likewise, a reduction in tool-chip friction does not necessarily imply reduced seizure between tool and chip, since the friction force often arises within the finite volume of the secondary shear zone and not at the actual tool-chip interface.

Strongly tied to tool-chip friction (i.e., the "friction force") is the concept of the tool-chip contact length, which is the length along the tool rake face over which the chip is engaged with the tool, or over which tool-chip friction occurs. Trent and Wright note that "the consequence of increasing either the shear yield strength at the rake face or the contact area (length) is to raise not only the feed force $\boldsymbol{F_t}$ but also the cutting force $\boldsymbol{F_c}$" (Forces and Stresses in Metal Cutting, 2000).

Forces in general, and therefore the friction force, are very sensitive to the work material being cut as well as the feed rate (uncut chip thickness) and depth of cut (or width of cut). With the exception of work material, more specifically the effect of minor chemical composition changes to otherwise the same family/class of work material, these variables will be excluded from discussion. The effects of other variables, specifically different variables in the cutting process, on tool-chip friction are herein discussed.

2.3.2 The Effect of Cutting Speed

Built-up edge formation and a flow zone at the tool-chip interface are both evidence of intensive seizure between tool and work materials. The presence of a built-up edge is

largely dependent upon the cutting speed employed in the operation. At extremely slow cutting speeds, a built-up edge may be absent, but as cutting speed is increased, built-up edge formation becomes prominent. With further increases in cutting speed, the built-up edge transitions to a built-up layer and/or flow zone at the tool-chip interface. It should be noted as well that with increases in feed rate, the initial appearance of a built-up edge and its transition to a flow zone occur at comparably lower cutting speeds.

All other variables held constant, the effect of increasing cutting speed is to increase the temperature within the body of the chip as well as at the tool-chip interface. Thus, the effect of cutting speed on tool-chip friction is primarily driven by temperature changes in the secondary shear zone and tool-chip interface influencing the flow velocity field within the chip. Bandyopadhyay (1984) demonstrated that built-up edge formation could be significantly reduced, even eliminated, during machining of Cr-alloy steel by heating the tool tip to upwards of 600 °C via electrical current, such that the tool-chip interface temperature exceeded the recrystallization temperature of the steel workpiece being cut.

At relatively low cutting speeds, increases in cutting speed can lead to appreciable reductions in forces. At higher cutting speeds, however, reductions in forces level off with further increases in cutting speed (Trent & Wright, Forces and Stresses in Metal Cutting, 2000). With regards to the tool-chip contact length, Friedman & Lenz (1970) note that above 20 m/min (presumably for steels – the referenced papers were not reviewed by the present author), the natural contact length tends to decrease as cutting speed increases.

2.3.3 The Effect of Tool Geometry

The tool rake angle has a significant effect on the forces experienced during cutting. All other variables held constant, use of a more positive rake angle tool tends to increase the primary shear plane (this can be inferred from **Figure 8**, but also confirmed via consultation of any standard textbook on metal cutting) and thereby reduce forces. As mentioned earlier, the apparent coefficient of friction tends to increase as the rake angle increases. This should not be misinterpreted as suggesting that tool-chip friction increases. Both the friction force $\boldsymbol{F}$ and the normal force $\boldsymbol{N}$ acting on the tool will decrease as the rake angle increases; however, the "coefficient of friction" (**Eq. 2.2.3.1**) is the ratio of these two force components.

Forces involved with cutting reduce with increasing rake angle because the shear plane angle increases, resulting in a smaller shear plane area. Another consequence of the increase in shear plane angle is an increase in chip thickness ratio (i.e., thinner chips of thickness $\boldsymbol{t_2}$ possessing higher velocity $\boldsymbol{V_c}$ flow over the tool rake face). However, the cutting edge of the tool becomes weaker as the rake angle increases, so there are limitations as to how small this can be made without jeopardizing the tool.

The use of restricted contact tools underscores the importance of the tool-chip contact length on tool-chip friction. A restricted contact tool is one in which a secondary rake face is ground (at an increased angle relative to the primary rake face) some distance back from the cutting edge. Restricted contact tools can be considered predecessors to modern-day chip-breaker type cutting inserts. As summarized by Friedman & Lenz (1970), the effects

of reducing the length of the primary rake face (i.e., the artificially controlled contact length) include:

a) Reduced forces (i.e., reduced "friction force");
b) Reduced "coefficient of friction";
c) Reduced tool-chip interface temperature;
d) Increased chip thickness ratio (i.e., thinner, faster flowing chips);
e) Increased shear plane angle; and
f) Increased tool life (more specifically, reduced width of flank wear land for the same volume of machined material).

However, as noted, the influence of built-up edge as well as contact between tool and chip on the secondary rake face may not have been properly accounted for in all of the referenced studies (Friedman & Lenz, 1970).

2.3.4 The Effect of Tool Material

The thermal properties of the tool, in particular the thermal conductivity, have a strong influence on the tool-chip contact length. Friedman & Lenz (1970) observed that tool-chip contact length increased as the thermal conductivity of the cutting tool increased, over a range of cemented carbide tools with different thermal conductivity. Specifically, these results were obtained when cutting SKF 1550 steel (0.35% C) without coolant at cutting speeds of 123 m/min and 185 m/min, 0.32 mm/rev feed rate and 2.5 mm depth of cut. At much lower cutting speeds (< 13 m/min), the measured tool-chip contact length showed no correlation with tool material thermal conductivity. The authors postulated that a tool

material with lower thermal conductivity better restricts heat from conducting into the tool body, resulting in a higher temperature-field in the tool-chip contact zone and altered chip flow velocity field that favours more chip curl and, thus, a shorter tool-chip contact length.

In their summary paper on chip control, Jawahir & van Luttervelt affirmed this hypothesis, stating "cutting tool materials with low thermal conductivity show short contact lengths and produce chips with small radii" (1993). They reason that the chip behaves as a thermal bi-metallic spring and that thermal stresses resulting from thermal gradients across the chip thickness are responsible for chip curl, with steeper gradients (stemming from higher tool-chip interface temperatures) driving chips to curl more tightly.

Friedman & Lenz later reported that cutting with tools of lower thermal conductivity involved lower forces and a reduced rate of crater wear (1973). Resolving the measured forces into components normal and tangential to the rake face, they observed a highly linear relationships between normal force and tool thermal conductivity. The correlation was still evident between friction force and tool thermal conductivity, albeit with greater scatter, which was attributed to variation in the sticking zones and sliding zones in the tool-chip contact length for each tool.

Balaji, Sreeram, Jawahir, & Lenz (1999) observed similar trends with grooved tools made of cemented carbide, possessing thermal conductivity values spanning 32 – 92 W/mK, when cutting AISI 1045 steel at 100 m/min under feed rates of 0.25 – 0.35 mm/rev. More specifically, cutting with tools possessing higher thermal conductivity resulted in overall longer tool-chip contact length (considering contact on both the primary and secondary rake face) and higher forces. Interestingly, the length of the sliding region of

tool-chip contact was seen to increase while the length of the sticking region was seen to decrease as the tool thermal conductivity increased. Over all conditions explored, the length of the sliding region was found to be greater than the length of the sticking region, being approximately 25% larger with the lowest thermal conductivity tool and about 70% larger with the highest thermal conductivity tool.

Except in rare circumstances, modern machining relies heavily on the use of coated tools, wherein the surface layers of a tool are of a fundamentally different microstructure and chemical composition than the bulk of the tool. Most often, such coatings (or multi-layer coatings) having been deposited by one or another variant of either chemical vapour deposition (CVD) or physical vapour deposition (PVD). While these coatings can possess very different thermal properties from the underlying tool substrate, there is also the potential that they exhibit different chemical compatibility/affinity for adhesion to the work material being cut. Thus, there is an opportunity for reduced seizure between tool and chip which can facilitate sliding at the tool-chip interface.

Candidates for low-friction coatings, over a range of application types, have included known lamellae-type materials (WS_2, MoS_2, graphite, h-BN) as well as low melting point metals, such as silver and indium (Donnet & Erdemir, 2004). The underlying mechanism for low friction in the former materials arises from shear-stress interactions between adjacent lamellae, often activated over specific temperature regimes and aided by the presence or absence of specific adsorbed chemical species (i.e., water vapour). As per soft (i.e., low melting point) metals, their low friction behaviour stems from a multiplicity of active slip planes and a tendency to not appreciably work harden during plastic work.

A wide array of hard ceramic-based materials based on carbides, nitrides and oxides form the other extreme of coating design, albeit the development focus on these has been more towards wear resistance than reduced friction (Donnet & Erdemir, 2004). However, among the class of hard coatings stands diamond and diamond-like coatings, which have gained increasing traction as a coating material for cutting inserts. In addition to their extreme hardness and abrasive wear resistance, diamond exhibits extreme low-friction characteristics. This behaviour is thought to arise primarily from passivation of the surface layers (dangling C bonds) by adsorbed hydrogen and hydroxyl groups due to tribochemical reactions involving the dissociation of H_2O in the surrounding environment (Konicek, et al., 2012). Regardless, the use of diamond or diamond-coatings as a cutting tool material can be extremely favourable in certain applications, specifically in cutting aluminum alloys wherein built-up edge formation can be largely reduced if not altogether eliminated (Trent & Wright, Machinability, 2000).

The McMaster Manufacturing Research Institute (MMRI) has contributed significantly to a class of PVD coatings one might refer to as adaptive or smart coatings, engineered to respond favourably to the adverse tribological conditions experienced by the tool during cutting to promote the formation of protective nano-scale films at the tool-chip interface. In particular, the TiAlCrSiYN/TiAlCrN class of coatings has enabled increases in both tool life as well as sustainable cutting speeds in the machining of hardened steels as well as nickel-base superalloys (Beake, et al., 2012), (Fox-Rabinovich, et al., 2010). Its success relies in part on its nanocrystalline structure, which provides ample intergranular diffusion pathways, as well as steep thermal gradients imposed upon it during machining, the result

of which is favourable tribochemical reactions at the tool-chip interface to form protective surface films comprised of Si-, Al- and Cr-based oxides. Such tribofilms are understood to possess a mixture of low thermal conductivity and low-friction characteristics.

2.3.5 The Effect of Work Material

Careful changes to the chemical composition of a given work material can also have a profound effect on tool-chip friction. Trent and Wright (Machinability, 2000) give an excellent overview of a range of "free-machining" grades of aluminum alloys, brasses and steels, outlining the current understanding of how the specific inclusions are thought to benefit the machining process.

Some of the improvements to "machinability" of these engineered alloys may be due to a reduction in ductility of the work material, resulting in earlier fracture of the chip – there is some acknowledgement of this possibility in the case of free-machining aluminum alloys (containing up to 0.5% addition of lead, bismuth and lead, or tin) and free-machining brass (containing up to 3% lead). However, there seems to be just as much evidence pointing to reduction of seizure at the tool-chip interface when machining these alloys, as well as free-machining steels (containing a few tenths of a percent of sulfur) and sulfur-containing brass (up to about 0.3%).

In some cases, the low-melting point metals exist as separate phases and thus may be drawn out into the secondary shear zone, wherein they are heated and melted. In the case of sulfur containing steels, the ribbon-like MnS formed on the tool rake face likely exhibits low shear-stress sliding. Interestingly, sulfur containing steel has only resulted in improved

machining with the use of steel-grade (i.e., TaC and TiC containing) cemented carbides, whereas cutting with straight grade (i.e., WC only) cemented carbides exhibit no appreciable reductions in built-up edge nor the presence of MnS at the cutting interface.

Regardless of the exact mechanism at play, strong adhesion of the intermediate phase to the tool surface has been observed and attributed to the success of these inclusions in reducing friction. However, the continual replenishment of such films at the tool-chip interface by the continual flow of new work material past the tool rake face is also, undoubtedly, an important factor to their sustained presence. In this way, engineered inclusions within a work material have an advantage over lubricating films that arise from the tool material itself. However, the end application of the work material to be cut may preclude their adoption for performance or economic reasons.

2.3.6 The Effect of Cutting Fluids

Cutting fluids can be divided into two main categories: coolants (largely water-based or water-miscible fluids) and lubricants (largely neat cutting oils). Additives are typically added to coolants to prevent corrosion and inhibit bacterial growth. To enhance lubricating qualities, animal or vegetable fats, or even chlorine and sulfur containing substances. In neat cutting oils, it is mainly fatty oils, chlorine and sulfur that are added to improve their lubricating effects.

Recognizing that the majority of the tool-chip interface is characterized by seizure, the effect of either coolants or lubricants at reducing friction in cutting is confined to those peripheral regions of the tool-chip interface where sliding occurs, which is towards the

edges and rear. The effect of introducing lubricating additives to cutting fluids is that they readily react with the chemically fresh undersurface of the chip, reducing the tendency for strong adhesion to the tool rake.

Oxygen has been shown to function in a very similar way to sulfur and chlorine additives, though not quite as effective at penetrating the tool-chip interface. Experiments of cutting different metals under vacuum or in dry nitrogen have shown much higher cutting force and feed force as well as a much longer tool-chip contact length and thicker chip compared with cutting in air (Trent & Wright, Coolants and Lubricants, 2000).

Childs (1972) observed that introduction of carbon tetrachloride during ultra low speed (0.01 in/min) orthogonal cutting of iron resulted in an increase in shear plane angle, with an associated reduction in chip compression, reduction in tool-chip contact length, increased tightness of chip curl (smaller chip curl radius) and reduction in cutting force components as compared with cutting in air. Shaw observed similar results with the introduction of various lubricants in the low-speed cutting (5.5 in/min) of aluminum and other metals with high-speed steel tools (Cutting Fluids, 1984).

Interestingly, the effect of lubricants is not always beneficial from a tool wear perspective. Trent and Wright summarize that sometimes the introduction of active lubricants has no effect on the tool wear rates, while in other situations it may greatly increase or decrease wear rates (Coolants and Lubricants, 2000). For example, they note that lubricants that act to reduce built-up edge intensity in low speed, low feed cutting of steels with carbide tools also results in increased flank wear rates. However, at medium

and high cutting speeds, some lubricants have been shown to result in a mild to moderate reduction of crater wear on the tool rake face.

2.3.7 Summary

Changes in cutting parameters (i.e., cutting velocity), tool geometry, tool material, work material chemistry, and cutting fluids all play a role in influencing tool-chip friction. Reductions in tool-chip friction caused by changes in the aforementioned variables do not necessarily correspond with reductions in the so-called friction coefficient as defined by Merchant (**Eq. 2.2.3.1**). Likewise, reductions in tool-chip friction do not necessarily reflect reductions in seizure between tool and chip but may result from a thinner, lower shear strength secondary shear zone. Lastly, reductions in tool-chip friction do not necessarily lead to lower rates of tool wear – specifically, in certain cases of externally applied cutting fluids.

2.4 Evaluation of Friction under Load and Temperature Typical of Cutting

2.4.1 A General Overview of Tribometers Aimed at Characterizing Friction in Cutting Processes

Replicating the tribological conditions present between the tool and chip in cutting operations in a bench-scale apparatus is no trivial objective. The contact zone is subject to elevated temperature and mechanical stress, and the undersurface of the chip is chemically fresh which tends to result in intensive seizure to the tool. A few researchers have devised experimental setups that have come close to capturing these conditions, though the setups

are quite involved and feature a dedicated machine tool. Without going into details, the reader is directed to the following published works (Bonnet, et al., 2008), (Claudin, Mondelin, Rech, & Fromentin, 2010), (Rech, Claudin, & D'Eramo, 2009), (Zemzemi, Rech, Ben Salem, Dogui, & Kapsa, 2008), (Puls, Klocke, & Lung, 2012), (Puls, Klocke, & Lung, 2014). Some more recent investigations have employed similar or slight adaptations of such setups (Smolenicki, Boos, Kuster, Roelofs, & Wyen, 2014), (Meier, Schaal, & Wegener, 2017), (Sterle, Pusavec, & Kalin, 2019).

The remainder of this literature review focuses on a subset of experimental setups introduced earlier as on-axis rotation pin-on-disc tribometers, wherein the tribological contact zone is a hemispherical imprint formed in the disc (softer counter body) by the pin (harder counter body). The mechanics involved are similar to those of a Brinell hardness test except that rotation of the specimens is also involved, either rotation of the pin about its central axis or rotation of the disc about that same axis of the pin.

2.4.2 The Adhesiometer Developed by Shuster

Professor Lev S. Shuster, a scholar in Russia, devised an instrument referred to as an adhesiometer, which is likely the original on-axis rotation pin-on-disc tribometer. The following paragraphs are adapted from a translation of Shuster's written works provided by Dr. German Fox-Rabinovich (2008), a research associate at the MMRI. Some details about the adhesiometer are also detailed in (Fox-Rabinovich, et al., 1997).

Shuster's adhesiometer design features a 5 mm diameter cylindrical pin with a 2.5 mm radius spherical, polished tip on either end. The pin is positioned between two flat, parallel

discs of the counter body material, which rest against water-cooled copper plates affixed to top and bottom ends of a mechanical press. The pin itself is fitted at the center of a cylindrical sleeve, which is connected via cable to an electric motor, so as to rotate the pin on-axis relative to the discs. The force required to rotate the sleeve and the pin, $\boldsymbol{F_{exp}}$, is monitored so as to be able to evaluate the torque acting at the contact interfaces between the pin and each disc. The normal load applied between the pin and discs is governed by the addition or subtraction of weights to the upper portion of the mechanical press. An electric potential is applied across the two copper plates, which are electrically isolated from the rest of the mechanical press, resulting in the flow of electrical current through the discs and pin and the heating of the contacting interfaces. Following the test, the radius of the imprint formed in the disc by the pin, under the applied load and electrical current, is evaluated by means of an optical microscope.

Evaluation of temperature at the pin-disc interface is accomplished by means of a thermocouple cemented close to the tip of the pin via a special non-electrically-conductive refractory compound. From these tests, repeated three times and averaged, two calibration curves are created – one relating the measured temperature to the applied electrical current, and the latter relating the radius of the resulting imprint in the disc to the measured temperature. In effect, during subsequent tests, involving rotation of the specimens, the required level of electrical current necessary to achieve a given temperature is estimated based on the first calibration curve. Following the test, the actual temperature at the pin-disc interface is estimated using the second curve, based on the measurement of the imprint

radius. From experience, the temperature is observed to have stabilized after approximately 60 seconds of heating under a given level of electrical current.

Shuster describes a "Method of Reducing Loads" in order to evaluate the friction coefficient between a material pair (the pin and disc) as a function of temperature. First the maximum load (weight) is applied and electric current passed through the specimens. Then, as the $\boldsymbol{F_{exp}}$ vs. time curve stabilizes, the load is reduced by removing one of the weights, resulting in a step-wise reduction of $\boldsymbol{F_{exp}}$. The range of loads can vary from about 5000 N down to 1000 N. This continues until only the lowest weight remains. Shuster has observed that the imprint size changes negligibly during these tests, in other words, the size of the imprint is a reflection of the hardness of the disc material and the maximum load applied. Accordingly, there is a step-wise reduction in normal stress whenever the load is reduced. Assuming the interface temperature remains the same, then a plot of shear stress versus normal stress for a particular temperature can be established, the relationship of which is typically linear, based on sample curves presented, though with a non-zero (positive) intercept through the axis of shear stress.

Drawing on the work of other scholars in contact mechanics, Shuster argues that two inequalities must be satisfied in order for the results of the adhesiometer test to be valid. First of all, in order for conditions of plastic contact to exist, the ratio of penetration depth of the spherical indenter into the disc, $\boldsymbol{h}$, to the radius of the imprint formed in the disc, $\boldsymbol{r}$, must satisfy:

$$\mathbf{0.02} < \frac{\boldsymbol{h}}{\boldsymbol{r}} \leq \mathbf{0.2} \qquad \textbf{Eq. 2.4.2.1}$$

Secondly, in order for 'external friction' (herein referred to as 'surface friction', or just 'friction') to be occurring, the sum of the above ratio plus that of the shear stress, τ, to normal stress, σ, acting at the pin disc interface must satisfy a second inequality:

$$\frac{\boldsymbol{h}}{\boldsymbol{r}} + \frac{\boldsymbol{\tau}}{\boldsymbol{\sigma}} \leq \mathbf{0.5} \qquad \textbf{Eq. 2.4.2.2}$$

If the inequality expressed in **Eq. 2.4.2.2** is not satisfied, the likelihood is that 'internal friction' is occurring (herein referred to as 'bulk shear', i.e., shearing of work material occurring within a finite volume surrounding the imprint).

Though not presented by Shuster, it can be shown that for a hard, spherical indenter of radius $\boldsymbol{R}$ loaded into a soft, flat disc to penetration depth $\boldsymbol{h}$, the radius of the imprint, $\boldsymbol{r}$, can be expressed as per **Eq. 2.4.2.3** below:

$$\boldsymbol{r} = \sqrt{\boldsymbol{h}(\boldsymbol{2R} - \boldsymbol{h})} \qquad \textbf{Eq. 2.4.2.3}$$

Or conversely, the penetration depth may be expressed as per **Eq. 2.4.2.4**:

$$\boldsymbol{h} = \boldsymbol{R} - \sqrt{(\boldsymbol{R^2} - \boldsymbol{r^2})} \qquad \textbf{Eq. 2.4.2.4}$$

The theoretical relationships between imprint radius, imprint depth and penetration ratio, for pin tips of different spherical radii, are plotted in **Figure 10** and **Figure 11**, respectively, for convenience.

Although a derivation is not explicitly provided, Shuster indicates that the ratio of shear stress $\boldsymbol{\tau}$ to normal stress $\boldsymbol{\sigma}$ acting at the pin-disc interface can be expressed as per the following equation:

$$\frac{\boldsymbol{\tau}}{\boldsymbol{\sigma}} = \frac{\boldsymbol{3M}}{\boldsymbol{4F_N r_{ind}}} \qquad \textbf{Eq. 2.4.2.5}$$

where $\boldsymbol{F_N}$ is the applied normal load resulting from application of the weights; $\boldsymbol{M}$ is the moment required to shear the adhesive bonds at the pin-disc interface, evaluated as the product of $\boldsymbol{F_{exp}}$ and the diameter of the cylindrical sleeve holding the pin; and $\boldsymbol{r_{ind}}$ is the radius of the spherical indentation made in the disc, evaluated by optical microscope.

Shuster's adhesiometer has been used to support a number of investigations into the machining performance of different PVD coatings (Fox-Rabinovich, et al., 2010), (Ning, Veldhuis, & Yamamoto, 2007), (Biksa, et al., 2010), (Chowdhury, et al., 2017), (Chowdhury, et al., 2020).

Ning, Veldhuis and Yamamoto (2007) studied the performance of several mono- and multi-layered PVD coatings in the ball-nose end milling of hardened H13 steel, studying the cutting forces, chip formation, wear morphology and material pick-up on the tool edge and relating some of these outputs to coefficient of friction results obtained via tests on the aforementioned adhesiometer.

Biksa, et al. (2010) studied the performance of various PVD AlTiN-based multi-layered coatings in the turning of aerospace alloys Ti6Al4V and Inconel DA 718, relating microhardness testing and friction coefficient evaluation using the same adhesiometer to explain observations in tool life, wear morphology and chip characteristics. Fox-Rabinovich, et al. (2010) used similar techniques to study the improved performance of TiAlCrSiYN/TiAlCrN coatings in the machining of Ni-based aerospace superalloys. More recently, Chowdhury, et al. studied the performance of TiB2 coatings in the rough turning

of Ti6Al4V (2017) and in a separate study the performance of CrN coatings in the finish turning of the same alloy was examined (2020).

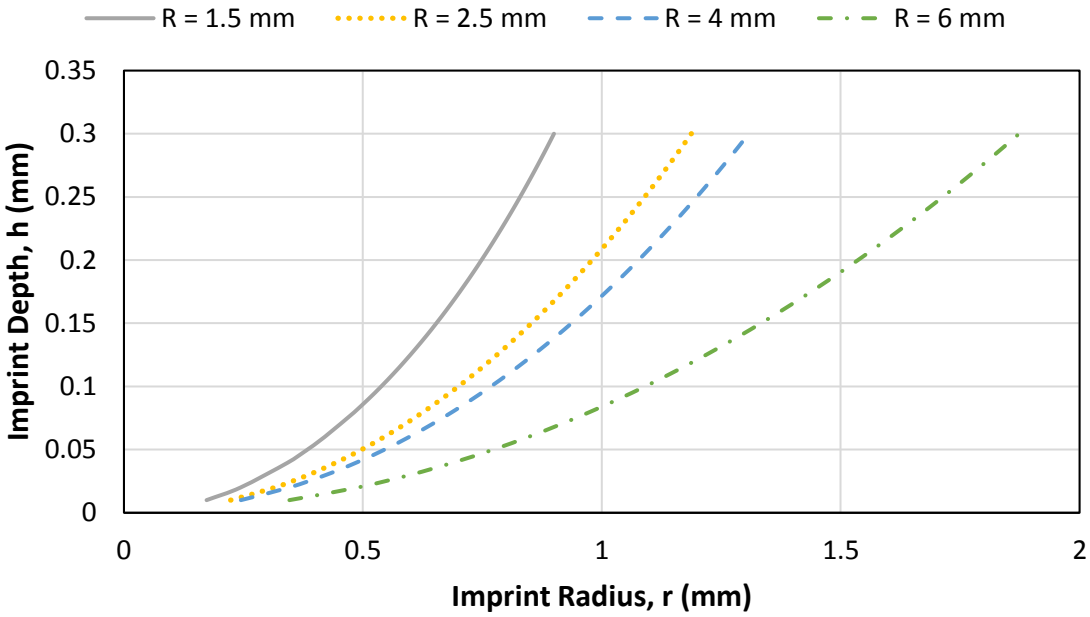

Figure 10: The relationship between imprint radius and imprint depth, per Eq. 2.4.2.3

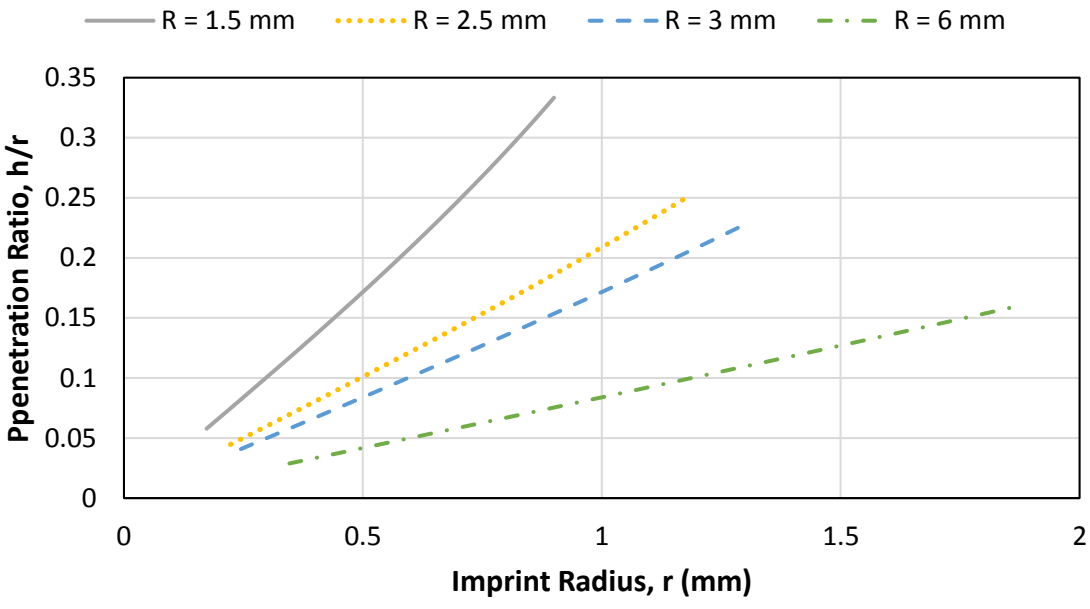

(b)

Figure 11: The relationship between imprint radius and penetration ratio, per Eq 2.4.2.4

2.4.3 The MMRI Tribometer – Mark I

Biksa (2010) took the basic concept of the adhesiometer used by Shuster and began the work of developing a heavy-load, high-temperature tribometer for use in the MMRI, herein referred to as the MMRI Tribometer (Mark I), or simply Mark I.

Biksa's design featured a 3 mm diameter pin, with a 1.5 mm radius spherical, polished tip on each end. Unlike Shuster's adhesiometer, the Mark I only interacted a single end of the pin with a flat disc of work material, while the other end was gripped in a collet mounted at the base of a load column. Directly above the collet was a Kistler torque sensor, which mounted to the bottom flange of a splined shaft running through a horizontal bar and connects to a load cell above. The torque required to shear adhesive bonds at the pin-disc interface was monitored via this sensor, which was coupled to a charge amplifier. Load was applied via two lead screws on either side of the load column and was regulated by a closed-loop PID controller based on measurements from the load cell.

Other differences in the MMRI Tribometer (Mark I) as compared with Shuster's adhesiometer were as follows:

(i) the disc, held on the four-jaw chuck of a spindle, rotated relative to the disc; and

(ii) heating of the pin-disc interface was achieved by induction heating via a custom-designed coil positioned around the pin and slightly above the disc;

(iii) temperature near the pin-disc interface was continuously monitored during tests by means of an Optris infrared pyrometer aimed at a spot of black, constant emissivity paint applied approximately 2 mm above the tip of the pin.

With regards to (i), Biksa took great care in aligning the pin to the axis of the spindle. As per (ii), Biksa explored a few different coil designs before settling on one that achieved an appropriate balance of heating the tip of the pin without simultaneously overheating and softening the disc. The active temperature measurements described in (iii) closed the loop in a PID-controller that governed the output of the induction heater, so as to regulate temperature in the pin close to the actual pin-disc interface.

From first principles, Biksa was able to derive expressions for the average shear stress, normal stress and coefficient of friction ***COF*** acting at the pin-disc interface, as shown in **Eq. 2.4.3.1** through **Eq. 2.4.3.3** below:

$$\boldsymbol{\sigma = \frac{F_N}{\pi {r_{ind}}^2}} \qquad \textbf{Eq. 2.4.3.1}$$

$$\boldsymbol{\tau = \frac{3M}{2{r_{ind}}^3}} \qquad \textbf{Eq. 2.4.3.2}$$

$$\boldsymbol{COF = \frac{\tau}{\sigma} = \frac{3M}{2F_N r_{ind}}} \qquad \textbf{Eq. 2.4.3.3}$$

Biksa also presented two sets of COF vs. Temperature plots for both uncoated and TiAlN-coated pins in contact with discs made of two materials: Ti-6Al-4V and Inconel DA 718. Tests were performed under an applied load of 1900 N and temperatures ranging from room temperature up to 800 °C. Specimens were subjected to rotation at 1 RPM for 10 s and the average torque, load and temperature signals recorded during the last 2 s of rotation were used in the calculation of COF, along with the measured radius of imprint in the discs. In both cases, some mild reductions in COF at elevated temperature conditions were

observed with the TiAlN-coated pin, which Biksa attempted to correlate with improved tool life from some limited machining studies.

Biksa noted that there tended to be a slight degree of material pile-up surrounding the imprint in the disc. Measurements of the imprint diameter at the top of the pile-up, as viewed via optical microscopy, were larger than those evaluated at the plane of the disc by means of white light interferometry (the average difference being 5%). In light of his review of contact mechanics, he argued that in-plane diameter measurements would lead to more meaningful calculations of the normal and shear stresses acting at the imprint and proposed a simple correction factor to calculate the in-plane measurement based on evaluation of the diameter at the top of the pile-up via optical microscope.

2.4.4 The MMRI Tribometer – Mark II

Boyd (2012) expanded upon Biksa's work by developing a custom NI LabVIEW®-based graphical user interface to integrate control and measurement into a single platform, enabling an automated test sequence of load application, heating and spindle rotation. Additionally, he integrated a welding power supply into the setup in order to enable through-specimen electrical resistance heating, similar to Shuster, as an alternative to the induction heat method implemented by Biksa. This involved significant redesign of many of the mechanical interfaces to ensure electrical isolation of all sensors and the mechanical structure of the tribometer.

Additionally, Boyd performed some baseline studies to understand the sensitivity of tribometer results to fundamental input parameters. Key findings were as follows:

(i) Depending on the load applied, the maximum normal stress acting at the pin-disc interface could vary from about 2-4 times the yield stress of the material. This level of stress corresponded to the period of initial loading, prior to any heating or the onset of friction during specimen rotation.

(ii) The diameter of the imprint formed in the disc was shown to grow appreciably during the rotating phase of a test, which corresponded to an increase in reaction torque as well as an increase in evaluated ***COF***. Given that the applied load was constant, this infered that the normal stress acting at the pin-disc interface was higher during the initial loading phase and at the onset of rotation, decreasing as the rotating phase of the test progressed. This was shown to be somewhat material and load dependent but only investigated at room temperature.

(iii) Pre-polishing the tip of PVD-coated pins significantly reduced the observed ***COF*** during friction tests, which was attributed to smoothing of microdroplets formed on the coated surface during the deposition process.

(iv) During elevated temperature tests, larger diameter imprints tended to form in the disc when the resistance method of heating was applied versus the induction heating method introduced by Biksa, despite the tests running for the same duration and the infrared pyrometer measuring the same temperature. This was attributed to differences in the thermal gradient in the pin due to differences in where the heat was primarily generated. Regardless of the heating method, however, increases in measured temperature corresponded to increases in imprint diameter, reflecting thermal softening of the disc.

The above results indicate that, at least under ambient temperature conditions, the size of the resulting imprint is strongly tied to (a) the severity of adhesion/friction at the pin-disc interface, and (b) the duration of specimen rotation. Additionally, the results of (iv) demonstrate that imprint size is also a function of the temperature achieved during heating, as well as the thermal gradient in the pin tip relative to the point of temperature measurement.

Boyd also alluded to a few trials involving a CVD multi-layer coating featuring an interlayer of Al_2O_3, the electrical resistivity of which was high enough to prevent the test from occurring properly (electrical current was unable to flow). Given that the whole premise for heating the pin-disc interface revolves around electrical resistance heating, and the coating layer is located right at this interface, this suggests that the electrical resistivity of the coating could have some bearing on Tribometer test results. However, this was not systematically explored at the time.

Additionally, Boyd presented a series of test results for uncoated and TiAlN-coated cemented carbide pins in contact with AISI 1045 steel discs, subject to normal loads of 500 N and temperatures ranging from ambient to 750 °C, with specimens rotating at 1 RPM for 5 s. The selection of such a short duration of rotation (as compared with Biksa's 10 s and Shuster's 60 s) was based on the observation that torque signatures were relatively stable during this period and would typically begin to rise subsequently. Boyd observed a reduction in ***COF*** with tests involving the TiAlN coating at elevated temperatures. Tool life results from turning tests were also presented, wherein TiAlN vastly outperformed the

uncoated insert, though causality by (or even correlation to) reduced tool-chip friction was not clearly demonstrated.

2.4.5 The MMRI Tribometer – Mark III

The work reported by Khoei (2019) was largely performed after the experimental work presented in the later sections of this dissertation. Khoei utilized the Mark III version of the MMRI tribometer and largely followed the experimental methodology described in **Chapter 3**: namely, the use of a 30 s loading phase; followed by 10 s of heating with no rotation; and concluded by 60 s of continued heating with the addition of specimen rotation at 2 RPM prior to removal of all rotation, heat and loading and evaluation of the test outputs. That being said, Khoei explored fundamentally different tool-work material combinations (Ti6Al4V and super duplex stainless steel (SDSS) alloys); performed tests under generally more aggressive loads (500 – 1000 N) and explored the influence of the pin tip curvature on the resulting shear stress, normal stress and ***COF*** values. Khoei continued the tradition of Biksa and Boyd in using closed-loop temperature control in contrast to the open-loop (constant electric current) approach used by Shuster. Also, Khoei observed that the magnitude of pile-up surrounding the imprint could lead to overestimation of the imprint diameter measured via optical microscope by as much 25% relative to the true diameter evaluated at the plane of the disc. Thus, Khoei resorted to using an advanced 3D imaging microscope to aid in more accurate evaluation of the imprint diameter and depth.

In general, Khoei observed that, under the same load and temperature conditions, the imprints formed after tribometer tests involving pins with a larger (flatter) radius of

curvature produced imprints larger in diameter but shallower in depth. Correspondingly, the larger the radius of curvature of the pin tip, the lower the normal contact stress between pin and disc.

Khoei drew heavily on the inequality presented by Shuster (**Eq. 2.4.2.2**) to distinguish between tribometer test results that are characteristic of 'external' (surface) friction vs. 'internal' friction (bulk shear in the work material), particularly in investigations involving super duplex stainless steel (SDSS). This is summarized in the paragraphs below.

At elevated temperatures (650 °C), all test results were characterized by bulk shear of the work material beneath or surrounding the contact interface – evidenced by ***COF*** values well in excess of 0.5 and tending to increase further with increasing temperature. However, even at more moderate temperatures (350 °C and lower), ***COF*** values ranged from about 0.42 to 0.55 for the different pin treatments (uncoated vs. different deposition times of $Ti_{0.5}Al_{0.5}N$) and pin tip radii (1.5 mm vs. 3 mm).

Penetration ratios (***h/r***) were evaluated to be approximately 0.04 for 3 mm radius tip pins and 0.08 mm for 1.5 mm radius tip pins, tending to increase slightly at temperatures of 650 °C and above. Interestingly, noted by the present author, these values are approximately 50% lower than the theoretical values for ***h/r*** that one would evaluate using **Eq. 2.4.2.4** based on the reported imprint diameter measurements and indenter radius.

Though not explicitly presented, combining the evaluated ***h/r*** values with ***COF*** (i.e., **τ/σ**) values presented would infer that the inequality expressed in **Eq. 2.4.2.2** would evaluate to greater than the 0.5 threshold under the vast majority of test cases. This implies

that material shear conditions were likely present even at lower temperatures; however, Khoei seemed to overlook this.

Negligible differences in ***COF*** for the different pin surface treatments were observed at a given temperature (and under the same 1000 N loading). The high roughness values measured on the surface of the pin tips (>0.5 μm Ra) very likely contributed to the similarity in ***COF*** values across all surface treatments under identical test conditions as well as the tendency for material shear conditions to be apparent (based on **Eq. 2.4.2.2**) even at low temperatures.

Khoei later examined the effect of Nitrogen Pressure and Bias Voltage on the tribological performance of Ti0.6Al0.4N coatings against SDSS, under similar test temperatures and a slightly lower test load (700 N). Smoothing of the coated pin surfaces was performed prior to the tests by loading the pin tips against 800 grit SiC paper under 10 N load and rotating at 400 RPM. The duration of this treatment was not specified, nor was it clear whether the same treatment was applied to the uncoated pin. Possibly the reduced load, the smoothing treatment, or a combination of both were effective in preventing bulk shear of work material during elevated temperature tests as all variants of the TiAlN coating exhibited a steady ***COF*** value of approximately 0.45 +/- 0.03 from temperatures in the 350-700 °C range. The uncoated pin exhibited higher ***COF*** values in this same temperature range, dipping to about 0.48 at 550 °C but then rising to 0.52-0.53 at 700 °C.

Subtle differences in ***COF*** values were noted for TiAlN coatings of different bias voltage at elevated temperatures, but in this author's opinion and experience, the differences are too small to be considered statistically significant (0.43 vs. 0.46).

Khoei also studied the tribological performance of uncoated and different PVD-coated (ALTINOS (TiAlN-based proprietary coating), ALTINOS + WC/C, ALTINOS + TiB_2) cemented tungsten carbide pins in contact with SAF 2507 super duplex stainless steel, this time using a lighter load (200 N) but otherwise similar test parameters. The ALTINOS + WC/C coating exhibited the lowest ***COF*** values over a wide range of temperatures. As well, for tests up to 500 °C, it produced a noticeably smaller diameter imprint compared with those of the other pin surface treatments (whose imprint diameters were similar to one another); while at 700 °C and 850 °C, the imprint it produced was effectively the same size as those produced in tests with the other surface treatments. Khoei attributed this to the relatively low hardness and elastic modulus of combined ALTINOS + WC/C coating and reasoned that this partly contributed to the lower ***COF*** values of this coating (a smaller imprint diameter corresponding to a higher normal stress, which is the denominator term in **Eq. 2.4.3.3** for the evaluation of ***COF***). However, the smaller imprint diameter could well be a reflection of reduced ***COF*** and shear stress at the coating interface due to lubricious qualities of the WC/C layer, in keeping with the earlier noted observation of Boyd (2012) that the imprint diameter is strongly tied to the degree of adhesion/friction present at the pin-disc interface (**Sec. 2.4.4**).

2.5 Gaps in Knowledge in the Literature to be Bridged in this Dissertation

A number of gaps in knowledge can be identified in the above literature review, which present opportunities for further investigation and exploration.

1) Under ambient temperature conditions, imprints formed during on-axis rotation pin-on-disc tribometer tests are understood to grow in size as a function of the duration of specimen rotation and proportional to the severity of adhesion/friction at the pin-disc interface. As well, during elevated temperature tests, the imprint size is understood to be dependent on the temperature achieved at or near the pin disc interface. *However, a systematic investigation of imprint growth during tests at elevated temperature has not yet been conducted.*
2) Thus far, determination of whether bulk shear (i.e., shearing of work material in the soft disc) or surface friction (i.e., shearing of adhesive bonds at the pin-disc interface) has been based solely on evaluation of the inequality presented in **Eq. 2.4.2.2**, which is dependent on the penetration ratio (**Eq. 2.4.2.1**) and the ratio of shear stress to normal stress, or ***COF*** (**Eq. 2.4.2.5**). However, to date, *there appears to have been no study of the microstructure of the work material surrounding imprints in the disc following tribometer tests to validate whether or not material shear was indeed absent (or present).*
3) There is some understanding that the method of heating (e.g., resistance heating vs. induction heating) can influence the temperature at the pin-disc interface as suggested by significant differences in imprint diameter despite similar temperatures being measured via infrared pyrometry at a location approx. 2 mm above the interface. Accordingly, *there is an opportunity to establish a methodology for estimating the true pin-disc interface temperature, which is inaccessible for direct measurement*.

4) The performance of various PVD coatings evaluated on Shuster's adhesiometer have been linked to evidence of reduced friction during machining trials in various papers. *In contrast, the relationship between COF vs. Temperature data generated by the MMRI Tribometer and machining results has not been well established.* Furthermore, while some studies have investigated the nature of tribofilms formed on the surface of coated tools during machining trials involving a given work material, *no investigation into the nature of tribofilms formed on the surface of pins from elevated temperature on-axis rotation pin-on-disc tribometer tests against the same work material has yet been reported.*

3. IMPRINT GROWTH ANALYSIS AT ELEVATED TEMPERATURES

3.1 Opening Remarks

This chapter presents an analysis of the growth and evolution of the pin imprint in the disc during elevated temperature on-axis rotation pin-on-disc tribometer tests.

First, an overview is provided of the hardware changes introduced to the MMRI Tribometer to realize the Mark III variant used in this and later chapters. Next, a detailed account of the testing methodology developed for the Mark III Tribometer is presented. For clarity, it is restated that these hardware changes and experimental procedures were implemented prior to the work reported by Khoei (2019). Finally, the experimental work and findings regarding imprint growth at elevated temperatures are given. Characterization of the pile-up surrounding imprints is also presented, and the benefits and drawbacks of evaluating the imprint diameter at the top of the pile-up versus at the plane of the disc of work material are discussed.

3.2 Changes Implemented in the MMRI Tribometer (Mark III)

A custom collet for gripping 3 mm diameter pins was designed and fabricated (**Figure 12**), along with a new mounting surface for the collet (**Figure 13a**), featuring precision dowels against which the collet can be repeatably positioned. Clamps were designed to hold the collet against the underside of the mounting surface. This new design simplifies the initial alignment of the pin with the axes of the spindle and the torque sensor, enabling the collet assembly to be removed for inspection of the pin and reinstalled in exactly the same way.

Figure 12: New collet designed for the MMRI Tribometer (Mark III)

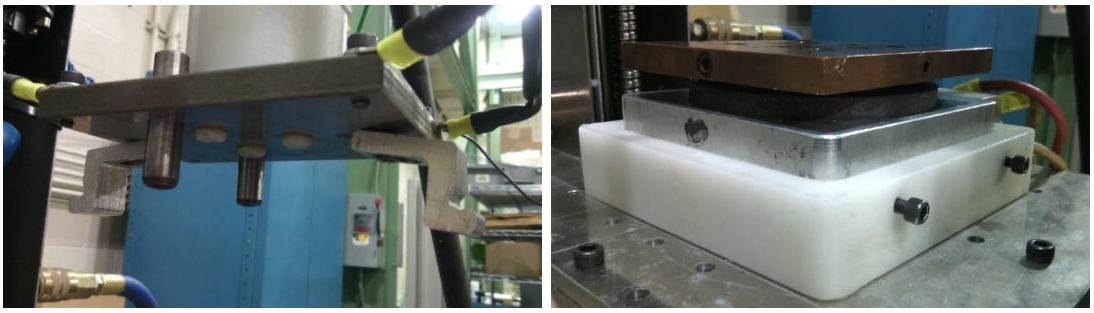

(a) (b)

Figure 13: (a) New mounting location for the collet; (b) new copper plate with spring-loaded graphite slipring

Figure 14: Snapshot of the new hardware elements of the Mark III Tribometer

Additionally, a new platform to support the discs was machined out of copper to replace the aluminum platform used by Boyd (2012), and eventually the concept of affixing jumper cables to the edge of the platform was replaced with a spring-loaded graphite slipring that contacts the underside of the platform (**Figure 13b**). In contrast to the Mark II design, wherein the length of the cables limited the number of spindle rotations, the spring-loaded slipring allows for an indefinite number of spindle rotations opening up the possibility of longer tests or higher spindle speeds. An overview of all new hardware elements is presented in **Figure 14**.

3.3 General Overview of the Test Methodology and Sample Preparation

3.3.1 General Overview

Similar to its predecessors, the MMRI Tribometer (Mark III) is a heavy-load, high-temperature tribometer which interacts a ball-tipped pin made of a cutting tool material against a small coupon or disc of a given work material. The interaction can occur under a load upwards of 2500 N, a through-specimen electrical current as high as 200 A (to achieve an elevated pin-disc interface temperature), and a rotational speed of up to 1000 RPM.

The pin is installed in the collet, which forms the bottom of the load column (comprising the load cell, the torque dynamometer, and other mechanical elements). The load column translates vertically on a pair of lead screws, driven by a small DC motor via a cogged belt. The disc rests on a flat, copper plate mounted to the flange of a spindle, which is driven by a brushed DC motor via belt and pulley. The axis of the pin, and that of the torque sensor located above it, is radially aligned with the axis of the spindle to within 0.020 mm.

Electrical current from a DC welding power supply is directed through cables and flows through the collet, pin, disc, copper plate, and a spring-loaded graphite slip ring. Sensitive electrical hardware is appropriately insulated from all electrical current. This current is responsible for generating the elevated temperature at the pin-disc interface. To help achieve a favourable thermal gradient along the length of the pin and also to prevent excess heat flow up the load column, two nozzles direct cold air from a vortex chiller toward the collet that grips the pin. Though the temperature at the pin-disc interface is inaccessible for direct measurement, an estimate is obtained via an infrared pyrometer aimed at a small spot of black, constant emissivity paint applied onto the pin approximately 2 mm above the tip.

A typical test with the instrument involves four stages, which are briefly described below and elaborated upon later. During the first stage, the pin is pressed into the disc under a load $\mathbf{F_n}$, forming a partial hemisphere imprint. At this point, the test is essentially indifferent from a Brinell hardness test. In the second stage, electrical current is passed through the specimens, raising the temperature at the pin-disc interface as well as in the bodies of the pin and disc. During the third stage, whilst the load and current are maintained, the disc is rotated about the axis of the pin and the frictional torque, **M**, associated with the relative motion of the specimens, is monitored via a torque sensor. In the fourth and final stage, specimen rotation and the flow of electrical current is stopped, the pin is retracted from the disc, and the diameter, **d**, of the resulting disc imprint is measured. As shown by Biksa (2010) and presented in **Chapter 2**, the average normal

stress, **σ**, average shear stress, **τ**, and average friction coefficient, **COF**, acting over the contact area are then evaluated as per **Eqs. 3.3.1.1**, **3.3.1.2** and **3.3.1.3**, respectively.

$$\sigma = \frac{4F_n}{\pi d^2} \qquad \textbf{Eq. 3.3.1.1}$$

$$\tau = \frac{12M}{\pi d^3} \qquad \textbf{Eq. 3.3.1.2}$$

$$COF = \frac{\tau}{\sigma} = \frac{3M}{F_n d} \qquad \textbf{Eq. 3.3.1.3}$$

3.3.2 Sample Preparation

The pin must have a 3 mm diameter circular cross-section in order to fit in the custom collet. The exact length of the pin is not as critical but should range from 25 - 35 mm (in practice to date, it has been nominally 33 mm). The assumption in all equations presented in ensuing sections is that the tip of the pin has a spherical profile whose center of curvature lies along the axis of the cylindrical body of the pin. In practice, the radius of curvature of the pin tip has been 1.5 mm, which makes the pin tip a perfect hemisphere. The tip should have a fairly low surface roughness so as to minimize the likelihood of hard, prominent asperities ploughing through the softer disc material in an abrasive fashion. Depending on the manufacturer of the pins used, typical roughness values on the tips of pins used in the research have ranged from about 50 nm to 150 nm Ra. The pin can be used as is (uncoated) or else sent to a coating supplier to have a thin, hard coating deposited onto the tip and some length of the cylindrical body. To date, coatings deposited by CVD, PVD and thermal

spray methods have been employed. In keeping with Biksa (2010), the pin is aligned to within 0.040 mm indicated diametral runout relative to the axis of the spindle.

The discs used have typically been of approximately square or circular cross-section with an exposed surface area of about 100 - 400 mm^2, which allows for a reasonable number of tests to be performed on a given disc. The thickness of the disc has ranged from about 6.5 mm up to 13 mm. Of greater importance is to ensure that the top and bottom surfaces are ground flat and parallel to one another. While a mirror finish is not a necessity, it is advisable that the top surface of the disc be at least lapped with medium grit emery paper to help remove any adhered coolant residue from manufacturing. Likewise, occasional lapping helps remove surface oxides that build up over time.

Prior to each test, cleaning the pin tip and the top surface of the disc with a solvent is also advisable. In practice, the author has exclusively used Isopropyl Alcohol, though it is expected that other solvents such as Ethanol or Acetone can be used just as effectively. It is worth noting that Shuster advises further cleaning of the both pin tip and disc with fine grain activated coal powder (Fox-Rabinovich G. , 2008), but this was not employed by the present author.

3.4 Stages of the Automated Test

A detailed description of the four main stages of a test on the MMRI tribometer is now presented. It is assumed that the pin is already installed, with a spot of black, constant emissivity applied for temperature measurement, and that the disc is positioned beneath the pin on the copper plate. The four stages are fully automated.

3.4.1 Applying Load to the Specimens

The first stage of the test involves loading the (hard) ball-tipped pin into the (soft) flat disc and maintaining a target load for a prescribed period of time. The load is regulated by a PID controller with feedback from a strain-based load sensor, rated up to 2500 N, which is installed at the top of the load column. During the initial loading, the applied load occasionally overshoots the setpoint by about 10-20 N but quickly converges thereafter. Under the applied load, a partial hemisphere imprint is formed in the disc, the size of which depends on the magnitude of the load, the hardness of the disc material, and, to a limited extent, the duration of the load. Boyd (2012) observed no appreciable difference in the size of the imprints formed in discs of Inconel DA718 subjected to 2000 N loads for 30 s vs. 120 s. Subsequent investigations by the author have shown there to be negligible growth in imprints after as little as 5 s of constant load, for a range of loads and work materials of varying hardness; however, to be conservative, the first stage is set to run until the target load has been maintained within a +/- 10 N tolerance about the target load for 30 s.

As presented in **Eq. 3.3.1**, the average normal stress acting on the contact interface can be estimated as the applied load, $\mathbf{F_n}$, divided by the projected area of the imprint, $\boldsymbol{\pi d^2}$. The achieved normal stress during this stage of the test depends strongly on the hardness of the work material as well as the magnitude of the load applied, as demonstrated by Boyd (2012) and depicted in **Figure 15**.

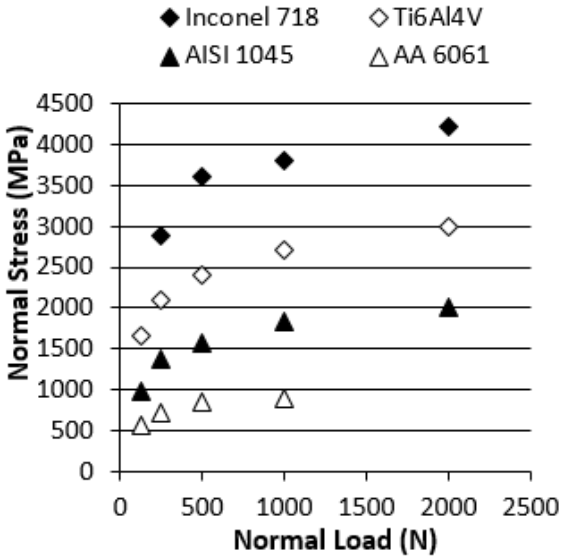

Figure 15: Normal stress achieved vs. normal load applied (first stage of the test)

The magnitude of the applied load should be selected in view of the hardness of the disc material so as to ensure the diameter of the resulting imprints are appropriately sized: if the imprints are too small, they are difficult to view and measure accurately during the fourth stage; if they are too large, the rate of heat generation and thus the maximum temperature achievable at the pin-disc interface is significantly reduced (Boyd J. M., 2012). Higher loads also cause increased stiction in the mechanical actuating elements, which translates to poorer regulation of the load about its setpoint (more drifting and overcompensation by the PID controller), as noted by Boyd (2012). As a rule of thumb, the load should be chosen such that the resulting imprint diameter is about 0.40 mm prior to activation of heat or rotation.

3.4.2 Heating the Specimens

3.4.2.1 General Remarks and Observations

After the desired load has been achieved and maintained for a fixed duration of time (the author has adopted 30 s as standard practice), the second stage of the test commences. While maintaining the mechanical load, electrical current is passed through the specimens in order to achieve an elevated temperature at the contact interface. This is achieved by connecting the leads of a 200 A capacity DC welder to carefully designed terminal locations on the tribometer, taking care to ensure proper electrical isolation of the sensors and structure in general. The current output of the welder is regulated by a 0-10 V command signal transmitted from a desktop computer to the remote receptacle of the welder.

The underlying heating principle is Joule's first law, whereby the rate of heat generation, $\boldsymbol{q_{gen}}$, is equal to the product of the square of the electrical current, **I**, and the electrical resistance in the circuit, $\boldsymbol{R}$, as shown in **Eq. 3.4.1**. The electrical resistance of a conductor can be expressed in terms of its length, $\boldsymbol{l}$, cross-sectional area, $\boldsymbol{A}$, and electrical resistivity, $\boldsymbol{\rho}$, as shown in **Eq. 3.4.2**. Substituting into **Eq. 3.4.2** gives an alternate expression for the rate of heat generation, as shown in **Eq. 3.4.3**.

$$\boldsymbol{q_{gen} = I^2 R} \qquad \textbf{Eq. 3.4.1}$$

$$\boldsymbol{R = \frac{\rho l}{A}} \qquad \textbf{Eq. 3.4.2}$$

$$\boldsymbol{q_{gen} = I^2 \frac{\rho L}{A}} \qquad \textbf{Eq. 3.4.3}$$

Through proper design of the entire electrical circuit, the majority of heat generation should occur within the specimens, particularly in the pin due to its comparably smaller

cross-sectional area and longer length relative to that of the disc. Furthermore, it can be shown that the rate of heat generation per unit length is actually highest at the very end of the ball-tipped pin due to the progressive reduction of cross-sectional area.

In practice, it has been observed by the author that a moderate amount of electrical resistance does exist at the interface between the bottom of the disc and the top of the copper plate, comparable in magnitude if not slightly larger than that present at the pin-disc interface. Unique to the Mark III configuration, there also exists appreciable electrical resistance at the interface of the slipring and the underside of the copper plate, approximately an order of magnitude greater than that present at the pin-disc interface. Given the large size of the graphite slip ring and the copper plate relative to the pin and disc, it is expected that the heat generated at these interfaces is largely conducted into these "heat sinks" and does not significantly affect the thermal gradients in the pin and disc.

A few points are worth mentioning regarding this second stage of the test:

- First of all, for ambient temperature tests, no electrical current is required.
- Secondly, for elevated temperature tests, both the pin and disc materials must possess adequate electrical conductivity to permit the flow of large amounts of electrical current (several tens of amperes). The exact cut-off is unknown to the author, but experience has demonstrated that coatings with even a few microns thickness of an insulative material (e.g., aluminum oxide) will render the test ineffective, let alone dangerous due to the effective open-loop conditions established when the welder is activated (Boyd J. M., 2012).

- Thirdly, at the onset of electrical current, there is a momentary spike in mechanical load. This is attributed to the rapid thermal expansion of the pin tip during heating. Within a few moments, the load controller responds and restores the applied load to its setpoint. To help reduce the severity of this load spike, the electrical current control algorithm was modified to limit the maximum output during the initial moments of heating, gradually increasing this limit by approximately 0.1 A every loop of the control algorithm, or 60 ms. Illustrative examples of this load spike from actual tests on the MMRI tribometer are presented in **Figure 16(a)** and **Figure 17(a)**.
- Fourthly, the temperature at the actual interface between pin and disc is physically inaccessible. Instead, temperature readings close to this interface are obtained by aiming an infrared pyrometer at a spot of calibrated, black, constant emissivity paint located approximately 2 mm above the interface. Under most circumstances, there will be some finite temperature difference between this measured spot and the real interface. Estimation of this difference is important for the purposes of comparing friction data from one test to another and is a topic of further discussion and investigation in **Chapters 5** and **6**.
- Lastly, both the hardness of the disc material as well as the magnitude of the applied mechanical load will govern the range of temperatures that can be obtained for a given electrical current passed through the specimens, since these strongly influence the size of the imprint formed in the disc. The size of the imprint sets the minimum

cross-sectional area of the electrical circuit, and thereby the maximum rate of heat generation. It also influences the rate of heat transfer between the specimens.

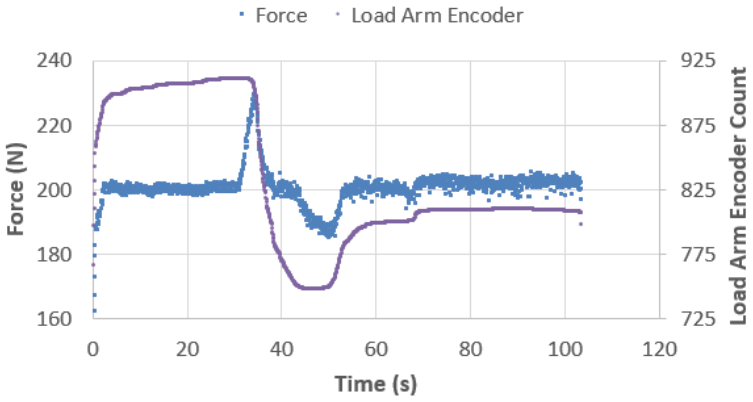

(a)

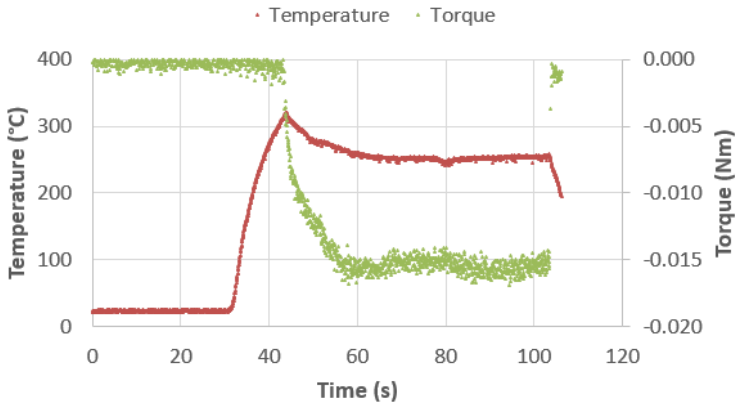

(b)

Figure 16: Illustrative data from a tribometer test between an AlTiN-coated WC-Co pin and AISI 4150 Steel disc under 200 N load and 93 A of current

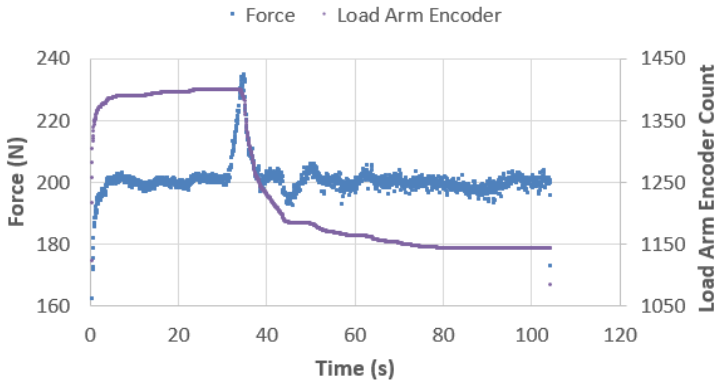

(a)

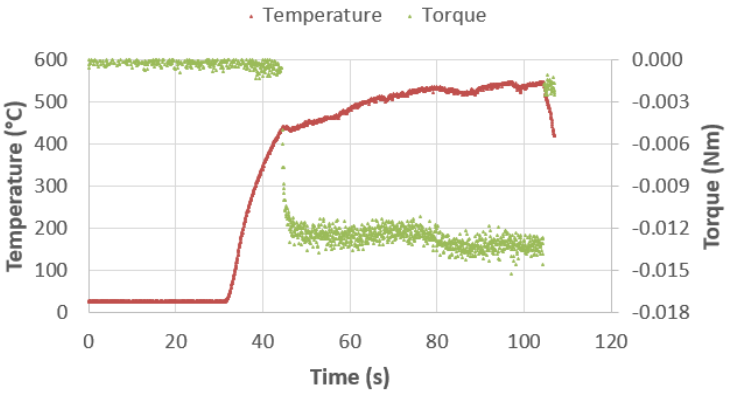

(b)

Figure 17: Illustrative data from a tribometer test between an AlTiN-coated WC-Co pin and AISI 4150 Steel disc under 200 N load and 113 A of current

3.4.2.2 Open-Loop vs. Closed-Loop Temperature Control

Initially, the welding power supply and infrared pyrometer comprised a closed-loop control system wherein output of electrical current from the welding power supply was varied so as to achieve a target temperature measured on the spot of black, constant emissivity paint applied on the pin via the infrared pyrometer. This is the configuration implemented by Boyd (2012). In practice, it was noted that this could sometimes lead to

marginal instability in the load and temperature signatures, particularly at elevated temperatures.

This instability is attributed in part to the level of coupling that exists between these parameters. Effectively, efforts on the part of the load controller to regulate the mechanical load will also influence the temperature (since the applied load influences the real area of contact and thus the electrical resistance at the pin-disc interface), and likewise corrective actions made by the temperature controller to adjust the electrical current output will also affect the applied load (since heating/cooling of the pin tip will result in volumetric expansion/contraction). In practice, the signal relayed from the computer to the welding power supply can vary significantly, resulting in considerable fluctuations in the electrical current output.

While refinement of the control algorithm could likely lead to improved stability, an open-loop configuration was subsequently implemented and employed, wherein a specified command signal is sent to the welding power supply so as to output a constant level of electrical current. Using this approach, the resulting test temperature is not known a priori but rather evaluated from the temperature data collected post priori. Accordingly, some preliminary trials with different levels of electrical current are required to estimate what level of electrical current should be specified in order to achieve a desired test temperature. It is worth noting that this open-loop approach to temperature control via constant electrical current heating is aligned with the method employed by Shuster (Fox-Rabinovich G. , 2008).

In practice, when the heating stage begins, the electrical current is slowly ramped up to the specified output level over the period of a few seconds (i.e., 0.1 A per 60 ms loop) to help prevent a sudden burst of heat generation at the pin-disc interface. Once the target output of electrical current has been achieved, it is maintained for a fixed period of time (the author has adopted 10 s as standard practice). During this time, the pin tip heats up significantly. However, except for tests at particularly elevated temperatures, the size of the imprint formed in the disc remains relatively unchanged. As well, the measured temperature rarely reaches steady-state prior to the start of the next stage in testing.

In the case of closed-loop configuration tests, a small number of which were performed as part of this dissertation, similar limits to the ramp-up rate of electrical current were implemented; however, the transition to the next stage of the test occurred after the temperature remained within +/- 10 °C of the setpoint for 5 s, similar to Boyd (2012).

3.4.3 Rotating the Disc about the Pin

The third and main stage of the test features the disc rotating about the axis of the pin at a fixed speed for a prescribed duration of time, during which the applied mechanical load and electrical current are held constant and the frictional torque acting at the pin-disc interface is monitored. Measurement of the torque is acquired via a Kistler 9329A piezoelectric torque dynamometer installed in the load column. Electrical charge signal from the torque dynamometer is converted to a proportional voltage signal at a Kistler 5010B charge amplifier.

Whereas Biksa (2010) and Boyd (2012) performed tests using a spindle speed of 1 RPM, the author observed that a reduction in torque sensor noise was achievable by increasing the spindle speed to 2 RPM. It is speculated that the origin of the noise pertains to vibrations in the motor at lower RPM, possibly related to stick/slip between the rotor and brushes of the motor used to drive the spindle.

At the onset of rotation, a decrease in the rate of temperature change is usually evident in the case of open-loop temperature control (i.e., constant electrical current heating). In most cases, temperature continues to rise before reaching a steady-state value (**Figure 17(b)**). In some instances, however, the test temperature starts decreasing after rotation has commenced (**Figure 16(b)**). Regardless, except in rare circumstances, the measured temperature is somewhat different during the early stages of rotation as compared to the later stages of the test. This has some important implications, as will be discussed later.

Coinciding with this transition in temperature is a temporary decrease in load of about 5% below the setpoint and a sudden shift in the rate of change of the load arm encoder position, reflective of the pin position (**Figure 16(a)** and **Figure 17(a)**). These phenomena are best explained by an increase in the real area of contact at the pin-disc interface as asperities of the softer work material shear and flatten out, leading to a reduction in contact resistance (and hence heat generation) as well as an increase in heat conduction between the pin and disc. However, some growth in the imprint size is likely to have occurred as well during this short time frame, which would explain the momentary decrease in load and a change in response of the load arm position encoder as the controller reacts to the decreased load.

With the progression of time and rotation, the torque signal tends to increase, as does the imprint diameter and the ***COF***. This was observed by Boyd (2012), who also noted that the imprints resulting from tests with higher torque levels tended to exhibit more smearing of work material in circular patterns, suggesting material transfer from the disc to the pin during rotation. An explanation for the increase in imprint diameter was presented by Boyd (2012), but is restated and expanded below.

By the end of the first stage, wherein the size of the imprint has reached a fixed value, the work material in the vicinity of the interface has already experienced a measure of strain hardening, raising the von Mises flow criterion to a value equal to or exceeding the present stress level acting on the work material at the interface. At the onset of rotation, additional shear stress now acts on the work material due to adhesive friction between pin and disc. If the additional shear stress causes the stress state to exceed the von Mises flow criterion established during the loading and heating stages, further material flow (plastic deformation and imprint growth) will ensue. As the imprint grows, the applied load remains relatively constant so that the normal contact stress decreases. The imprint will continue to grow until the stress state reaches a level equal to or less than the von Mises flow criterion, which will tend to increase with accumulated strain hardening.

Strictly speaking, the investigations carried out by Boyd (2012) were only under room temperature conditions. Investigations into the growth of imprints during elevated temperature tests are detailed later in this chapter.

For reasons that will become evident in ***Sec. 3.5***, the duration of rotation has been set to 60 s for the vast majority of tests reported in this dissertation. At a spindle speed of 2 RPM, this translates to two complete revolutions of the disc about the tip of the pin.

3.4.4 Test End

In the final stage, the spindle rotation is stopped, the flow of electric current through the specimens ceases, and the pin retracts from the disc. A measurement file is saved of all sensor data logged via the custom National Instruments LabView® software since the start of the test. The disc is taken to an optical microscope for measurement of the diameter of the resulting imprint. In practice, imprints are viewed under Mitutoyo TM microscope with an XY stage, equipped with 0.001 mm resolution micrometers on each axis.

As noted by Biksa and reiterated by Khoei, there is a difference between the size of the imprint evaluated with the aid of an optical microscope and the size of the imprint evaluated at a height that is co-planar with the surface of the disc. Biksa noted a difference of about 5% for his tests, which featured 10 s of disc rotation about the pin at 1 RPM, and resorted to the use of a simple correction factor applied to measurements obtained using the optical microscope (2010). Khoei reported that the difference in diameter measurements could reach upwards of 25% and thus resorted to the exclusive use of an advanced 3D imaging system to characterize the imprint diameter in the plane coinciding with the disc surface (2019). In the present work, unless otherwise stated, evaluation of the imprint diameter was performed solely using the Mitutoyo TM microscope, without the use of any correction factor. Limitations to this approach will be discussed in ***Sec. 3.5.3***.

As per the load, torque and temperature data acquired during the test, an average value is evaluated based on the data sampled over a specified portion of the previous stage (i.e., Rotating the Disc about the Pin). For tests involving 60 s rotation at 2 RPM, taking an average of data over the last 30 s of rotation was chosen, corresponding to the second complete revolution of the disc about the pin. For such tests, a Matlab script was developed to extract the load, temperature and torque signals from the saved measurement file and output the average values over the last 30 s of rotation into an Excel file, along with plots of the corresponding signals versus time for qualitative analysis. The operator need only input the measured imprint diameter in order to calculate the friction coefficient ***COF*** as per **Eq. 3.3.3** presented earlier. For shorter duration tests, different criteria must be chosen for the range of data used to calculate the load, temperature and torque data. These must be manually evaluated, with the aid of Microsoft Excel, in order to calculate a ***COF*** value.

Typically, at least 3 test replicates are performed in order to determine a mean and standard deviation for the ***COF***. The mean ***COF*** value can then be plotted against the mean temperature from those test replicates, which itself can vary from one test to another. Presented this way, one can compare the tendency for reduced friction of different tool materials and/or coatings interacting with a common work material under specific temperature regimes. For completeness, the variation of normal stress (**Eq. 3.3.2**) and shear stress (**Eq. 3.3.3**) as a function of temperature should be presented, in keeping with Shuster (Fox-Rabinovich G. , 2008) and as adopted by Khoei (2019). Likewise, the penetration ratio should be evaluated and a verification for surface friction conditions performed using **Eq. 2.4.2.2**.

3.5 Experimental Work – Imprint Growth during Elevated Temperature Tests

3.5.1 Correlating growth in imprint diameter with reaction torque and observations of adhesion at and work material distortion surrounding the imprint

A series of tests at room temperature and elevated temperatures (200 °C and 400 °C) were performed under two levels of applied load, 200 N and 2000 N, between uncoated cemented WC-Co pins and discs of AISI 1045 steel. Closed-loop temperature control was employed during these particular tests. Discs were rotated at 2 RPM for 3 s, 10 s and 60 s. For short duration tests (3 s of rotation), the torque data over the last 0.5 s of rotation was averaged. For longer duration tests (10 s and 60 s of rotation), the torque data over the last 2 s of rotation was averaged. In all cases, the underlying torque signal averaged over a 0.5 s window just prior to rotation was subtracted from the average torque calculated during the end of rotation. Plots of torque vs. imprint diameter for the full range of test scenarios are presented in **Figure 20** (for tests at 200 N) and in **Figure 23** (for tests at 2000 N).

There is significant correlation between the torque measured at the end of the test and the diameter of the imprint measured subsequent to the test, the relationship being roughly linear. The correlation appears weaker in the 200 N, 400 °C data set, but is significantly improved when the end torque is replaced by the peak torque for the longer duration tests.

As exemplified in **Figure 24**, the torque signature for some of the 60 s tests exhibited a peak in torque early in the test (within the first half a rotation) followed by a decrease to near steady-state conditions thereafter. Thus, choosing to report the peak torque instead of the end torque when the two do not coincide is logical in such instances, as in **Figure 20(c)**.

The torque curves for select tests under 2000 N load at both room temperature and 400 °C are presented in **Figure 26(a)** and (**b)**. In the majority of these cases, the torque signal at the end of the test had not yet stabilized but was rather on an upward trajectory. The imprints resulting from these tests are shown in **Figure 27**. Consistent with Boyd (2012), the degree of work material smearing or adhesive wear marks in the imprint appeared to scale with the maximum torque exhibited during the test and the size of the resulting imprint. Additionally, and not noted previously by Boyd (2012), the degree of distortion or deformation in the surrounding volume of work material also increased.

Test cases A through E presented in **Figure 25** correspond to progressively larger imprint diameters in **Figure 27(a)** to **(e)**, all of which stem from room temperature tests. However, similar observations can be made for test cases F through I, performed at 400 °C, as shown in **Figure 26** and **Figure 27(f)** to **(i)**. Thus, it can be fairly stated that under both room temperature and elevated temperature conditions, increases in torque up to the peak value experienced during the test correspond to an increase in the imprint diameter, an increase of adhesive wear marks in the imprint itself, and an increased level of disturbance or deformation in the surrounding volume of work material.

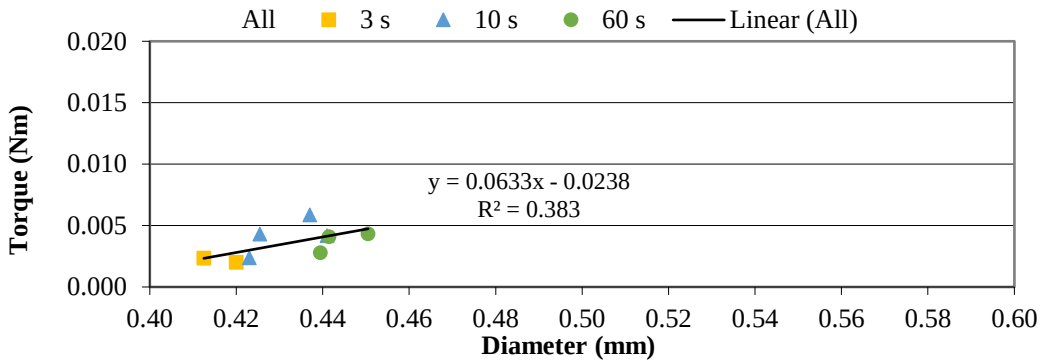

Figure 18: Torque vs. imprint diameter under 200 N and ambient temperature

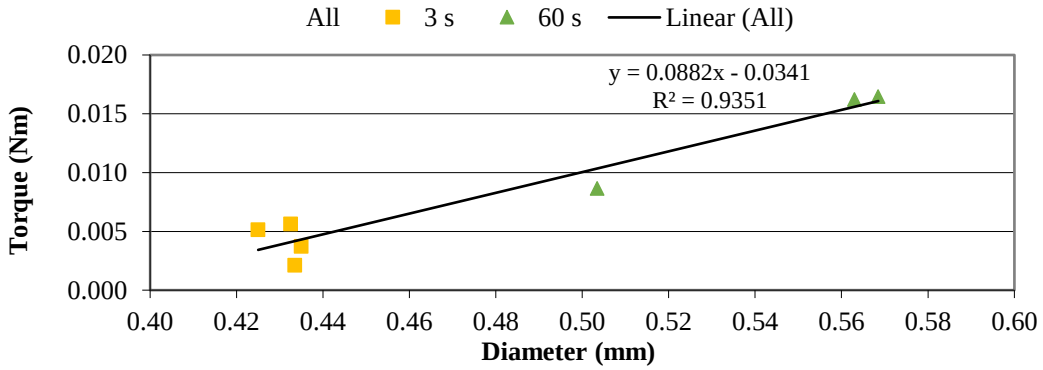

Figure 19: Torque vs. imprint diameter under 200 N and 200 °C

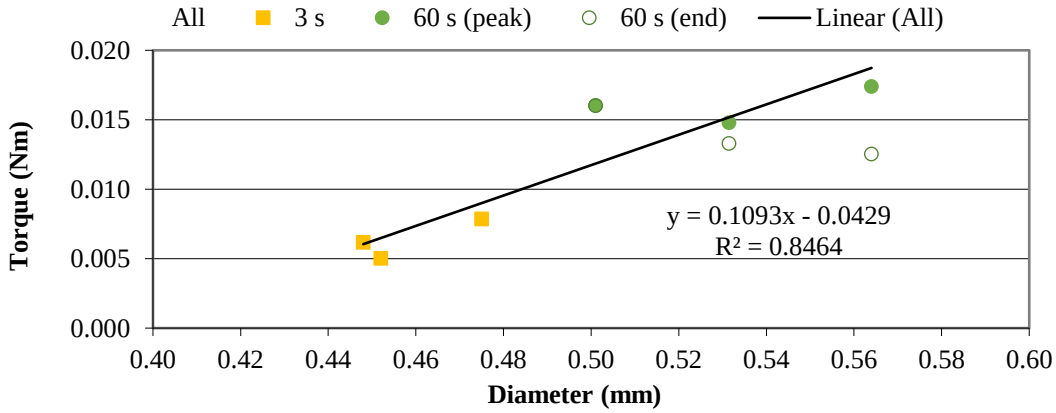

Figure 20: Torque vs. imprint diameter under 200 N and 400 °C

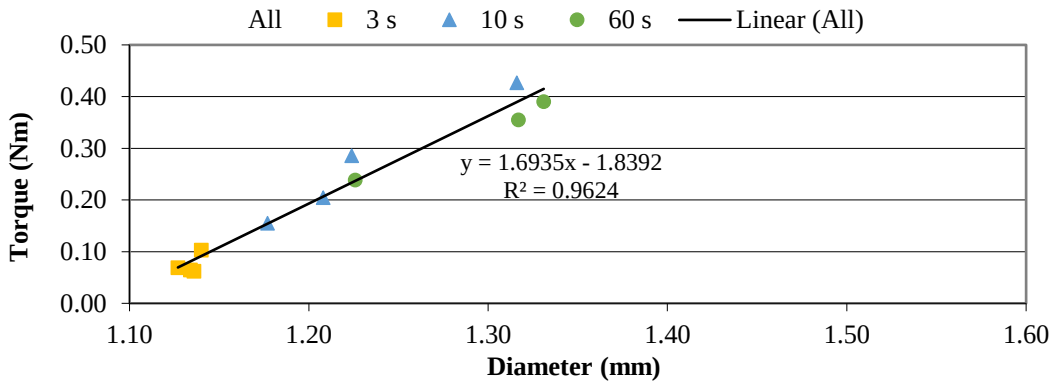

Figure 21: Torque vs. imprint diameter under 2000 N and ambient temperature

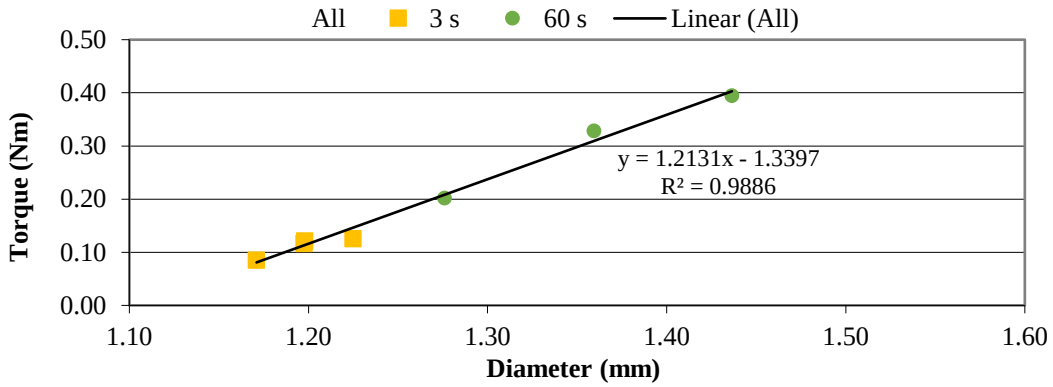

Figure 22: Torque vs. imprint diameter under 2000 N and 200 °C

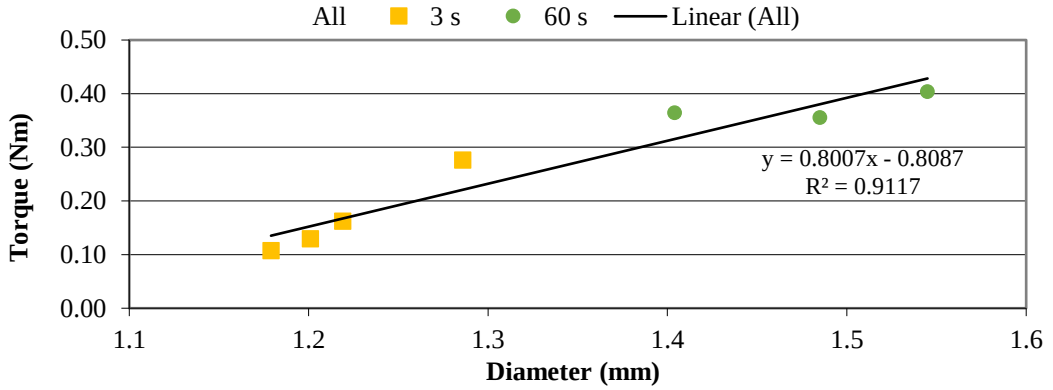

Figure 23: Torque vs. imprint diameter under 2000 N and 400 °C

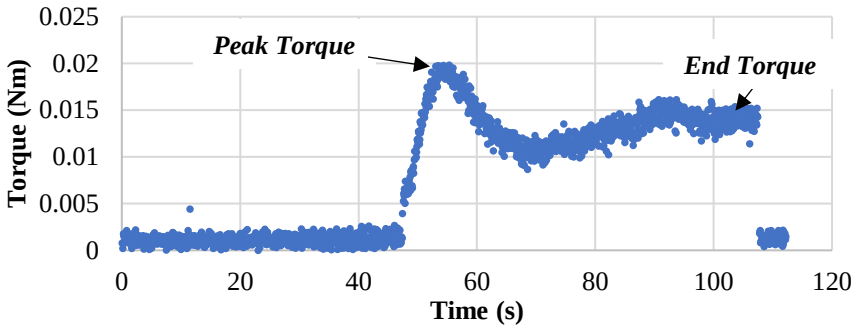

Figure 24: Torque vs. time curve highlighting peak vs. end torque

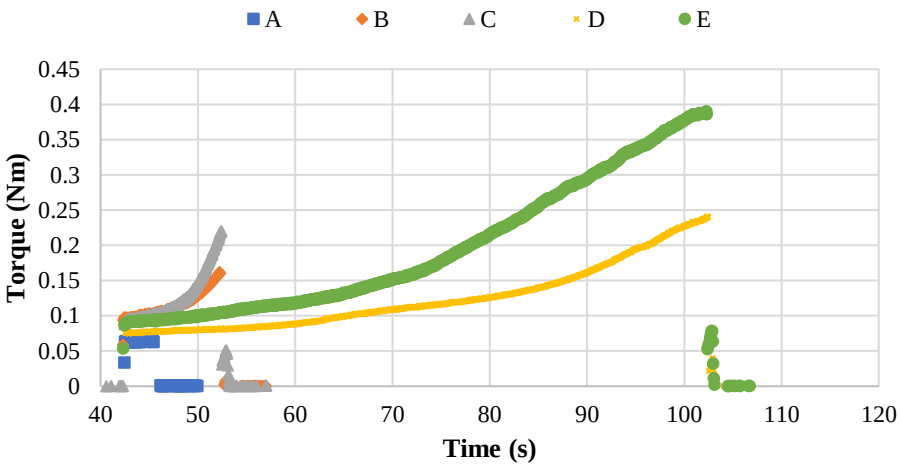

Figure 25: Torque curves from select tests presented in Figure 21

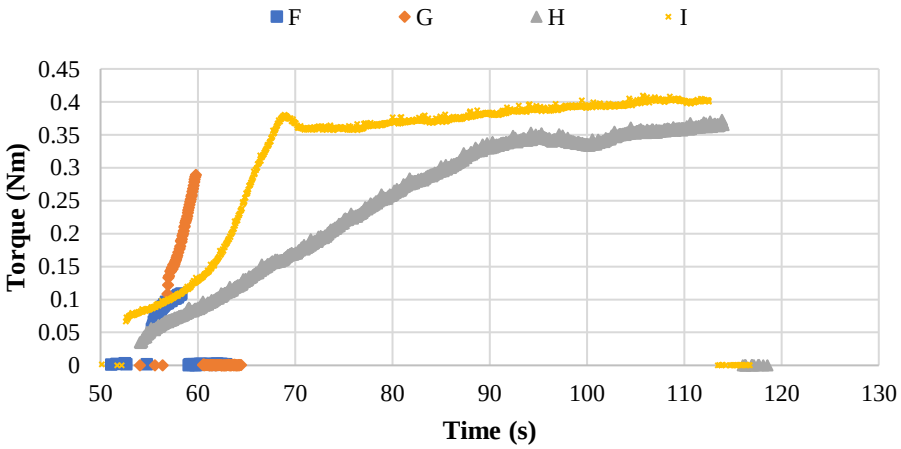

Figure 26: Torque curves from select tests presented in Figure 23

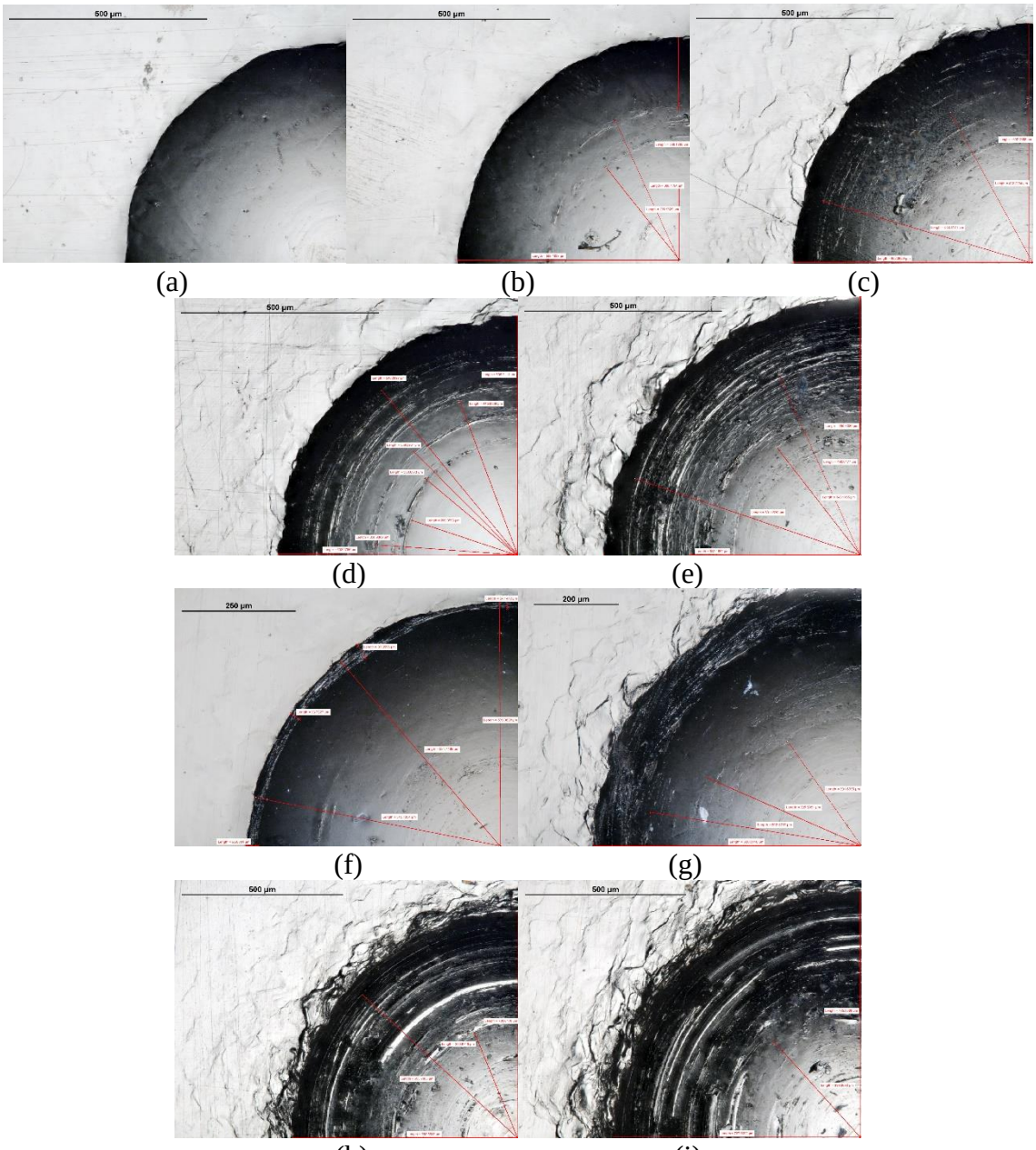

Figure 27: Imprints corresponding to tests presented in Figure 25 and Figure 26

As Boyd (2012) pointed out, the measured ***COF*** tends to increase as the torque signal and imprint diameter increase, which led to the idea of keeping the duration of specimen rotation relatively short (i.e., < 5 s) so that the torque signal was more likely to remain stable and measured ***COF*** would be repeatable. Boyd (2012) also noted that the evaluated

COF seemed relatively insensitive to the applied normal load when test duration was shorter. However, these conclusions were based off of room temperature tests only. As evidenced by torque signals presented in **Figure 26**, the torque can increase significantly and by varied amounts within even 5 s of rotation at elevated temperatures.

In many regards, extending the duration of rotation until the torque signal approaches steady-state conditions is preferable and less subjective to the initial contact conditions at the onset of rotation. In the case of AISI 1045 steel discs in contact with uncoated cemented tungsten carbide pins, the needed duration of specimen rotation until steady-state torque signatures are achieved is somewhat load and temperature dependent. For tests at 2000 N of applied load, steady-state torque was not achieved after even 60 s of rotation under ambient temperature conditions, whereas at 400 °C, near steady-state torque was achieved after approx. 40 s of rotation. For tests at 200 N load, steady-state torque was achieved within ~30 s of rotation under all temperature conditions and often within as little as 10 s.

3.5.2 Establishing the rate at which the imprint diameter grows during on-axis rotation pin-on-disc tribometer tests

A series of tests were performed between an uncoated WC-Co pin and a disc of AISI 1045 steel under a 200 N load as well as an uncoated WC-Co pin and a disc of an aluminum alloy of unknown designation under a load of 150 N. The load was maintained for 30 s prior to applying any electrical current or commencing disc rotation at 2 RPM. For elevated temperature tests, current was maintained for 10 s prior to rotating the discs. Rotation duration was set at 0 s, 5 s, 10 s, 20 s, 30 s and 60 s. Two separate trials were performed

for each combination of electrical current, rotation duration and disc material, in order to obtain an average value of the imprint diameter.

Figure 28(a) presents the imprint diameter as a function of rotation duration for both ambient temperature and elevated temperature tests involving AISI 1045 steel discs. **Figure 28(b)** presents the same test results in terms of the relative growth in imprint diameter, normalized to the imprint diameter evaluated after 60 s of rotation. **Figure 29(a)** and **(b)** present the Torque vs. Time profiles and the Temperature vs. Time profiles, respectively, for some of the elevated temperature tests. Note that the time scale has been adjusted such that rotation commences at t = 5 s. **Figure 30** and **Figure 31** present the same set of plots for the tests involving the aluminum alloy.

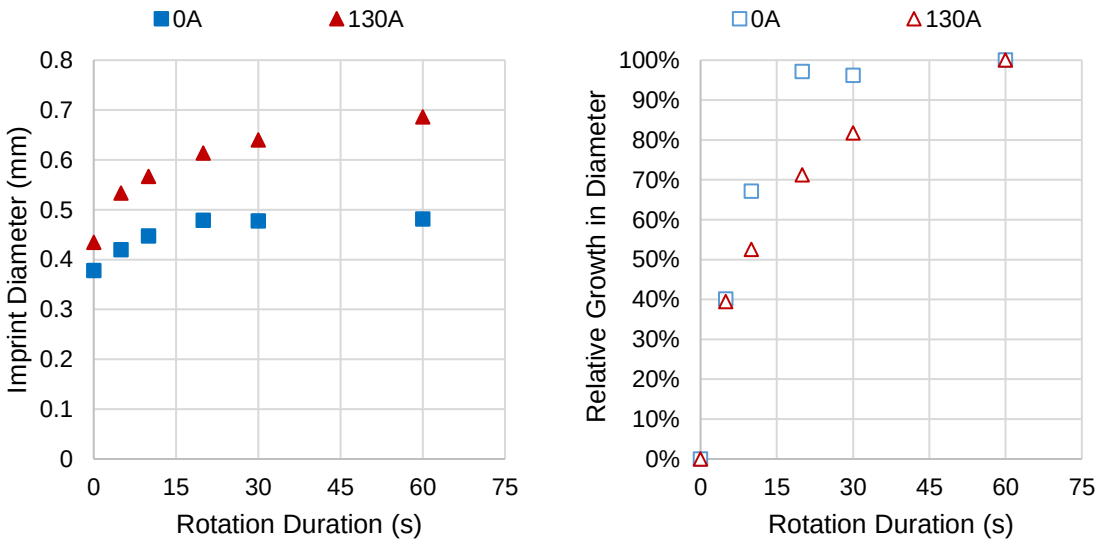

(a) (b)

Figure 28: Imprint diameter vs. rotation duration for the AISI 1045 steel disc

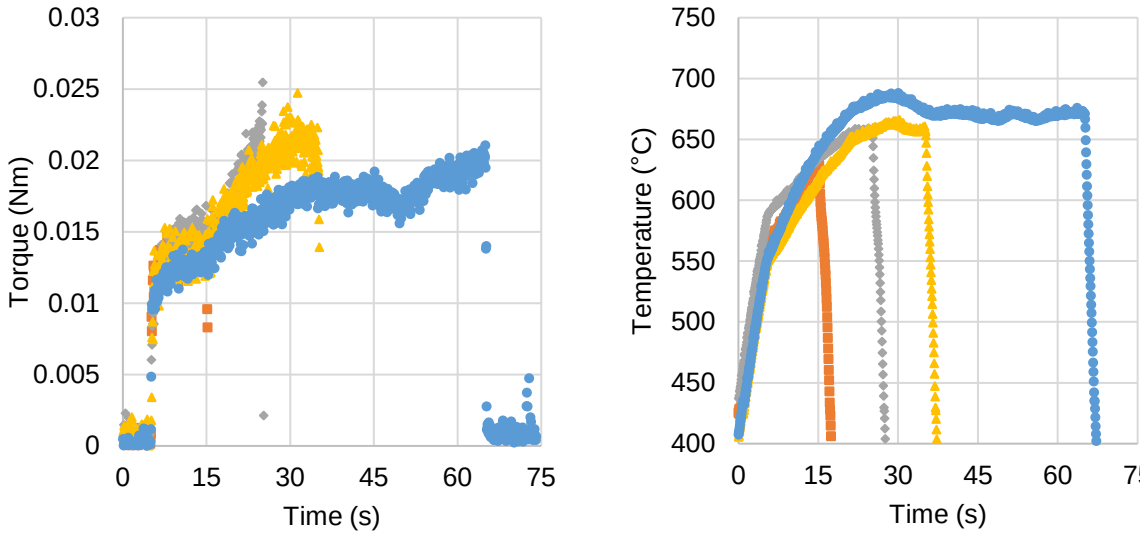

(a) (b)

Figure 29: (a) Torque vs. Time profiles and (b) Temperature vs. Time profiles for elevated temperature tests with the AISI 1045 steel disc

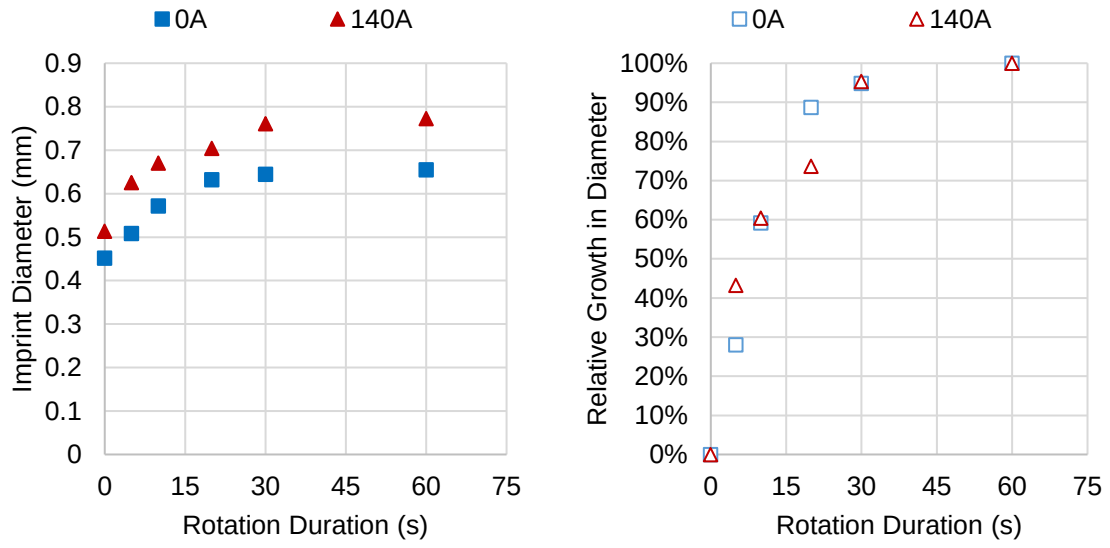

(a) (b)

Figure 30: Imprint diameter vs. rotation duration for the aluminum disc

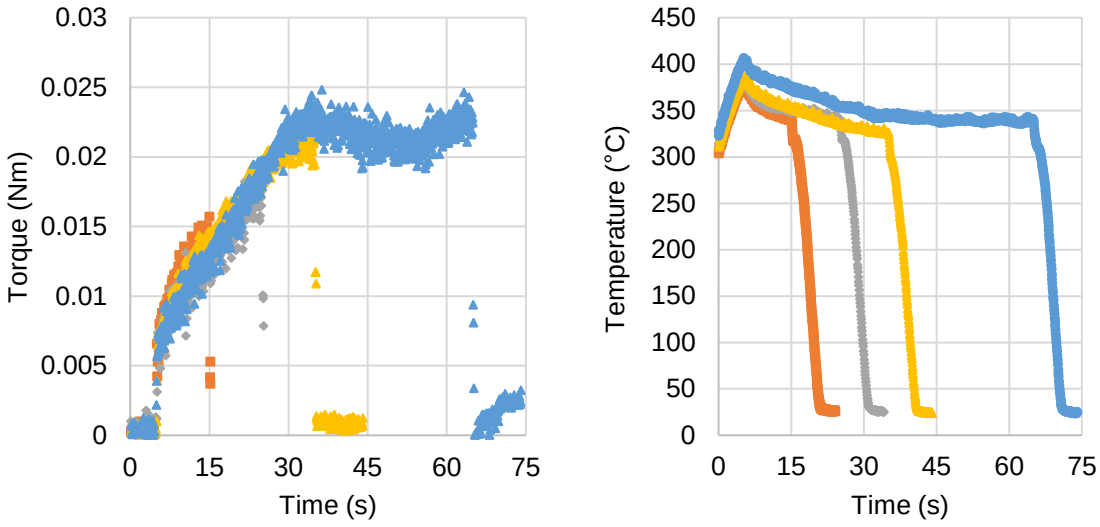

(a) (b)

Figure 31: (a) Torque vs. Time profiles and (b) Temperature vs. Time profiles for elevated temperature tests with the aluminum disc

In the case of the AISI 1045 disc, the temperature increased from about 625 °C to 675 °C from about 15 s to 60 s during rotation, whereas for the aluminum alloy, the temperature decreased from about 350 °C to 325 °C during the same time frame. Interestingly, the torque signature from the 60 s test at 130 A against the AISI 1045 steel disc was noticeably lower at 15 s and 30 s into rotation vs. the tests run for 20 s and 30 s rotation duration. This coincided with relatively higher temperatures at these times during the 60 s test, which could suggest that the imprint diameter for this particular test was somewhat smaller at these times than in the 20 s or 30 s duration tests (a smaller imprint resulting in greater heat generation at the pin-disc interface and less heat transfer into the disc). That being said, the maximum torque signal for the 60 s duration test (which occurred close to the end of the 60 s of rotation) was slightly lower than the maximum torque experienced during the 20 s and 30 s duration tests, yet the imprint diameter was noticeably larger. Thus, at least at the elevated temperatures in this particular test (>650 °C), it would seem that the duration

of rotation and the magnitude of elevated temperature sustained during rotation also played a contributing role in the resulting size of the imprint.

In contrast, for the tests with the aluminum alloy disc, the torque signatures from the different tests overlapped much more closely. The torque signal after 30 s of rotation during the 60 s duration test was nearly identical to the torque signal at the end of the 30 s duration test and did not see any appreciable change in magnitude during the latter 30 s of rotation. Thus, it is not surprising that the imprint diameter had only seen an additional 10% growth in imprint diameter relative to the imprint diameter prior to rotation during the latter 30 s of rotation. As noted earlier, the increase in torque correlates more clearly with the increase in imprint diameter during the elevated temperature tests with the aluminum alloy disc.

It can be seen from **Figure 28(a)** and **Figure 30(a)** that the addition of temperature alone, prior to the imposition of added shear stress due to friction during rotation, had the effect of increasing the imprint diameter slightly; however, this contribution was small (approx. 10-15%) relative to that which resulted during rotation. That being said, it is unclear from these tests how much the growth in imprint diameter experienced during rotation could have been from thermal softening effects at sustained elevated temperatures alone. Prior to the onset of rotation, the specimens had been subject to only 10 s of heating under constant electrical current. Throughout the entirety of rotation phase, the specimens were subject to the same level of heating and the temperature at the end of the rotation phase could have been slightly higher (e.g., by 75-125 °C in the case of AISI 1045) or lower (e.g., by 50 °C in the case of the aluminum alloy) compared to the temperature at the start

of rotation. Regardless, an additional 30-60 s of load under elevated temperatures could have contributed to imprint growth, as was suggested earlier in the case of AISI 1045 discs.

To quantify this potential contribution, a series of "stationary" tests were performed, wherein the load and electrical current were maintained for the 60 s during which rotation would normally occur except the spindle was not activated. Such tests were repeated for a range of constant electrical current heating scenarios to see the effect of a range of sustained elevated temperatures on imprint growth. The reported temperature is based on averaging the temperature signal over the last 30 s of the test.

A plot of imprint diameter vs. temperature for these "stationary" tests is presented in **Figure 32**. The effect of temperature on the imprint diameter appears relatively insignificant and almost non-existent until about 700 °C, after which further increases in temperature are marked by clear increases in imprint diameter. However, it is important to note that that even at temperatures as high as 750-800 °C, the imprint diameter formed from a "stationary" specimen test was noticeably smaller than that resulting from the "rotating" specimen test which saw temperatures of only 675 °C (**Figure 28** and **Figure 29**).

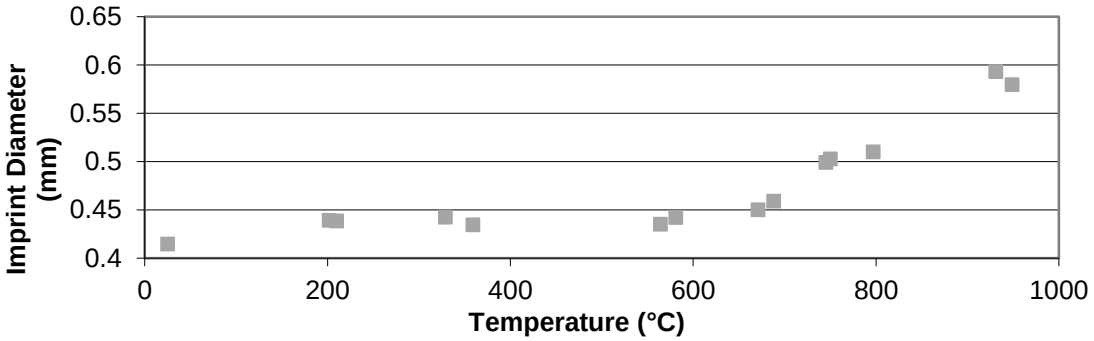

Figure 32: Imprint diameter vs. temperature during stationary specimen tests with AISI 1045 steel

3.5.3 The influence of pile-up on imprint diameter measurements and COF evaluation

The reported values of imprint diameter in the preceding two sub-sections were all evaluated using the Mitutoyo TM microscope, meaning that the imprint diameter was evaluated at or very near to the top of the material pile-up surrounding the imprint. As noted previously (Khoei, 2019), the size of the imprint evaluated at the top of the pile-up can be considerably larger than that evaluated in the same plane as the surface of the disc itself.

A handful of imprints resulting from tests involving AISI 1045 steel discs with uncoated and TiAlCrSiYN/TiAlCrN-coated cemented WC-Co pins were characterized on the Mitutoyo TM Microscope as well as a Zygo Newview 5000 white light interferometer. This latter instrument provides a 3D mapping of the imprint, through which data slices can be extracted and analyzed to evaluate the diameter of the imprint at both the top of the pile-up ($\boldsymbol{d_{pile\ up}}$) as well as coplanar to the surface of the disc ($\boldsymbol{d_{plane}}$), such as is shown in **Figure 33**. This is in contrast to the evaluation of imprint diameter denoted $\boldsymbol{d_{opt}}$ which is obtained on the Mitutoyo TM Microscope.

The imprints studied were the results of tests involving the aforementioned specimens subject to 200 N load, 60 s of rotation at 2 RPM and a mixture of ambient and elevated temperatures, the latter being the result of open-loop heating configuration. Over a range of imprints studied, measurements of $\boldsymbol{d_{pile\ up}}$ agreed well with measurements of $\boldsymbol{d_{opt}}$, with discrepancies consistently less than 5% relative error (denoted by the error bars about $\boldsymbol{d_{opt}}$ in **Figure 34**), confirming that $\boldsymbol{d_{opt}}$ evaluated on the Mitutoyo TM Microscope is indeed an evaluation of the imprint diameter at the top of the pile-up surrounding the imprint.

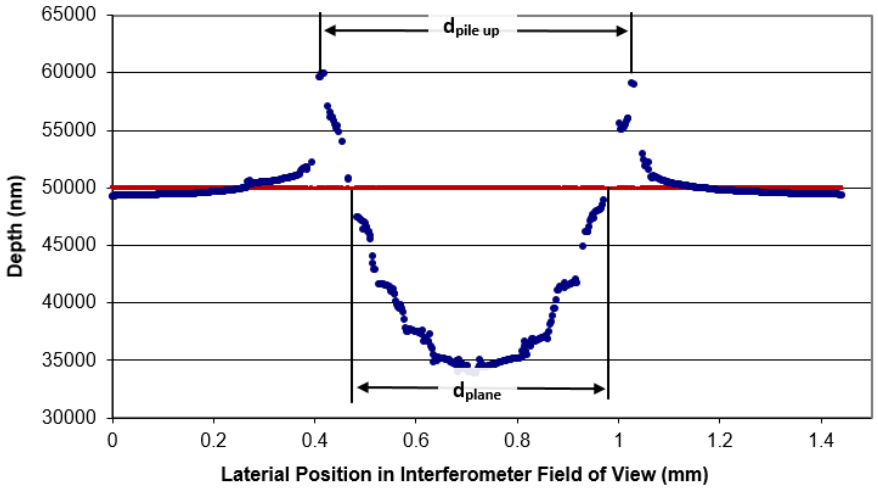

Figure 33: Cross-sectional profile obtained from a white light interferometer measurement of an imprint

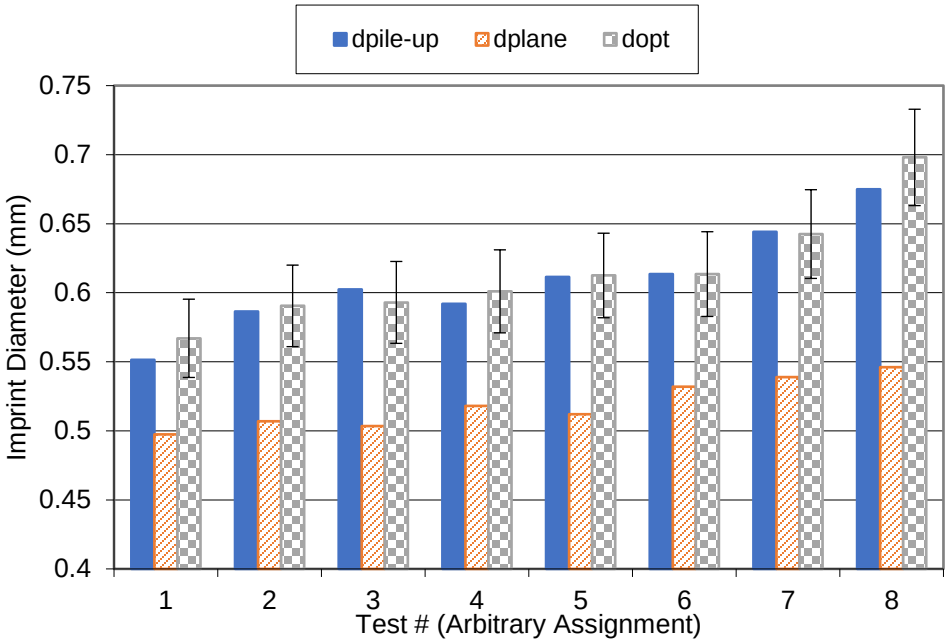

Figure 34: Comparison of $d_{pile\text{-}up}$, d_{plane} and d_{opt}

Consistent with Khoei (2019), however, the magnitude of $d_{pile\ up}$ (or d_{opt}) is considerably larger than that of d_{plane}. As shown in **Figure 35**, the ratio of d_{opt} to d_{plane} increases roughly linearly in proportion to d_{plane}, reaching as high as 1.4 (i.e., d_{opt} may be upwards of 40% larger than d_{plane}). Whereas Khoei (2019) opted to neglect the pile-up region and only report stress and COF values based on d_{plane}, the present author would argue that the pile-up region ought not to be discarded entirely. Admittedly, the choice to use d_{opt}, evaluated on the optical microscope, was motivated primarily out of convenience and efficiency: measurements on the Mitutoyo TM Microscope can be obtained considerably faster than those on the Zygo Newview 5000. However, there are grounds for characterizing the imprint in terms of its diameter at the top of the pile-up zone.

Consider for a moment the relative surface area of material in contact with the pin in the region of the imprint bounded by d_{plane} versus that bounded within the annulus between d_{plane} and d_{pileup}. These are denoted as area A_1 and A_2, respectively, in **Figure 36**. For an imprint with d_{pileup} that is 20% larger than d_{plane}, this translates into A_2 being 44% the size of area A_1. Likewise, for an imprint exhibiting d_{pileup} that is 35% larger than d_{plane}, A_2 becomes 82% of the size of area A_1.

Arguably, the contact stress in the region A_2 will be considerably less than that present in region A_1, as there simply isn't the volume of work material to support the load in the same way. However, it is reasoned that region A_2 must still contribute to the tribological interactions between pin and disc in some important way insomuch as the torque signature has been shown to correlate so well with the imprint diameter (that being d_{opt}, evaluated on the Mitutoyo TM Microscope).

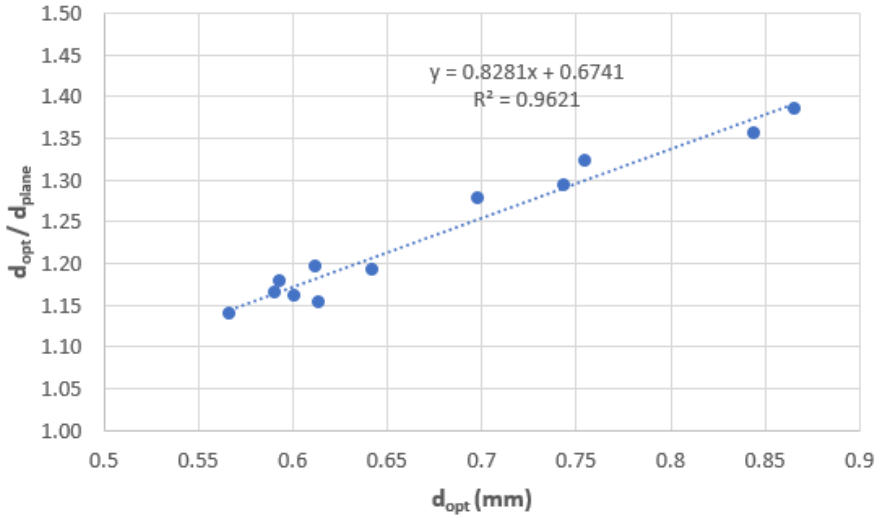

Figure 35: The ratio of d_{opt}/d_{plane} increases linearly with respect to d_{opt}

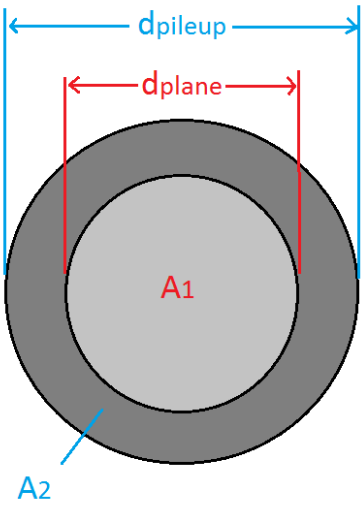

Figure 36: Schematic depicting A1 and A2 relative to d_{plane} and $d_{pile\ up}$

This is not to say that evaluating ***COF*** per **Eq. 3.3.3** using $\boldsymbol{d_{opt}}$ is the correct approach, or even a better approach than using $\boldsymbol{d_{plane}}$, but rather that until a better approach is defined that somehow incorporates $\boldsymbol{d_{plane}}$ and $\boldsymbol{d_{opt}}$ (or $\boldsymbol{d_{pile\ up}}$), evaluation of ***COF*** using $\boldsymbol{d_{opt}}$ should not be treated as invalid but rather as an alternative.

It is important to note that, for $d_{pile\ up}/d_{plane} = B$, evaluation of ***COF*** using $d_{pile\ up}$ results in a ***COF*** value that is smaller by a factor of 1/***B***, as expressed in **Eq. 3.5.1**.

$$COF_{opt} = COF_{pile\ up} = \left(\frac{1}{B}\right) COF_{plane} \qquad \textbf{Eq. 3.5.1}$$

Conversely, the penetration ratio ***h/r*** is somewhat larger when evaluated at the pile-up instead of the plane surface of the disc. For a range of ***B*** values based on the results of **Figure 35**, and assuming a spherical pin of radius ***R*** = 1.5 mm and $d_{plane} \leq 0.700$ mm, it can be shown that $(h/r)_{pile\ up}$ evaluated at the top of the pile-up is approximately a factor of ***B*** greater than $(h/r)_{plane}$ evaluated at the plane, as expressed in **Eq. 3.5.2**.

$$(h/r)_{pile\ up} \approx B * (h/r)_{plane} \qquad \textbf{Eq. 3.5.2}$$

Exactly how **Eq. 2.4.2.2** evaluates using the imprint diameter/radius at the top of the pile-up as compared with at the surface of the disc varies depending upon COF_{plane} and $(h/r)_{plane}$. **Table 1** presents a few different scenarios and illustrates that in all cases, $(COF+h/r)_{pile\ up}$ is always smaller than $(COF+(h/r))_{plane}$, but by how much appears to be a function of both $(COF/(h/r))_{plane}$ as well as ***B***.

The greatest discrepancies occur for relatively large values of ***COF*** and relatively small values of ***h/r***, such as the second column of data in **Table 1** (COF_{plane} = 0.45 and $(h/r)_{plane}$ = 0.075). However, the inequality in **Eq. 2.4.2.2** is not satisfied (i.e., ***COF*** + ***(h/r)*** > 0.5) if d_{plane} (r_{plane}) is used, suggesting the work material is shearing. However, if $d_{pile\ up}$ ($r_{pile\ up}$) is used, then the inequality holds (i.e., ***COF*** + ***(h/r)*** ≤ 0.5), supporting the likelihood of surface friction. Thus, the use of **Eq. 2.4.2.2** must be used with some reservation when evaluating the imprint size at the top of the pile-up, particularly when ***COF*** values are high.

Table 1: The effect of using d_{pileup} vs. d_{plane} in the evaluation of COF and (h/r)

COF_{pileup}	0.35			0.35			0.2			0.2		
$(h/r)_{pileup}$	0.15			0.1			0.15			0.1		
$(COF/(h/r))_{pileup}$	2.33			3.5			1.33			2		
$(COF + (h/r))_{pileup}$	0.5			0.45			0.35			0.3		
B	1.4	1.25	1.1	1.4	1.25	1.1	1.4	1.25	1.1	1.4	1.25	1.1
COF_{plane}	0.490	0.438	0.385	0.490	0.438	0.385	0.280	0.250	0.220	0.280	0.250	0.220
$(h/r)_{plane}$	0.107	0.120	0.136	0.071	0.080	0.091	0.107	0.120	0.136	0.071	0.080	0.091
$(COF + (hr))_{plane}$	0.597	0.558	0.521	0.561	0.518	0.476	0.387	0.370	0.356	0.351	0.330	0.311
$(COF + (h/r))_{pileup} - (COF + (hr))_{plane}$	0.097	0.058	0.021	0.111	0.068	0.026	0.037	0.020	0.006	0.051	0.030	0.011
$(COF + (h/r))_{pileup} / (COF + (hr))_{plane}$	1.194	1.115	1.043	1.248	1.150	1.058	1.106	1.057	1.018	1.171	1.100	1.036

3.6 Concluding Remarks

The main findings regarding imprint growth during on-axis rotation pin-on-disc tribometer tests, based on the experimental results presented thus far, are as follows:

- Increases in imprint diameter closely correlate with increases in torque signal and a greater number of adhesive wear marks visible on the imprint surface.
- For tests wherein the peak torque signal occurs mid-way through the rotation phase and not near the end, the peak or maximum torque signal better correlates with the size of the imprint than does the average torque signal evaluated over the last 30 s of rotation (one full revolution, for tests run at 2 RPM).
- Steady-state torque signal generally occurs after 30-40 s of rotation, although sometimes in considerably less time, suggesting that 60 s of rotation and evaluation of test parameters (i.e., load, torque, temperature) based on the average of measurements during the last 30 s of rotation is a reasonable approach.
- During elevated temperature tests, approximately 50% of imprint growth can occur within the first 15 s of rotation (first half revolution at 2 RPM) and approximately 80-90% of imprint growth can occur within the first 30 s of rotation (first full revolution).
- For sufficiently elevated temperatures (i.e., > 650 °C in the case of AISI 1045 steel), the added 60 s of load under sustained elevated temperatures will itself contribute a measure of imprint growth due to thermal softening of the work material. However, this contribution to imprint growth is relatively small

compared to that resulting from increased shear stress (flow stress) due to friction experienced during rotation.

- The diameter of the imprint evaluated at the top of the pile-up has been seen to range from about 15-40% greater than the diameter evaluated at the plane of the surrounding disc material. The method employed to measure the imprint diameter can have a significant effect on the value of imprint diameter obtained, not to mention the evaluation of ***COF*** and the inequality for evaluating the likelihood of surface friction being present (**Eq. 3.3.1.1** and **Eq. 2.4.2.2**, respectively).
- The region of the imprint bounded between the plane diameter and the pile-up diameter is reasoned to be of significance to the tribological interactions occurring at the pin-disc interface owing to its relatively large size and in light of the fact that all correlations identified in the above studies were based on evaluation of the imprint diameter at the top of the pile-up, not at the plane of the disc.

These conclusions will be brought to bear on the results presented and discussed in the ensuing chapters.

4. SHEAR PATTERNS IN THE IMPRINT MICROSTRUCTURE

4.1 Opening Remarks

The present chapter introduces experimental results from on-axis rotation pin-on-disc tribometer tests involving PVD-coated and uncoated cemented tungsten carbide pins in contact with two different counter bodies: AISI 1045 steel and SAE J434 D5506 ductile iron. While these results form the basis for further discussions in the body of this dissertation; the focus of the present chapter is an exploration of the microstructure of disc material in the vicinity of the imprint itself, specifically shear deformation patterns, in order to elucidate the nature of tribological contact occurring between pin and disc. Additional analytical techniques, including scanning electron microscopy (SEM) and secondary ion mass spectroscopy (SIMS), are utilized to help explain the surprisingly low friction coefficient of uncoated cemented carbide in contact with SAE J434 D5506 ductile iron at elevated temperatures.

4.2 Materials and Methods

4.2.1 Materials

Pins were fashioned from 3 mm ground rod of grade EMT 100 cemented carbide, which is composed of 93% WC, 6% Co and 1% other carbide and possesses an average grain size of 0.8 μm (EMT 100, n.d.). The supplier generated a 1.5 mm radius spherical tip on each end and polished the tip to a roughness of about 150 nm Ra. Some pins were left uncoated, while others had PVD coatings deposited on them by commercial vendors: TiN was

deposited by Brycoat (USA), while TiAlN and TiAlCrSiYN/TiAlCrN were deposited by Kobac (USA). In each case, coating thickness was nominally 3 µm.

Discs were prepared out of two different materials: AISI 1045 steel and SAE J434 D5506 ductile iron. The discs of AISI 1045 steel were square shaped, nominally 6 mm thick x 15 mm wide x 15 mm long. Discs of SAE J434 D5506 ductile iron were wedge shaped, approximately 10 mm wide at one end, 25 mm wide at the other, 40 mm long and 8 mm thick. The steel discs AISI 1045 steel were prepared by bandsaw cutting a slice from a cylindrical billet, milling and grinding the faces flat and parallel, waterjet cutting out the square sections, and then lapping the faces to approximately 10 nm Ra. The iron discs were bandsaw cut out of a cast component of somewhat irregular geometry (hence their wedge shape) and subject to similar processing steps to achieve a similar level of roughness.

Select discs were subjected to Rockwell B hardness tests as well as metallographic analysis (etched in 2% Nital and digital images acquired via a Nikon microscope). AISI 1045 steel discs exhibited a hardness of 92.9 ± 0.4 HRB, slightly lower than that of the SAE J434 D5506 ductile iron discs (97.3 ± 0.6 HRB). Images of the microstructure are presented in **Figure 37** and reveal that the steel contained relatively more pearlite than ferrite phase. In contrast, the ductile iron contained similar amounts of pearlite and ferrite, as well as graphite nodules.

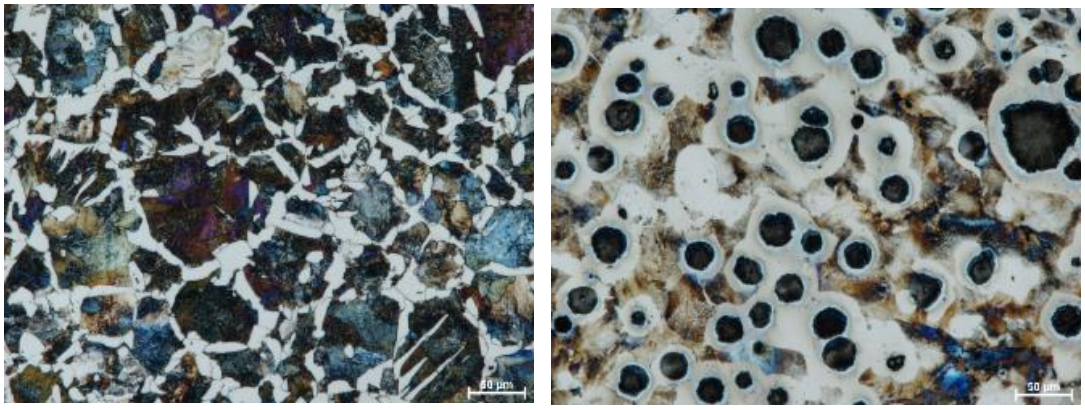

(a) **(b)**

Figure 37: Microstructure of (a) AISI 1045 steel discs and (b) SAE J434 D5506 ductile iron discs

4.2.2 Methods

4.2.2.1 Tribometer Tests

Tests were carried out on the Mark III tribometer under an applied load of 200 N for the steel discs and 300 – 500 N for the ductile iron discs (specifically, 500 N for TiN < 200 °C). The tests were carried out at different times and the author opted for a slightly increased load in the case of ductile iron at the time. Otherwise, testing conditions were similar; loads were maintained for 30 s prior to application of electrical current (which was gradually ramped up and held constant for 10 s) and rotation of the disc about the axis of the pin at 2 RPM for 60 s (while maintaining constant load and electrical current). The electrical current was adjusted over the course of multiple tests to achieve temperatures ranging from 20 °C to 950 °C. Prior to each set of tests at a given temperature, pin tips were polished using a 0.05 µm alumina paste on a polishing pad. Prior to each individual test, pin tips as well as disc surfaces were cleaned with isopropyl alcohol. In general, three test replicates were performed per test temperature and a mean friction coefficient

determined as per **Eq. 3.3.1.3**. The ratio of ***h/r*** was also computed so as to establish whether plastic contact and surface friction were occurring at the interface, per the inequalities presented in **Eq. 2.4.2.1** and **Eq. 2.4.2.2**. For simplicity, ***r*** was calculated based on measurements of the imprint diameter $\boldsymbol{d_{opt}}$, measured at the top of any pile-up. The depth ***h*** was not explicitly measured, rather the theoretical ***h*** was evaluated per **Eq. 2.4.2.4**.

4.2.2.2 Post-Test Analyses of Friction Surfaces Pin Tips and Imprints in Discs

Select pins were subjected to secondary electron (SE) imaging and energy dispersive x-ray (EDX) analysis using a JEOL-6610 scanning electron microscope. Additionally, some pins were sent to Winnats Scientific Services (United Kingdom) for static secondary ion mass spectroscopy (SIMS) analysis using a Millbrook MiniSIMS® instrument (SAI Ltd) equipped with a 5kV gallium ion source. After ion sputtering off the organic overlayer, positive and negative ion spectra were obtained in pairs at three sequential focus dimensions (magnifications) centered over the contact area, resulting in mean analysis depths of 1.5 nm, 30 nm and 500 nm beneath the original surface.

The severity of shear strain in the work material surrounding select imprints was investigated as follow:

- First, the profile of the initial imprint was acquired via white light interferometry using a Zygo NewView 5000.
- Subsequently, the discs were manually lapped with fine grit SiC paper and polished on a 1 µm diamond impregnated pad for approximately 2 minutes, prior

to washing in ethanol, drying under forced hot air and reinspection via interferometry to assess the amount of stock removal (as per **Figure 38**).

- After 2 to 3 iterations, removing approximately 10 microns total from the original disc surface, specimens were etched using 2% Nital to reveal the microstructure, and digital images obtained using the aforementioned Nikon microscope.

As well, select imprints were subjected to secondary electron (SE) imaging and energy dispersive x-ray (EDX) analysis using a JEOL-6610 scanning electron microscope to better understand the nature of contact at different locations within the imprint.

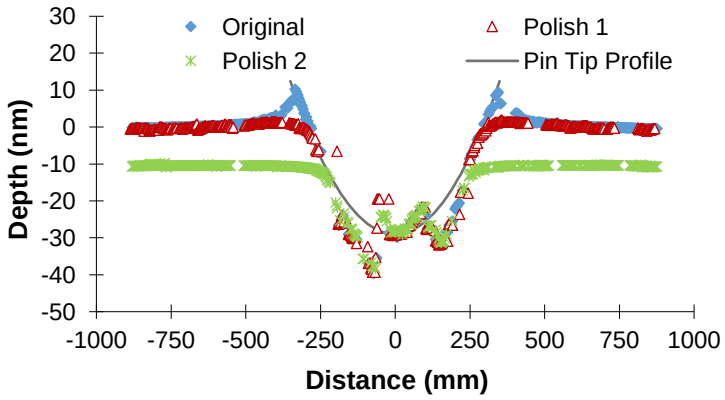

Figure 38: Imprint profiles from white light interferometry scans

4.3 Results and Discussion

4.3.1 Quantitative Results from Tribometer Tests

The friction coefficient (τ/σ) vs. temperature results from tests involving both AISI 1045 steel and SAE J434 D5506 ductile iron are presented in **Figure 39**. Likewise, the variation in h/r vs. temperature and $h/r + \tau/\sigma$ vs. temperature are presented in **Figure 40**

and **Figure 41**, respectively. Data points shaded red denote conditions wherein fewer than three test replicates were performed. Several observations are noteworthy:

- At elevated temperatures (> 400 °C), friction coefficients were lower for all pins in contact with SAE J434 D5506 ductile iron (***COF*** < 0.30) as compared with AISI 1045 steel (***COF*** > 0.30).
- At elevated temperatures (> 400 °C), friction coefficients were lower for the TiAlCrSiN/TiAlCrN-coated pins as compared with the TiN-coated pins, regardless of disc material.
- The trends in friction coefficient vs. temperature for the uncoated carbide pin were completely different for tests involving AISI 1045 steel as compared with SAE J434 D5506 ductile iron.
    - In contact with AISI 1045 steel at elevated temperatures (> 400 °C), the uncoated pin exhibited a higher friction coefficient than any of the coated pins, reaching a peak of ***COF*** = 0.57 at just shy of 600 °C.
    - In contact with SAE J434 D5506 ductile iron at elevated temperatures (> 300 °C), the uncoated pin exhibited a lower friction coefficient than any of the coated pins, reaching a value of ***COF*** = 0.10 at just shy of 600 °C.
    - The ***h/r*** ratio was similar for all pin and disc combinations, varying between about 0.08 and 0.12 (within the range that corresponds to plastic contact at the pin-disc interface (Fox-Rabinovich G. , 2008)), with the exception of tests between TiAlCrSiYN/TiAlCrN at temperatures greater than 800 °C, where the imprint size grew considerably due to thermal softening.

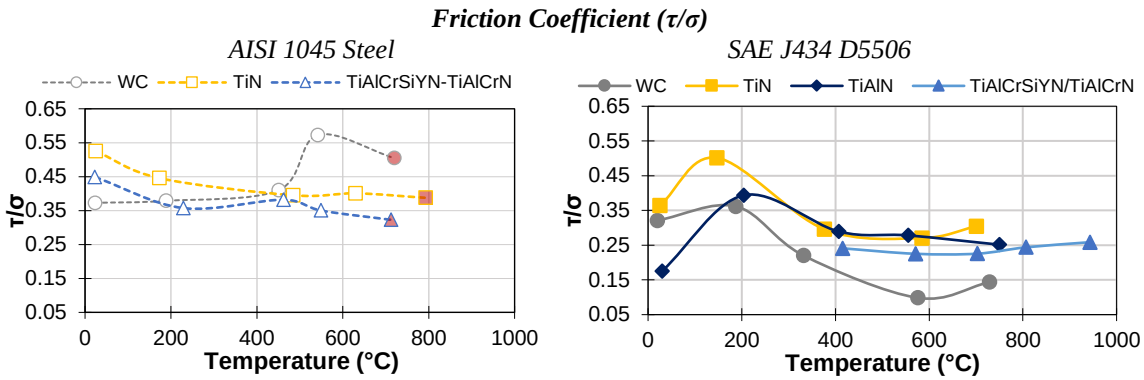

Figure 39: τ/σ vs. temperature for tests involving (a) AISI 1045 steel discs and (b) SAE J434 D5506 ductile iron discs

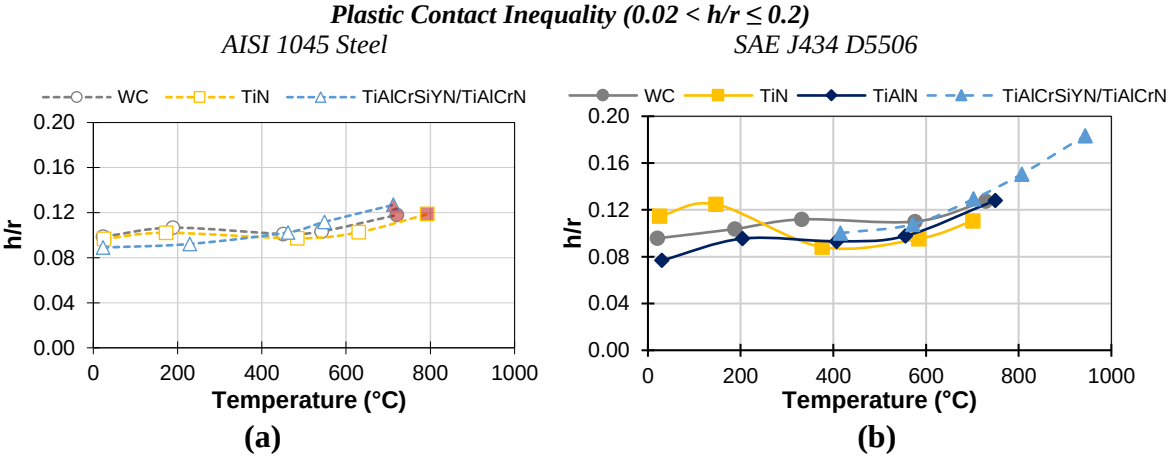

Figure 40: h/r vs. temperature for tests involving (a) AISI 1045 steel discs and (b) SAE J434 D5506 ductile iron discs

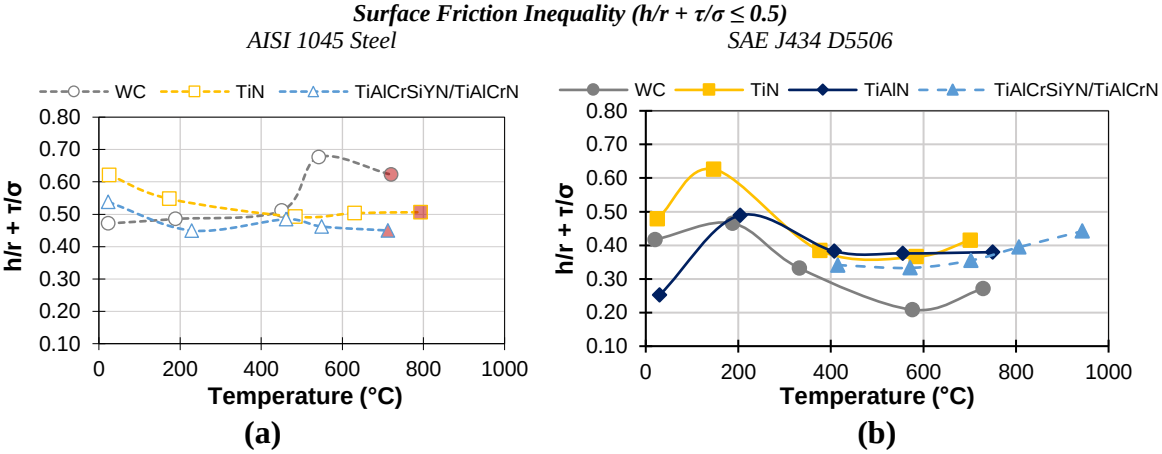

Figure 41: h/r + τ/σ vs. temperature for tests involving (a) AISI 1045 steel discs and (b) SAE J434 D5506 ductile iron discs

- The $\boldsymbol{h/r + \tau/\sigma}$ vs. temperature curves (**Figure 41**) were qualitatively similar to the ***COF*** vs. temperature curves (**Figure 39**), in so much as $\boldsymbol{h/r}$ varied so little with respect to temperature.
- The majority of the tests with AISI 1045 steel discs exhibited $\boldsymbol{h/r + \tau/\sigma}$ values equal to or greater than 0.5, suggesting material shear, i.e., seizure or shearing of the disc material (Fox-Rabinovich G. , 2008). However, tests involving TiAlCrSiYN/TiAlCrN exhibited values at or less than 0.5, suggesting surface friction, i.e., sliding at the pin-disc interface (Fox-Rabinovich G. , 2008).
- The majority of tests with the SAE J434 D5506 ductile iron discs exhibited $\boldsymbol{h/r + \tau/\sigma}$ values less than 0.5, suggesting surface friction was present (Fox-Rabinovich G. , 2008). The one exception was TiN at temperatures < 200 °C (coincidentally, these were the only tests performed at 500 N, all other tests were performed at 300 N load).

4.3.2 Analysis of Friction Surfaces

Additional tests were performed with select uncoated and coated pins under specific operating conditions so as to study the friction surfaces (pin tip and disc imprint) and elucidate the tribological interactions occurring, particularly in the case of ductile iron. In many cases, the resulting temperatures from these tests did not exactly match the temperatures of the data points in **Figure 39** to **Figure 41**.

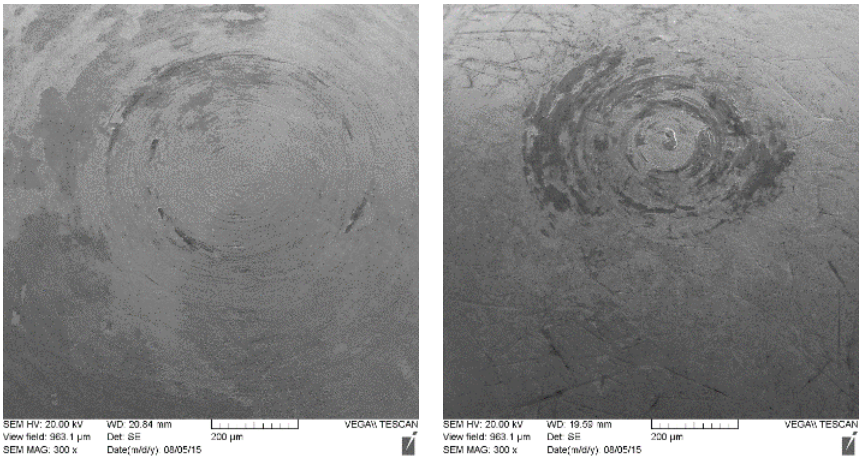

(a) **(b)**

Figure 42: SE images of uncoated pins after tribometer tests at 550 °C in contact with (a) AISI 1045 steel and (b) SAE J434 D5506 ductile iron

Figure 42 presents SE images of the uncoated pin tips after tribometer tests at about 550 °C in contact with both AISI 1045 steel and SAE J434 D5506 ductile iron. The amount of adhered work material was negligible on the pin that was in contact with carbon steel, located only at the very periphery of the contact zone. In contrast, the majority of the contact area of the pin after engagement with ductile iron was covered with adhered work material. Replicate tests with both work materials and visual inspection of the pin tip under optical microscope confirmed that these were not one-off occurrences. It is likely that the increased amount of material transfer observed between the uncoated pin and ductile iron was due to the greater abundance of soft ferrite phase in the disc of ductile iron compared to the disc of carbon steel (recall **Figure 37**).

Figure 43 presents images of select imprints in ductile iron acquired after the iterative white light interferometry and polishing technique (and subsequent etching) described in **Section 4.1.2.2**. The first two images are of imprints in ductile iron after tribometer tests with the uncoated pin at approximately 225 °C (**Figure 43(a)**) and 675 °C (**Figure 43(b)**).

Polishing of the pin tip had been performed prior to each of these particular tests. The third image (**Figure 43(c)**) is of an imprint in ductile iron resulting from the test performed immediately after and under identical operating conditions to the test which produced the imprint shown in **Figure 43(b)**, save that the pin tip was not polished prior to the test. The imprints shown in **Figure 43(a)** and **Figure 43(b)** exhibit significant distortion of the microstructure in the work material surrounding the imprint. In contrast, no such distortion is evident in the work material surrounding the imprint in **Figure 43(c)**.

The torque curves from the tribometer tests that produced the aforementioned imprints are presented in **Figure 44**. Curve ***a*** quickly climbs and remains steady for the duration of rotation, exhibiting only a mild decrease with time. In contrast, curve ***b*** exhibits a peak in torque very early on followed by a rapid decrease to low, stable torque values. In curve ***c***, the initial torque is low but rises gradually during the test, becoming nearly equal to the end torque value of curve ***b***.

Seemingly, the peak torque values in curves ***a*** and ***b*** are reflective of seizure between the pin and disc, resulting in shear deformation of the work material surrounding the pin. In the case of scenario ***a***, the evaluated ***COF*** at the test end was 0.32 and the imprint was 0.65 mm in diameter; per **Eq. 2.4.2.4** and **Eq 2.4.2.2** translates to $h/r = 0.11$ and $\tau/\sigma + h/r = 0.43 (< 0.5)$.

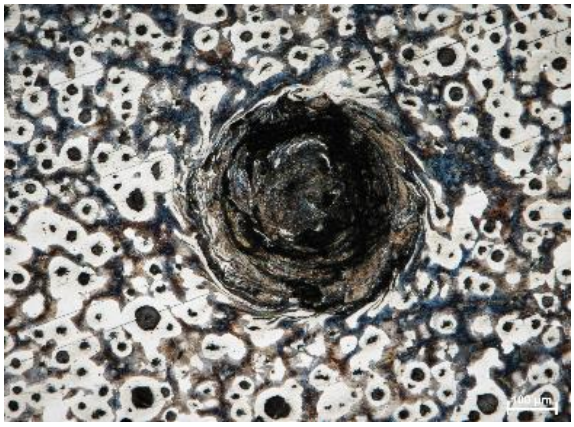

(a)

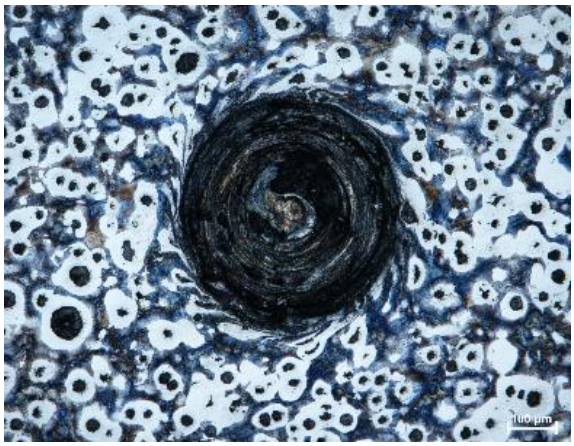

(b)

(c)

Figure 43: Optical micrographs of select imprints in SAE J434 D5506 after tribometer tests with an uncoated carbide pin

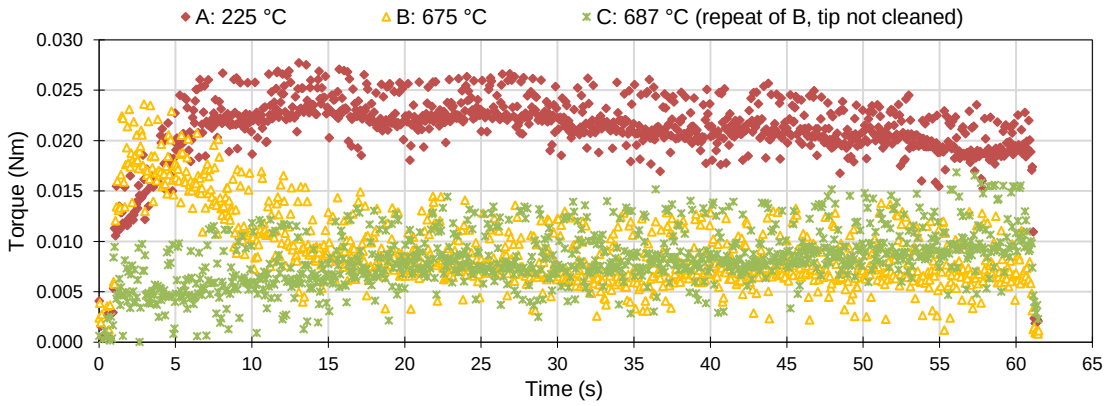

Figure 44: Torque curves from tests corresponding to the imprints shown in Figure 43

As per Shuster (Fox-Rabinovich G. , 2008), bulk shear should not be occurring when $\tau/\sigma + h/r < 0.5$, yet evidence of shear in the work material surrounding the disc imprint was observed during test ***a*** (**Figure 43 (a)**). The peak torque occurred after about 10 s of rotation and endured until about 30 s of rotation. Assuming the imprint diameter was in the range of 0.57 to 0.63 mm during this time, then the peak ***COF*** may have been as high as 0.37 to 0.41 and ***h/r*** in the range of 0.096 to 0.106, which puts the evaluation of **Eq. 2.4.2.2** very close to if not slightly exceeding the 0.5 limiting value for material shear.

In the case of test ***b***, the peak torque occurred much earlier and decayed much more rapidly, within about the first 2-3 s of rotation. Assuming the imprint diameter was in the range of 0.55 to 0.67 mm during this time (the final imprint measuring 0.69 mm), the peak ***COF*** may have ranged from 0.30 to 0.37, dropping to 0.12 by the end of the test. Likewise, the ***h/r*** values would have had a corresponding range of 0.093 to 0.109, which puts the evaluation of **Eq. 2.4.2.2** somewhat lower than the 0.5 threshold. Though not an exhaustive investigation, this suggests that material shear may actually have been occurring at τ/σ + ***h/r*** values somewhat lower than 0.5 (closer to 0.45).

In contrast, seizure between the pin and the disc never occurred in the case of scenario ***c***; rather sliding conditions at the pin-disc interface predominated resulting in continued low torque values and no shear deformation in the surrounding work material. Assuming the imprint diameter was in the range of 0.55 to 0.67 mm at the start of the test, the ***COF*** could have been as low as 0.070 to 0.085, with corresponding ***h/r*** values of 0.092 to 0.113 and $\tau/\sigma + h/r$ values well below the 0.5 threshold, supporting the notion of surface friction. By the test end, the diameter had reached 0.70 mm and the ***COF*** had only risen to 0.13.

Since the pin tip was not polished prior to test ***c***, it can be understood from **Figure 42(b)** that a significant amount of adhered work material would have been present. Similarity in torque and ***COF*** values suggest the same mechanism was at play during the balance of the test ***b*** as was occurring throughout the entirety of test ***c***. Thus, it would seem that material shear was a necessary pre-requisite for the surface friction that developed. Elevated temperatures also appeared to be a pre-requisite, as repeat tests at lower temperatures without intermediate polishing did not reveal the same low torque/low ***COF*** results.

Figure 45 presents images of select imprints in AISI 1045 steel acquired by the same technique. Significant distortion of the microstructure in the work material surrounding the imprint is evident in all three cases, which one would expect based upon evaluation of **Eq. 2.4.2.2**. ***COF*** values from these particular tests were all higher than those observed with the ductile iron, ranging from 0.34 to 0.48 by the end of the tests.

Based on the above, it seems that shear deformation in the work material adjacent to the imprint (i.e., material shear) can be expected for tests with values of ***COF*** = 0.35 and $\tau/\sigma + h/r = 0.45$ or higher (when evaluating imprint diameter at the top of the pile-up).

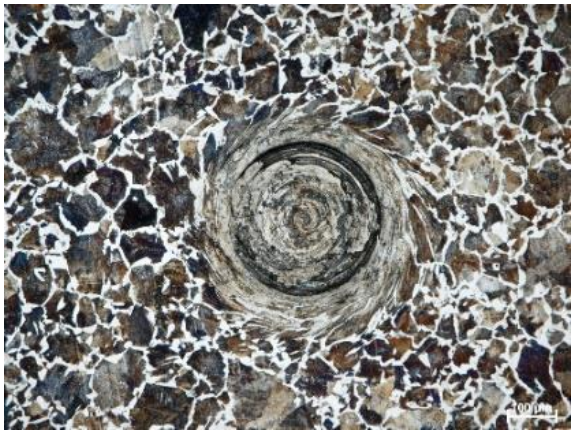

(a)

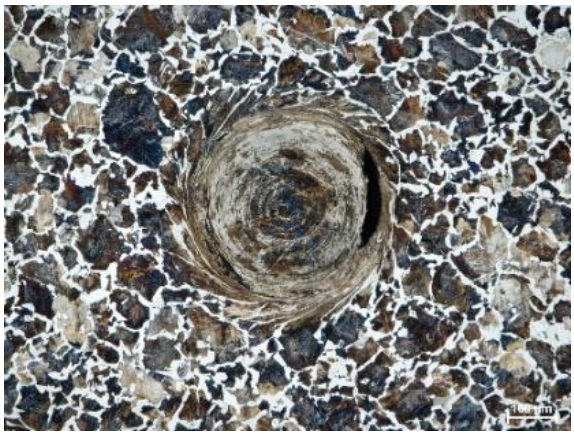

(b)

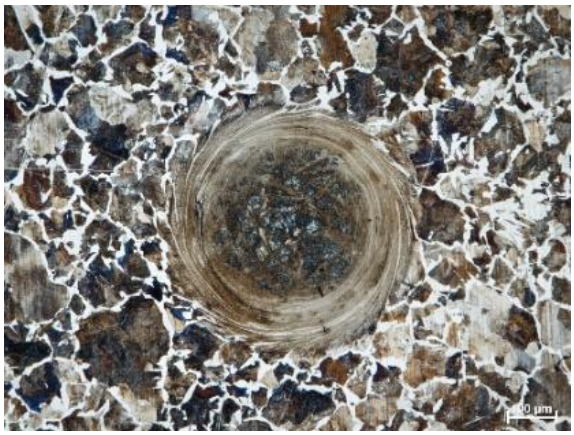

(c)

Figure 45: Optical micrographs of select imprints in AISI 1045 steel after tribometer tests with an uncoated carbide pin: (a) at 300 °C; (b) at 525 °C; and (c) at 660 °C

At the same time, the fact that ***COF*** and $\boldsymbol{\tau/\sigma + h/r}$ values are low based on evaluation of data over final 30 s of rotation are low does not imply that shear deformation in the work material did not occur. As illustrated by test ***b*** above for ductile iron (**Figure 43(b)** and **Figure 44**), an appreciable peak in torque signal during the earlier part of the rotation phase and subsequent decay suggests that shear in the work material most likely occurred at the start of rotation due to strong adhesion, giving way to surface friction during the later stages of the test. This shift to surface friction may have been due to some kind of lubricating tribofilm forming at the pin-disc interface or due to sufficient strain hardening in the work material associated with the earlier material shear, resulting in the adhesive bonds at the pin-disc interface becoming the so-called 'weakest link'.

Secondary Electron (SE) imaging of select imprints resulting from moderate and elevated temperature tests are presented in **Figure 46**, the test conditions for which are summarized in **Table 2** (along with the results of EDX spectra, discussed later). All imprints inspected showed two distinct regions: an inner region whose topography mirrors that of the pin and an outer region characterized by circular striations. At a first glance, these observations could be thought to denote "seizure" and "sliding" conditions, respectively. Closer inspection of the imprints formed with the TiAlN-coated pin (**Figure 46(c)** and **(f)**) reveals circular striations present in the inner region as well. These are more evident in **Figure 46(f)** (ductile iron). The circular striations in the inner regions of these two imprints are smoother and less obvious than those in the outer region, most likely reflecting actual texture on the tip of the pin imparted during pre-test polishing treatments (see **Figure 47** for a photograph of the pin tip used to form the imprint shown in **Figure**

46(f)). This would also support the notion that "seizure" occurred between the inner region of the imprint and the pin.

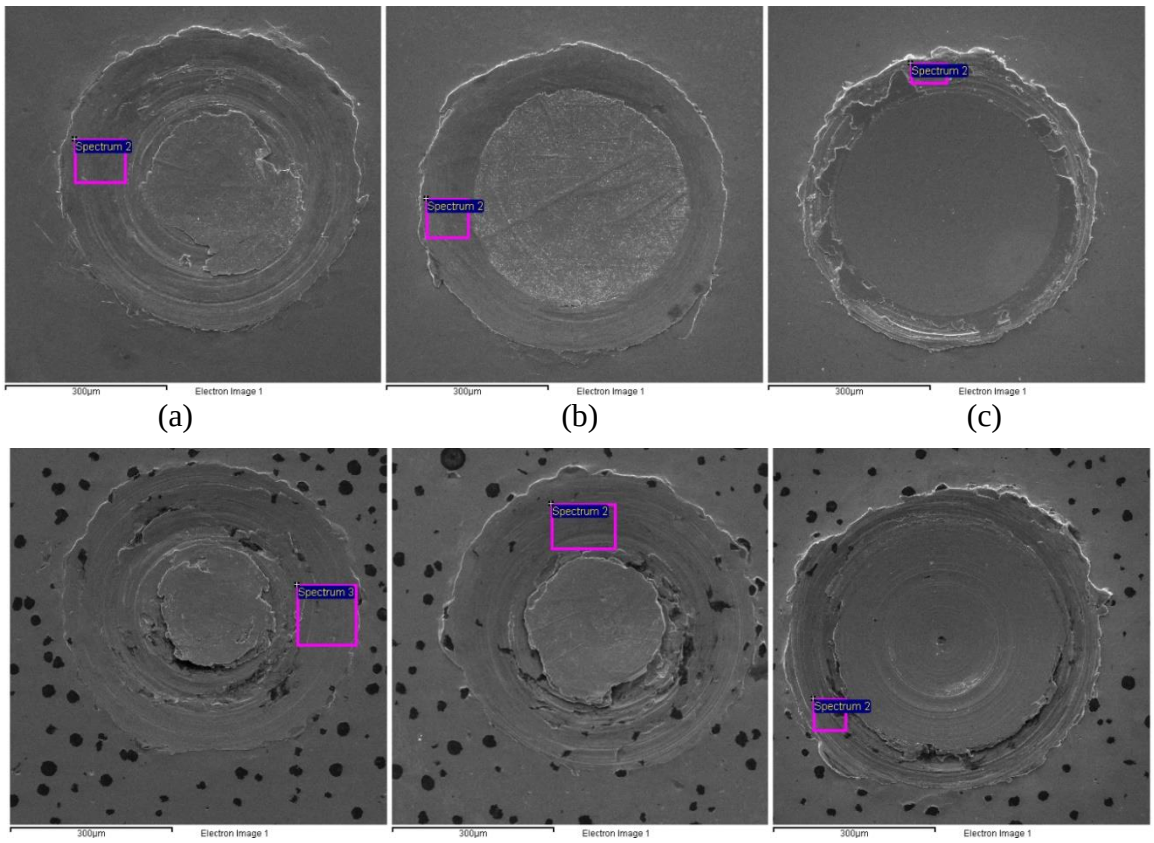

(a) (b) (c)

(d) (e) (f)

Figure 46: SE images of imprints from select trials

Table 2: Summary of friction test conditions and yields from EDX spectroscopy analyses in the outer region of imprints shown in Figure 46

	Disc	*Carbon Steel*			*Ductile Iron*		
Test Details	***Pin Coat***	*none*	*none*	*TiAlN*	*none*	*None*	*TiAlN*
	Temp.(°C)	*385*	*605*	*615*	*300*	*490*	*540*
	Imprint	*(a)*	*(b)*	*(c)*	*(d)*	*(e)*	*(f)*
EDX yields (at%)	***O (K)***	*38.2*	*45*	*21.9*	*17.2*	*32.7*	*25.1*
	Si (K)	--	--	--	*5.6*	*4.1*	*4.9*
	Mn (K)	*0.6*	*0.5*	*0.5*	--	--	--
	Fe (K)	*60.9*	*52.9*	*77.6*	*77.2*	*63.2*	*70.0*
	W (M)	*0.4*	*1.6*	--	--	--	--

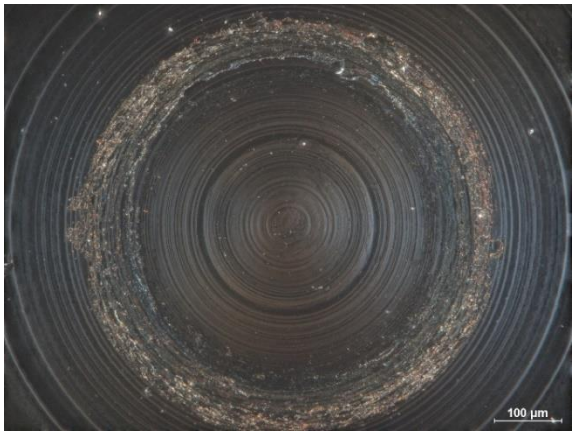

Figure 47: Circular striations and adhered work material present on the tip of the TiAlN-coated pin

Also shown in **Figure 47**, there is an abundance of adhered work material around the periphery of the contact zone on the pin, which coincides with the outer region of the imprint shown in **Figure 46(f)**. As such, it is unlikely that sliding occurred at the pin-disc interface, at least not by the end of the test; instead, sufficient metal-to-metal adhesion must have occurred to cause "seizure" in this outer region, resulting in shear deformation and eventual ductile fracture inside within the work material some distance below the pin.

Adhered work material will undergo a proportionally higher amount of strain per angle of rotation of the disc about the pin as the point of contact moves radially outward from the center of the pin. Likewise, the normal contact stress begins to decrease away from the center of the pin. Both of these factors help to explain the propensity for ductile fracture in the work material in the outer regions of the imprint. The circular striations would instead reflect strain-hardened asperities in the adhered work material ploughing through the outer region of the imprint as the disc rotates about the pin.

Interestingly, the area of the outer region is relatively smaller in the imprints formed after tests with the PVD coated pins as compared with the uncoated carbide pins tested at

similar temperatures. This may be the result of less intensive 'seizure' resulting, perhaps, in more frequent stick-slip cycles and thus less accumulation of strain in the volume of work material below the imprint, thereby less overall ductile failure in the outer region of the imprint. This would be consistent with the comparably lower oxygen (O) signal in this region of the imprints resulting from tests with the PVD coated pins, discussed later.

Also noteworthy is the lack of graphite nodules visible in the inner regions of imprints formed in ductile iron (**Figure 46(d)**, **(e)** and **(f)**). Intuitively, one might expect to see the nodules still present if "seizure" had occurred at the pin-disc interface in this inner region of contact, since relative motion between pin and the contacting surface of work material should be zero. However, "seizure" would likely only occur between the ferrite phase and the pin, not the graphite nodules. Instead, it is likely that either (i) the graphite nodules were covered over by adjacent ferrite phases during disc rotation (i.e., the graphite is trapped below the surface of the imprint in the inner region); or (ii) the graphite was extruded into the pin-disc interface by shear deformation of the nodules by surrounding ferrite phases adhered to the pin and distributed in the contact interface. Similar observations and explanations have been proposed by other researchers (Sugishita & Fujiyoshi, 1981), (Ghasemi & Elmquist, 2014). It is worth noting that graphite nodules are still visible in the outer regions of the imprints, albeit distorted from their original circular (spherical) form in the base work material, which lends credibility to either of the two scenarios above or a combination of both.

Energy dispersive x-ray (EDX) spectroscopy analyses were performed in both inner and outer regions of each imprint. Although carbon (C) was detected, its quantification is

not reliable (Konopka, 2013), hence these peaks were omitted during analyses. In the inner region, negligible differences were observed in the analyses of imprints of the same disc material. Notably, no O signal was detected in this region of any of the imprints. The quantitative results of analyses in the outer regions are summarized in Error! Reference source not found..

Significant O signal was detected in the outer region of all imprints, suggesting oxidation, but it was most prevalent in imprints resulting from contact with the uncoated pin. As well, O signal was usually higher in the steel imprints than in those of ductile iron.

At a first glance, one might be tempted to attribute this to the higher temperatures associated with the particular imprints analyzed, as oxidation rates increase with temperature. However, the imprint in the carbon steel after contact with an uncoated pin at 385 °C showed somewhat higher O and lower iron (Fe) signal than did the imprint in ductile iron after contact with an uncoated pin at 490 °C, despite having experienced temperatures almost 100 °C lower. The interaction volume in EDX spectroscopy analysis is known to be relatively deep, on the order of a few microns, suggesting the formation of relatively thick tribo-oxides in the peripheral contact region of the imprints where sliding occurred.

The small amount of tungsten (W) in the outer region of the carbon steel imprints that engaged with the uncoated pin suggests diffusion/dissolution of W into the steel. The lack of W in the imprints in both carbon steel and ductile iron after contact with the TiAlN-coated pin is not surprising when one considers that PVD coatings in general are well-known to reduce crater wear (an often diffusion-driven wear form) on the rake face of

carbide inserts during machining of steels (Kramer & Judd, 1985). In contrast, the lack of W signal in the imprints in ductile iron after contact with WC-Co pins does not preclude the possibility of diffusion/dissolution. Possibly, its absence reflects the thick layer of work material transferred to the pin surface during post-test pin retraction. Alternatively, the peaks for W overlap closely with many of those for Si and, thus, its detection may be difficult in small concentration when Si is abundant. Either way, it is expected that interdiffusion of W and Fe between the counter bodies would be a necessary precursor to the extensive work material transfer to the pin that has been observed.

To further clarify the nature of tribological interactions between uncoated and coated pins against ductile iron, SIMS analyses of select pin tips after tests at around 600 °C were performed, the results of which are presented in **Figure 48**. Note that positive ions (solid lines) and negative ions (dashed lines) were obtained from separate runs but combined into a single plot. At a mean depth of analysis of 1.5 nm and progressing to 30 nm, the uncoated pin featured a significant amount of Fe+ (consistent with observations of adhered work material) and a moderate amount of O-, both decreasing in intensity, as well as an increasing intensity of C4- and C5- fragments, which suggests a mixture of iron and iron oxides combined with graphite. At the same depths of analysis, the TiAlN-coated pin showed increases in O-, SiO_2-, AlO-, SiN-, Si+ and Mn+, all of which reached a peak at a mean depth of analysis of 30 nm, as well as Al+ and Ti+, which continued to increase in intensity during the final analysis of 500 nm mean depth. The C4- fragment was considerably lower in intensity on the TiAlN-coated pin than on the uncoated WC-Co pin, decreasing from the 1 nm to 30 nm mean depth.

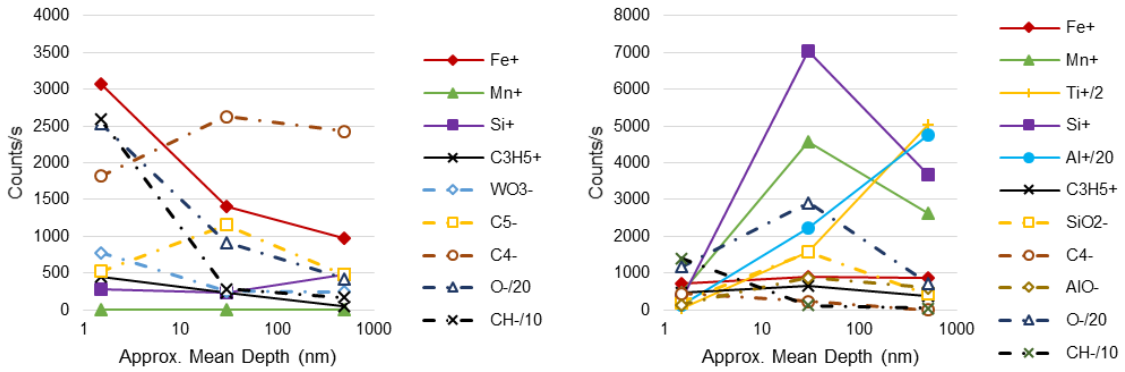

Figure 48: SIMS data obtained from (a) uncoated pin and (b) TiAlN-coated pin

4.3.3 Proposed Mechanism for Low Friction between Tungsten Carbide and Ductile Iron

In light of the above results, it is proposed that the low friction behaviour observed in the case of uncoated cemented tungsten carbide vs. SAE J434 D5506 ductile iron was the result of intensive adhesion between the carbide pin and the abundance of soft ferrite phase present in the ductile iron disc. This adhesion resulted in significant shear deformation in the surrounding work material during specimen rotation such that the graphite nodules were squeezed and elongated into semi-continuous layers in the sub-surface layers of the work material beneath the pin-disc interface. This squeezing of graphite from cast iron alloys has been observed by other researchers before (Ghasemi & Elmquist, 2014), (Sugishita & Fujiyoshi, 1981). Graphite is known to be an effective lubricant at low temperatures as well as above about 450 °C, though its lubricious nature is active only in the presence of certain species (e.g., water vapour, metal oxides) (Sliney, 1982).

The increase in friction coefficient from room temperature up to about 200 °C was characteristic of all the pin materials tested against ductile iron (**Figure 39(b)**) and most likely reflects loss of moisture from the contact zone. At higher temperatures, however,

oxidation of the iron work material occurred sufficiently, and the oxide intermixed with the graphite, enabling it to resume low shear stress sliding along its basal planes.

In contrast, SIMS analysis of the PVD coated pin suggests that oxidation of the coating (Ti, Al) as well as alloying elements such as Mn and Si prevented the intensive sticking necessary to initiate shearing of work material, with its associated squeezing and elongation of graphite nodules. Consequently, despite a reduction in friction at elevated temperatures (as compared to 200 °C and below), friction coefficient values remained higher for the PVD-coatings than for uncoated WC-Co.

It is expected that similarly strong adhesion occurred between the uncoated carbide and AISI 1045 steel, despite proportionally less ferrite phase compared with pearlite phase. However, the lack of graphite nodules precluded the possibility of low friction coefficient at elevated temperatures. The coatings reduced the tendency for adhesion at elevated temperatures, resulting in comparably lower friction coefficients.

Although extrusion of the graphite phase from within the surrounding metal matrix has been observed in cast irons before (Ghasemi & Elmquist, 2014), (Sugishita & Fujiyoshi, 1981), the importance of intense work material transfer as a prerequisite does appear to be unique to the present study. Interestingly, Sugishita & Fujiyoshi (1981) observed fundamental differences in friction and wear depending on the surface preparation of the ductile iron. More precisely, friction coefficients were low (< 0.15) and the resulting wear tracks in the ductile iron samples were very smooth when the ductile iron samples were either etched in Nital or polished to a mirror finish. In the case of etched surfaces, the graphite phase stood proud above the surrounding parent material. In the case of the mirror-

polished surfaces, the graphite nodules and/or flakes were still present at the surface, albeit slightly recessed below the surface height of the ferrite-pearlite matrix. In contrast, when ductile iron samples were prepared with a ground finish, the friction coefficient was relatively high (> 0.22) and the wear tracks in the iron comparably rough, indicating significant adhesion and material transfer. In this latter case, the entire exposed surface consisted of deformed metallic layers from the grinding treatment, with all graphite phase laying somewhere below. In essence, exposure of the graphite phase at the contacting surface was a prerequisite to low friction and smooth wear tracks.

During the aforementioned tests, the ductile iron samples had been polished to a mirror finish, however intensive material transfer still occurred. For comparison sake, ductile iron samples were also prepared with an etched and ground surface finish. These were subjected to tests at both room temperature and elevated temperatures (~600 °C) and exhibited results that were qualitatively and quantitatively similar to what was observed with the mirror-polished samples. In effect, intensive work material transfer and corresponding low friction was observed for all samples of ductile iron, irrespective of the surface preparation, when in contact with the uncoated carbide pin at elevated temperatures. This is fundamentally different to the observations of Sugishita & Fujiyoshi in (1981). The comparably lower sliding speeds and distances characteristic of the tribometer configuration used in the present study may be a strong contributor to these differences. Furthermore, it should be emphasized that this low friction behaviour was only observable during tests at elevated temperatures. Testing at low temperatures immediately following high temperature tests, without any intermediate polishing of the pin tip, did not manifest the same low friction

behaviour despite adhered work material remaining on the pin tip from the previous low-friction test.

4.4 Concluding Remarks

The results of several sets of on-axis rotation pin-on-disc tribometer tests at elevated temperatures were presented, involving uncoated and PVD-coated cemented carbide pins vs. AISI 1045 Steel as well as SAE J434 D5506 Ductile Iron discs. The major findings of this chapter can be summarized as follows:

- In general, ***COF*** values were lower for tests involving the ductile iron discs as compared with the steel discs, particularly at elevated temperatures (> 400 °C).
- The pin surface treatment (uncoated) that yielded the highest COF values among those tested in contact with the steel disc (***COF*** = 0.57 at $\boldsymbol{T} \approx$ 550 °C) produced the lowest ***COF*** values in contact with the ductile iron disc at very similar temperatures (***COF*** = 0.10 at $\boldsymbol{T} \approx$ 575 °C).
- Significant shear deformation was evident in the microstructure of work material surrounding the imprint, approximately 6 – 12 μm below the disc surface, for tests involving uncoated pins in contact with both work materials when ***COF*** = 0.35 or higher and $\boldsymbol{\tau/\sigma} + \boldsymbol{h/r} = 0.45$ (<0.5). The fact that parameters were evaluated based on an imprint diameter measured at the top of the pile-up, not at the plane of the disc surface, may well influence the seeming reduction in threshold for material shear per **Eq. 2.4.2.2** from 0.5 to 0.45.

- Even when ***COF*** and $\boldsymbol{\tau/\sigma}$ + ***h/r*** values are low based on evaluation of parameters at the end of test (final 30 s of data), shear deformation in the work material may be expected to be present when the torque signal sees an appreciable peak during the earlier part of the rotation phase. In other words, material shear may precede surface friction, the latter occurring either due to some form of lubricious tribofilm forming near the pin-disc interface or due to sufficient strain hardening occurring in the work material such that the adhesive bonds between pin and disc become the 'weakest link' and are more easily sheared.
- SEM and EDX spectroscopy analysis of various imprints revealed two distinct zones:
    - an inner zone, characterised by a lack of O signal and a topography that mirrors the features present on the pin tip, suggesting 'seizure' of the pin to the disc (i.e., relative motion/shearing is occurring in the work material below the imprint); and
    - an outer zone, featuring strong O signal and circular striations, most likely the result strain hardened asperities of adhered material ploughing through the bulk of work material in these regions of the disc, which would have been preceded by 'seizure' and sufficient strain to produce ductile failure.
- The extremely low friction observed between uncoated tungsten carbide and ductile iron was the result of intensive adhesion between the two materials, resulting in extrusion of a semi-continuous layer of graphite in the volume of work material adjacent to the pin-disc interface. This film of graphite exhibited lubricious

properties at elevated temperatures when intermixed with oxides formed in the outer region due to the aforementioned ductile fracture. The same intensive adhesion occurred between uncoated tungsten carbide and steel, but the comparably lower amount of ferrite relative to pearlite in the microstructure likely prevented the same level of material transfer. Likewise, the absence of graphite precluded the possibility of lubrication at the interface.

Assessment of the sub-surface microstructure (shear deformation patterns) at and surrounding the imprint, among other analytical techniques, played an important role in identifying and distinguishing the mechanisms of friction at play, particularly for tests involving the uncoated carbide pins. In **Chapter 5**, the microstructure in the imprints formed in the AISI 1045 steel discs will be studied more closely to reveal clues about the real pin-disc interface temperature achieved during tests.

5. INSIGHTS INTO THE TEST TEMPERATURE FROM THE IMPRINT

5.1 Opening Remarks

The size of the imprint resulting from an on-axis rotation pin-on-disc tribometer test is an important output. For a given load and work material, the magnitude of the imprint diameter is in part a reflection of the temperature achieved in the work material (larger imprints resulting from higher temperature tests, **Sec. 2.4.4**). As well, the imprint size strongly correlates with the severity of friction present at the pin-disc interface, as evidenced by the peak torque in the torque signal, adhesive wear marks present in the imprint and distortion in the surrounding work material (**Sec. 3.5.1**). The present chapter builds on the above understanding and results presented in **Chapter 4**, exploring the influence of the electrical resistivity of the PVD coating on the size of the imprint formed in the disc from a tribometer test at a given temperature.

5.2 Results and Analyses

5.2.1 Examination of Command Signal vs. Temperature and Imprint Diameter vs. Temperature from Tribometer Tests

Friction coefficient (***COF***), command signal and imprint diameter results from friction tests involving AISI 1045 steel, reported in **Chapter 4**, are displayed in **Figure 49**. The variation in COF with temperature is depicted in **Figure 49(a)** and is a copy of **Figure 39(a)**, while **Figure 49(b)**, **(c)** depict the variation in temperature as a function of command signal and the variation in diameter as a function of temperature, respectively. Data from a single test involving a ZrN/NbN-coated pin is also shown in **Figure 49(b)**, **(c)**.

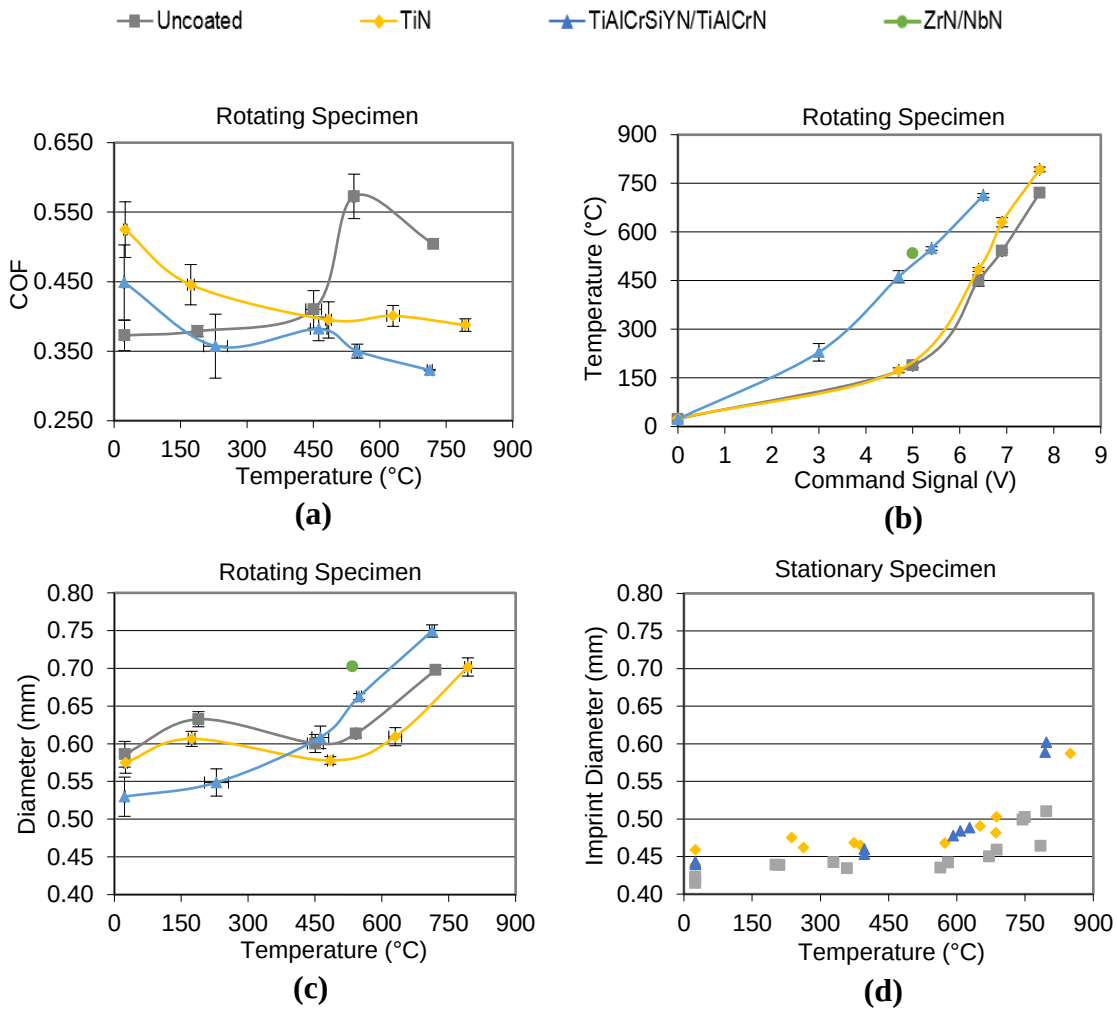

Figure 49: Results from rotating specimen (a - c) and stationary specimen (d) tribometer tests with AISI 1045 carbon steel

Data in **Figure 49(a)** through **(c)** all correspond to "rotating specimen" tests (i.e., friction tests). In contrast, **Figure 49(d)** depicts the variation in imprint diameter as a function of temperature for a set of "stationary specimen" tests, in which the test procedures were otherwise identical to those used in the "rotating specimen" tests except that the disc remained stationary for 60 seconds instead of rotating at 2 RPM. The results for uncoated tungsten carbide were presented previously in **Figure 32**. For clarity, the temperature reported (i.e., the "test temperature") is measured 2 mm above the pin-disc interface.

The results displayed in **Figure 49(b)** indicate that for a given level of electrical current (proportional to Command Signal (V) sent from the PC to the welding power supply), rotating specimen tests with the TiAlCrSiYN/TiAlCrN-coated pin resulted in an appreciably higher temperature compared with the uncoated or TiN-coated pin. A similar observation can be made for the data point corresponding to the ZrN/NbN coating. In other words, tests featuring either of these two coatings required about 1.5-2.0 V less command signal (translating to approx. 30-40 A less electrical current) to achieve the same temperature. This is related to differences in the electrical resistivity of the coatings, as will be shown later.

Correspondingly, the results presented in **Figure 49(c)** indicate that, at elevated temperatures, imprint diameters from tests involving the TiAlCrSiYN/TiAlCrN-coated pin were comparably larger than those for the uncoated or TiN-coated pins at otherwise similar test temperatures. A similar observation can also be made for the imprint diameter from the single test involving the ZrN/NbN coating.

The data from stationary specimen tests (**Figure 49(d)**) suggests that, for a load of 200 N, appreciable increases in imprint diameter due to thermomechanical changes in the work material did not occur until the temperature had exceeded approximately 700 °C, which, incidentally, is about the temperature above which the austenite phase can begin to exist (727 °C) (Callister, J., 2003). The curves are virtually indistinguishable for all three surface treatments. If anything, the diameter of imprints resulting from tests with the uncoated WC-Co appear systematically smaller than those of the other two pins by about 0.030 mm,

although at approximately 750 °C, there is a nearly 0.100 mm difference in imprint diameter resulting from tests between the uncoated and TiAlCrSiYN/TiAlCrN-coated pins.

Assuming there is no variation in hardness among the discs of AISI 1045 used in the tests, then differences in imprint diameter should be attributable to differences in the severity of pin-disc adhesion/COF, the resulting temperature achieved at the pin-disc interface, or some combination. As per **Figure 49(a)**, the COF was much higher for the uncoated pin vs. AISI 1045 steel than it was for the TiN- and TiAlCrSiYN/TiAlCrN-coated pins, at elevated test temperatures of approx. 550 °C and above. If the actual interface temperature was equivalent between two data points that exhibited the same test temperature, then the fact that imprints resulting from tests with uncoated pins were slightly larger than imprints from tests with the TiN-coated pins can be accounted for by the difference in COF. However, that the imprints from the TiAlCrSiYN/TiAlCrN-coated pins were so much larger than those from the uncoated pin is incongruent.

5.2.2 Analysis of Imprints

Observations of the imprints resulting from the tests suggest that differences in interface temperature likely occurred during the tests in question, particularly for tests involving the TiAlCrSiYN/TiAlCrN-coated pin. Images of representative imprints from tests involving the TiN-coated and TiAlCrSiYN/TiAlCrN-coated pins were acquired from both the as-tested surface as well as a few microns beneath the original surface, achieved by polishing and subsequent etching in 2% Nital (following the method described in **Sec. 4.2.2.2**). The images are shown in **Figure 50** and **Figure 51**, respectively.

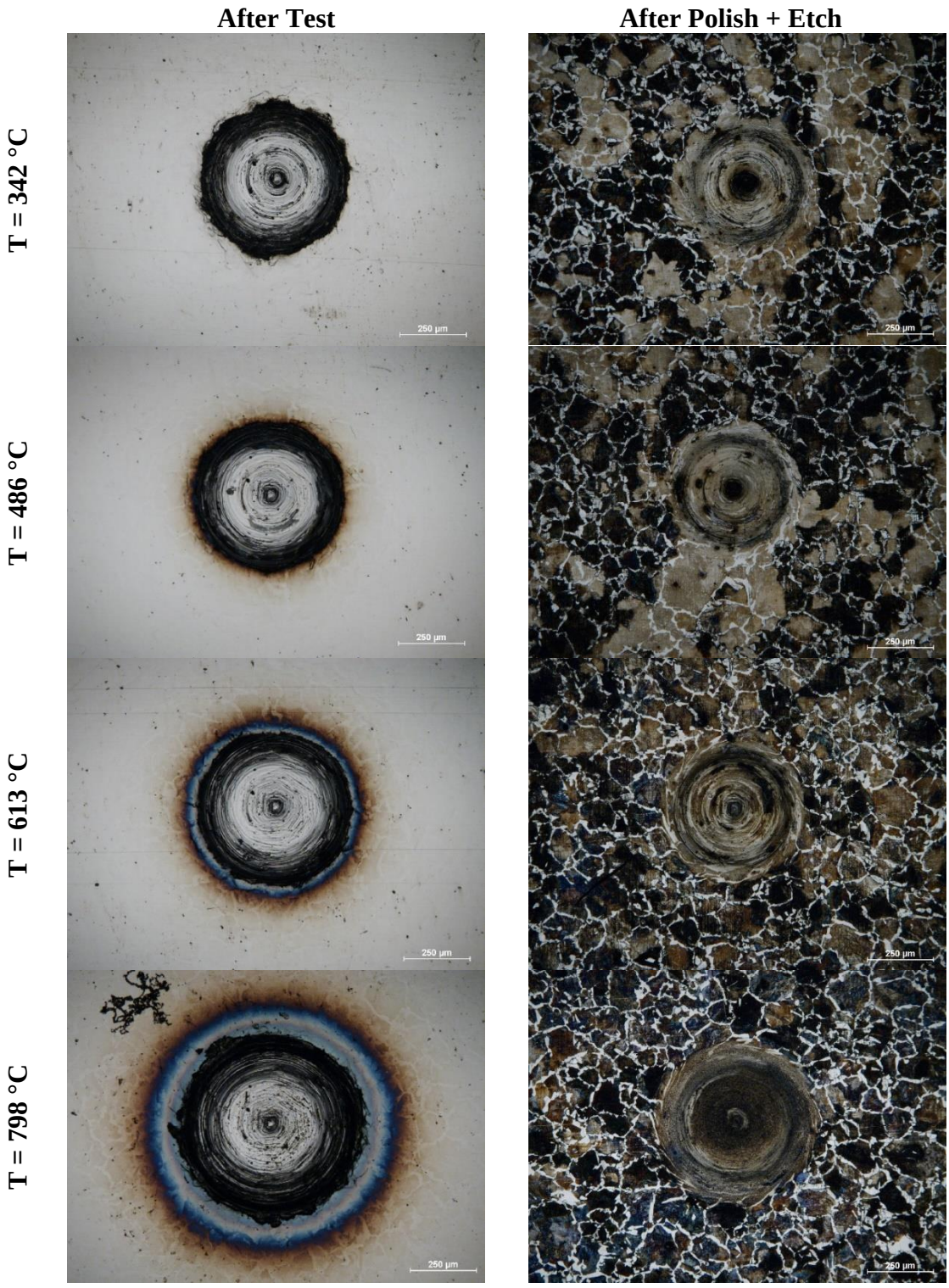

Figure 50: Select imprints from tests involving TiN-coated pins

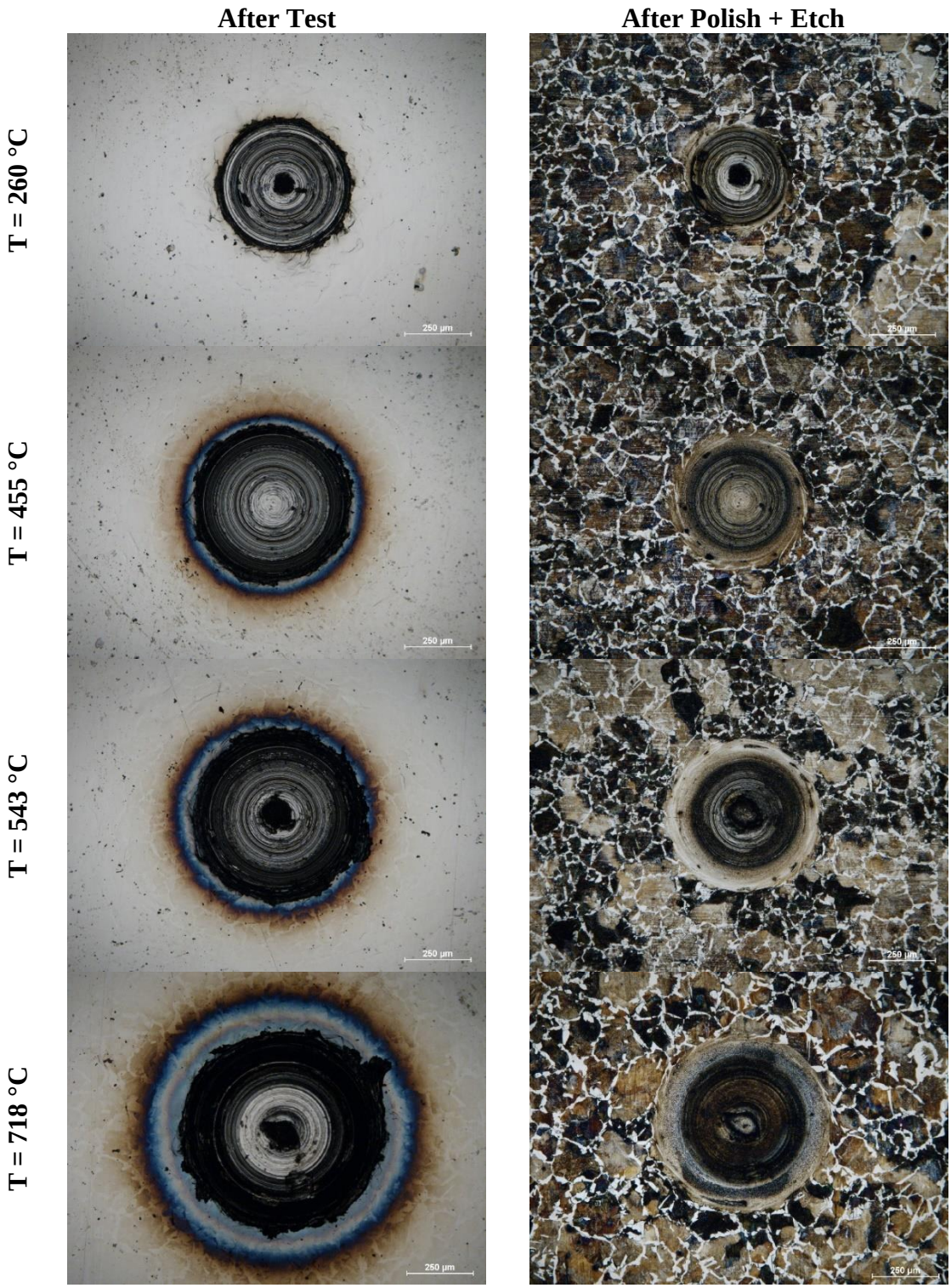

Figure 51: Select imprints from tests involving TiAlCrSiYN/TiAlCrN-coated pins

First of all, for similar test temperatures, the imprints formed during tests with the TiAlCrSiYN/TiAlCrN-coated pin featured a thicker, more pronounced band of oxidized material surrounding them compared with those formed during tests with the TiN-coated insert. As well, for similar test temperatures, differences could be seen in the microstructure of the work material in the vicinity of the imprints formed. Some semblance of the base microstructure remained evident in the periphery of the imprint for the 613 °C test between TiN vs. AISI 1045 steel, whereas the microstructure at the periphery of the imprint from the 543 °C test between TiAlCrSiYN/TiAlCrN vs. AISI 1045 steel was highly refined, nearly amorphous, suggesting that recrystallization may have occurred. This same microstructure was apparent in the imprint resulting from the test involving the TiN-coated pin at a test temperature of 798 °C.

Though not shown, images of the as-tested as well as the polished and etched imprints from tests with the uncoated carbide pin were qualitatively similar to those from tests with the TiN-coated pin in terms of the thickness of the surrounding oxide band microstructural features within the imprint. Also, the as-tested imprint from the test with the ZrN/NbN-coated pin showed an even thicker band of oxidized material surrounding it compared with that of the TiAlCrSiYN/TiAlCrN-coated pin at a similar temperature.

The above observations suggest that the test temperature may not be representative of the actual temperature at the pin-disc interface, where tribological interactions occur, that would give rise to the differences in imprint size, severity of surface oxidation surrounding the imprint and microstructure of work material in the vicinity of the imprint. Potential reasons for this are herein explored.

5.2.3 Examination of Temperature-Time Profiles

First, as presented in **Sec. 3.4.4**, it should be restated that the reported test temperature is an average of measurements during the last 30 s of rotation. In reality, the measured temperature is not constant over the entire duration of the rotation stage of the test due to the open-loop heating configuration employed. Closer inspection of the temperature-time profiles from the various tests performed reveals some differences, as shown in **Figure 52** (note that the heating stage commences at about t = 32 s, whereas rotation commences at about t = 42 s to t = 46 s, depending on the electric current applied). The test temperature (2 mm above the pin-disc interface) on the TiAlCrSiYN/TiAlCrN-coated pin was about 150 °C higher at the onset of rotation as compared with the uncoated WC-Co pin. The temperature-time profile for the test involving ZrN/NbN closely mimicked that of TiAlCrSiYN/TiAlCrN.

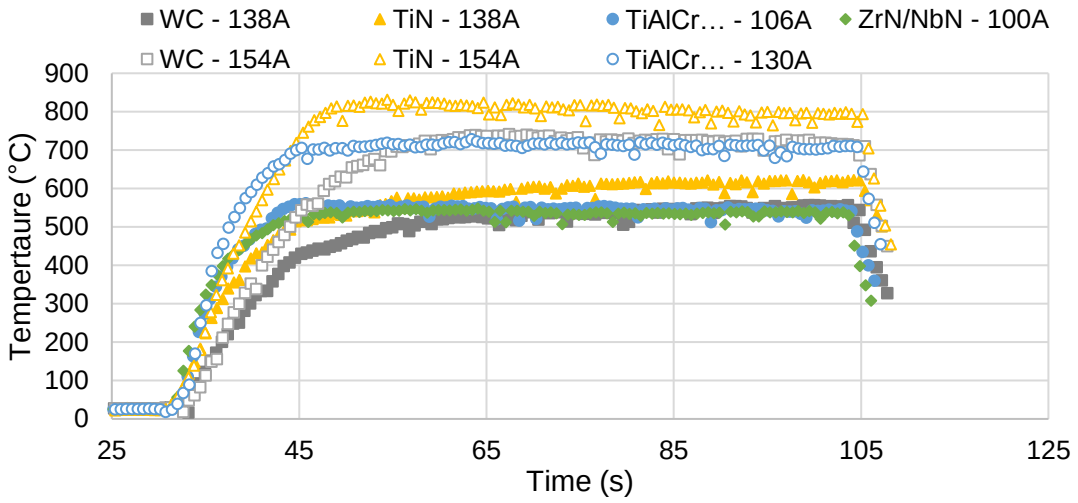

Figure 52: Temperature-time profiles from various tests against an AISI 1045 steel disc

A difference in temperature persisted throughout the first 10-20 s of rotation, after which both TiAlCrSiYN/TiAlCrN-coated and uncoated pins exhibited the same temperature through to the end of the test. Per **Section 3.5.2**, it is expected that more than 50% of the overall growth in the imprint diameter will have occurred during the first 15 s of rotation, which coincides with the period of time during which the measured temperature 2 mm above the pin-disc interface was higher for tests with TiAlCrSiYN/TiAlCrN-coated and ZrN/NbN-coated pins relative to tests with the uncoated pin, despite equivalent test temperatures during the last 30 s of rotation. Thus, differences in imprint size can in part be explained by differences in the temperature-time profile during the first 15-30 s of rotation, during which time the majority of imprint growth occurs. However, this does not explain the smaller imprint diameter resulting from tests with the TiN-coated pin. Notably, the temperature-time profile for the TiN-coated pin tested at 154A was actually 100°C higher than that of the TiAlCrSiYN/TiAlCrN-coated pin tested at 106A test for the entirety of disc rotation (**Figure 52**).

5.2.4 Examination of Coating Electrical Resistivity

An alternative hypothesis is that a coating with a significantly higher electrical resistivity as compared with another coating (or the pin substrate) may lead to a much higher temperature at the actual pin-disc under test conditions producing otherwise identical test temperatures, as measured 2 mm above the pin-disc interface.

As shown in **Figure 49(b)**, rotating specimen tests involving TiAlCrSiYN/TiAlCrN-coated and ZrN/NbN-coated pins demonstrated a considerably higher test temperature than

did tests involving uncoated or TiN-coated pins for the same command signal (i.e., electrical current passing through the specimens). The likely cause for this is a higher electrical resistivity for TiAlCrSiYN/TiAlCrN and ZrN/NbN coatings.

Established methods for evaluating the electrical resistivity of materials include the Two-Point method, Four-Point method and the van der Pauw method, as detailed in (Heaney, 2003). However, all of these methods require that the sample be flat (the Two-Point and Four-Point methods further restrict the sample geometry be rectangular).

In order to get a sense of the relative electrical resistivity of the coating materials deposited onto the pins used on the MMRI tribometer, which are not flat, a simple test was devised. The pin was laid flat on a workbench while the leads of an Ohmmeter were pressed against the cylindrical portion of the pin adjacent to the hemispherical tip at either end of the pin, as depicted in **Figure 53**. The average values from three separate measurements for the pin and various coating materials deposited onto available pins are listed in **Table 3**. It should be noted that the Ohmmeter used could not resolve resistance measurements lower than 0.2 Ω. While the electrical resistivity of each coating could not be directly evaluated, the differences in electrical resistance measurements across different coated pins reflects differences in the relative magnitude of the coating electrical resistivity.

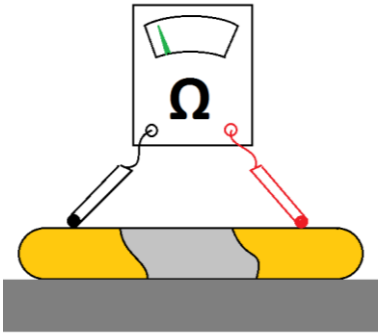

Figure 53: Illustration of ohmmeter measurements

Table 3: Comparison of electrical resistance measurements

Material	***Resistance (Ω)***
WC-6%Co (pin)	*0.2*
TiN	*0.2*
TiCN	*0.2*
TiAlN	*0.2*
CrN	*0.5*
AlTiN	*1.8*
CrAlON	*2.5*
TiAlCrSiYN/TiAlCrN	*7.5*
ZrN/NbN	*25*
DLC	*>20x10^6*

The results presented in **Table 3** suggest that the TiAlCrSiYN/TiAlCrN coating must have an electrical resistivity at least 1-2 orders of magnitude higher than the uncoated substrate and/or the TiN coating. Likewise, it can be inferred that the ZrN/NbN coating possesses an electrical resistivity even higher than that of TiAlCrSiYN/TiAlCrN. Arguably, these are only room temperature measurements, but it is expected that the relative ranking of these materials in terms of electrical resistivity will remain the same at elevated temperatures as well.

5.3 Concluding Remarks

The following conclusions can be drawn from the above results:

- The greater the electrical resistivity of the coating deposited onto cemented tungsten carbide pins, the lower the electrical current required to pass through the specimens to achieve a given test temperature – measured 2 mm above the pin-disc interface.

- Tests involving coatings with a higher electrical resistivity (inferred from electrical resistance measurements presented in **Table 3**) will tend to produce larger imprints with a thicker band of oxides around the periphery of the imprint and a greater degree of grain refinement/recrystallization in the outer regions of the imprint microstructure as compared with tests involving lower electrical resistivity coatings at the same test temperature.

The likelihood is that the electrical resistivity of the coating influences the thermal gradient in the pin tip, with higher electrical resistivity resulting in a steeper thermal gradient (i.e., higher pin-disc interface temperatures), for the same apparent test temperature. This hypothesis will be explored via numerical modeling in **Chapter 6**.

6. MODELING THE TEMPERATURE DISTRIBUTION IN THE PIN AND DISC

6.1 Opening Remarks

The motivation for modeling the temperature distribution in the pin and disc is twofold:

(i) The actual pin-disc interface temperature is inaccessible during physical tests. While the test temperature at a location approximately 2 mm above the interface is measured, a means of estimating the actual pin-disc interface temperature would be useful.

(ii) As hypothesized in **Sec. 5.2.4**, the electrical resistivity of the coating may have an influence on the temperature gradient in the pin tip such that a coating with relatively high electrical resistivity may cause the actual temperature at the pin-disc interface to be considerably higher than a coating with relatively low electrical resistivity, despite exhibiting similar test temperatures 2 mm above the interface. Modeling the temperature distribution in the pin and disc will be helpful to confirm if this hypothesis is true.

6.2 Initial Model Formulation

6.2.1 Formulating A One-Dimensional Thermal Model of the Pin subject to Internal Heat Generation via Electric Current

The pin was subdivided into a series of nodes ***(i)*** located along its axis, each with a temperature T_i. **Figure 54** illustrates the concept for a generalized radially symmetric object. Surrounding each node ***(i)*** is a cylindrical control volume whose radius r_i is equal to that of the circle realized by slicing the pin perpendicular to its axis at the vertical location

z_i of the node. The control volume extends vertically to the midpoint between adjacent nodes ***(i-1)*** and ***(i+1)***. Accordingly, the nodes are not centered vertically within their surrounding control volumes if the distance between node ***(i)*** and node ***(i-1)***, that is Δz_{i-1}, is not equal to the distance between node ***(i)*** and node ***(i+1)***, or Δz_i.

Heat $q_{gen,i}$ is generated within the control volume surrounding node ***(i)*** due to the flow of electric current I through the control volume, which is essentially a conductive element with length l_i, cross-sectional area A_i and electrical resistivity ρ_{pin}, in accordance with **Eq. 6.2.1.1**:

$$q_{gen,i} = I^2 R_i = I^2 \left(\frac{\rho_{pin} l_i}{A_i} \right) = \frac{0.5 I^2 \rho_{pin} (\Delta z_{i-1} + \Delta z_i)}{\pi r_i^2} \qquad \textbf{Eq. 6.2.1.1}$$

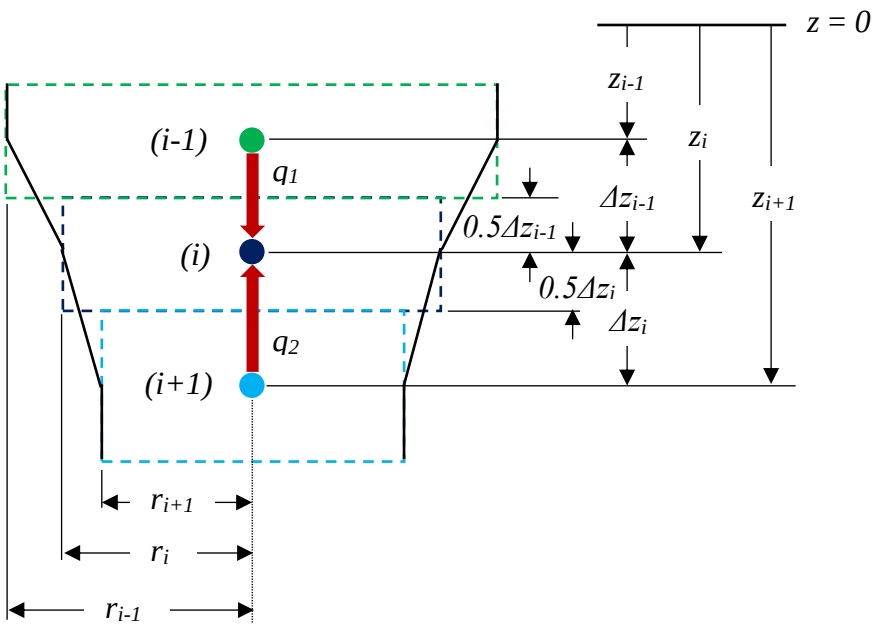

Figure 54: Defining nodes and spacing for a one-dimensional model of heat transfer in a generalized radially symmetric object (e.g., the pin)

Additionally, there is heat transfer via conduction between adjacent nodes. Referencing **Figure 54**, q_1 denotes heat conduction from node ***(i-1)*** into node ***(i)*** while q_2 denotes heat conduction from node ***(i+1)*** into node ***(i)***, as expressed in **Eq. 6.2.1.2** and **Eq. 6.2.1.3**, respectively.

$$q_1 = kA_1\left(\frac{T_{i-1} - T_i}{\Delta z_{i-1}}\right) \qquad \textbf{Eq. 6.2.1.2}$$

$$q_2 = kA_2\left(\frac{T_{i+1} - T_i}{\Delta z_i}\right) \qquad \textbf{Eq. 6.2.1.3}$$

Given that the radius of adjacent control volumes can be different, depending on the local geometry of the radially symmetric object being modeled, the following expressions are used to evaluate the effective cross-sectional areas A_1 and A_2 through which heat conduction occurs:

$$A_1 = 0.5\pi\left({r_{i-1}}^2 + {r_i}^2\right) \qquad \textbf{Eq. 6.2.1.4}$$

$$A_2 = 0.5\pi\left({r_i}^2 + {r_{i+1}}^2\right) \qquad \textbf{Eq. 6.2.1.5}$$

Under steady-state conditions, the conservation of energy dictates that the net flow of heat into a control volume plus any heat generated within that same control volume must be equal to zero. For node ***(i)***, this translates to:

$$q_1 + q_2 + q_{gen,i} = 0 \qquad \textbf{Eq. 6.2.1.6}$$

Substituting **Eq. 6.2.1.2** and **Eq. 6.2.1.3** into **Eq. 6.2.1.6**, and introducing some coefficients for simplification, the following expression can be obtained:

$$C_1T_{i-1} + C_2T_{i+1} + C_3T_i + q_{gen,i} = 0 \qquad \textbf{Eq. 6.2.1.7}$$

where the coefficients C_1, C_2 and C_3 are defined below.

$$C_1 = \frac{kA_1}{\Delta z_{i-1}} \qquad \textbf{Eq. 6.2.1.8}$$

$$C_2 = \frac{kA_2}{\Delta z_i} \qquad \textbf{Eq. 6.2.1.9}$$

$$C_3 = -(C_1 + C_2) \qquad \textbf{Eq. 6.2.1.10}$$

The pin used in the tribometer studies featured a cylindrical portion of radius r = 1.5 mm as well as a hemispherical tip of equal radius. While the overall length of the pin was about 33 mm, approximately 21 mm extended beyond the face of the collet used to secure it onto the load column. As such, the pin was divided into two distinct regions for modeling purposes: a 20 mm long cylindrical portion and a nominally 1.5 mm radius hemispherical tip. Node ***(0)*** was located at the transition between the cylindrical and hemispherical portions of the pin and was chosen as the vertical reference position (i.e., $z_0 = 0$). Nodes located further up the cylindrical portion of the pin were designated with negative indices (*i.e.*, i = -1, -2, -3, …) while nodes located in the hemispherical portion of the pin were designated with positive indices (*i.e.*, i = 1, 2, 3, …).

Typically, the pin featured a nominally 3 μm thick coating deposited over its hemispherical and cylindrical portions. Assuming that the coating material possesses a higher electrical resistivity compared to the pin material, then electric current should not flow through the coating layer except at the contact between pin and disc.

In reality, the hemispherical tip of the pin would extend into the disc and form an imprint of diameter $d < 2r$. For simplicity, the contact between the pin and disc was modeled as a 3 μm thick cylinder of diameter d. The very tip of the pin was accordingly truncated with the bottommost node ***(N)*** positioned at z_N such that $r_N = 0.5d$. In the author's experience, d typically ranges from about 0.4 to 0.8 mm, depending on the load applied, the disc material and the resulting temperature achieved.

Figure 55 contrasts the actual pin-disc interface with the simplified representation used in the thermal model. Effects of real vs. apparent contact as well as potential contaminants/oxides at the surface are addressed in a later section.

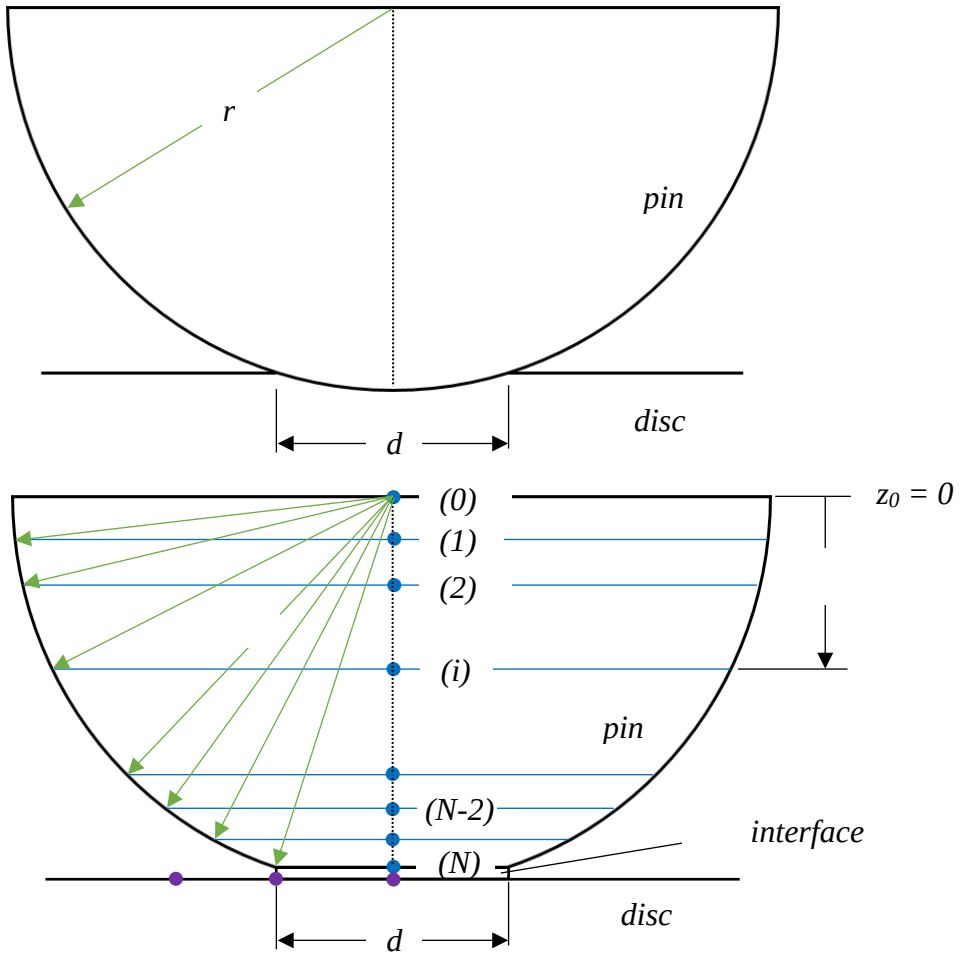

Figure 55: (Top) simplified schematic of the actual pin-disc interface. (Bottom) approximate representation of the pin-disc interface used in the thermal model

6.2.2 Formulating a Two-Dimensional Thermal Model of the Disc including Convective Heat Transfer at the Top and Sides but Neglecting Internal Heat Generation

The disc was assumed to be cylindrical and was modeled as array of $\boldsymbol{M}$ x $\boldsymbol{J}$ nodes and associated control volumes, as shown in **Figure 56**. For nodes laying on the axis of the disc, the associated control volume was cylindrical. For all other nodes, the associated control volume was annular. Contact with the pin was assumed to be centred on the axis of the disc.

For simplicity, **Figure 56** depicts the nodes as being equally spaced in both radial and vertical directions. In this case, the nodes would be centered within their associated control volumes. In practical implementation, however, nodes were spaced more closely together in the vicinity of the pin contact (i.e., nodes of smaller $\boldsymbol{m}$ and $\boldsymbol{j}$ values) and, conversely, spaced further apart in regions more removed from the pin contact (i.e., nodes of higher $\boldsymbol{m}$ and $\boldsymbol{j}$ values). Insomuch as the boundary of the control volume was set to pass through the midpoint between adjacent nodes, it follows that nodes were not centered within their associated control volumes in instances where adjacent nodes in the radial directions or in the vertical directions were not equally spaced (see **Figure 57** for example).

Nodes laying at the bottom of the disc, that is nodes $\boldsymbol{(1, J)}$ through $\boldsymbol{(M, J)}$, were assumed to be at a fixed temperature of $\boldsymbol{T_{bot}}$. All other nodes $\boldsymbol{(m, j)}$ would then possess a temperature $\boldsymbol{T_{m,j}}$ that must be solved for based on the set of linear equations derived from the principle of energy conservation applied to each node.

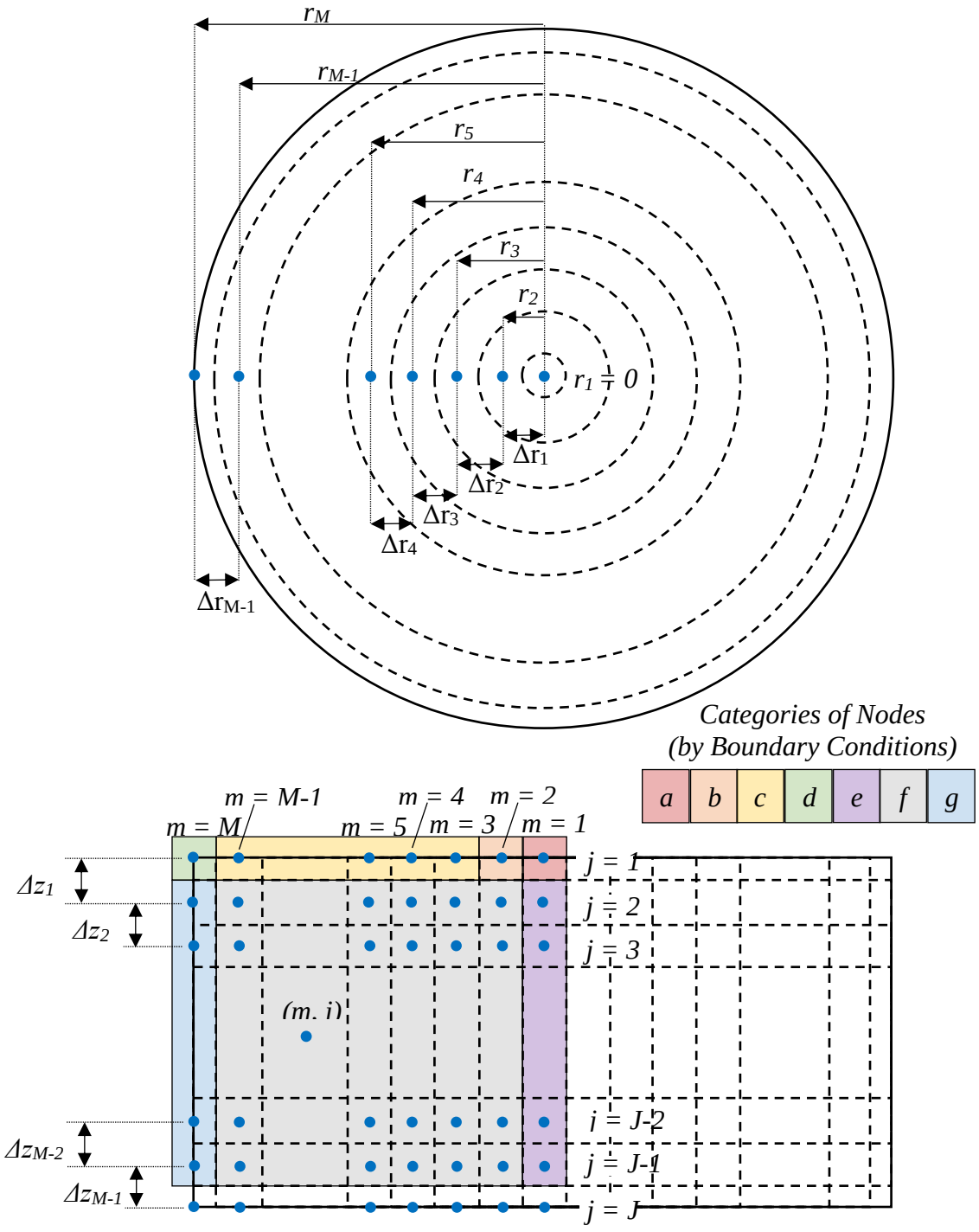

Figure 56: Overview of nodes and control volumes used to model heat transfer in the disc

There are seven different categories or types of nodes identified in **Figure 56**, each with slightly different boundary conditions. The formulation of the linear equation governing heat flow into a node of type ***f*** is presented below with reference to **Figure 57**. For this particular node type, heat transfer through all four sides of the control volume is by conduction only.

Under steady-state conditions, the conservation of energy dictates that the net flow of heat into a control volume plus any heat generated within that same control volume must be equal to zero, as expressed in **Eq. 6.2.2.1**.

$$\boldsymbol{q_1 + q_2 + q_3 + q_4 + q_{gen} = 0} \qquad \textbf{Eq. 6.2.2.1}$$

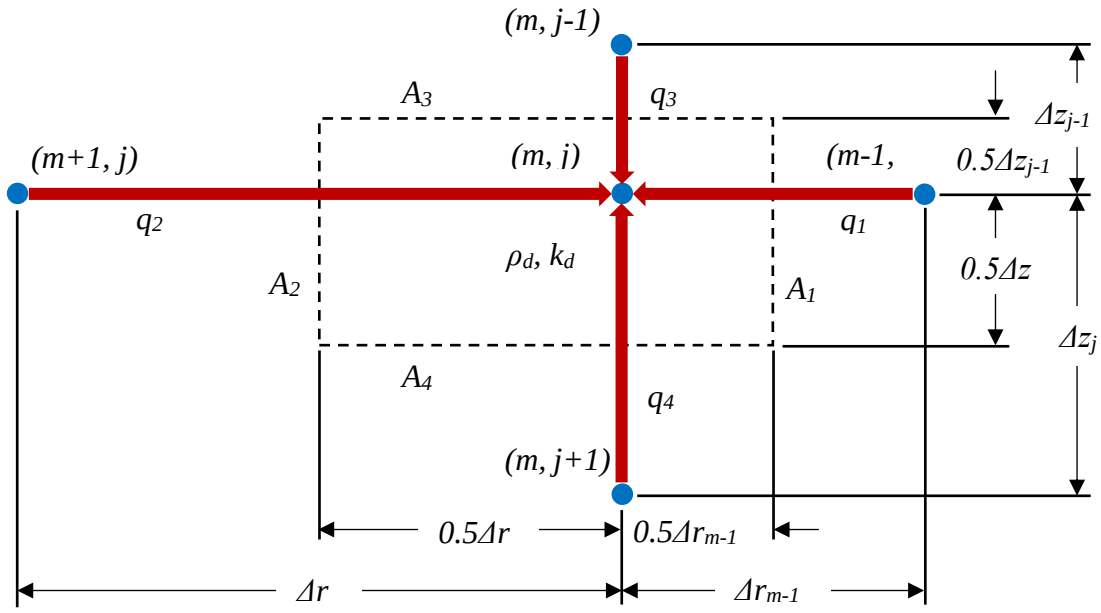

Figure 57: General depiction of a Category f Node in the disc

Except where noted, internal heat generation due to electric current flow within the disc was neglected ($\boldsymbol{q_{gen}} = 0$) in part due to the relatively lower value of electrical resistivity for typical disc materials as compared with coating materials, but more significantly due to the overall larger cross-sectional area of the disc resulting in a comparably small amount of electric current flowing through each individual control volume within a given vertical slice of the disc.

With reference to **Figure 57**, the heat flowing into node ***(m, j)*** from node ***(m-1, j)***, or $\boldsymbol{q_1}$, is given as per **Eq. 6.2.2.2** through **Eq. 6.2.2.4**.

$$\boldsymbol{q_1 = kA_1 \frac{\left(T_{m-1,j} - T_{m,j}\right)}{\Delta r_{m-1}} = C_1\left(T_{m-1,j} - T_{m,j}\right)} \qquad \textbf{Eq. 6.2.2.2}$$

$$\boldsymbol{C_1 = \frac{kA_1}{\Delta r_{m-1}}} \qquad \textbf{Eq. 6.2.2.3}$$

$$\begin{aligned} \boldsymbol{A_1} &= \boldsymbol{2\pi(r_m - \Delta r_{m-1}) \cdot 0.5\left(\Delta z_{j-1} + \Delta z_j\right)} \\ &= \boldsymbol{\pi(r_m - \Delta r_{m-1})\left(\Delta z_{j-1} + \Delta z_j\right)} \end{aligned} \qquad \textbf{Eq. 6.2.2.4}$$

The heat flowing into node ***(m, j)*** from node ***(m+1, j)***, or $\boldsymbol{q_2}$, is given as per **Eq. 6.2.2.5** through **Eq. 6.2.2.7**.

$$\boldsymbol{q_2 = kA_2 \frac{\left(T_{m+1,j} - T_{m,j}\right)}{\Delta r_m} = C_2\left(T_{m+1,j} - T_{m,j}\right)} \qquad \textbf{Eq. 6.2.2.5}$$

$$\boldsymbol{C_2 = \frac{kA_2}{\Delta r_m}} \qquad \textbf{Eq. 6.2.2.6}$$

$$\begin{aligned} \boldsymbol{A_2} &= \boldsymbol{2\pi(r_m + \Delta r_m) \cdot 0.5\left(\Delta z_{j-1} + \Delta z_j\right)} \\ &= \boldsymbol{\pi(r_m + \Delta r_m)\left(\Delta z_{j-1} + \Delta z_j\right)} \end{aligned} \qquad \textbf{Eq. 6.2.2.7}$$

The heat flowing into node ***(m, j)*** from node ***(m, j-1)***, or $\boldsymbol{q_3}$, is given as per **Eq. 6.2.2.8** through **Eq. 6.2.2.10**.

$$q_3 = kA_3 \frac{\left(T_{m,j-1} - T_{m,j}\right)}{\Delta z_{j-1}} = C_3\left(T_{m,j-1} - T_{m,j}\right) \qquad \textbf{Eq. 6.2.2.8}$$

$$C_3 = \frac{kA_3}{\Delta z_{j-1}} \qquad \textbf{Eq. 6.2.2.9}$$

$$\begin{aligned} A_3 = \pi\left(r_m + \frac{\Delta r_m}{2}\right)^2 + \pi\left(r_m - \frac{\Delta r_{m-1}}{2}\right)^2 \\ = \pi\Big(r_m(\Delta r_m + \Delta r_{m-1}) \\ + 0.25\left(\Delta {r_m}^2 - \Delta {r_{m-1}}^2\right)\Big) \end{aligned} \qquad \textbf{Eq. 6.2.2.10}$$

The heat flowing into node ***(m, j)*** from node ***(m, j+1)***, or q_4, is given as per **Eq. 6.2.2.11** through **Eq. 6.2.2.13**.

$$q_4 = kA_4 \frac{\left(T_{m,j+1} - T_{m,j}\right)}{\Delta z_j} = C_4\left(T_{m,j+1} - T_{m,j}\right) \qquad \textbf{Eq. 6.2.2.11}$$

$$C_4 = \frac{kA_4}{\Delta z_j} \qquad \textbf{Eq. 6.2.2.12}$$

$$\begin{aligned} A_4 = A_3 = \pi\Big(r_m(\Delta r_m + \Delta r_{m-1}) \\ + 0.25\left(\Delta {r_m}^2 - \Delta {r_{m-1}}^2\right)\Big) \end{aligned} \qquad \textbf{Eq. 6.2.2.13}$$

Introducing an additional coefficient, C_5, then Eq. (6.2.2.1) can be re-written as follows:

$$\begin{aligned} C_1 T_{m-1,j} + C_2 T_{m+1,j} + C_3 T_{m,j-1} + C_4 T_{m,j+1} + C_5 T_{m,j} \\ + q_{gen} = 0 \end{aligned} \qquad \textbf{Eq. 6.2.2.14}$$

$$C_5 = -(C_1 + C_2 + C_3 + C_4) \qquad \textbf{Eq. 6.2.2.15}$$

Strictly speaking, the above equations for coefficients C_1 through C_4 apply only for type ***f*** nodes, as depicted in **Figure 56** and **Figure 57**. Differences in boundary conditions for other node types introduce slight changes to the equations defining these coefficients.

Node ***(1, 1)***, which is of type ***a***, lays directly beneath the pin along the centerline of the radially symmetric disc. Node ***(2, 1)***, which is of type ***b***, lays at the very edge of the imprint made by the disc. Part of the control volumes surrounding these two nodes comprises a

portion of the coating layer on the pin, which features a different thermal conductivity as compared with the disc material. The thermal conductivity of the coating layer is denoted k_{coat} while the thermal conductivity of the disc material is denoted k_{disc}. In the case of these two nodes, the term q_{gen} in **Eq. 6.2.2.14**, or equivalently **Eq. 6.2.2.1**, should not be considered as negligible but rather evaluated as

$$q_{gen} = (I")^2 \frac{\rho l}{A"} \qquad \textbf{Eq. 6.2.2.16}$$

where ***I"*** denotes the portion of total electric current, ***I***, flowing through the control volume surrounding node ***(m, j)*** and ***A"*** denotes the cross-sectional area of the control volume that is normal to the current flow. For simplicity, heat generation in the disc material portion of the control volumes is neglected. As such, ***l*** is taken as the vertical length of the control volume extending into the coating layer.

On a related note, since both node ***(1, 1)*** and node ***(2, 1)*** see conductive heat transfer from the bottommost node of the one-dimensional pin, it is only appropriate that the bottommost node of the pin sees conductive heat transfer from both of these nodes. For simplicity, the term T_{i+1} in **Eq. 6.2.1.7** was taken as a weighted average of the temperature at the two nodes in the disc. The author assigned a weight of 0.7 to node ***(1, 1)*** and 0.3 to node ***(2, 1)***.

Given their location on the centerline of the disc, nodes of category ***a*** and ***e***, that is node ***(1, 1)*** and nodes ***(1, 2)*** through ***(1, M-1)***, respectively, do not feature an adjacent node radially inward, so C_1 and/or $T_{m-1,j}$ were neglected.

Nodes of category ***b***, ***c***, ***d*** and ***g***, that is node ***(2, 1)***, nodes ***(3, 1)*** through ***(M-1, 1)***, node ***(M, 1)*** and nodes ***(M, 2)*** through ***(M, J-1)***, respectively, feature some measure of convective

heat transfer through the top and/or radially outward portions of their surrounding control volumes. Convective heat transfer to these nodes is driven by convective heat transfer coefficients $\boldsymbol{h_{top}}$ and $\boldsymbol{h_{side}}$ assuming an ambient temperature of $\boldsymbol{T_\infty}$ = 25°C.

The specific expressions for coefficients $\boldsymbol{C_1}$ through $\boldsymbol{C_4}$ as well as $\boldsymbol{q_{gen}}$ for all node types are summarized in **Appendix A**.

6.2.3 Modeling Contact Resistance at the Pin-Disc Interface

It is widely recognized in literature and industry that electrical contact between two surfaces is not ideal, but rather the contact zone between two conductors exhibits its own resistance. This resistance is thought to be comprised of two components: a *constrictive* component, reflecting the reality that contact occurs between local asperities and not the entirety of the apparent area of contact; and a *contaminant* or *film* component, related to oxides and absorbed films on the contacting surfaces of either conductor (Song, Zhang, & Bay, 2005), (Volger & Sheppard, 1993).

In reality, the contact between the pin (or coating) and disc is not perfectly intimate, meaning that the real area of contact (i.e., the sum of all areas of contact between asperities of both materials) is somewhat smaller than the apparent area of contact (i.e., the area of the circular imprint measured after the pin is retracted from the disc). The ratio of the real area of contact to the apparent area of contact is herein referred to as the Contact Ratio, or $\boldsymbol{CR}$. Accordingly, $\boldsymbol{CR}$ = 1 denotes perfect contact whereas $\boldsymbol{CR}$ = 0.1 implies that the real area of contact is only 10% of the apparent area of contact. Fundamentally, the real area of contact between asperities of the pin and disc restricts both electrical current (thereby

increasing heat generation at the interface) as well as heat conduction between the pin and disc, albeit over a very limited distance. Accordingly, the relevant expressions for coefficient C_3 and q_{gen} used in **Eq. 6.2.2.14** need to be modified for nodes of category ***a*** and ***b*** located at the pin-disc interface. These modified expressions are included in **Appendix A** and denoted by the symbol '!' (i.e., $C!_3$, $q!_{gen}$).

The properties of a surface are not necessarily equal to those of the bulk material. In reality, the surface of most materials exhibits a layer of oxides and adsorbed gases, not all of which can be removed by cleaning. Generally speaking, surface oxides exhibit an electrical resistivity several orders of magnitude higher than the base material, be it a metal, metal carbide or metal nitride. Although simplistic, the effects of an oxide/contaminant layer on the tip of the pin in the contact region were modeled assuming a thickness of 0.1 μm (30x less than the assumed thickness of the coating itself) and a resistivity, ρ_{contam}, which was treated as a scalar multiple of the pin resistivity, ρ_{pin}. The thermal conductivity of the contaminant layer k_{contam} was assumed to be equal to that of the pin k_{pin}.

6.3 Initial Model Implementation

6.3.1 Solution Technique

Rearranging **Eq. 6.1.7** and **Eq. 6.2.14** to solve for T_i and $T_{j,m}$, respectively, the steady-state temperature distribution in the pin and disc was evaluated by means of Gauss-Seidel iteration, for assumed initial and boundary conditions. The model was implemented in Microsoft Excel, with subsequent columns calculating the next iteration of the solution until changes in nodal temperatures between successive iterations were less than 10^{-5} °C.

6.3.2 Assumptions regarding Model Parameters and Conditions

Prior to solving, several material parameters, operating conditions and boundary conditions needed to be defined. These are summarized in **Table 4**.

In reality, the contact ratio and imprint diameter are a result of the material properties of the pin and disc materials as well as the load and electrical current applied. The same can be said for the boundary conditions. In the model, however, an imprint diameter must be defined a priori, along with values for the contact ratio and the temperature boundary conditions.

The imprint diameter ***d*** was selected based on observed results from various tests with coated and uncoated WC-Co pins (3 mm in diameter with a 1.5 mm radius tip) in contact with AISI 1045 steel discs subject to 200 N of load and a range of electric current. Given that the nodes in the disc in the immediate vicinity of the imprint diameter must be suitably spaced, five separate model variants were generated to simulate imprint diameters ranging from 0.40 to 0.60 mm, in 0.05 mm increments. The corresponding radial position of nodes in the disc for each model are summarized in **Table 5**.

The vertical position of nodes in the disc were invariant relative to the topmost layer of nodes, as is summarized in **Table 6**. In all five variants, the disc was assumed to be cylindrical with a diameter of 15 mm and a height of 8.5 mm.

The contact ratio ***CR*** is not readily discernable from tribometer tests. For simplicity, two assumed values were selected, 0.1 and 0.5, for the purposes of studying the effect of contact ratio on the model results.

Table 4: Description of Model Parameters and Notation as well as Values Used in the Initial Model Implementation

Model Parameter Description and Notation	Value
Electrical Resistivity of the Pin Substrate, $\boldsymbol{\rho_{pin}}$ (Ωm)	= 1.90×10^{-7} (3.80×10^{-7})
Thermal Conductivity of the Pin Substrate, $\boldsymbol{k_{pin}}$ (W/m°C)	= 8.5×10^{1}
Electrical Resistivity of the Disc, $\boldsymbol{\rho_{disc}}$ (Ωm)	= 1.62×10^{-7}
Thermal Conductivity of the Disc, $\boldsymbol{k_{disc}}$ (W/m°C)	= 5.2×10^{1}
Electrical Resistivity of the Coating, $\boldsymbol{\rho_{coat}}$ (Ωm)	= $\boldsymbol{N_1} * \boldsymbol{\rho_{pin}}$
Multiplier for Coating Electrical Resistivity, $\boldsymbol{N_1}$	Selected based on tuning, for an assumed value of ***CR*** and $\boldsymbol{N_3}$
Thermal Conductivity of the Coating, $\boldsymbol{k_{coat}}$ (W/m°C)	= $\boldsymbol{N_2} * \boldsymbol{k_{pin}}$
Multiplier for Coating Thermal Conductivity, $\boldsymbol{N_2}$	= 1
Electrical Resistivity of the Contaminant Layer, $\boldsymbol{\rho_{contam}}$ (Ωm)	= $\boldsymbol{N_3} * \boldsymbol{\rho_{pin}}$
Multiplier for Contaminant Layer Electrical Resistivity, $\boldsymbol{N_3}$	Selected based on tuning, for an assumed value of ***CR***
Thermal Conductivity of the Contaminant Layer, $\boldsymbol{k_{contam}}$ (W/m°C)	= $\boldsymbol{N_4} * \boldsymbol{k_{pin}}$
Multiplier for Contaminant Layer Thermal Conductivity, $\boldsymbol{N_4}$	= 1
Imprint Diameter, ***d*** (mm)	Selected based on empirical measurements
Contact Ratio, ***CR***	Assumed (0.1, 0.5)
Electrical Current, ***I*** (A)	User defined
Temperature at Top Node of Pin, $\boldsymbol{T_{top}}$ (°C)	Selected based on empirical measurements
Temperature at Bottom Nodes of Disc, $\boldsymbol{T_{bot}}$ (°C)	Selected based on empirical measurements
Ambient Temperature, $\boldsymbol{T_\infty}$ (°C)	25
Convective Heat Transfer Coefficient, ***h*** ($W/M^2°C$)	20

The boundary conditions were selected based on actual measurements during stationary specimen tests between a WC-Co pin and AISI 1045 steel disc under 200 N load and different levels of electrical current. During each test, the infrared pyrometer was aimed either 2 mm above the interface, at the mid-section or at the top-most region of the pin. The duration of the test was sufficient to allow near steady-state temperatures to be reached.

Table 5: Radial position of disc nodes with subscript m, as a function of modeled imprint diameter

Radial Subscript of Node, m	***Imprint Diameter, d (mm)***				
	0.4	0.45	0.5	0.55	0.6
	Radial Position of Node, r_m (mm)				
1	0	0	0	0	0
2	0.2	0.225	0.25	0.275	0.3
3	0.5	0.5	0.55	0.625	0.650
4	1	1	1	1	1
5	1.5	1.5	1.5	1.5	1.5
6	2.5	2.5	2.5	2.5	2.5
7	3.5	3.5	3.5	3.5	3.5
8	5.5	5.5	5.5	5.5	5.5
9	7.5	7.5	7.5	7.5	7.5

Table 6: Vertical position of disc nodes with subscript j

Vertical Subscript of Node, m	***Vertical Position of Node Relative to Top of Disc, z(n)***
1	0
2	0.005
3	0.01
4	0.02
5	0.03
6	0.05
7	0.09
8	0.15
9	0.25
10	0.5
11	1
12	2
13	3.5
14	5.5
15	8.5

At the end of each test, the temperature of the copper plate adjacent to the disc was also measured by means of a thermocouple probe. In this way, reasonable values for $\boldsymbol{T_{top}}$ and $\boldsymbol{T_{bot}}$ were established for different levels of electric current. The resulting imprint diameters were also noted. The average temperature and imprint diameter from these tests are listed in **Table 7**.

Table 7: Temperature measurements at different positions along the length of the pin

Command Signal (V)	*3.0*	*4.5*	*6.0*
Current, I (A)	*61*	*91*	*121*
$T_{pin,top}$ ***(°C)***	*60*	*132*	*305*
$T_{pin,mid}$ ***(°C)***	*90*	*212*	*535*
$T_{pin,test}$ ***(°C)***	*125*	*280*	*715*
T_{bot} ***(°C)***	*36*	*43*	*55*
d (mm)	*0.403 ± 0.005*	*0.566 ± 0.025*	*0.976 ± 0.120*

During these particular tests, the electrical current was applied at the same time as the initial application of the load, instead of the standard 30 s after the load had stabilized. In effect, the contact area between pin and disc would have been extremely small at the onset of electrical current, likely causing extremely high temperatures and thermal softening in the underlying disc, which likely explains why the measured imprint diameters for tests subject to 91 A and 121 A (4.5 V and 6.0 V command signal) were much larger than those reported previously in **Figure 49 (b)**.

For simplicity, the ambient temperature was assumed to be 25 °C and a convective heat transfer coefficient of 20 W/m°C was held constant across all simulations. However, over a wide range of values tested, the convective heat transfer coefficient was seen to have very little influence on results.

As per the electrical resistivity and thermal conductivity of the pin, disc, coating and contaminant layer listed in **Table 4**, these were specified in part based on reported values available through web-based material databases as well as tuning efforts to achieve reasonable agreement with some empirical tests.

The values of thermal conductivity for the pin substrate (WC-Co) and the disc (AISI 1045) were taken from online sources. For simplicity, the values of thermal conductivity for the coating and the contaminant layer were set equal to that of the pin substrate. From

the author's investigations, the selection of thermal conductivity primarily influenced the partition of heat between the pin tip and the disc at the pin-disc interface, with lower values of thermal conductivity giving rise to significant gradients across the coating/contaminant layer.

The electrical resistivity values for cemented tungsten carbide and AISI 1045 steel were reportedly valid at 25°C and were assumed not to vary significantly with temperature.

6.3.3 Empirical Measurements of Electrical Potential Drop along Pin and Disc

In order to validate the choice of electrical resistivity for the pin substrate; and in order to guide the selection of scalar multiples governing the electrical resistivity values for a TiAlCrSiYN/TiAlCrN coating and a layer of surface contaminants present on either coated or uncoated pin; measurements of electrical potential drop across various elements in the tribometer setup were performed under different levels of electrical current flowing through the specimens, for both uncoated and TiAlCrSiYN/TiAlCrN-coated pins loaded against a disc of AISI 1045 steel under 200 N. The relative positions of the multimeter probes across the test setup are depicted in **Figure 58**. From these measurements, the corresponding electrical resistance values were calculated based on Ohm's law. Measurements of imprint diameter after each test were also obtained.

Table 8 summarizes the measurements of potential drop and imprint diameter as well as the corresponding value of electrical resistance calculated for each test condition. There was some scatter in the calculated values of electrical resistance, which may reflect limitations in the repeatability of positioning the probes of the multimeter at precise

locations in the test setup. Alternatively, it may also reflect the temperature sensitivity of the electrical resistivity of the pin substrate (WC-Co) and the coating (TiAlCrSiYN/TiAlCrN). For simplicity, the average value of resistance across the three tests for a given pin surface treatment was taken.

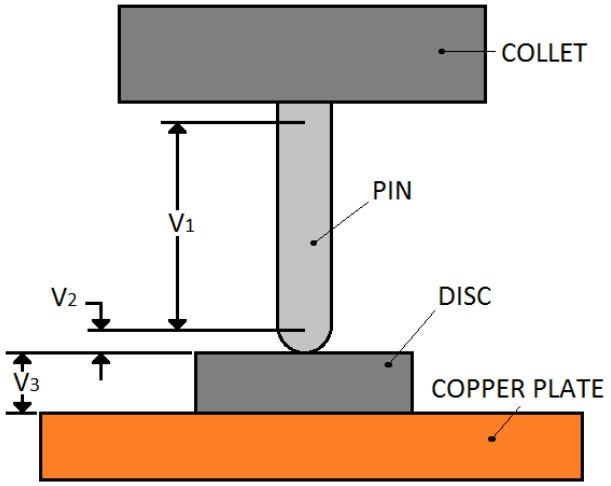

Figure 58: Location of Voltage Measurements Obtained during Stationary Disc Tests for Initial Model Calibration

Table 8: Summary of Voltage and Imprint Diameter Measurements from select Stationary Disc Tests, as well as Corresponding Resistance Calculations

Coating	Current, I (A)	V_1 (V)	V_2 (V)	V_3 (V)	d (mm)	R_1 (mΩ)	R_2 (mΩ)	R_3 (mΩ)
Uncoated	*61*	*0.045*	*0.126*	*0.209*	*0.44*	*0.737*	*2.07*	*3.43*
	81	*0.078*	*0.147*	*0.208*	*0.43*	*0.963*	*1.81*	*2.57*
	101	*0.113*	*0.174*	*0.377*	*0.45*	*1.12*	*1.72*	*3.73*
					Average	*0.94*	*1.9*	*3.2*
TiAlCrSiYN/ TiAlCrN	*61*	*0.067*	*0.292*	*0.206*	*0.45*	*1.10*	*4.79*	*3.38*
	81	*0.109*	*0.292*	*0.159*	*0.47*	*1.34*	*3.60*	*1.96*
	101	*0.170*	*0.345*	*0.166*	*0.56*	*1.68*	*3.42*	*1.64*
					Average	*1.4*	*3.9*	*2.33*

Interestingly, the value of $\boldsymbol{R_3}$ (or rather $\boldsymbol{V_3}$) was larger than anticipated, reflecting considerable contact resistance between the disc and the copper plate (which was previously thought to be negligible). With an assumed electrical resistivity of 1.62×10^{-7} Ωm, a thickness of 8.5 mm and a cross sectional area of 100 mm^2, the electrical resistance of the disc would be on the order of only 0.014 mΩ, roughly two orders of magnitude smaller than $\boldsymbol{R_3}$.

6.3.4 Tuning Model Parameters to Achieve Agreement with Empirical Values of R_1 and R_2

The measured values of $\boldsymbol{V_1}$ and $\boldsymbol{V_2}$, and the associated values of $\boldsymbol{R_1}$ and $\boldsymbol{R_2}$, served as a reality check and a means of tuning model parameters to achieve alignment between the model and empirical results. Equivalent values of $\boldsymbol{R_1}$ and $\boldsymbol{R_2}$ were calculated in the model by summing up the electrical resistance between nodes along the length of the pin. $\boldsymbol{R_1}$ was taken as the electrical resistance between nodes at $\boldsymbol{z}$ = -1.5 mm and $\boldsymbol{z}$ = -18 mm (recall that the exposed portion of the cylindrical body of the pin extends from $\boldsymbol{z}$ = 0 mm to $\boldsymbol{z}$ = -21 mm), whereas $\boldsymbol{R_2}$ was taken as the electrical resistance between the node at z = -1.5 mm and the node at the very tip of the pin, in contact with the disc.

Interestingly, for a given value of electrical current $\boldsymbol{I}$, the measured $\boldsymbol{R_1}$ could not be reproduced apart from increasing the electrical resistivity of the pin substrate, $\boldsymbol{\rho_{pin}}$, to a value approximately double that reported online. This likely reflects a change in electrical resistivity in the pin substrate at elevated temperatures relative to the room temperature value reported. For simplicity, the electrical resistivity of the pin substrate, $\boldsymbol{\rho_{pin}}$, was assumed to be 3.80×10^{-7} Ωm (shown in parentheses in **Table 4**).

For an assumed value of contact ratio ***CR*** (0.1 or 0.5), the electrical resistivity of the contaminant layer was then be tuned such that the resulting electrical resistance $\boldsymbol{R_2}$ in the model matched those values based on empirical measurements, reported in **Table 8**.

6.3.5 Simulation Results: Coated and Uncoated Pins, Low Electric Current

Table 9 details the model parameters and results from a few simulation scenarios with the uncoated pin (**Scenarios 1 – 4**) and coated pin (**Scenarios 5 – 8**), subject to low levels of electrical current (50 A and 61A). The temperature at the top node of the pin, $\boldsymbol{T_{top}}$, was fixed at 60 °C. The temperature at the bottom of the disc, $\boldsymbol{T_{bot}}$, was set to 35 °C.

Scenario 1 was the result of an initial guess of $\boldsymbol{N_3}$ = 500 for the contaminant electrical resistivity multiplier when the electrical current is set to ***I*** = 61 A, the imprint diameter is ***d*** = 0.40 mm, the contact ratio is ***CR*** = 0.5 and the coating electrical resistivity multiplier is $\boldsymbol{N_1}$ = 1 (i.e., uncoated pin). The predicted value of $\boldsymbol{R_2}$ was only 0.43 mΩ, which is roughly five times lower than that which was calculated based on the measurements of $\boldsymbol{V_2}$ reported in **Table 8**. As well, the temperature at the pin-disc interface was predicted to be lower than the test temperature by 7 °C. Due to the poor agreement between the model and the empirical results for $\boldsymbol{R_2}$, the reported test temperature and pin-disc interface temperature were not believed to be reliable.

Scenario 2 was the result of a few rounds of tuning the value $\boldsymbol{N_3}$ to achieve better agreement between empirical and model values of $\boldsymbol{R_2}$, all other model parameters kept the same. The predicted test temperature and pin-disc interface temperature more than doubled compared with **Scenario** 1. Moreover, the predicted interface temperature was about 30

°C higher than the test temperature. Similar temperatures were predicted in **Scenarios 3** and **4**, which featured a contact ratio of $\boldsymbol{CR} = 0.1$ and suitably tuned values of $\boldsymbol{N_3}$. **Scenario 3** featured the same imprint diameter of $\boldsymbol{d} = 0.4$ mm, while ***Scenario 4*** assumed a slightly larger imprint diameter of $\boldsymbol{d} = 0.45$ mm. Not surprisingly, a higher value of $\boldsymbol{N_3}$ was required in **Scenario 4** to achieve similar $\boldsymbol{R_2}$ values as in **Scenario 3** due to the increase in $\boldsymbol{d}$.

For **Scenarios 5- 8**, involving the coated pin, only the $\boldsymbol{CR} = 0.1$ condition was explored, for simplicity, and the contaminant layer electrical resistivity multiplier was assumed to be the same as that used during the equivalent simulations with the uncoated pin ($\boldsymbol{N_3} = 1000$ for $\boldsymbol{d} = 0.40$ mm in **Scenarios 5** and **6**, similar to **Scenario 3**; $\boldsymbol{N_3} = 1300$ for $\boldsymbol{d} = 0.45$ mm in **Scenarios 7** and **8**, similar to **Scenario 4**). For a given imprint diameter $\boldsymbol{d}$, the coating electrical resistivity multiplier $\boldsymbol{N_1}$ was tuned so as to achieve good agreement between $\boldsymbol{R_2}$ in the model and empirical results.

Table 9: Model Parameters and Simulation Results for Low Current Simulations

Parameter		***Scenario***							
Description	*Notation*	*1*	*2*	*3*	*4*	*5*	*6*	*7*	*8*
Electrical Current	*I (A)*	61	61	61	61	61	50	61	50
Imprint Diameter	*d (mm)*	0.40	0.40	0.40	0.45	0.40	0.40	0.45	0.45
Contact Ratio	*CR*	0.5	0.5	0.1	0.1	0.1	0.1	0.1	0.1
Multiplier for Coating Electrical Resistivity	N_1	1	1	1	1	28	28	34	34
Multiplier for Contaminant Layer Electrical Resistivity	N_3	500	5300	1000	1300	1000	1000	1300	1300
Electrical Resistance between Point of Test Temperature and Disc Top	R_2 *(x* 10^{-3} *Ω)*	0.43	1.87	1.88	1.91	3.87	3.87	3.92	3.92
Test Temperature	$T_{z=-1}$ *(°C)*	116	266	261	254	365	261	353	253
Pin-Disc Interface Temperature	T_{int} *(°C)*	109	297	291	281	420	297	403	286
Difference between Pin-Disc Interface Temperature and Test Temperature	ΔT *(°C)*	-7	31	30	27	55	36	50	33

For the same level of electrical current and the same assumed diameter, the model predicted higher test and pin-disc interface temperatures with the introduction of the coating (e.g., compare **Scenario 5** with **Scenario 3**, or **Scenario 7** with **Scenario 4**). However, when the electrical current was reduced such that the predicted test temperature matched that of the uncoated pin, then for both imprint diameters explored (***d*** = 0.40 mm and ***d*** = 0.45 mm), the predicted interface temperature was approximately 6 °C higher than in the simulations with the uncoated pin (e.g., compare **Scenario 6** with **Scenario 3**, or **Scenario 8** with **Scenario 4**). While this difference is arguably small, it is in qualitative agreement with the hypothesis that a coating with increased electrical resistivity results in a higher interface temperature despite exhibiting an equivalent test temperature.

6.3.6 Simulation Results: Coated and Uncoated Pins, Moderate Electric Current

Table 10 presents the parameters and results from scenarios with both uncoated and coated pins subjected to an increased level of electrical current ***I*** (101 A vs. the former 61 A). The temperature at the top node of the pin, T_{top}, was increased to 200 °C, based on empirical observations from the aforementioned stationary specimen tests (interpolating values listed in **Table 7**), while the temperature at the bottom of the disc, T_{bot}, was assumed to remain at 35 °C. The electrical resistivity of the contaminant layer was tuned for each simulation involving the uncoated pin to achieve agreement between the model and empirical results for R_2. For the simulations with the coated pin, the same value of contaminant layer electrical resistivity was used and the coating electrical resistivity was tuned to achieve agreement in R_2 between the model and empirical results.

Table 10: Model Parameters and Simulation Results for High Current Scenarios

Model Parameter	***Scenario***					
	10	*11*	*12*	*13*	*14*	*15*
I (A)	101	83	101	83	101	83
d (mm)	0.45	0.45	0.50	0.50	0.55	0.55
CR	0.1	0.1	0.1	0.1	0.1	0.1
N_1	1	34	1	41	1	47
N_3	1300	1300	1600	1600	2000	2000
R_2 (x 10^{-3} Ω)	1.91	3.92	1.88	3.91	1.91	3.88
$T_{z=-1}$ (°C)	684	685	648	650	625	626
T_{int} (°C)	748	764	700	720	672	687
ΔT (°C)	64	79	52	70	47	61

Scenarios 10 and **11** compared an uncoated pin subjected to 101 A of current and a coated pin subjected to 83 A of current with an imprint diameter of $\boldsymbol{d}$ = 0.45 mm. **Scenarios 12** and **13**, and likewise **Scenarios 14** and **15**, compared uncoated and coated pins for imprint diameters of $\boldsymbol{d}$ = 0.50 mm and $\boldsymbol{d}$ = 0.55 mm, respectively.

The results of scenarios summarized in **Table 10** demonstrated that the coated pin resulted in a higher pin-disc interface temperature and an equivalent test temperature at a lesser value of electrical current flowing through the specimens, consistent with empirical observations. However, the change in $\boldsymbol{\Delta T}$ between scenarios with uncoated and coated pins was still not very high, increasing to only 14-18 °C at this higher level of current.

Figure 59(a) presents the thermal profile along the length of the pin for **Scenarios 4** and **10**, while **Figure 59(b)** and **(c)** depicts the vertical distribution along the centermost nodes and the radial distribution of temperature along the topmost nodes in the disc. The temperature along the pin varied in a nearly linear fashion for the majority of its length, both for the cylindrical portion (-21 to 0 mm) as well as for much of the pin tip ($\boldsymbol{z}$ > 0 mm).

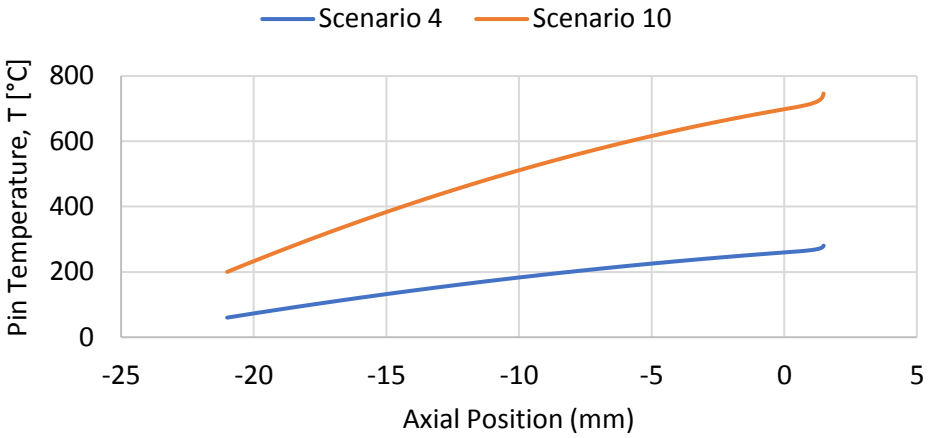

(a)

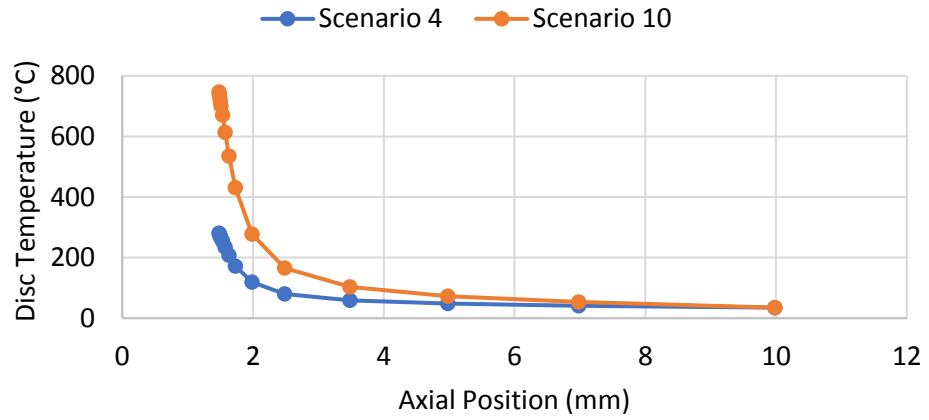

(b)

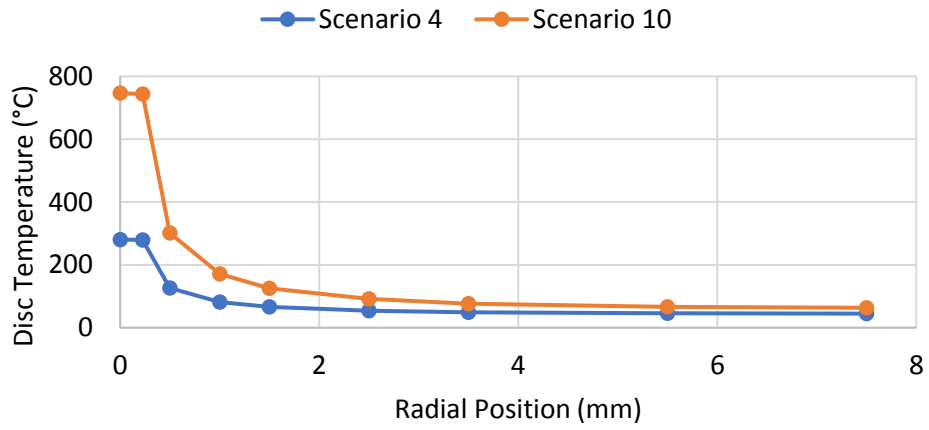

(c)

Figure 59: Predicted distribution of temperature in the pin and disc for Scenarios 4 and 10: (a) the pin; (b) the centermost nodes of the disc; (c) the topmost nodes of the disc

However, there was a sudden increase in temperature close to the interface due to the low contact ratio (***CR*** = 0.1) and the high electrical resistivity of the contaminant layer relative to that of the pin (N_3 = 1300). This was more prominent in **Scenario 10** (uncoated pin, 101 A of current), such that the interface temperature was 64°C higher than the test temperature.

6.3.7 Discussion of Results from the Initial Model Implementation

Given the uncertainties and limitations of the model, the results obtained and presented do qualitatively agree with the underlying hypothesis that the electrical resistivity influences the thermal gradient in the pin tip, such that a coating with a higher electrical resistivity will result in a higher temperature at the pin-disc interface despite otherwise equivalent test temperature 2 mm above the interface. At the same time, the predicted increase in temperature at the pin-disc interface was not as high as anticipated, being only about 6 °C higher at 50 – 61 A of current (and a simulated test temperature of 261 °C) and 14-18 °C higher at 83 – 101 A of current (and a simulated test temperature of 650 °C). One could argue that such differences in temperature are unlikely to cause an appreciable difference in imprint diameter.

Interestingly, the model suggests that linear extrapolation of temperature measurements along the length of the cylindrical portion of the pin tip is not an accurate approach to estimating the temperature at the pin-disc interface, as evidenced by the steep increase in temperature at the extremity of the pin tip (**Figure 59(a)**).

The predicted test temperatures for the assumed values of electrical resistivity for the pin, contaminant and coating did not correspond well to data for stationary specimen tests. **Figure 60** shows the resulting test temperature vs. command signal for the same set of stationary specimen tests presented in **Chapter 5**. **Scenarios 3** and **5** predicted a test temperature of 261 °C and 365 °C for uncoated and coated pins subjected to 61 A of current (3V) and for an imprint diameter of 0.40 mm. By extrapolation of data points in **Figure 60**, one would expect a test temperature of approximately 150 °C and 300 °C, respectively.

At higher levels of electrical current, the model results were even more divergent. **Scenarios 10**, **12** and **14** (101 A or 5 V) predicted a test temperature in the range of 626 – 684 °C for the uncoated pin and imprint diameters ranging from 0.45 – 0.55 mm, whereas actual stationary specimen tests resulted in a test temperature of about 375 °C. For the coated pin subjected to 83 A (4.1 V command signal), the test temperature was observed to be about 400 °C, which was again much lower than the simulation results (**Scenarios 11**, **13** and **15**).

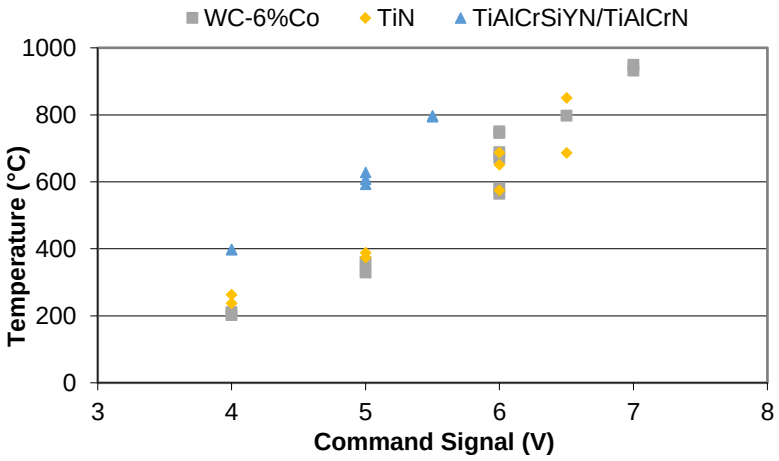

Figure 60: Test Temperature vs. Command Signal corresponding to the Stationary Specimen Tests presented in Figure 49(d)

6.4 Revised Model Implementation

6.4.1 Motivation for a Revised Model

In light of the measure of quantitative disagreement between test temperature predicted by the thermal model and the empirical test results presented in the above section, it was deemed advisable to review and revise assumptions and estimates regarding the parameters employed in the model, in an effort to gain greater confidence in the accuracy of the models.

6.4.2 Revised Assumptions regarding Model Parameters and Conditions

6.4.2.1 Selecting a Literature-based Value of Contact Ratio

In the previous section, two different values for the contact ratio (***CR*** = 0.1 and ***CR*** = 0.5) were somewhat arbitrarily selected, as a starting point, and the model tuned accordingly to achieve agreement between the electrical resistance value $\boldsymbol{R_2}$ predicted in the model and that calculated based on empirical measurements of potential drop along the pin. Upon further reflection, given the significant levels of normal compressive stress generated at the pin disc interface, these contact ratios seemed low. According to Bay and Wanheim (1976), depending on the friction factor (i.e., severity of adhesion), ***CR*** should actually range between 0.75 – 0.95 when the normal stress is in the range of 2 – 3 times the yield stress. Assuming the AISI 1045 steel discs have a yield strength of 553 MPa (Jaspers & Dautzenberg, 2002), then the ratio of normal stress to yield strength for imprints of diameter 0.40 mm and 0.45 mm works out to 2.88 and 2.27, respectively. Accordingly, a value of ***CR*** = 0.85 was chosen for the revised model.

6.4.2.2. A Temperature-dependent Model of Electrical Resistivity for the Pin (WC-Co)

As discussed earlier, the observation of increasing electrical resistance measurements along the length of the pin with increasing electrical current (**Figure 58** and **Table 8**), combined with an intuitive understanding that the average temperature in the pin increases as electrical current increases, suggested that the electrical resistivity of cemented tungsten carbide increases with temperature. The available literature confirms this, albeit over a much lower range of temperatures. One study showed that the electrical resistivity of cemented tungsten carbide increased linearly with temperature from approximately 150 to 300 K, while below 150 K the relationship was non-linear, the electrical resistivity becoming temperature insensitive at about 60 K and lower (Fransden & Williams, 1991). The same study also indicated that the electrical resistivity of cemented tungsten carbide was dependent on the cobalt content (increasing resistivity with increasing cobalt) as well as the average WC grain size (increasing resistivity with finer grains). Unfortunately, electrical resistivity values for cemented tungsten carbide at elevated temperatures were not readily available in the literature.

In order to determine a temperature-dependent electrical resistivity model for cemented tungsten carbide to use in the thermal model, a series of stationary specimen tests were performed, similar to those described earlier and summarized in **Table 7**, **Figure 58** and **Table 8**. A single disc of AISI 1045 steel was used in all tests. The load was set to 200 N. Temperature, voltage and imprint diameter measurements were evaluated during the same tests. Heating started after 30 s of constant load had been maintained, to be consistent with standard practice. To allow sufficient time to perform voltage measurements, the

specimens were subjected to 100 s of constant electrical current instead of the typical 70 s (10 s after ramp up + 60 s).

Black constant emissivity paint was applied over one half of the circumference of the pin along its entire exposed length (approx. 23 mm), just short of the very tip of the pin. A FLIR ThermaCam™ SC3000 infrared camera was setup to obtain temperature readings over the length of the pin. Temperature readouts were set for 3 key positions, approximately 2.5 mm, 11 mm and 21 mm from the very tip of the pin, which correspond to the "Test Temperature", "Mid Temperature" and the "Top Temperature". A K-type thermocouple was held in contact with the top surface of the copper plate, in close proximity to the disc of AISI 1045 steel, which corresponds to the "Bottom Temperature". The thermocouple was inserted into a Fluke 52 II Thermometer, which yielded the temperature readout. Temperature readings at all four locations were recorded twice – once after 30 seconds of constant electrical current heating, and a second time after 90 seconds of constant electrical current heating.

Three separate voltage measurements were made during a 60 s window of time, after 30 s and 90 s of constant electrical current heating. Voltage measurements were obtained using a Mastercraft Multimeter (Model 52-0052-2). The locations of temperature and voltage measurements are depicted in **Figure 61** for clarity.

Imprint diameter was measured after all tests had been performed. Imprints were measured on the Mitutoyo TM Microscope (to evaluate $\boldsymbol{d_{opt}}$) as well as on an Alicona Infinite Focus G5 Microscope (to evaluate $\boldsymbol{d_{plane}}$).

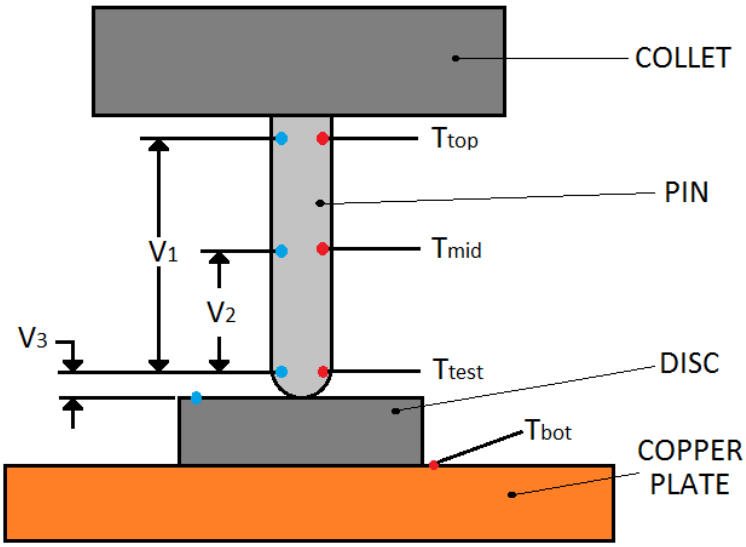

Figure 61: Location of Voltage Measurements and Temperature Measurements Obtained during Stationary Disc Tests for Refined Model Calibration

The measured values of temperature, voltage and imprint diameter are recorded in **Table 11**. Different infrared lenses internal to the FLIR ThermaCam SC3000 were selected depending upon the expected temperature range along the pin during the test. In some instances, the temperature range along the pin fell outside the temperature range for the lens used during the test. In these instances, the displayed temperature value on the associated FLIR software indicated that the measured temperature was out of range and offered the best estimate of the temperature. Such data points are denoted with an '*'.

From these measurements, the electrical resistance as well as the corresponding average electrical resistivity and the average temperature along different sections of the pin were calculated, as tabulated in **Table 12**. For clarity, ***R1-2***, ***ρ1-2*** and ***T1-2*** refer to the electrical resistance, average electrical resistivity and average temperature between the top and mid-point along the pin (approx. 21 mm and 11 mm above the very tip of the pin).

Table 11: Temperature, Voltage and Imprint Diameter Measurements from Second Round of Stationary Specimen Tests

Pin	Current (I)	Bot Temp (°C)	Test Temp (°C)	Mid Temp (°C)	Top Temp (°C)	V1 (V)	V2 (V)	V3 (V)	Imprint Diameter (mm)	
									Mitutoyo (d_{opt})	*AliCona* (d_{plane})
Uncoated	78	30	197.3	159.5	**76.8*	0.063	0.031	0.096	0.428	0.428
		40	208	168.1	**83.3*				0.425	0.433
	100	40	333.7	270.1	131.7	0.112	0.059	0.121	0.42	0.431
		50	364.8	297.2	147.2				0.425	0.44
	120	43	600.8	489.4	**237.8*	0.202	0.099	0.217	0.457	0.447
		65	669.4	544.6	**247.9*				0.437	0.46
	130	45	729	620	**290*	0.258	***0.072*	0.432	0.538	0.467
		61	695	597.8	**294*				0.554	0.449
TiAlCrSiYN/TiAlCrN	60	28	371.3	259.5	131.7	0.072	0.041	0.347	0.47	0.468
		35	365.2	258.1	133.7				0.474	0.452
	80	36	511.3	385.3	194.4	0.12	0.068	0.323	0.466	0.461
		49	513.8	392	201.9				0.451	0.443
	100	36	656.9	531.7	**260.8*	0.18	0.098	0.328	0.527	0.484
		53	672.3	550.8	**278.6*				0.514	0.47
	110	40	773.6	636.4	**323.5*	0.222	0.108	0.335	0.564	0.465
		57	773	643.5	**339.9*				0.578	0.466

** denotes temperature measurements beyond the range of the infrared lens of the FLIR ThermoCam 3000 used during the test in question.*
*** while this is the value of voltage recorded, the author believes it was recorded erroneously as it does not follow the expected trend.*

Table 12: Calculated Electrical Resistance, Electrical Resistivity and Mean Temperature based on Measurements in Table 11

Pin	Current (I)	R1 (Ω)	R2 (Ω)	R1-2 (Ω)	R3 (Ω)	ρ1 (Ωm)	T1 (°C)	ρ2 (Ωm)	T2 (°C)	ρ1-2 (Ωm)	T1-2 (°C)
Uncoated	78	8.08E-04	3.97E-04	4.10E-04	1.23E-03	3.09E-07	1.41E+02	3.31E-07	1.83E+02	2.90E-07	1.22E+02
	100	1.12E-03	5.90E-04	5.30E-04	1.21E-03	4.28E-07	2.44E+02	4.91E-07	3.16E+02	3.75E-07	2.12E+02
	120	1.68E-03	8.25E-04	8.58E-04	1.81E-03	6.43E-07	4.39E+02	6.86E-07	5.76E+02	6.07E-07	3.80E+02
	130	1.98E-03	5.54E-04	1.43E-03	3.32E-03	7.58E-07	5.02E+02	4.61E-07	6.60E+02	1.01E-06	4.50E+02
TiAlCrSiYN/TiAlCrN	60	1.20E-03	6.83E-04	5.17E-04	5.78E-03	4.59E-07	2.50E+02	5.68E-07	3.14E+02	3.65E-07	1.96E+02
	80	1.50E-03	8.50E-04	6.50E-04	4.04E-03	5.73E-07	3.55E+02	7.07E-07	4.51E+02	4.59E-07	2.93E+02
	100	1.80E-03	9.80E-04	8.20E-04	3.28E-03	6.88E-07	4.67E+02	8.15E-07	6.03E+02	5.80E-07	4.05E+02
	110	2.02E-03	9.82E-04	1.04E-03	3.05E-03	7.71E-07	5.53E+02	8.16E-07	7.07E+02	7.33E-07	4.86E+02

Figure 62 presents the variation in test temperature, mid temperature and top temperature on the pin as a function of electrical current used in the stationary specimen tests, for both the uncoated and TiAlCrSiYN/TiAlCrN-coated cemented tungsten carbide pin. Second order polynomial curves with a forced intercept of T = 0 °C were fit to the data points using Microsoft Excel's Least Square Fitting routine. Though not shown, the associated R^2 value was greater than 0.90 for each curve, which signifies a good fit. The curves for test temperature vs. electrical current, for both coated and uncoated pins, are quite similar to those presented in **Figure 60**, although there are slight discrepancies in the temperature values for the coated pin under lower levels of electrical current.

Figure 63 depicts the distribution of temperature along the length of the pin (that is to say, the test temperature, mid temperature and top temperature of the pin) for the different levels of electrical current and both uncoated and coated pins evaluated during the stationary specimen tests. Position 0 denotes the transition between the cylindrical body and the hemispherical tip of the pin. Arguably, the temperature profiles look qualitatively similar for both uncoated and coated pins. For example, the profiles for the uncoated pin at 120 A and the coated pin at 100 A are essentially overlapping, as are the profiles for the uncoated pin at 100 A and the coated pin at 80 A.

Figure 64 presents the variation in average electrical resistivity as a function of the average temperature, based on the calculated values shown in **Table 12**. The data points include measurements from both the uncoated and TiAlCrSiYN/TiAlCrN-coated pin in so much as the coating is not expected to affect the electrical resistance between two points along the length of the pin (current is flowing parallel to the coating, not through the

coating). The Least Squares fit is linear with an R^2 value of 0.92 (signifying a good fit). Vertical error bars denote +/- 20%, which roughly corresponds to the range of variation in electrical resistivity calculated when allowing for +/- 1 A uncertainty in electrical current output from the welder and +/- 1 mm uncertainty in the location of probe measurement. Horizontal error bars denote +/- 5%, which is deemed an upper bound for temperature uncertainty.

Accordingly, the electrical resistivity of the grade of cemented tungsten carbide out of which the pin was made was assumed to vary with temperature, over the range of about 100 °C to 700 °C, as expressed in **Eq. 6.5.1**, where $\boldsymbol{T}$ is in units $°C$ and $\boldsymbol{\rho_{WC\text{-}Co}}$ is in units of Ωm.

$$\rho_{WC-Co}(T) = 9.85 \times 10^{-10} T + 1.90 \times 10^{-7} \qquad \textbf{Eq. 6.5.1}$$

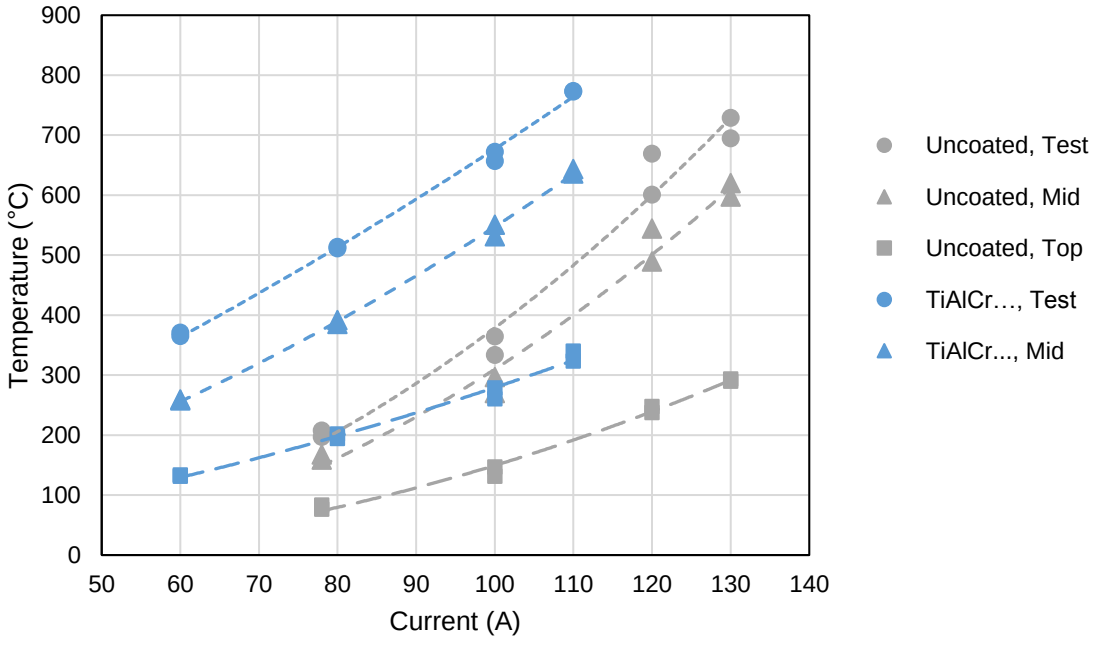

Figure 62: Temperature (Test, Mid and Top) vs. Electrical Current for Second Round of Stationary Specimen Tests

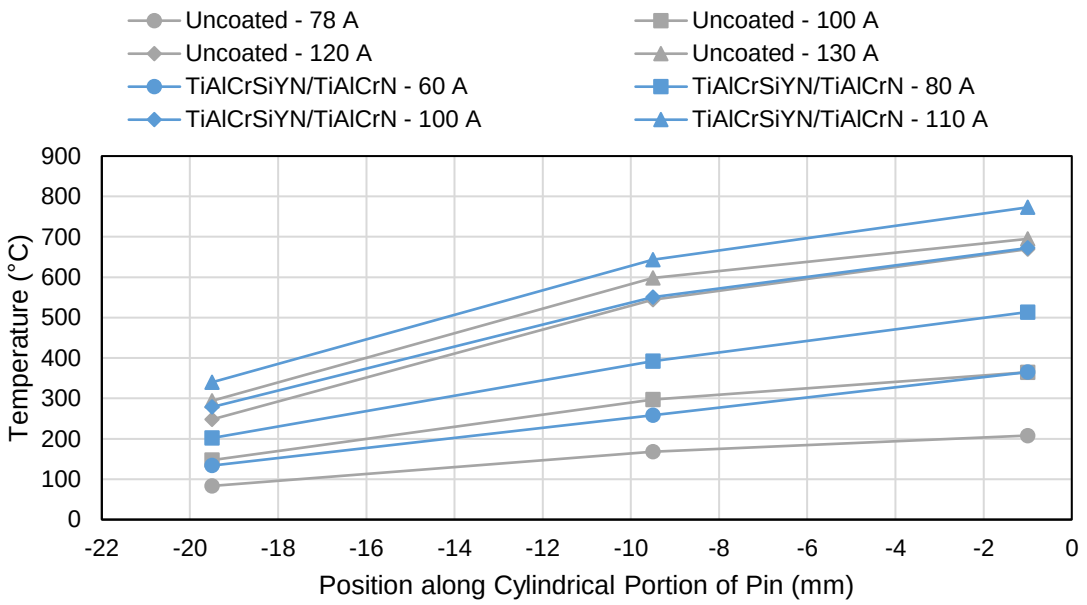

Figure 63: Distribution of Temperature along the Cylindrical Body of the Pin as measured during Second Round of Stationary Specimen Tests

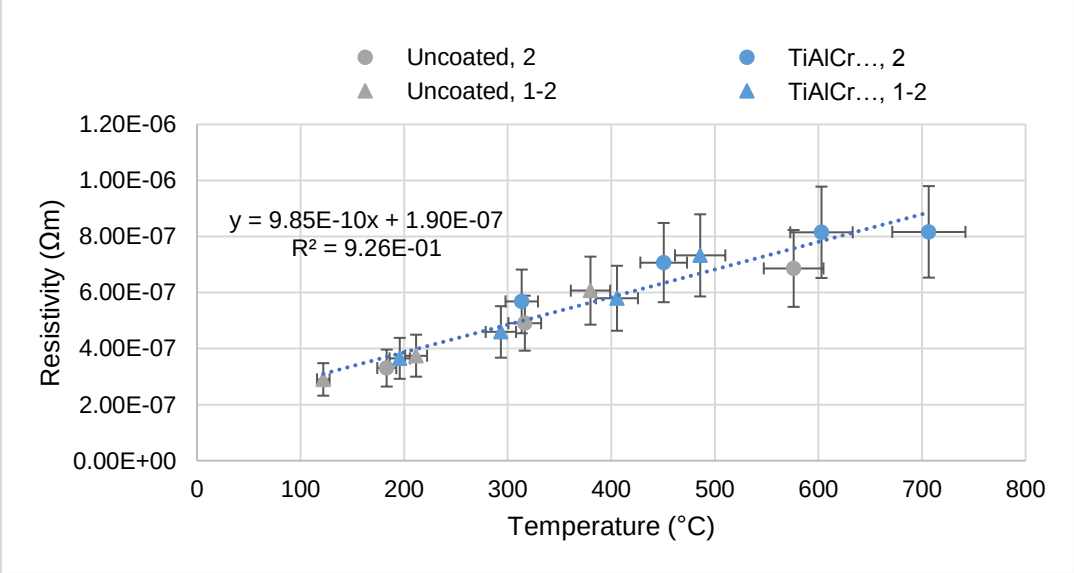

Figure 64: Electrical Resistivity vs. Temperature based on Calculation of Average Values from Second Round of Stationary Specimen Tests

6.4.2.3 A Temperature-dependent Model of Thermal Conductivity for the Pin and Disc

In addition to using an improved estimate of ***CR*** based on the available literature; as well as incorporating an empirically evaluated relationship for the temperature-dependence of electrical resistivity of cemented tungsten carbide; it seemed advisable to include the temperature-dependence of thermal conductivity for both the pin (cemented tungsten carbide) as well as the disc (AISI 1045 steel) in the revised thermal model. The variation in thermal conductivity with temperature for AISI 1045 steel is expressed in **Eq. 6.5.2**, where ***T*** is in units of °C and ***k*** is in units of W/m°C. The equation was derived using a quadratic fit of data used by Halim (2008), which upon further investigation appears to have originated from tests reported by Grzesik, Nieslony and Bartoszuk (2009).

$$k_{AISI\ 1045}(T) = 1.24 \times 10^{-5}T^2 - 3.43 \times 10^{-2}T + 4.73 \times 10^{1} \quad \textbf{Eq. 6.5.2}$$

The temperature-dependence of thermal conductivity in fine-grained WC-6%Co is estimated based on a few available sources in the literature. Fransden & Williams (1991) reported significant variation in the thermal conductivity of cemented tungsten carbide, both as a function of temperature as well as the Cobalt content. In particular, the thermal conductivity increased with temperature starting from 0 K, reached a maximum between 30 – 180 K (depending on the Co content and grain size) and then decreased gradually with further increases in temperature up to 300 K, beyond which values were not reported. However, for grades of carbide possessing 3.5 μm WC grain size and Cobalt content in the range of 1.5 – 23 wt%, the corresponding range in thermal conductivity values at 275 K was roughly 75 – 140 W/mK, the thermal conductivity increasing with decreasing Cobalt content. Williams (1991) showed that the thermal conductivity of WC-30%Co decreased

from approximately 80 to 55 W/mK in a roughly linear manner over a temperature range of 150 to 1200 K. Based on reported curves in Fransden & Williams (1991), it was estimated that the thermal conductivity of WC-6%Co should be about 30% higher than WC-30%Co, leading to the relationship expressed in **Eq. 6.5.3**, where ***T*** is in units of °C and ***k*** is in units of W/m°C.

$$k_{WC-Co}(T) = -3.10 \times 10^{-2} T + 1.00 \times 10^{2} \qquad \textbf{Eq. 6.5.3}$$

Interestingly, the relationship in **Eq. 6.5.3** shows the opposite trend to that reported in Jawahir & van Lutterwelt (1993), which has been used relatively widely in the metal cutting community in simulation work. The works of Fransden & Williams (1991) as well as Williams (1991) clearly indicate that the thermal conductivity of cemented tungsten carbide clearly decreases as a function of temperature, at least above the 30 – 180 K range.

6.4.2.4 Other Assumptions

The electrical resistivity and thermal conductivity of the contaminant layer was assumed to be a scalar multiple of the electrical resistivity of the pin, which itself was taken to be temperature dependent. Of the five models developed prior, each with a different imprint diameter, only the model with ***d*** = 0.45 mm was modified in this way, as it best matched the imprint diameters measured during the stationary specimen tests (**Table 11**).

6.4.3 Solution Technique

6.4.3.1 Original Approach

The model was adjusted in order to incorporate the temperature dependency of electrical resistivity for cemented tungsten carbide, expressed in **Eq. 6.5.1** and the temperature dependency of thermal conductivity for cemented tungsten carbide and AISI 1045 steel expressed in **Eq. 6.5.2** and **Eq. 6.5.3**, respectively.

In practice, the model was executed as per the following procedure:

i) initial values for the electrical resistivity and thermal conductivity were calculated for all nodes based on the initial temperature conditions assumed;

ii) the temperature at each node was updated through Jacobi iteration for 4000 iterations, using the same value of electrical resistivity and thermal conductivity evaluated from the initial conditions;

iii) the electrical resistivity and thermal conductivity values were re-calculated based on the updated temperature at each node;

iv) the temperature at each node was updated through Jacobi iteration for another 4000 iterations using the updated values for electrical resistivity and thermal conductivity evaluated after the previous round of iterations;

v) the electrical resistivity and thermal conductivity values were re-calculated based on the updated temperature at each node;

vi) steps iv) and v) were repeated until the maximum difference in temperature for all nodes between successive iterations was less than 10^{-5}.

After the simulation converged, the predicted values of electrical resistance ($\boldsymbol{R_1}$, $\boldsymbol{R_2}$, $\boldsymbol{R_3}$) and temperature ($\boldsymbol{T_{test}}$, $\boldsymbol{T_{mid}}$) were compared with those measured during physical experiments, as reported in **Table 11** and **Table 12**. The better the agreement between simulation and experiments across these five variables, the greater the confidence in the accuracy of the pin-disc interface temperature ($\boldsymbol{T_{int}}$) predicted by the simulation.

6.4.3.2 Observations and Further Adjustments to the Model

During the first few attempts at running simulations using the revised thermal model, a few issues were noted. First, the simulations required considerably more iterations (approximately 10 times as many) before converging to a solution. Thus, the process of tuning parameters to achieve good agreement between simulated outputs and empirical measurements took longer, but not unreasonably so given the increase in complexity.

Second, despite efforts in tuning the multiplier for the electrical resistivity of the contaminant layer, good agreement between the simulated and empirically measured values of electrical resistance ($\boldsymbol{R_1}$, $\boldsymbol{R_2}$, $\boldsymbol{R_3}$) and temperature ($\boldsymbol{T_{test}}$, $\boldsymbol{T_{mid}}$) could not be simultaneously obtained. Through experimentation, better agreement was achievable when the electrical resistivity model for cemented tungsten carbide was reduced by ten percent and when a tunable convective heat transfer coefficient was introduced along the cylindrical portion of the pin. When reduced by ten percent, the linear equation for the electrical resistivity still fit the lower bounds of the empirical data shown in **Figure 64**, so it was deemed a reasonable adjustment. Additionally, it was observed that the resulting least squares fit of data when the location of the top probe measurement is shifted up 1 mm and the location

of the bottom probe measurement is shifted down 1 mm, relative to the nominal locations estimated for the purposes of calculation, almost perfectly coincides with this adjusted relationship, which is shown in **Eq. (6.5.4)**:

$$\rho_{WC-Co\,(Modified)}(T) = 8.87 \times 10^{-10}T + 1.71 \times 10^{-7} \qquad \textbf{Eq. 6.5.4}$$

6.4.4 Simulation Results: Uncoated Pin, Varying Levels of Electric Current

The inputs and outputs for various scenarios explored with the revised thermal model are detailed in **Table 13**. In each scenario, the pin was treated as uncoated (N_1 = 1), the contact ratio ***CR*** was set to 0.85 and the imprint diameter was chosen as 0.45 mm. As noted above, five of the seven outputs have empirical measurements recorded in **Table 11** and **Table 12**, which were used for comparison in order to estimate the model error. The outputs T_{int} and its variant ΔT (the difference between the pin-disc interface temperature T_{int} and the test temperature ***T@z=-1***) are shaded in grey in **Table 13** to distinguish them from the other outputs, as T_{int} was inaccessible for measurement in the physical setup.

The errors in simulated versus empirically measured electrical resistance and temperature values have been shaded with different colours for ease of comparison. Errors less than 15% are shaded green; errors between 15-25% are shaded yellow; errors greater than 25% are shaded orange. The assumption is that the smaller the error between model and experiments for these five outputs, the more accurate the estimate of T_{int} and ΔT.

Table 13: Model Inputs, Outputs and Errors for Scenarios Explored using the Revised Thermal Model

Scenario		Scen 20	Scen 21	Scen 22	Scen 23	Scen 24	Scen 25	Scen 26
Model Inputs	I (A)	78	78	78	100	120	120	120
	N_3 (x10^3)	10	12	9	5.1	2	2.5	2.75
	T_{top} (°C)	77	77	77	139.5	243	243	243
	T_{bot} (°C)	30	30	30	45	54	54	54
	T∞ (°C)	25	25	25	25	25	25	25
	h (W/m^2)	2.00E-04	4.00E-04	1.50E-04	2.00E-04	2.00E-04	2.00E-04	2.00E-04
Model Outputs	R1 (Ω)	7.89E-04	7.47E-04	8.26E-04	1.11E-03	1.36E-03	1.48E-03	1.61E-03
	R2 (Ω)	4.13E-04	3.88E-04	4.07E-04	5.70E-04	6.67E-04	7.58E-04	8.50E-04
	R3 (Ω)	1.05E-03	1.18E-03	9.03E-04	1.06E-03	6.81E-04	9.37E-04	1.19E-03
	$T_{@z=-10}$ (°C)	152	130	151	275	378	435	493
	$T_{@z=-1}$ (°C)	212	194	201	374	439	548	660
	Tint (°C)	242	237	223	418	444	578	718
	ΔT (°C)	**30**	43	22	**44**	5	30	**58**
Model Error	R1 (Ω)	-1%	-8%	-3%	-6%	-23%	-16%	-8%
	R2 (Ω)	4%	-2%	3%	-3%	-19%	-8%	3%
	R3 (Ω)	-15%	-4%	-27%	-13%	-62%	-48%	-34%
	$T_{@z=-10}$ (°C)	-7%	-20%	-8%	-3%	-27%	-16%	-5%
	$T_{@z=-1}$ (°C)	5%	-4%	-1%	7%	-31%	-14%	4%

Scenarios 20 to **22** all featured the pin subject to 78 A of electric current, with slightly different multipliers for the contaminant layer electrical resistivity, N_3, and the convective heat transfer coefficient along the length of the pin, h. **Scenario 23** featured the pin subject to 100 A of current, while **Scenarios 24** to **26** explored the pin subject to 120 A of current with a common convective heat transfer coefficient along the length of the pin but slightly different multipliers for the contaminant layer electrical resistivity.

Of the scenarios explored, only **Scenario 23** (the only scenario for I = 100 A) yielded less than 15% error in all five comparable outputs. However, many scenarios yielded less than 15% error in four of five comparable outputs, specifically **Scenarios 20**, **21** and **26**.

Of those scenarios featuring 78 A of current, **Scenario 20** yielded the lowest maximum error (15%) and a temperature difference of 30 °C between the simulated test temperature, $\boldsymbol{T@z = -1}$, and interface temperature, $\boldsymbol{T_{int}}$. Reasonably good agreement in outputs was also achieved when the contaminant electrical resistivity, $\boldsymbol{N_3}$, and convective heat transfer coefficient, $\boldsymbol{h}$, were simultaneously increased (**Scenario 21**) or decreased (**Scenario 22**). As these parameters were increased, the difference between test temperature and interface temperature also increased (i.e., $\boldsymbol{\Delta T}$ = 43 °C for **Scenario 21**).

Of the scenarios featuring 120 A of current, only **Scenario 26** came close to predicting the electrical resistance as well as test and mid-temperatures with reasonable accuracy.

It is anticipated that better agreement between simulation and experimental outputs could be achieved via further efforts at tuning $\boldsymbol{N_3}$ and $\boldsymbol{h}$. However, as noted in **Sec. 6.4.3.2**, the number of iterations required to reach adequate convergence is quite high in the revised model, so the process of tuning is quite tedious.

Figure 65 through **Figure 67** present the simulated temperature distribution along the length of the pin, the centermost axial nodes of the disc, and the topmost radial nodes of the disc, respectively, for **Scenarios 20**, **23** and **26**. **Figure 65** also presents the experimentally obtained temperatures $\boldsymbol{T_{test}}$, $\boldsymbol{T_{mid}}$ and $\boldsymbol{T_{top}}$ as well as the temperature distribution along the length of the pin from **Scenarios 4** and **10** from the initial model, for visual comparison.

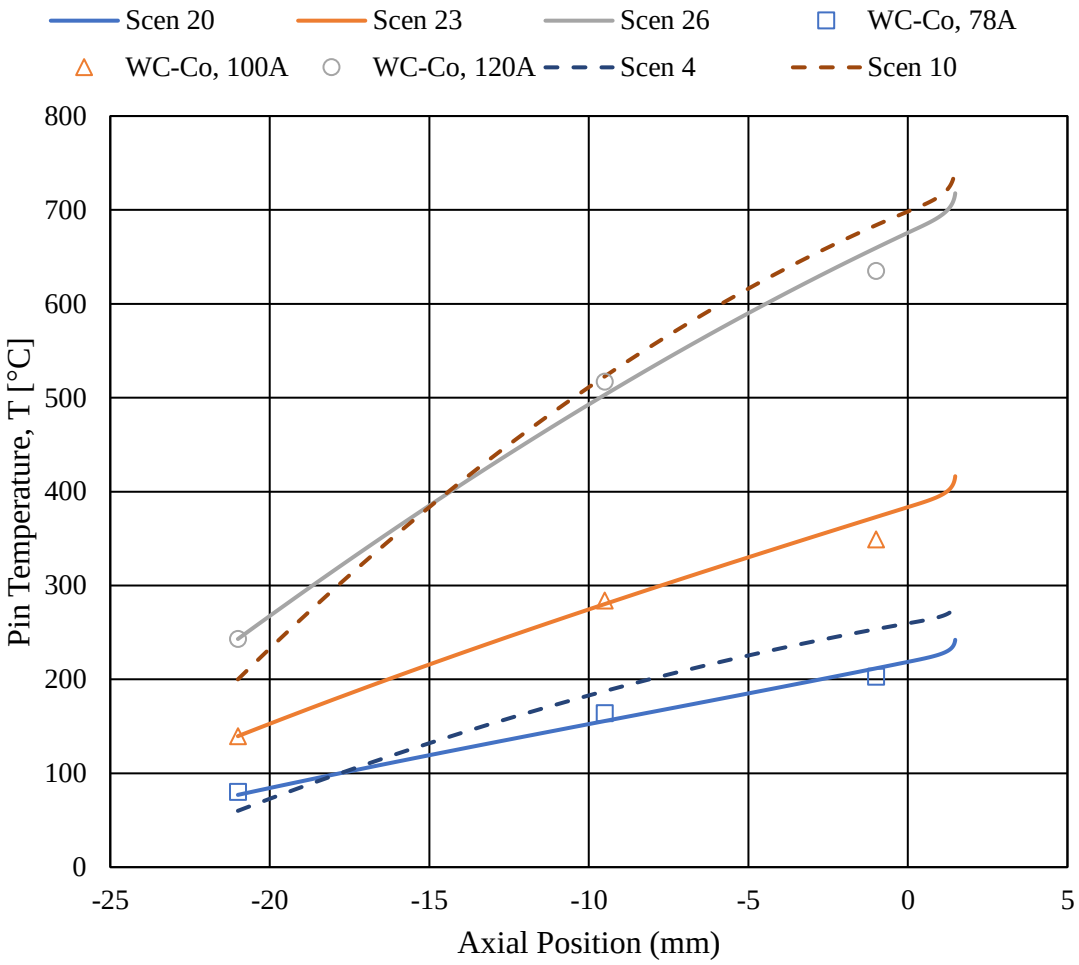

Figure 65: Temperature distribution along the length of the pin for various scenarios

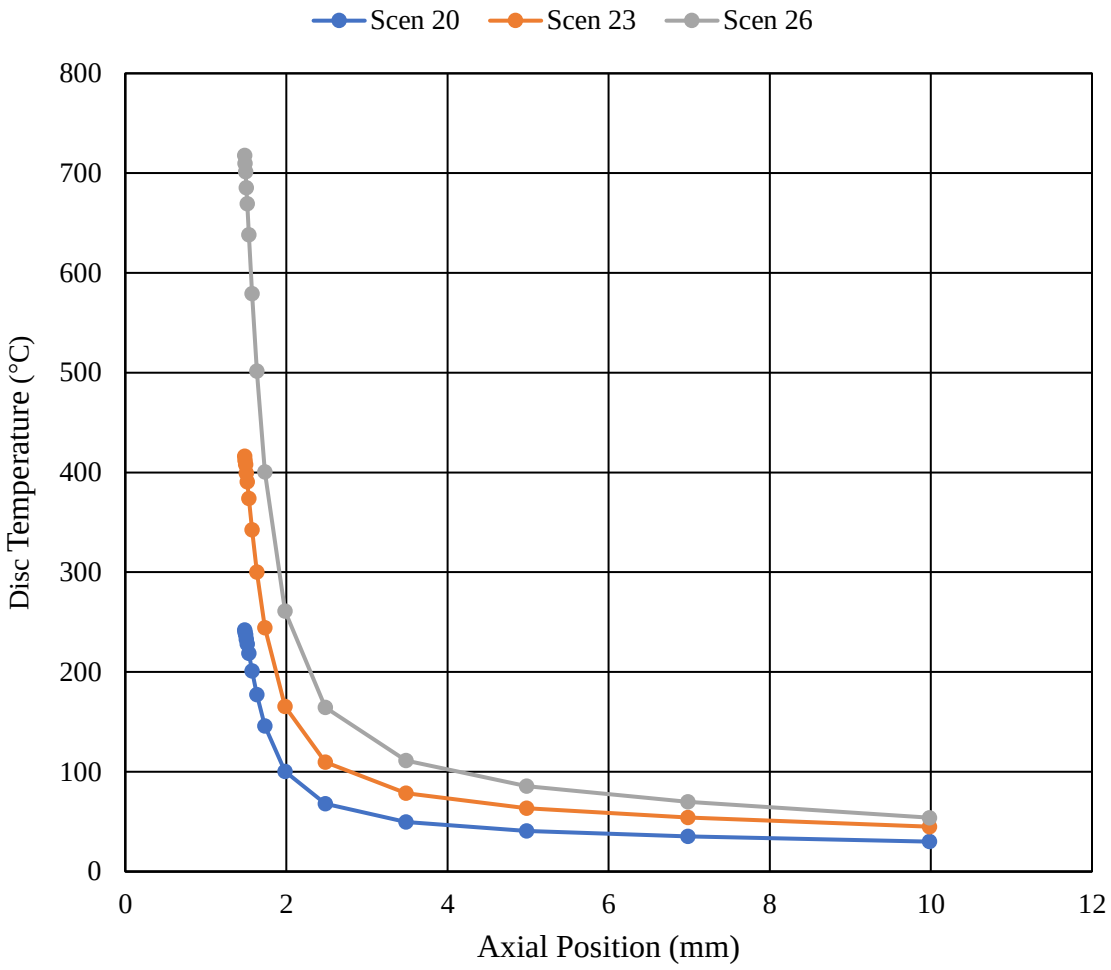

Figure 66: Axial temperature distribution along the centermost nodes of the disc for various scenarios

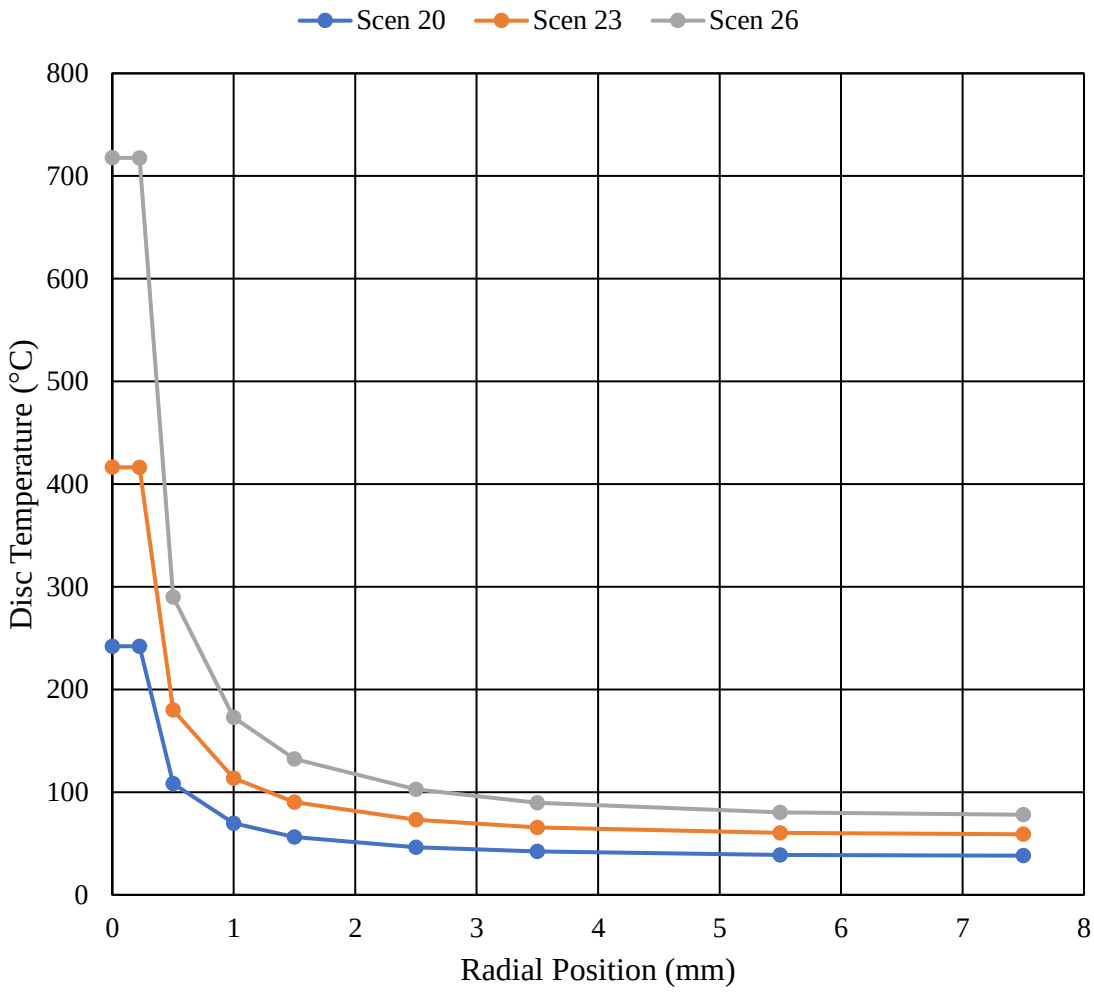

Figure 67: Radial temperature distribution along the topmost nodes of the disc for various scenarios

6.4.5 Discussion of Results from the Revised Model Implementation

The revised model exhibited considerably more accuracy in its outputs of temperature and electrical resistance as compared with the initial model, although with much greater effort in programming, not to mention tuning and solving. It is unclear how much the incorporation of a temperature-dependent thermal conductivity model for the pin and disc contributed to the improved accuracy in the revised model; however, the incorporation of a temperature-dependent electrical resistivity model for the pin (combined with some adjustments after initial tuning efforts) combined with the addition of convective heat transfer along the length of the pin appear to have been critical.

With proper tuning, the model predicted the test temperature and the temperature along the midpoint of the pin within +/- 7% error relative to the empirically observed temperatures from experiments. In comparison, the first model implementation overestimated the test temperature by as much as 70-80% for a given set of conditions. The increased accuracy in predicting the test temperature and midpoint temperature in the pin, along with the accuracy in electrical resistance values (at least 2 out of 3), allows for reasonable confidence in the estimates of the interface temperature.

On this basis, per **Table 13**, the model suggests that for an uncoated cemented tungsten carbide pin in contact with AISI 1045 steel, forming an imprint with a diameter of approximately 0.45 mm, the temperature at the interface between pin and disc can be expected to be in the range of 30 – 60 °C higher than the test temperature, for test temperatures in the range of 210 – 660 °C. The difference between interface temperature

and pin-disc interface temperature can also be seen to increase as the test temperature increases (considering **Scenarios 20**, **23** and **26**).

It should be emphasized that these results are valid for stationary specimen tests. Conceivably, with the addition of specimen rotation and the encompassing increase in imprint diameter (i.e., reduced heat generation at the pin-disc interface), differences between the test temperature and interface temperature may be reduced.

Overall, the temperature distributions predicted by the revised model are qualitatively similar to those predicted by the initial model, with all of its simplifications. Thus, insomuch as efforts were not made at modeling the effects of a coating layer in the revised model, it is expected that the revised model would predict similar differences between the interface and test temperatures as was yielded by the initial model – namely, that a coating with an increased electrical resistivity does increase the thermal gradient across the pin tip, but not by an appreciable amount. This is further supported by the similarity in temperature distributions along the pin observed during empirical tests documented in **Section 6.4** (**Figure 63**).

With regards to the observations in **Chapter 5**, which suggest that a coating with increased electrical resistance results in higher thermal gradients in the pin tip, and thus appreciably higher interfacial temperatures for the same test temperature as compared with an uncoated pin; it is worth noting that the observations favouring this hypothesis (differences in imprint diameter and differences in microstructural appearance) were made for tests involving specimen rotation. Differences in imprint diameter were not very

apparent for stationary specimen tests (**Figure 49(d)**). Thus, the rotation of specimens may play a critical role in the apparent differences.

Noting the very steep gradients in the disc in both axial and radial directions (**Figure 66** and **Figure 67**), it is conceivable that thermally softened material in the immediate vicinity of the pin has nowhere to displace except upwards, being constrained by a relatively cool volume of surrounding disc material. Thus, it would form a steep pile-up zone around the periphery of the imprint, which increases in size as temperature grows (recall **Section 3.5.3** and **Figure 33** through **Figure 35**). It is expected that the shear stress imposed by rotation would force this 'extrusion' of thermally softened work material upward into a pile-up more effectively than normal contact stress alone experienced during a stationary test. From this perspective, when the temperature is sufficiently high, relatively small increases in temperature at the interface could have a more pronounced effect on thermal softening and extruding material upward to form a large pile-up.

At first glance, it appears that the revised model requires a considerably higher value of electrical resistivity for the contaminant layer (reflected in the multiplier $\boldsymbol{N_3}$) compared with the initial model. However, it is important to note that the initial model assumed much smaller values of contact ratio $\boldsymbol{CR}$ (most scenarios featured $\boldsymbol{CR}$ = 0.1 in the initial model, as compared with $\boldsymbol{CR}$ = 0.85 in the revised model). As described in **Sec. 6.2.3**, both of these terms influence the overall electrical contact resistance present at the pin-disc interface. It is worth underscoring that the ability of either model to predict temperature distributions in the pin and disc remotely similar to those observed empirically is reliant upon modeling this contact resistance in some fashion. A comparison of **Scenarios 24** to

26 highlights how changed in the multiplier N_3 on the order of only 20-30% can have an appreciable influence on the temperature profile, changing the predicted test temperature and pin-disc interface temperature by a few hundred degrees Celsius. Simply ignoring the contact resistance (e.g., setting CR =1 or N_3 = 0) would yield altogether unsatisfactory results. Simplifying assumptions were made with regards to the thickness of the contaminant film, which undoubtedly influences the value of N_3 required for a given scenario in the revised model to achieve reasonable agreement with empirically observed temperature and resistance values.

6.5 Concluding Remarks

Notable findings and contributions that arose in the course of the investigation presented above are as follows:

- A thermal model was developed and implemented in Microsoft Excel, featuring:
    - temperature-dependent thermal conductivity in the pin and disc;
    - temperature-dependent electrical resistivity in the pin;
    - convective heat transfer along the length of the pin and over the top and side surfaces of the disc;
    - electrical contact resistance at the pin-disc interface, reflected by a contact ratio (percentage of real area of contact relative to the apparent area of contact) and electrical resistivity in a thin contaminant layer.
- The thermal model was able to predict the test temperature and temperature at the midpoint of the pin with less than 7% error and electrical resistance along various

portions of the pin with less than 35% error (less than 10% error in two of the three resistances) relative to empirical measurements obtained during experiments under the same electrical current inputs.

- An empirical relationship for the temperature-dependence of electrical resistivity for fine-grained cemented tungsten carbide (6% cobalt binder) was established via experimental techniques, which was not otherwise available in the literature. This relationship was employed in the thermal model employing a correction factor of 0.9 to improve alignment of the model predictions with empirical observations.
- Modeling of contact resistance between pin and disc was shown to be of great importance to the accuracy of the thermal model. Changes in the electrical resistivity on the order of 20-30% in an assumed 0.1 μm thick layer changed the predicted test and interface temperatures by a few hundred degrees Celsius.

In regards to the first objective of this chapter, outlined in **Section 6.1 (i)**, bearing in mind the errors present in the model outputs, it is reasonable to expect that the interface temperature does not exceed the test temperature by more than 30 – 60 °C in the case of an uncoated pin in contact with a disc of AISI 1045 steel, forming an imprint of approximately 0.45 mm and resulting in test temperatures in the range of 210 – 660 °C.

In regards to the second objective of this chapter, outlined in **Section 6.1 (ii)**, the empirical testing and modeling effort suggests it is unlikely the thermal gradient in the hemispherical pin tip of the TiAlCrSiYN/TiAlCrN is significantly different from that of the uncoated pin when the test temperatures are identical, in contrast to what was proposed in **Chapter 5**.

7. COMPARISON OF TRIBOMETER TESTS WITH CUTTING TRIALS

7.1 Opening Remarks

Whereas previous chapters explored fundamental aspects of on-axis pin-on-disc tribometer tests, the present chapter aims to identify correlations between tribometer outputs (namely ranking of surface treatments in COF values at similar elevated temperatures) with outputs of the cutting process, including built-up edge formation, tool forces and characteristics of the chips produced.

To this end, the results of short duration turning tests of a cylindrical billet of AISI 1045 steel using uncoated as well as TiN- and TiAlCrSiYN/TiAlCrN-coated cemented tungsten carbide cutting inserts are presented. These same tool and work material pairs were featured in tribometer tests discussed in **Chapters 4** and **5**, wherein it was noted that at temperatures above about 550 °C, appreciable differences in COF were discernable among the three surfaces treatments of pins.

Additionally, a comparison of tribofilm formation on the surfaces of pins and inserts from select tribometer and cutting tests is made via X-ray Photoelectron Spectroscopy (XPS), to determine if such surface films are qualitatively similar in nature.

7.2 Materials and Methods

7.2.1 Materials

Triumph TNMA 332 Grade C2 carbide inserts were selected for use in the machining trials described below. To clarify the chemical composition and grain size, a sample insert was lapped and chemically etched prior to performing Secondary Electron (SE) imaging

and Energy Dispersive X-ray (EDX) analysis at 1500x magnification on a JEOL-6610 scanning electron microscope. Inspection of grain size and EDX analysis at 1500x magnification suggested the carbide type to be fine grain CC F7 as per ASTM B390, possessing 7 wt% Co and the balance W and C. **Figure 68** shows the SE image at 1500x magnification. Spot EDX analysis at 5000x magnification centered on one of the darker grains identified these as NbTiC, though their content was trace enough to have not been detected at the full view field analysis conducted at 1500x magnification.

PVD TiN and PVD TiAlCrSiYN/TiAlCrN coatings were deposited on select inserts by Byrcoat (USA) and Kobac (USA), respectively, consistent with the treatments applied to select tribometer pins used in the experiments described in **Chapter 4**.

The work material selected for machining trials was a billet of AISI 1045 steel of 115 mm diameter. The nominal composition of AISI 1045 is listed in **Table 14**.

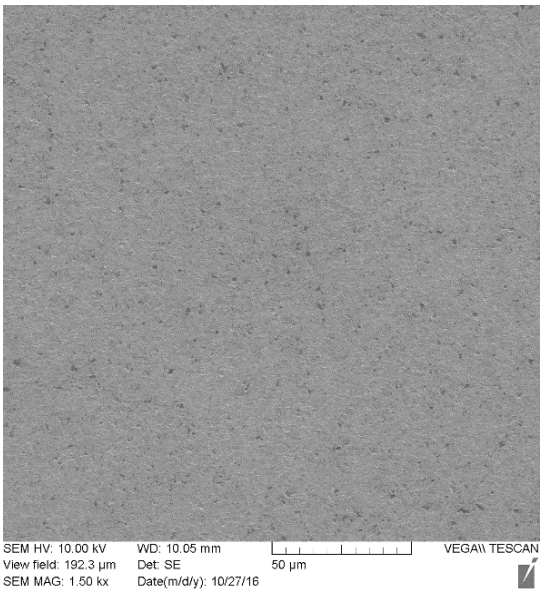

Figure 68: SE image obtained from a Triumph TNMA 332 Grade C2 carbide insert

Table 14: Nominal composition of AISI 1045 steel

C	Mn	P	S	Fe
0.42 – 0.50	0.60 – 0.90	≤ 0.040	≤ 0.050	Balance

7.2.2 Machining Conditions

Turning tests were performed at two cutting speeds, $\boldsymbol{V}$ = 50 m/min and 100 m/min. A constant feed rate $\boldsymbol{f}$ = 0.20 mm/rev and depth of cut $\boldsymbol{DOC}$ = 0.75 mm were employed for all tests. No coolant was used and cutting tests were kept short (8 s duration) to minimize the progression of wear on the inserts. Each set of cutting conditions was tested three times, using a different corner of the triangular inserts. Due to negligible flank wear, the same three corners were used in tests at 100 m/min after having completed the tests at 50 m/min, after all necessary observations had been documented.

7.2.3 Machining Outputs

A Kistler 9121 three-axis piezoelectric dynamometer was used to monitor the three components of cutting forces acting on the tool during tests (**Figure 69**). Sampling was performed at 500 Hz over a 20 s window to ensure the entire duration of actual cutting (approx. 8 s) was captured. Signal from the last 3 s of cutting (1500 data points) was processed, from which the ***average*** (arithmetic mean) and the ***fluctuation*** (standard deviation) of the measured signal was determined (**Figure 70**). The mean and the standard deviation of the average and fluctuation in cutting force components were then determined using values from all three test replicates per a given set of tool material and cutting speed.

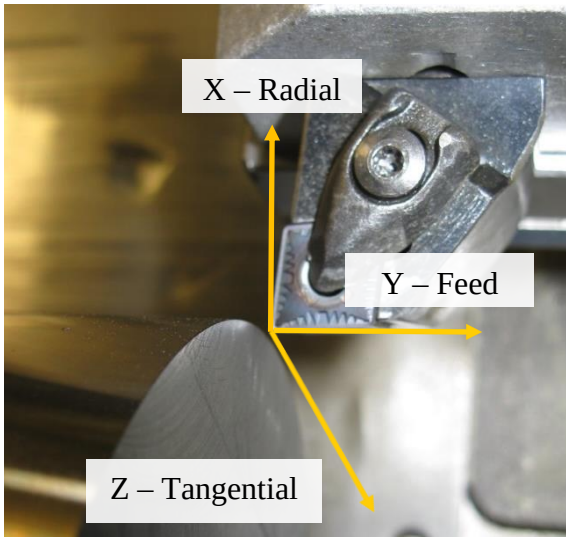

Figure 69: Cutting force components

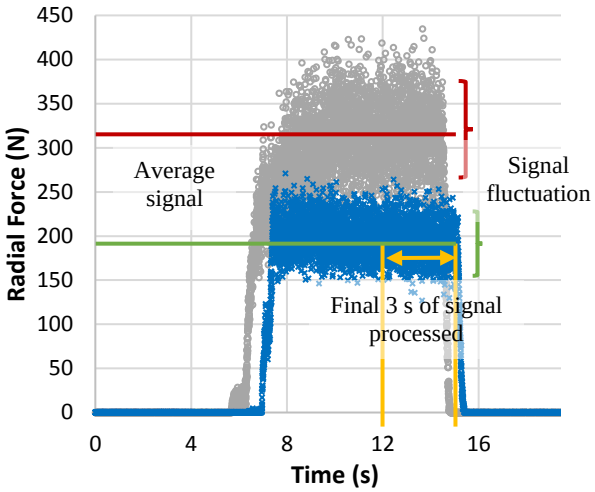

Figure 70: Example force measurement

After each test, observations were made of any built-up edge (BUE) forming on the cutting edge of the insert, using a Mitutoyo TM Microscope (for BUE height) and a Nikon AZ100M Stereoscope (for photo documentation).

Chips were collected and quantitative measurements of their length and tightness of curl were made with a pair of Vernier calipers. Chip colour was also noted, distinguishing between the sliding and free surface of the chip, as depicted in **Figure 71**. The length of the shortest and longest chip collected was reported based on a single measurement, rounded to the nearest millimeter. The chip curl diameter was measured in three locations over the length of chips (or in five locations for particularly long chips) and the average reported. For extremely short chip lengths, only a single measurement was performed and reported.

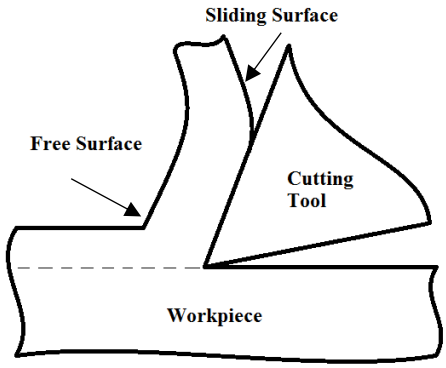

Figure 71: Distinguishing the 'free surface' and 'sliding surface' of the chip (not to scale)

7.3 Results

7.3.1 Tool Forces

The average tool force components measured during the turning tests are displayed in **Figure 72**, the error bars denoting a single standard deviation based on three test replicates. Likewise, the fluctuation in measurement signal in each force component is presented in **Figure 73**. In general, the TiN- and TiAlCrSiYN/TiAlCrN-coated inserts demonstrated both reduced forces and reduced levels of fluctuation in force signals compared with the uncoated insert. At 50 m/min, the TiAlCrSiYN/TiAlCrN-coated insert exhibited slightly lower average forces than the TiN-coated insert; however, with the exception of fluctuations in force in the feed direction, there is considerable overlap in error bars.

For uncoated inserts, forces decreased slightly and fluctuations in forces reduced considerably when the cutting speed changed from 50 m/min to 100 m/min. In contrast, for coated inserts, tool forces increased slightly when cutting speed was increased, though error bars overlap for the TiN-coated insert. Fluctuations in tool forces decreased in radial and tangential directions but increased in feed direction with increasing cutting speed.

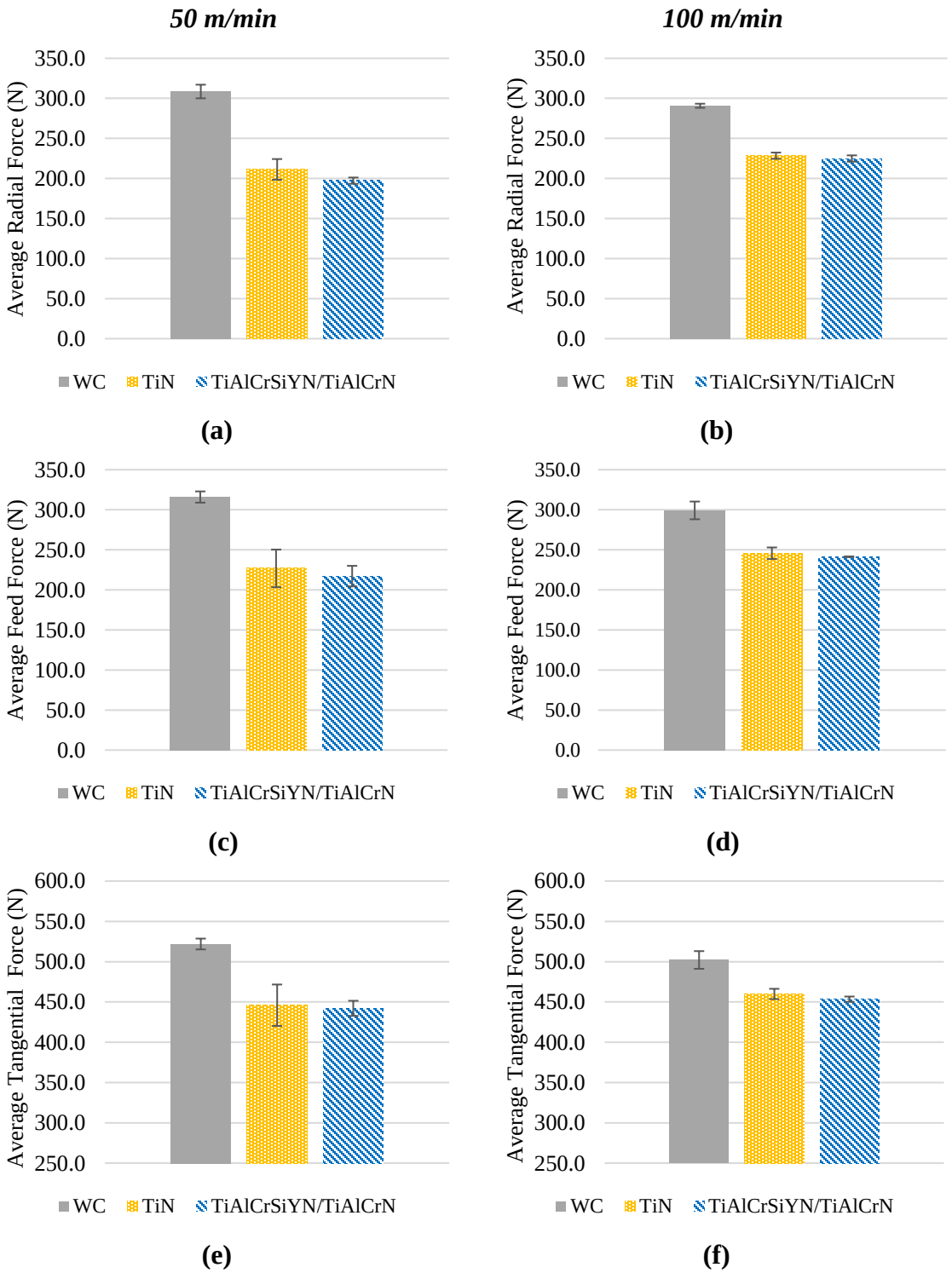

Figure 72: Average cutting force components at 50 m/min (left) and 100 m/min (right)

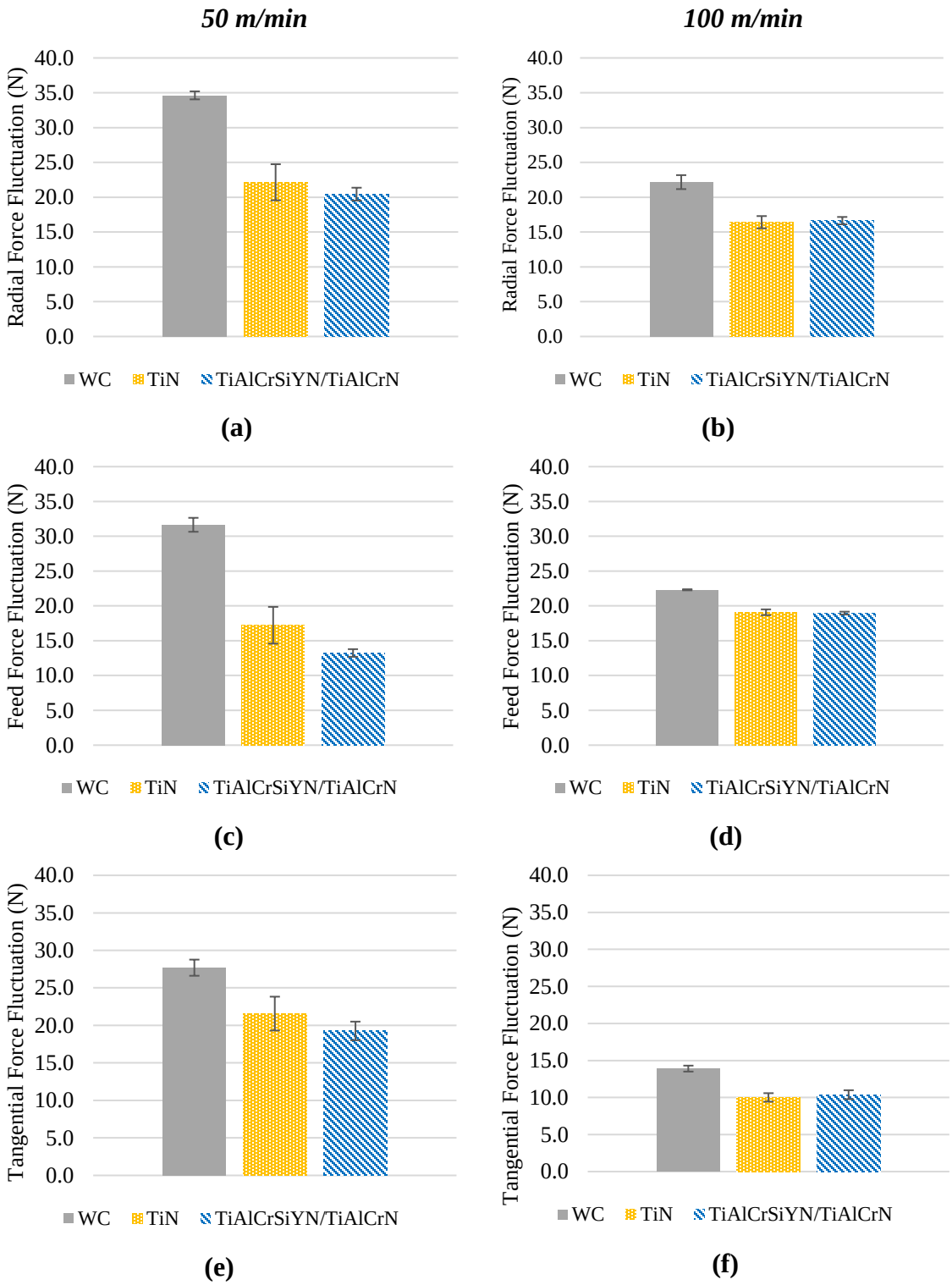

Figure 73: Fluctuation in cutting forces at 50 m/min (left) and 100 m/min (right)

7.3.2 Built-Up Edge Intensity

The average height of BUE adhered to the cutting inserts is presented in **Figure 74**, with the error bars denoting the standard deviation of measurements across three test replicates. Images of the BUE adhered to the cutting inserts after tests at 50 m/min are shown in **Figure 75**, showing the view from the rake face for all corners of the insert and the view from the flank face for select corners of the insert, denoted by the gold stars.

At 50 m/min, a sizeable BUE formed on the uncoated insert. Though still present, it was considerably smaller in size on the TiN-coated insert and virtually non-existent on the TiAlCrSiYN/TiAlCrN-coated insert (visible on only one of the three corners of the insert, or one of three test replicates – the actual height in this instance was 0.219 mm). At 100 m/min, BUE intensity was much less on all insert types, though it was still largest on the uncoated insert, followed by the TiN-coated insert (although error bars in BUE height on the two coated inserts overlap considerably). The BUE is an unstable phenomenon in cutting, growing and collapsing in a cyclical fashion, which likely explains this scatter.

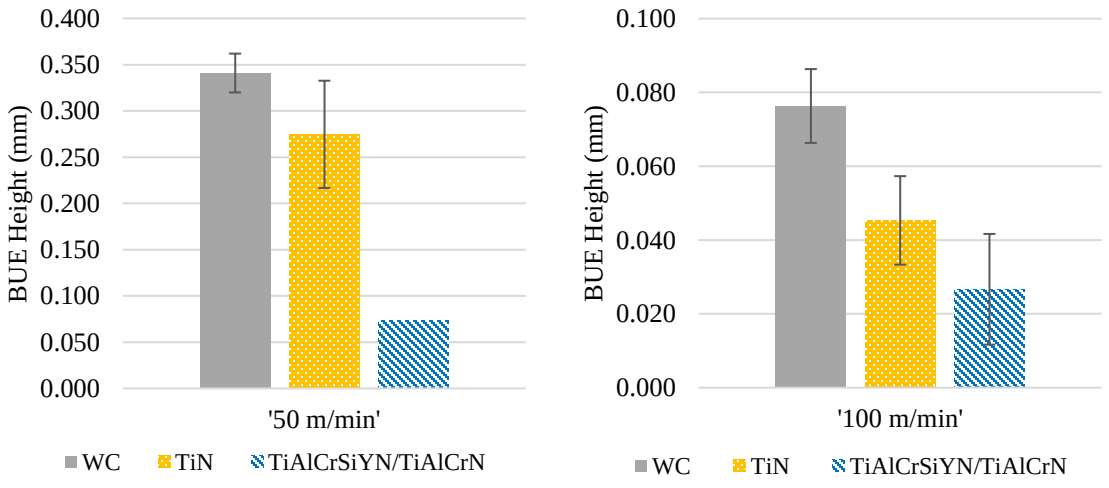

Figure 74: Average BUE height observed on inserts after tests at (a) 50 m/min and (b) 100 m/min

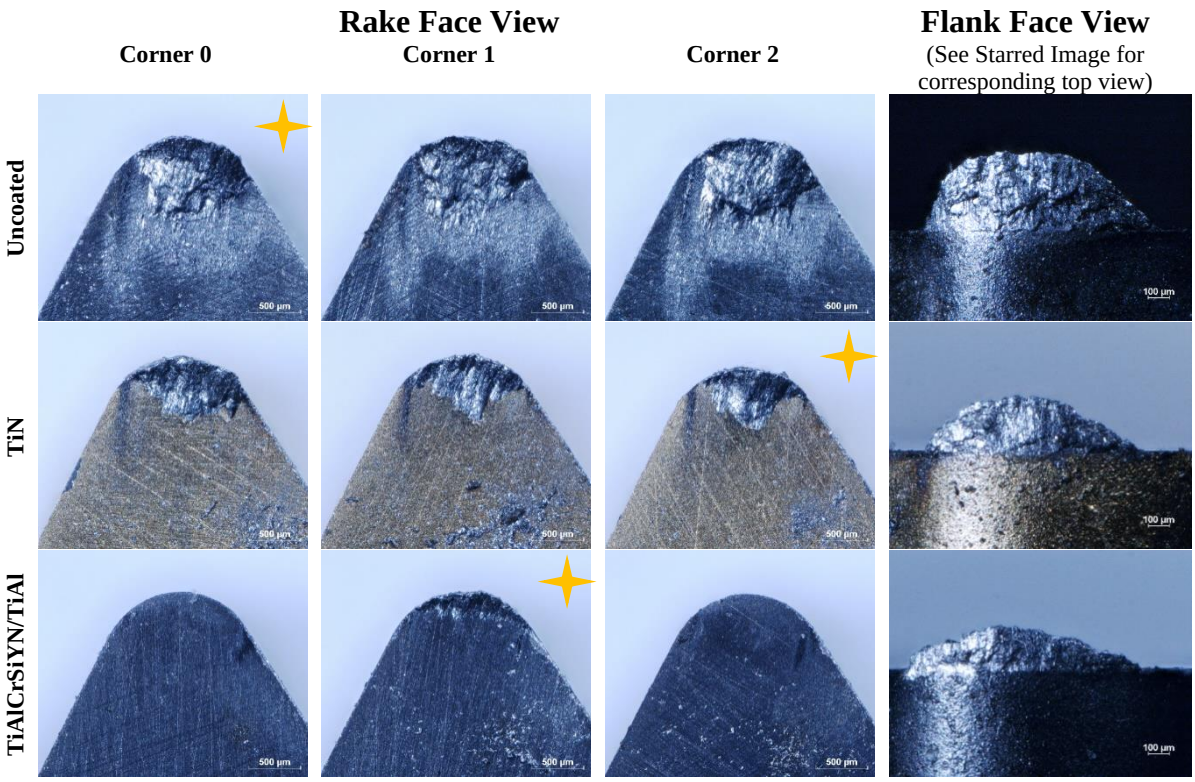

Figure 75: Differences in built-up edge intensity at 50 m/min cutting speed, as viewed from the rake face and the flank face

7.3.3 Chip Characteristics

Observations regarding the chip length, curl diameter as well as colour are detailed in **Table 15** and **Table 16** for turning tests performed at 50 m/min and 100 m/min, respectively. At the lower speed, it was noted that initial chips formed were short and tightly curled, becoming increasingly longer and exhibiting a larger curl diameter as cutting progressed. Of the different tool materials, the shortest and most tightly curled chips resulted from tests with the TiAlCrSiYN/TiAlCrN-coated insert, followed by the TiN-coated insert. Both of these inserts created chips that were gold/brown in colour. Chips produced by the uncoated inserts were much longer, possessed a larger curl diameter and exhibited a blue/purple hue with traces of gold.

At the higher cutting speed (100 m/min), all inserts generated long (>100 mm), continuous chips with a curl diameter noticeably larger and colours different than those chips resulting from tests at 50 m/min. Similar to the lower speed tests, chips produced by the TiN- and TiAlCrSiYN/TiAlCrN-coated inserts were the most tightly curled. However, they possessed a turquoise/silver appearance on the sliding surface and a dull blue/green appearance on the free surface. The uncoated inserts produced chips with a larger curl diameter, manifesting a grey sliding surface and dull indigo/blue free surface.

Table 15: Observations of chips collected after short duration tests at 50 m/min

Tool	**Chip Length (mm)**		**Chip Curl Dia. (mm)**		**Chip Colour**	
	Short	*Long*	*Short*	*Long*	*Sliding Surface*	*Free Surface*
WC	25 ± 4	52 ± 10	6.7 ± 0.5	6.7 ± 0.1	Gold/blue/purple	Blue/brown
TiN	3 ± 1	20 ± 7	5.6 ± 0.8	4.7 ± 0.4	Gold	Dull brown
TiAlCrSiYN/ TiAlCrN	2 ± 1	6 ± 2	4.5 ± 0.2	4.5 ± 0.2	Gold	Dull brown

Table 16: Observations of long, continuous chips collected after short duration tests at 100 m/min

Tool	**Chip Curl Dia. (mm)**	**Chip Colour**	
		Sliding Surface	*Free Surface*
WC	14.7 ± 0.5	Grey	Dull indigo
TiN	9.7 ± 0.5	Grey/turquoise	Dull blue/green
TiAlCrSiYN/TiAlCrN	9.5 ± 0.8	Grey/turquoise	Dull grey/blue

7.4 Discussion

The above results highlight noticeable differences in terms of cutting forces, BUE intensity and chip characteristics when turning AISI 1045 steel with different tool materials, namely uncoated as well as TiN- and TiAlCrSiYN/TiAlCrN-coated cemented tungsten carbide inserts. As a quick summary, turning with the coated inserts (particularly the TiAlCrSiYN-TiAlCrN) tended to yield lower and less fluctuations in forces; reduced BUE intensity; and shorter, more tightly curled chips.

Of the varying parameters that can affect forces in cutting, detailed previously in **Section 2.3**, only the cutting speed and the tool material were varied – the tool geometry remained unchanged, as did the work material and the cutting fluid (in this case, no fluid was applied). Interpreting the change of forces with changes in cutting speed is complicated in so much as a built-up edge of some size is present in all scenarios. As outlined in **Section 2.2.3**, the BUE tends to function as an extension of the tool edge, thereby its geometry changes the local rake angle, which has a known effect on forces in cutting.

Thus, within tests performed at the same cutting speed, it can be concluded that differences in the tool (or more specifically, the coating) material are responsible for differences in the cutting forces measured. However, observations of chip characteristics and BUE intensity as well as a knowledge of friction coefficient behaviour between these tool materials and AISI 1045 Steel (from **Chapter 4**) are necessary to help elucidate the underlying mechanism at play.

At 50 m/min, the reduction in cutting forces with the use of coated tools (**Figure 72**) correlates well with measurements of BUE height (**Figure 74**) and general observations of BUE size from the photographs shown in **Figure 75**. In other words, a smaller BUE correlates with smaller cutting forces. The same can generally be said when comparing cutting forces and BUE size for the same inserts cutting at 100 m/min as well, albeit the BUE are much smaller overall.

Intuitively, a smaller BUE will result from a tool exhibiting a lower friction coefficient in contact with the base work material, as a BUE is predicated on seizure between the tool and chip. Certainly, the results from tribometer tests reported earlier indicate that a reduced COF exists for TiN and TiAlCrSiYN/TiAlCrN coatings in contact with AISI 1045 Steel as compared with uncoated cemented tungsten carbide at temperatures above 500 °C (**Section 4.3.1**).

However, as discussed earlier in **Section 2.3.2**, the temperature at the tool-chip interface also plays an important role in BUE formation, the BUE tending to disappear as the tool-chip interface temperature exceeds a certain threshold, namely the recrystallization temperature of the work material. Likewise, as noted in **Section 2.3.4**, the tool thermal conductivity influences the temperature field at the tool-chip interface, a lower thermal conductivity tool (or coating, presumably) forcing more heat to remain in the chip. **Table 17** presents room temperature and elevated temperature thermal conductivity values for select tool materials with compositions similar to those used in the present study (Jawahir & van Lutterwelt, 1993), (Martan & Benes, 2012). WC possesses the highest thermal conductivity, followed by TiN.

Table 17: Reported thermal conductivity values for select tool materials

Tool Material	**Thermal Conductivity ($W \cdot m^{-1} \cdot K^{-1}$)**	
	25 °C	*400 °C*
WC (Jawahir & van Lutterwelt, 1993)	30	38
TiN (Jawahir & van Lutterwelt, 1993)	20	24
$Ti_{0.84}N$ (Martan & Benes, 2012)	22	25
$Ti_{0.52}Al_{0.48}N$ (Martan & Benes, 2012)	11	13
$Ti_{0.35}Al_{0.65}N$ (Martan & Benes, 2012)	4.6	5.2
$Cr_{0.50}Al_{0.41}Si_{0.09}N$ (Martan & Benes, 2012)	2.7	3.3

In actuality, **Eq. 6.5.3** (estimated based on Fransden & Williams (1991) and Williams (1991)) suggests the thermal conductivity of WC (with 6% Co) will be 2-3 higher than that reported for WC in the range of 25 to 400 °C (Jawahir & van Lutterwelt, 1993). Arguably, TiAlCrSiYN/TiAlCrN will possess a lower thermal conductivity than TiN, likely on a similar order as that of $Ti_{0.35}Al_{0.65}N$ and $Cr_{0.50}Al_{0.41}Si_{0.09}N$. It seems reasonable to believe that the thermal conductivity of TiN will be about 4 times smaller than that of WC-Co, and the thermal conductivity of TiAlCrSiYN/TiAlCrN about 5-6 times smaller than that of TiN, at elevated temperatures of 400 °C and above. Thus, the reduced forces and smaller BUE experienced when cutting with the TiN- and TiAlCrSiYN/TiAlCrN-coated inserts could just as likely reflect increased heat flow into the chip instead of into the tool, thereby softening the work material in the secondary shear zone.

Analysis of the chip characteristics becomes of great importance in discerning which of these two possible mechanisms is at work. Based on the works summarized in **Sections 2.3.4** and **2.3.6**, both mechanisms would tend to result in more tightly curled chips (the author is assuming that reduced affinity for adhesion between tool and chip due to intrinsic qualities in the coating would manifest in a similar way to the introduction of a lubricant). Thus, the more tightly curled chips produced when cutting with either of the coated inserts

does not point to one mechanism over the other. However, it stands to reason that reduced adhesion between tool and chip would result in lower tool-chip interface temperatures and thus lower temperatures on the undersurface of the chip. In contrast, a lower thermal conductivity tool/coating will result in higher temperatures at the tool-chip interface and chip undersurface. Thus, a means of distinguishing the temperature at the tool-chip interface and/or the chip undersurface becomes of critical importance.

One study in literature related the colour of the undersurface of steel chips from machining operations to the thickness of the oxide layer as well as an estimate of tool-chip interface temperature (Venkatesh, Zhou, Xue, & Quinto, 1993). This study concluded that chips with a golden-brown undersurface resulted from a cooler tool-chip interface than did chips exhibiting blue on their undersurface. Other researchers observed chips of a greenish colour when cutting steel at speeds higher than those which produced chips of a bluish colour (Ning, Rahman, & Wong, 2001), which suggests that green coloured chips result from a higher tool-chip interface temperature, cutting temperature being strongly dependent on cutting speed. A much earlier report (McAdam & Geil, 1939) noted that the sequence of interference colours that appear with increasing thickness of oxide layer on iron-based alloys is as follows: straw, light yellow or gold, golden brown, brown with reddish or purple tint, brownish purple, light purple, dark purple, dark blue, light blue, very light greenish blue with a silvery gray appearance. Complicating matters, this colour sequence is then repeated as oxide film thickness increases, albeit the colours are less brilliant and less easily distinguished from one another (the ring of coloured oxides surrounding the imprint corresponding to the test at **T = 798 °C** in **Figure 50** (**Chapter 5**) confirm this ordering

and repetition of colours, moving radially inward). For the moment, it is assumed that only the first instance of interference colours has been observed and reported in **Table 15** and **Table 16**.

Considering the chip colour observations for cutting tests at 50 m/min (**Table 15**), chips from the TiN- and TiAlCrSiYN/TiAlCrN-coated inserts (gold coloured undersurface) likely encountered a cooler tool-chip interface compared with chips from the uncoated inserts (blue/purple undersurface). This would suggest reduced adhesion between tool and chip is the dominant mechanism, consistent with friction measurements on the tribometer.

Considering the chip colours observed from tests at 100 m/min (**Table 16**), it is evident that the chip undersurface for all three inserts was higher than what was experienced at 50 m/min, which is to be expected. However, it is unclear whether the grey/turquoise chip undersurface corresponding to the coated inserts denotes a higher temperature than the grey chip undersurface associated with the uncoated insert. Both appear to align closely with the last interference colour in the sequence identified by McAdam & Geil (1939).

The temperature associations with chip colour (830 °C to 980 °C) reported by Venkatesh, Zhou, Xue & Quinto (1993) are somewhat higher than the range of temperatures tested on the tribometer wherein differences in friction coefficient across the surface treatments was evident (550 °C to 800 °C). It is quite likely that the differences in friction coefficient persist in the range of 800 °C to 1000 °C, but friction data in this temperature range was not obtained. Furthermore, it is worth pointing out differences in the cutting conditions used in the tests. Venkatesh, Zhou, Xue & Quinto (1993) performed dry turning of AISI 1018 (lower strength than AISI 1045) under more aggressive cutting

parameters (216 m/min, 0.25 mm/rev, 2.5 mm depth of cut) using coated inserts with chip control features. It is anticipated that a tendency towards lower tool-chip interface temperatures involving the cutting of lower strength steel with chip control features would not outweigh the tendency towards higher tool-chip temperatures involved with increased cutting speed and, to a lesser extent, depth of cut. Thus, lower tool-chip interface temperatures (< 800 °C) seem reasonable to expect for the cutting conditions explored in this work.

In comparing the average and fluctuations in cutting forces as well as the built-up edge and chip characteristics between TiN- and TiAlCrSiYN/TiAlCrN-coated inserts for cutting tests at 100 m/min, admittedly there are very negligible differences. If the lower thermal conductivity of the coating layer is the driving mechanism behind the reduced cutting forces, BUE and more tightly curled chips resulting from cutting tests at 100 m/min with the coated inserts, then one could argue that differences in forces, BUE and chip characteristics ought also to be evident between the two coatings themselves, given that TiAlCrSiYN/TiAlCrN is reasoned to have a thermal conductivity approximately 5-6 times lower than that of TiN.

First of all, it should be emphasized that the thermal conductivity of TiAlCrSiYN/TiAlCrN is not known. That it is lower than that of WC-Co by at least a similar magnitude as that of TiN is undisputable. That it is lower than that of TiN is highly probable, given lower thermal conductivity values reported in (Martan & Benes, 2012) for coatings of similar composition.

Secondly, the COF for TiAlCrSiYN/TiAlCrN is lower than that of TiN at elevated temperatures and appears to decrease with further increases in temperature. Thus, it stands to reason that increases in tool-chip interface temperature driven by the lower thermal conductivity of TiAlCrSiYN/TiAlCrN would be counteracted to some degree by reduced tool-chip friction at elevated temperatures, which would tend to reduce the rate of heat generation at the tool-chip interface.

It should be emphasized that both mechanisms (tool-chip adhesion as well as tool (coating) thermal conductivity) are expected to have a certain influence on the resulting cutting forces, BUE and chip characteristics when using a different tool material to cut a work material under otherwise identical conditions. In many ways, decoupling these two mechanisms is extremely difficult, but the above analyses have attempted to estimate which of the two may be more dominant in contributing to the differences observed under the conditions explored.

7.5 X-ray Photoelectron Spectroscopic Analysis of Coated Pin and Cutting Inserts

In order for tribometer test results to correlate with machining results, for a given set of tool and work materials, then tribochemical reactions occurring at the pin-disc interface on the tribometer should likewise occur at the tool-chip interface in machining. X-ray Photoelectron Spectroscopy (XPS) was employed to study changes in Al and Cr bonds on the surface of a TiAlCrSiYN/TiAlCrN-coated pin and insert employed in the tests, as compared with the signature of an unused TiAlCrSiYN/TiAlCrN-coated insert. This spectroscopic method is capable of analyzing the chemical constituents and discerning

shifts in the associated binding energies within a very thin layer of the surface under study, on the order of a few tens of nanometers.

A Physical Electronics, Inc. (PHI) Quantera II spectrometer was used for XPS analysis, comprising a hemispherical energy analyzer, an Al anode source for X-ray generation, and a quartz crystal monochromator for focusing the generated X-rays. The X-ray source was monochromatic Al K-α (1486.7eV), operated under a base pressure between 1.0x10-9 to 2.0x10-8 Torr. Samples were sputter-cleaned for 2-5 minutes with a 4kV Ar+ beam before collecting the data, to remove carbon-based surface contaminants. The beam diameter for data collection was 200 μm, and all spectra were obtained at a 45˚ take off angle. A dual beam charge compensation system was utilized to ensure neutralization of all samples. The pass energy to obtain high resolution data was 55eV. The instrument was calibrated with a freshly cleaned Ag reference foil, where the Ag 3d5/2 peak was set to 368eV. Data analysis was performed in PHI Multipak software (version 9.4.0.7).

High resolution spectra of the Al2p Al2s, and Cr2p peaks are presented in **Figure 76**, **Figure 77** and **Figure 78**, respectively, along with a summary of the binding energies, relative area and proposed assignments associated with the fitted peaks. The assignments were based on consultation of reported binding energies for known chemical bonds, as obtained from the NIST X-Ray Photoelectron Spectroscopy Database (Naumkin, Kraut-Vass, Gaarenstroom, & Powell, 2012) and summarized in **Table 18**. However, these should be viewed as guidelines only. Emphasis is made on qualitative changes in the nature of the peaks between the unused insert, representative of the as-deposited coating, and the used pin and insert. The pin was used in successive tests under 200 N load, 110 A of current

and 60 s rotation in contact with AISI 1045 steel. The insert was used to cut AISI 1045 steel under the conditions reported earlier in this section, approx. 10 s at 50 m/min cutting speed followed by 10 s at 100 m/min cutting speed.

Both underlying Al2p peaks in the unused insert (**Figure 76a**) shift to slightly higher and identical binding energies in the spectra obtained from the used pin (**Figure 76b**) and used insert (**Figure 76c**). Higher binding energies in the Al2p peak are characteristic of bonding with oxygen, suggesting the formation of aluminum oxide like tribofilm films. The ratio of the area beneath the two peaks is quite similar for both the used pin and used insert, albeit the spread of the higher binding energy peak in the pin appears slightly broader. The exact nature of these aluminum-containing oxides is unclear. Binding energies ranging from 73.6 eV to 75.9 eV have been detected in Al_2O_3 samples of various types, the majority confined between 74.0 eV and 74.7 eV. A range of mixed oxides containing Al, Si and O in varying stochiometric ratios have also manifested binding energies in the range of 74.3 eV to 74.9 eV.

Analysis of the Cr 2p peaks (**Figure 78**) is less conclusive. The lowest binding energy of the fitted 2p 3/2 peaks falls within the range associated with metallic Cr in all three samples, although the binding energy increases slightly and the relative magnitude of this peak decreases in both the used insert and used pin samples relative to the unused insert.

The second lowest binding energy of fitted 2p 3/2 peaks most likely reflects CrN. This peak shifts to a slightly lower binding energy in the used insert and a slightly higher binding energy in the used pin, but the relative area beneath the peak increases for both samples relative to the unused insert.

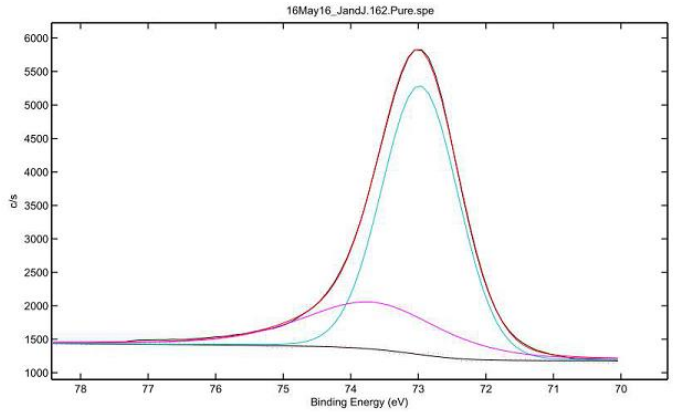

Energy	Assignment	%
73.0	Al	73.2
73.7	Al_2O_3	26.8

Sample: *rake face of unused cutting insert*

(a)

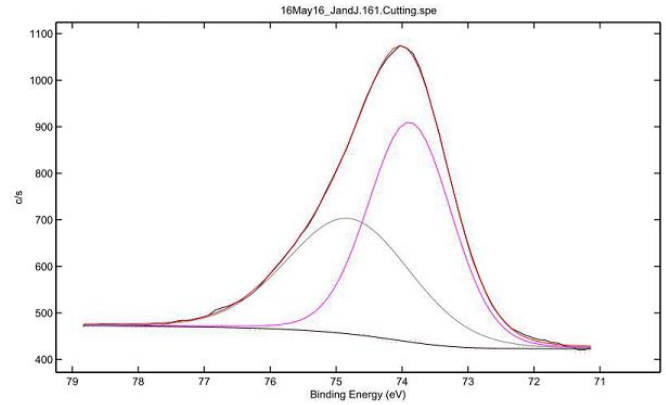

Energy	Assignment	%
73.9	Al_2O_3	56.2
74.8	Al_2O_3	43.8

Sample: *rake face of used cutting insert*

(b)

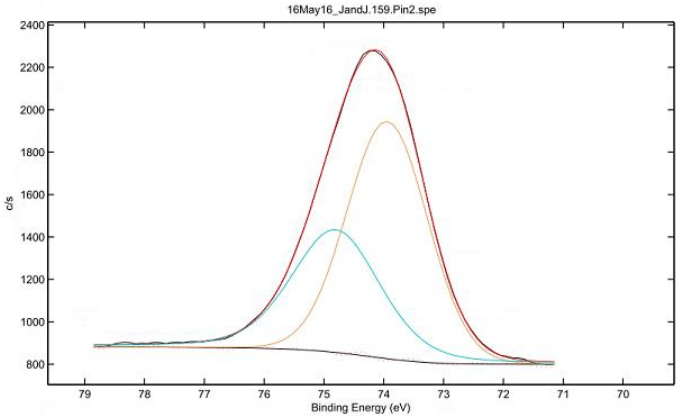

Energy	Assignment	%
73.9	Al_2O_3	60.9
74.8	Al_2O_3	39.1

Sample: *pin tip after friction tests*

(c)

Figure 76: High-resolution XPS spectra obtained at the Al2p peak on different TiAlCrSiYN/TiAlCrN coated samples

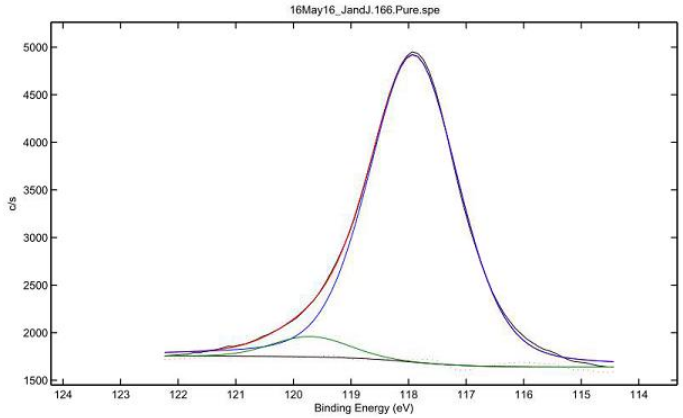

Energy	Assignment	%
117.9	Al	95.3
119.7	Al_2O_3	4.8

Sample: *rake face of unused cutting insert*

(a)

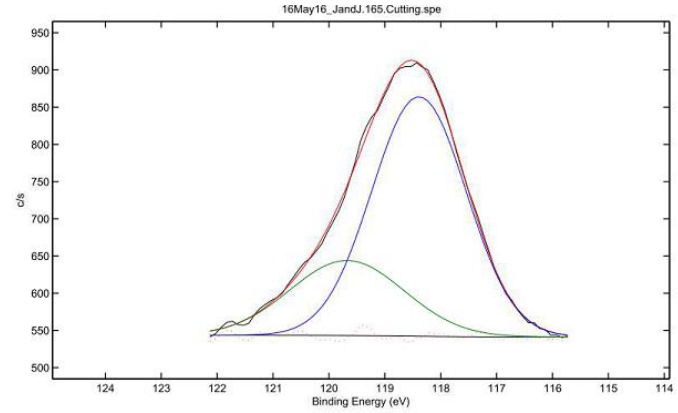

Energy	Assignment	%
118.4	Al_2O_3	72.5
119.7	Al_2O_3	27.5

Sample: *rake face of used cutting insert*

(b)

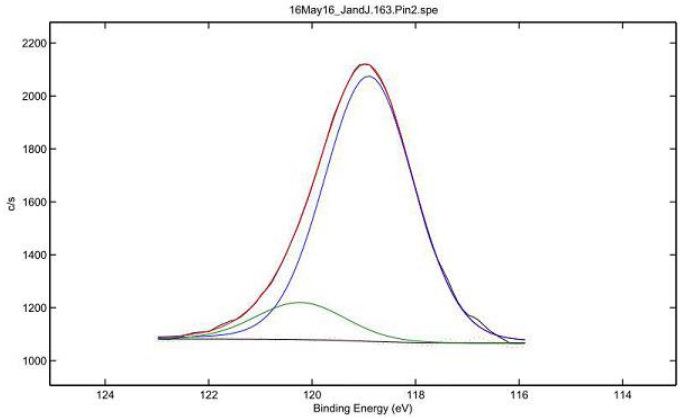

Energy	Assignment	%
118.9	Al_2O_3	87.9
120.2	Al_2O_3	12.1

Sample: *pin tip after friction tests*

(c)

Figure 77: High-resolution XPS spectra obtained at the Al2s peak on different TiAlCrSiYN/TiAlCrN coated samples

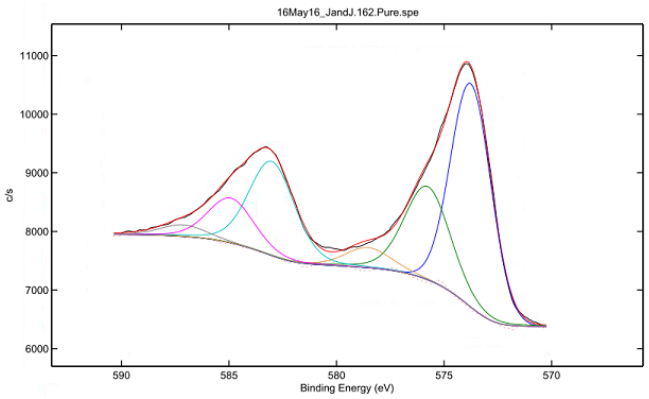

Energy	Assignment	%
573.8	Cr	40.6
575.8	CrN	21.0
578.5	CrO_3	4.5
583	Cr	21.2
584.9	?	10.1
587.1	CrO_3?	2.6

Sample: *rake face of unused cutting insert*

(a)

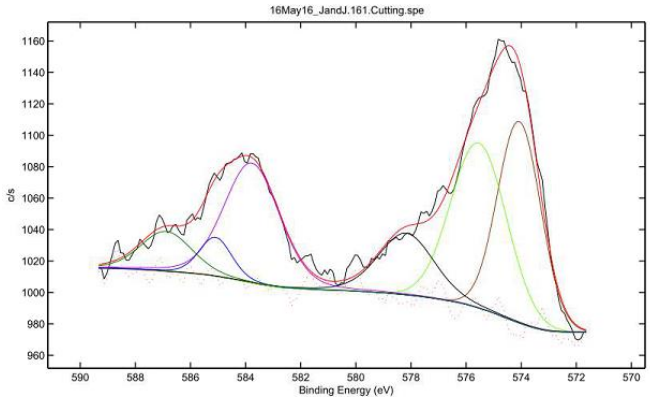

Energy	Assignment	%
574	Cr	26.7
575.5	CrN	28.2
578.2	CrO_3	11.6
583.8	Cr	22.4
585	?	4.2
586.9	CrO_3?	6.9

Sample: *rake face of used cutting insert*

(b)

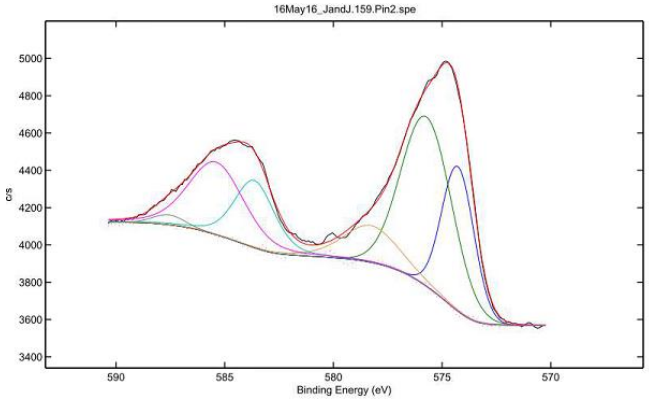

Energy	Assignment	%
574.3	Cr	19.8
575.7	CrN	36.4
578.3	CrO_3	9.9
583.6	Cr	13.1
585.4	?	19.5
587.6	?	1.3

Sample: *pin tip after friction tests*

(c)

Figure 78: High-resolution XPS spectra obtained at the Cr2p 1/2 and 3/2 peaks on different TiAlCrSiYN/TiAlCrN coated samples

Table 18: Binding energies and assignments reported in the NIST X-Ray Photoelectron Spectroscopy Database

Peak	Assignment	Binding Energy (eV)
Al2p	Al (metal)	72.5 – 72.9
	AlN	73.1, 73.5
	Al_2O_3	73.7 – 74.8
Al2s	Al (metal)	117.9 – 118.2
	AlN	115.5, 119.4
	Al_2O_3	118.7 – 119.5
Cr2p ½	Cr (metal)	583.5
	Cr2N	-
	CrN	-
	CrO2	-
	Cr2O3	586.0 – 586.4
	CrO3	-
Cr2p 3/2	Cr (metal)	573.8 – 574.3
	Cr2N	574.8, 576.1
	CrN	575.6 – 575.8
	CrO2	575.5, 576.3
	Cr2O3	575.9 – 577.3
	CrO3	578.3 – 580.1

The final fitted 2p 3/2 peak likely corresponds to CrO_3 or some non-stochiometric version of similar ratio. The binding energies decrease slightly but the relative area beneath the peak more than doubles for both the used insert and the used pin relative to the unused insert. There are some changes in the binding energies and relative area beneath the fitted 2p ½ peaks as well, but there appears to be much less reported in literature regarding assignment of these peaks, so they will not be discussed.

The sum of the area beneath the 2p 3/2 peaks adds to 66.1 – 66.5 % for all three samples. Thus, there is a clear reduction in metallic-like Cr and a doubling of CrO3-like oxides present on both the insert used in cutting trials as well as the pin used during tribometer tests.

Regardless of the exact assignment of fitted peaks within the Al 2p and Cr 2p spectra, it appears that transformation in the surface chemistry on a TiAlCrSiYN/TiAlCrN-coated pin used in tribometer tests is qualitatively similar to those changes manifesting on the rake face of a TiAlCrSiYN/TiAlCrN-coated insert used in cutting trials.

7.6 Conclusion

Evidence for reduced tool-chip adhesion in the cutting of AISI 1045 steel with coated inserts (notably TiAlCrSiYN/TiAlCrN and TiN) relative to the uncoated substrate (WC-Co), supported by tribometer tests reported in **Chapter 4**, was carefully studied, analysing cutting force components, built-up edge formation and characteristics of the resultant chips. The possibility that changes in tool thermal conductivity introduced by the PVD coatings were a contributing and even dominating factor in the observed changes in machining outputs was also carefully considered. Analysis of the colour of the chip undersurface, indicative of the thickness of oxide species formed during the brief moments of elevated temperatures prior to cooling, played a primary role in deciding between these conflicting mechanisms.

The main findings from this study are as follows:

- At 50 m/min cutting speed, reduced tool-chip adhesion is thought to be primarily responsible for the reduction in cutting force components, BUE formation and chip curl radius observed when cutting with either of the coated inserts, since the colour of chip undersurface suggests a thinner layer of oxide

formation associated with cooler temperatures that would arise from reduced adhesion.

- At 100 m/min cutting speed, differences in the colour of chip undersurface were also noted across the trials featuring different tool (coating) materials; however, interpretation as to the relative temperature of the chip undersurface is unclear.
- Transformations in the surface chemistry of a TiAlCrSiYN/TiAlCrN-coated pin used in friction tests against AISI 1045 steel on the tribometer are qualitatively similar to those on a TiAlCrSiYN/TiAlCrN-coated insert used in cutting trials against the same work material: a decrease in metallic bonds and an increase in metal-oxide bonds appears evident in both Al 2p and Cr 2pspectra, suggesting formation of Al- and Cr-based oxides, but particularly Al-based ones.

8. CONCLUSIONS AND RECOMMENDATIONS

8.1 Restatement of Objectives

As stated in **Section 1.2**, the objectives of the research presented in this dissertation were as follows:

i) Increase the understanding of the evolution of the contact zone between pin and disc, both macroscopically and microstructurally, during on-axis rotation pin-on-disc tribometer tests under varying operating conditions;

ii) Establish a means of more accurate estimation of the temperature at the contact zone during an on-axis rotation pin-on-disc tribometer test, which is physically inaccessible for direct measurement; and

iii) Study the correlations between the outputs of on-axis rotation pin-on-disc tribometer tests with those of metal cutting processes featuring the same tool (substrate + coating) and work material pair.

8.2 Summary of Contributions in Fulfillment of Research Objectives

With respect to the aforementioned objectives, the contributions and main conclusions of this research work are summarized below.

8.2.1 Key Findings with regards to Objective 1

The imprint formed in the disc experiences considerable growth during the rotation stage of on-axis pin-on-disc tribometer tests, which is the stage wherein adhesive interactions between pin and disc occur and a coefficient of friction is evaluated. The majority of growth occurs during the first half revolution of the disc about the pin. Growth

decays during the second half revolution and is relatively negligible beyond the first complete revolution. Such behaviour was observed in different materials, both room temperature and elevated temperatures. Presumably, such behaviour would also occur over a range of loads, but this was not systematically explored.

Tests exhibiting a higher value of peak torque correlate with a larger diameter imprint characterized with a greater abundance of adhesive wear marks. This was observed both at ambient and elevated temperatures, specifically under heavy load conditions.

Considerable pile-up of material occurs at the periphery of the imprint, such that the diameter of the imprint evaluated at the top of the pile-up can exceed the diameter evaluated at the plane surface of the disc by upwards of 40%. Accordingly, care needs to be taken in reporting the method used to evaluate the imprint diameter, as this parameter directly influences the evaluation of friction coefficient.

Different torque-time as well as temperature-time signatures can manifest depending on the nature of adhesive interaction and test conditions applied; however, torque and temperature signals tend to stabilize during the second revolution of the disc about the pin, making it a suitable portion of the test during which to evaluate the friction coefficient.

At the surface of the imprint, two distinct zones can be observed, as revealed by SEM analysis: an inner zone, characterized by a lack of oxygen and a topography that mirrors that of the pin tip, suggesting ‘seizure’ of the pin to the disc; and an outer zone, featuring significant oxygen and circular striations, likely the result of strain hardened asperities of adhered material ploughing through the bulk of work material in these regions of the disc.

Below the disc surface, shear deformation patterns (or the absence thereof) in the work material immediately surrounding the imprint reveal clues as to the severity of adhesive interaction between pin and disc and whether bulk material shear or surface friction conditions dominated the test.

The electrical resistivity of any coating deposited on the pin has a significant effect on the resulting test temperature (measured 2 mm above the pin-disc interface) for a given set of test conditions. Evidence was presented suggesting that tests involving a pin with a coating of greater electrical resistivity feature a higher pin-disc interface temperature despite the test temperature being similar to tests performed with uncoated or coatings with a lower electrical resistivity. If true, this raises the question as to how to compare COF vs. Temperature plots for coatings (or pin surface treatments) of considerably different electrical resistivity.

8.2.2 Key Findings with regards to Objective 2

A numerical model was developed to estimate the pin-disc interface temperature during stationary specimen tests involving a given tool-work material pair. The model requires inputs from empirical tests, specifically the resulting imprint diameter, the magnitude of electrical current used and the temperature at as well as voltage between different locations along the test specimens. The latter provides a basis for evaluating the accuracy of the model estimation, since the properties of surface films (oxides and/or contaminants) present at the pin-disc interface are unknown. These properties (specifically, the electrical resistivity of these surface films, for an assumed thickness and contact ratio) must be tuned

iteratively, comparing the model outputs of temperature and electrical voltage (more specifically, electrical resistance) at or between defined locations along the specimens with equivalent empirical measurements.

For a handful of test conditions, simulations were generated that realized agreement with empirical measurements of temperature and electrical resistance with less than 10% error (for 4 of 5 outputs); however, the electrical resistance between the top of the disc and the start of the cylindrical portion of the disc was consistently underestimated in these simulations, the error increasing from 13% to 35% for increasing test temperature (corresponding to increasing levels of electrical current). For these same simulations, the estimated pin-disc interface temperature was higher than the test temperature, this difference increasing as the electrical current increased. The exact accuracy of this estimation is unknown, but it is believed to be of a similar magnitude to the errors in predicting the known outputs (i.e., 10%).

In theory, the model can be used to predict the pin-disc interface temperature for tests involving coated pins as well. However, knowledge of the electrical and thermal conductivity of the coating layer should be obtained first, to reduce the number of variables that need to be tuned in order to achieve agreement between simulations and empirical tests.

The accuracy of the above simulations depends in part on an empirical model for the variation of the electrical resistivity of WC-6%Co with temperature, over the range of approximately 100-700 °C. Such a relationship was not available in the literature and was developed based on the temperature and voltage measurements obtained during stationary specimen tests performed on the tribometer.

8.2.3 Key Findings with regards to Objective 3

A correlation between on-axis rotation pin-on-disc tribometer tests and machining tests was identified for (coated) cemented tungsten carbide and AISI 1045 steel. Specifically, coatings that exhibited a lower coefficient of friction at elevated temperatures on the tribometer resulted in various manifestations of reduced tool-chip adhesion when applied to cutting inserts subjected to short duration turning tests. Notably, these coatings resulted in reduced cutting force components, reduced built-up edge intensity, and more tightly curled chips. Qualitative similarities in tribofilm formation on the rake surface of cutting inserts used in the turning tests and the tip of pins subjected to tribometer tests were also identified, strengthening the correlation between tribometer and machining results.

It was identified from literature that coatings with a reduced thermal conductivity may have a similar effect as reduced tool-chip adhesion on these key machining outputs. Accordingly, care needs to be taken to distinguish between mechanisms. To this end, comparison of the colour of the oxide layer formed on the undersurface of the chip resulting from cutting with inserts of different surface treatments was utilized, the colour of the chip reflecting the thickness of the oxide layer formed and thereby the relative temperature achieved at the tool-chip interface. A cooler chip is anticipated as a result of reduced tool-chip adhesion, whereas a hotter chip is expected when the low thermal conductivity of the coating forces more heat into the chip, reducing the flow stress in the secondary shear zone.

8.3 Recommendations for Further Work

8.3.1 Refinement of the Thermal Model, Experimental Methods to Support it, and Implementation in More Efficient Software

The numerical model developed in **Chapter 6** was a first attempt at predicting the temperature distribution in the pin and disc during a stationary specimen test. In the absence of available temperature-dependent electrical resistivity and thermal conductivity data for the PVD coating under investigation (TiAlCrSiYN/TiAlCrN), simplifying assumptions were made. The accuracy and reliability of the model could likely be improved by obtaining such data through available experimental techniques, which may allow for better estimation of the pin-disc interface temperature.

Due to the significant influence of electrical contact resistance on the predicted temperature distribution, experimental tests involving temperature and electric potential (voltage) measurements at various points along the pin and disc will still be required in order to tune the model to achieve good agreement between simulation and experimental results. Improvements in such an experimental setup would be prudent, suggestions for which follow.

Use of multiple infrared pyrometers, each aimed at a spot of black constant emissivity paint applied to different discrete locations along the pin length (e.g., top, middle, bottom), is likely a preferred approach to temperature measurement as compared to the use of a thermal camera, given the limited temperature range of the lenses/sensors contained therein. Alternatively, investment in a newer, higher temperature range and higher sensitivity thermal camera may be effective. The advantage of measuring at discrete

locations with different pyrometers is likely increased precision in measuring and defining the location of these temperature measurements relative to the pin tip, which is more difficult with a thermal camera. The disadvantage of the multiple pyrometer approach is the greater involvement in calibrating and aligning the measurements of multiple instruments.

Likewise, a means of simultaneously monitoring and recording electric potential drop between discrete locations along the specimens for the entire duration of the test would be beneficial, offering both more information as to the changes in these values over the duration of the test as well as increasing confidence in the location of and the distance between these measurement locations. These would synergistically improve confidence in electrical resistance calculations and also support greater accuracy in relating electrical resistance measurements to temperature measurements, enabling a more accurate model for the temperature-dependence of the electrical resistivity of the pin substate material.

Lastly, implementing the numerical model into a different software platform is advisable for continued work. Matlab or even Finite Element software would likely enable greater efficiency in simulation execution as well as greater ease in modifying the model.

8.3.2 Studies on the Oxide Thickness on the Chip Undersurface and Evaluation of the Colour of Chip Undersurface as a function of Cutting Speed

Both reduced tool-chip adhesion as well as lower tool thermal conductivity can have similar effects on machining outputs, making it difficult to distinguish which mechanism is at play. Knowledge of the thickness and thermal conductivity of the coatings, over a

range of elevated temperatures, may be of some assistance. However, evaluation of the thickness of oxide layer on the underside of the chips is the most direct approach, as it stands to reason that a thicker oxide layer would result from a more elevated tool-chip contact temperature.

Evaluation of the colour of the undersurface of the chips as a function of cutting speed may also prove useful, as it stands to reason that increased cutting speed will tend to result in a higher tool-chip contact temperature. However, appreciable changes in the colour of the chip undersurface may evolve rather slowly with increasing cutting speed, depending on the rate of oxidation of the material being cut. This has been the author's experience during cutting trials with stainless steel, known for its oxidation resistance.

8.3.3 Comparative Tribofilm Studies on the Pin Tip and Cutting Insert

Preliminary comparison of tribofilm formation on the tip of a pin used during on-axis rotation pin-on-disc tribometer experiments with those formed on the rake face of a cutting insert used during cutting tests was presented in **Chapter 7**. While qualitative similarities were observed, it is recommended that a more in-depth study be performed, sampling multiple locations on multiple specimens, subjected to a broad range of test conditions. Such a study would further increase confidence in relating the results of tribometer tests to the results of machining trials, possibly providing guidance as to what range of temperature-dependent COF data ought to be used when comparing the performance of different coatings under specific cutting conditions.

LIST OF REFERENCES

Balaji, A. K., Sreeram, G., Jawahir, I. S., & Lenz, E. (1999). The effects of cutting tool thermal conductivity on tool-chip contact length and cyclic chip formation in machining with grooved tools. *Annals of the CIRP, 48*(1), 33-38.

Bandyopadhyay, B. P. (1984). Mechanisms of formation of built-up edge. *Precision Engineering, 6*(3), 148-151. doi:10.1016/0141-6359(84)90115-6

Bay, N., & Wanheim, T. (1976). Real area of contact and friction stress at high pressure sliding contact. *Wear, 38*(2), 201-209.

Beake, B. D., Fox-Rabinovich, G. S., Losset, Y., Yamamoto, K., Agguire, M. H., Veldhuis, S. C., . . . Kovalev, A. I. (2012). Why can TiAlCrSiYN-based adaptive coatings deliver exceptional performance under extreme frictional conditions? *Faraday Discussions, 156*, 267-277. doi:10.1039/C2FD00131D

Biksa, A. (2010). *Tribological characterization of surface engineered tooling.* Hamilton, ON, Canada: McMaster University.

Biksa, A., Yamamoto, K., Dosbaeva, G., Veldhuis, S. C., Fox-Rabinovich, G. S., Elfizy, A., . . . Shuster, L. S. (2010). Wear behavior of adaptive nano-multilayered AlTiN/MexN PVD coatings during machining of aerospace alloys. *Tribology International, 43*(3), 1491-1499. doi:10.1016/j.triboint.2010.02.008

Bonnet, C., Valiorgue, F., Rech, J., Claudin, C., Hamdi, H., Bergheau, J. M., & Giles, P. (2008). Identification of a friction model - Application to the context of dry cutting

of an AISI 316L austenitic stainless steel with a TiN coated carbide tool. *International Journal of Machine Tools and Manufacture, 48*, 1211-1223.

Boyd, J. M. (2012). *Tribometer-based quantifying of friction in metal cutting.* Hamilton: McMaster University.

Boyd, J. M., & Veldhuis, S. C. (2016). Manifestations of reduced tool-chip friction during turning of AISI 1045 steel with PVD-coated carbide inserts. *The International Journal of Advanced Manufacturing Technology*, 1-12. doi:10.1007/s00170-016-9775-x

Callister, J., W. D. (2003). 10. Phase Transformations in Metals: Development of Microstructure and Alteration of Mechanical Properties. In *Materials Science and Engineering: An Introduction* (pp. 298-331). John Wiley & Sons, Inc.

Childs, T. H. (1972). Rake Face Action of Cutting Lubricants: An Analysis of, and Experiments on, the Machining of Iron Lubricated by Carbon Tetrachloride. *Proceedings of the Institution of Mechanical Engineers, 186*(63), 717-727.

Chowdhury, M., Bose, B., Yamamoto, K., Shuster, L. S., Paiva, J., Fox-Rabinovich, G. S., & Veldhuis, S. C. (2020). Wear performance investigation of PVD coated and uncoated carbide tools during high-speed machining of TiAl6V4 aerospace alloy. *Wear, 446-447*. doi:10.1016/j.wear.2019.203168

Chowdhury, M., Chowdhury, S., Yamamoto, K., Beake, B., Bose, B., Elfizy, A., . . . Veldhuis, S. C. (2017). Wear behaviour of coated carbide tools during machining of Ti6Al4V aerospace alloy associated with strong built up edge formation. *Surface and Coatings Technology, 313*, 319-327. doi:10.1016/j.surfcoat.2017.01.115

Claudin, C., Mondelin, A., Rech, J., & Fromentin, G. (2010). Effects of straight oil on friction at the tool-workmaterial interface in machining. *International Journal of Machine Tools and Manufacture, 50*, 681-688.

Donnet, C., & Erdemir, A. (2004). Historical developments and new trends in tribological and solid lubricant coatings. *Surface and Coatings Technology, 180-181*, 76-84. doi:10.1016/j.surfcoat.2003.10.022

EMT 100. (n.d.). Retrieved December 2, 2015, from Extramet: https://extramet.net/tungsten-carbide-grades/

Fox-Rabinovich, G. (2008). Translation of Select Content by L. S. Shuster on the Operating Principles of the Adhesiometer.

Fox-Rabinovich, G. S., Beake, B. D., Yamamoto, K., Aguirre, M. H., Veldhuis, S. C., Dosbaeva, G., . . . Shuster, L. S. (2010). Structure, properties and wear performance of nano-multilayered TiAlCrSiYN/TiAlCrN coatings during machining of Ni-based aerospace superalloys. *Surface and Coatings Technology, 204*(21-22), 3698-3706. doi:10.1016/j.surfcoat.2010.04.050

Fox-Rabinovich, G. S., Kovalev, A. I., Shuster, L. S., Bokiy, Y. F., Dosbaeva, G. K., Wainstein, D. L., & Mishina, V. P. (1997). Characteristic features of alloying HSS-based deformed compound powder materials with consideration for tool self-organization at cutting 1. Characteristic features of wear in HSS-based deformed compound powder materials at cutting. *Wear, 206*, 214-220.

Fransden, M. V., & Williams, W. S. (1991). Thermal Conductivity and Electrical Resistivity of Cemented Transition-Metal Carbides at Low Temperatures. *Journal of the American Ceramic Society, 76*(6), 1411-1416. doi:10.1111/j.11

Friedman, M. Y., & Lenz, E. (1970). Investigation of the tool-chip contact length in metal cutting. *International Journal of Machine Tool Design and Research, 10*, 401-416.

Friedman, M. Y., & Lenz, E. (1973). The effect of thermal conductivity of tool material on cutting forces and crater wear rate. *Wear, 25*, 39-44.

Ghasemi, R., & Elmquist, L. (2014). A study on graphite extrusion phenomenon under the sliding wear response of cast iron using microindentation and microscratch techniques. *Wear, 320*(15), 120-126. doi:10.1016/j.wear.2014.09.002

Global Metal Cutting Tools Market 2017-2021. (2017, January). (Technavio) Retrieved October 14, 2019, from Technavio: https://www.technavio.com/report/global-tools-and-components-global-metal-cutting-tools-market-2017-2021

Grzesik, W., Nieslony, P., & Bartoszuk, M. (2009). Modeling of the cutting process analytical and simulation methods. *Advances in Manufacturing Science and Technology, 33*(1), 5-29.

Halim, S. T. (2008). *Finite element modeling of the orthogonal metal cutting process: modeling the effects of coefficient of friction and tool holding structure on cutting forces and chip thickness.* Hamilton: McMaster University.

Heaney, M. B. (2003). Electrical Conductivity and Resistivity. In J. G. Webster (Ed.), *Electrical Measurement, Signal Processing, and Displays.* CRC Press.

Jaspers, S., & Dautzenberg, J. (2002). Material behaviour in conditions similar to metal cutting: flow stress in the primary shear zone. *Journal of Materials Processing Technology, 122*, 322-330.

Jawahir, I. S., & van Lutterwelt, C. A. (1993). Recent developments in chip control: Research and applications. *CIRP Annals, 45*(1), 659-693.

Khoei, A. A. (2019). *A Method for Assessing the Tribological Performance of Tool and Workpiece Interactions.* Hamilton: McMaster University. Retrieved from http://hdl.handle.net/11375/24580

Konicek, A. R., Grierson, D. S., Sumant, A. V., Friedmann, T. A., Sullivan, J. P., Gilbert, P. U., . . . Carpick, R. W. (2012). Influence of surface passivation on the friction and wear behaviour of ultrananocrystalline diamond and tetrahedral amorphous carbon thin films. *Physical Review B, 85*. doi:10.1103/PhysRevB.85.155448

Konopka, J. (2013). *Options for Quantitative Analysis of Light Elements by SEM/EDS.* Thermofisher Scientific.

Kramer, B. M., & Judd, P. K. (1985). Computational design of wear coatings. *Journal of Vacuum Science & Technology, 3*(6), 2439-2444.

Machine Tools Market: Global Industry Trends, Share, Size, Growth, Opportunity and Forecast 2019-2024. (2019, August). (Markets, Research and) Retrieved October 14, 2019, from Research and Markets: https://www.researchandmarkets.com/reports/4828702/machine-tools-market-global-industry-trends

Martan, J., & Benes, P. (2012). Thermal properties of cutting tool coatings at high temperatures. *Thermochimica Acta, 539*, 51-55.

Martan, J., & Benes, P. (2012). Thermal properties of cutting tool coatings at high temperatures. *Thermochimica Acta, 539*, 51-55. doi:10.1016/j.tca.2012.03.029

McAdam, J. D., & Geil, G. W. (1939). Rate of oxidation of steels as determined from interference colors of oxide films. *Journal of Research of the National Bureau Standards, 23*, 63-124.

McAdam, Jr., D. J., & Geil, G. W. (1939, July). Rate of oxidation of steels as determined from interference colors of oxide films. *Journal of Research of the National Bureau Standards, 23*, 63-124. Retrieved from nvlpubs.nist.gov/nistpubs/jres/23/jresv23n1p63_A1b.pdf

Meier, L., Schaal, N., & Wegener, K. (2017). In-process measurement of the coefficient of friction on titanium. *Procedia CIRP, 68*, 163-168. doi:10.1016/j.procir.2017.03.212

Merchant, M. E. (1945). Mechanics of the metal cutting process. I. Orthogonal cutting and a type 2 chip. *Journal of Applied Physics, 16*(5), 267-275.

Naumkin, A. V., Kraut-Vass, A., Gaarenstroom, S. W., & Powell, C. J. (2012). *NIST X-ray Photoelectron Spectroscopy Database*. Retrieved June 2016, from https://srdata.nist.gov/xps/

Ning, L., Veldhuis, S. C., & Yamamoto, K. (2007). Investigation of nano-structured PVD coatings for dry high-speed machining. *Machining Science and Technology, 11*, 45-59. doi:10.1080/10910340601172230

Ning, Y., Rahman, M., & Wong, Y. S. (2001). Investigation of chip formation in high speed end milling. *Journal of Materials Processing Technology, 113*, 360-367.

Ning, Y., Rahman, M., & Wong, Y. S. (2001). Investigation of chip formation in high speed end milling. *Journal of Materials Processing Technology, 113*, 360-367.

Puls, H., Klocke, F., & Lung, D. (2012, September). A new experimental methodology to analyze the friction behaviour at the tool-chip interface in metal cutting. *Production Engineering, 6*(4-5), pp. 349-354.

Puls, H., Klocke, F., & Lung, D. (2014). Experimental investigation on friction under metal cutting conditions. *Wear, 310*, pp. 63-71.

Rech, J., Claudin, C., & D'Eramo, E. (2009). Identification of a friction model - Application to the context of dry cutting of AISI 1045 steel with a TiN-coated carbide tool. *Tribology International, 82*, pp. 738-744.

Shaw, M. C. (1984). Cutting Fluids. In *Metal Cutting Principles* (pp. 292-332). New York: Oxford University Press.

Shaw, M. C. (1984). Friction. In *Metal Cutting Principles* (pp. 202-223). New York: Oxford University Press.

Shaw, M. C., Ber, A., & Mamin, P. (1960). Friction characteristics of sliding surfaces undergoing subsurface plastic flow. *Journal of Basic Engineering, 82*, 342-346.

Sliney, H. E. (1982). Solid lubricant materials for high temperatures - A review. *Tribology International, 15*(5), 303-315. doi:10.1016/0301-679X(82)90089-5

Smolenicki, D., Boos, J., Kuster, F., Roelofs, H., & Wyen, C. F. (2014). In-process measurement of friction coefficient in orthogonal cutting. *CIRP Annals - Manufacturing Technology, 63*, 97-100. doi:10.1016/j.cirp.2014.03.083

Song, Q., Zhang, W., & Bay, N. (2005). An experimental study determines the electrical contact resistance in resistance welding. *Welding Journal, 84*(5), 73s-76s.

Sterle, L., Pusavec, F., & Kalin, M. (2019). Determination of friction coefficient in cutting processes: comparison between open and closed tribometers. *Procedia CIRP, 82*, 101-106. doi:10.1016/j.procir.2019.04.159

Sugishita, J., & Fujiyoshi, S. (1981). The effect of cast iron graphites on friction and wear performance. I: graphite film formation on grey cast iron surfaces. *Wear, 66*, 209-221.

Trent, E. (1988). Metal cutting and the tribology of seizure: I Seizure in metal cutting. *Wear, 128*, 29-45.

Trent, E. (1988). Metal cutting and the tribology of seizure: II Movement of work material over the tool in metal cutting. *Wear, 128*, 47-64.

Trent, E. (1988). Metal cutting and the tribology of seizure: III Temperatures in metal cutting. *Wear, 128*, 65-81.

Trent, E. M., & Wright, P. K. (2000). Coolants and Lubricants. In *Metal Cutting, 4th Ed.* (pp. 311-337). Boston: Butterworth-Heinemann.

Trent, E. M., & Wright, P. K. (2000). Forces and Stresses in Metal Cutting. In *Metal Cutting* (Fourth Ed. ed., pp. 57-96). Boston: Buterworth-Heinemann.

Trent, E. M., & Wright, P. K. (2000). Heat in Metal Cutting. In *Metal Cutting* (Fourth Ed. ed., pp. 97-131). Boston: Butterworth-Heinemann.

Trent, E. M., & Wright, P. K. (2000). Machinability. In *Metal Cutting* (Fourth Ed. ed., pp. 251-310). Boston: Butterworth-Heinemann.

Trent, E. M., & Wright, P. K. (2000). The Essential Features of Metal Cutting. In *Metal Cutting* (Fourth Ed. ed., pp. 21-55). Boston: Butterworth-Heinemann.

Trent, E. M., & Wright, P. K. (2001). Forces and Stresses in Metal Cutting. In *Metal Cutting, Fourth Edition* (pp. 57-96). Boston: Buterworth-Heinemann.

Venkatesh, V. C., Zhou, D. Q., Xue, W., & Quinto, D. T. (1993). A study of chip surface characteristics during the machining of steel. *Annals of the CIRP, 42*, 631-636.

Venkatesh, V. C., Zhou, D. Q., Xue, W., & Quinto, D. T. (1993). A study of chip surface characteristics during the machining of steel. *Annals of the CIRP, 42*, 631-636. doi:DOI: 10.1016/S0007-8506(07)62526-8

Volger, M., & Sheppard, S. (1993). Electrical contact resistance under high loads and elevated temperatures. *Welding Journal, 72*, 231s-238s.

Williams, W. S. (1991). The Thermal Conductivity of Metal Ceramics. *JOM, 50*(62), 62-66. doi:10.1007/s11837-998-0131-y

Zemzemi, F., Rech, J., Ben Salem, W., Dogui, A., & Kapsa, P. (2008). Identification of a friction model at tool/chip/workpiece interfaces in dry machining of AISI 4142 treated steels. *Journal of Materials Processing Technology, 209*, 3978-3990.

APPENDIX A: SUMMARY OF COEFFICIENTS FOR ALL TYPES OF NODES USED IN THE TWO-DIMENSIONAL THERMAL MODEL OF THE DISC

Below is a summary of the expressions defining coefficients C_1 through C_4 and q_{gen} in **Eq. 6.2.2.14**, for nodes of type ***a*** through ***e*** and also ***g***, as was developed in **Section 6.2.2**. For convenience, **Eq. 6.2.2.14** is presented again below.

$$C_1 T_{m-1,j} + C_2 T_{m+1,j} + C_3 T_{m,j-1} + C_4 T_{m,j+1} + C_5 T_{m,j} + q_{gen} = 0$$

Where present, the notation '!' refers to modified terms that reflect the effect of contact resistance ***CR***. Both the original as well as modified terms are presented, but where both are presented for a given node type, only the modified terms are actually implemented. In effect, the modified terms are equal to the original terms when ***CR*** = 1.

*Coefficients for Type **a** Nodes*

$$C_1 = 0$$

$$C_2 = \frac{\pi\left(r_m + \frac{\Delta r_m}{2}\right)\left(\Delta z_j k_d + \Delta z_{j-1} k_c\right)}{\Delta r_m}$$

$$C_3 = \frac{\pi\left(\frac{\Delta r_{m-1}}{2}\right)^2 k_c}{\Delta z_{j-1}};\ C!_3 = CR\frac{\pi\left(\frac{\Delta r_{m-1}}{2}\right)^2 k_c}{\Delta z_{j-1}}$$

$$C_4 = \frac{\pi\left(\frac{\Delta r_m}{2}\right)^2 k_d}{\Delta z_j}$$

$$q_{gen} = (I")^2\frac{\rho l}{A"};\ q!_{gen} = \left(\frac{1}{CR}\right)(I")^2\frac{\rho l}{A"}$$

*Coefficients for Type **b** Nodes*

$$C_1 = \frac{\pi\left(r_m - \frac{\Delta r_{m-1}}{2}\right)\left(\Delta z_j k_d + \Delta z_{j-1} k_c\right)}{\Delta r_{m-1}}$$

$$C_2 = \frac{\pi\left(r_m + \frac{\Delta r_m}{2}\right)\Delta z_j k_d}{\Delta r_m}$$

$$C_3 = \pi h_{TOP}\left(r_m \Delta r_m + 0.25\Delta {r_m}^2\right) + \frac{\pi\left(r_m \Delta r_{m-1} - 0.25\Delta {r_{m-1}}^2\right)k_c}{\Delta z_{k-1}}$$

$$C!_3 = \pi h_{TOP}\left(r_m \Delta r_m + 0.25\Delta {r_m}^2\right) + CR\frac{\pi\left(r_m \Delta r_{m-1} - 0.25\Delta {r_{m-1}}^2\right)k_c}{\Delta z_{k-1}}$$

$$C_4 = \frac{\pi\left(r_m(\Delta r_m + \Delta r_{m-1}) + 0.25\left(\Delta {r_m}^2 - \Delta {r_{m-1}}^2\right)\right)k_d}{\Delta z_j}$$

$$q_{gen} = (I")^2\frac{\rho l}{A"};\ q!_{gen} = \left(\frac{1}{CR}\right)(I")^2\frac{\rho l}{A"}$$

*Coefficients for Type **c** Nodes*

$$C_1 = \frac{\pi\left(r_m - \frac{\Delta r_{m-1}}{2}\right)\Delta z_j k}{\Delta r_{m-1}}$$

$$C_2 = \frac{\pi\left(r_m + \frac{\Delta r_m}{2}\right)\Delta z_j k}{\Delta r_m}$$

$$C_3 = \pi h_{top}\left(r_m(\Delta r_m + \Delta r_{m-1}) + 0.25\left(\Delta {r_m}^2 - \Delta {r_{m-1}}^2\right)\right)$$

$$C_4 = \frac{\pi\left(r_m(\Delta r_m + \Delta r_{m-1}) + 0.25\left(\Delta {r_m}^2 - \Delta {r_{m-1}}^2\right)\right)k}{\Delta z_{j-1}}$$

$$q_{gen} = 0$$

*Coefficients for Type **d** Nodes*

$$C_1 = \frac{\pi\left(r_m - \frac{\Delta r_{m-1}}{2}\right)\Delta z_j k}{\Delta r_{m-1}}$$

$$C_2 = \pi h_{side} r_m \Delta z_j$$

$$C_3 = \pi h_{top}\left(r_m \Delta r_{m-1} - 0.25{\Delta r_{m-1}}^2\right)$$

$$C_4 = \frac{\pi\left(r_m \Delta r_{m-1} - 0.25{\Delta r_{m-1}}^2\right)k}{\Delta z_j}$$

$$q_{gen} = 0$$

*Coefficients for Type **e** Nodes*

$$C_1 = 0$$

$$C_2 = \frac{\pi\left(r_m + \frac{\Delta r_m}{2}\right)(\Delta z_j + \Delta z_{j-1})k}{\Delta r_m}$$

$$C_3 = \frac{\pi\left(\frac{\Delta r_m}{2}\right)^2 k}{\Delta z_{j-1}}$$

$$C_4 = \frac{\pi\left(\frac{\Delta r_m}{2}\right)^2 k}{\Delta z_j}$$

$$q_{gen} = 0$$

*Coefficients for Type **g** Nodes*

$$C_1 = \frac{\pi\left(r_m - \frac{\Delta r_{m-1}}{2}\right)(\Delta z_j + \Delta z_{j-1})k}{\Delta r_{m-1}}$$

$$C_2 = \pi h_{side} r_m (\Delta z_j + \Delta z_{j-1})$$

$$C_3 = \frac{\pi \left(r_m \Delta r_{m-1} - 0.25 {\Delta r_{m-1}}^2 \right) k}{\Delta z_{j-1}}$$

$$C_4 = \frac{\pi \left(r_m \Delta r_{m-1} - 0.25 {\Delta r_{m-1}}^2 \right) k}{\Delta z_j}$$

$$q_{gen} = 0$$

APPENDIX B: REPRODUCTION OF THE FIRST SIX PARAGRAPHS IN THE DISCUSSION SECTION OF AN ARTICLE WRITTEN BY THE AUTHOR

As noted in the Declaration of Academic Achievement section (pp. xxviii – xxx), the content presented in Section 7.4 is partly adapted from the first six paragraphs in the *Discussion* section of an article written by the author (Boyd & Veldhuis, 2016). The content below is reprinted by permission from **Springer Nature Customer Service Centre GmbH: Springer, The International Journal of Advanced Manufacturing Technology (Manifestations of reduced tool-chip friction during turning of AISI 1045 steel with PVD-coated carbide inserts, Jeremy M. Boyd, Stephen C. Veldhuis) © Springer 2016.**

Cutting AISI 1045 steel with TiN- as well as TiAlCrSiYN/TiAlCrN-coated inserts yielded significant differences in terms of cutting forces, BUE intensity and chip characteristics as compared with the other coated and uncoated inserts: the average cutting forces were lower and less fluctuation in force was observed; BUE intensity was greatly reduced (particularly for TiAlCrSiYN/TiAlCrN at 50 m/min); and chips were generally shorter and of a tighter curl radius. In light of friction coefficient measurements obtained on the heavy-load, high-temperature tribometer, one possible explanation is that of reduced friction and sticking intensity at the tool-chip interface with the TiN- and TiAlCrSiYN/TiAlCrN-coated inserts.

However, an alternative explanation may relate to differences in the thermal properties of the tool materials. For instance, Friedman & Lenz (Friedman & Lenz, Investigation of the tool-chip contact length in metal cutting, 1970) demonstrated that uncoated cemented

carbide tools with lower thermal conductivity result in a shorter tool-chip contact length (as well as reduced cutting forces and crater wear rate (Friedman & Lenz, The effect of thermal conductivity of tool material on cutting forces and crater wear rate, 1973)), which they reasoned was due to a higher temperature-field in the tool-chip contact zone, thereby affecting the chip flow velocity field. These results were obtained when cutting SKF 1550 steel (0.35% C) without coolant under slightly more aggressive cutting conditions (123 m/min and 180 m/min cutting speed, 0.32 mm/rev feed rate and 0.25 mm/rev depth of cut). They acknowledged that this mechanism exists only for sufficiently high cutting temperatures; at lower cutting speeds (below 13 m/min), the measured tool-chip contact length showed no correlation with tool material thermal conductivity, with measurements from all inserts confined to a relatively narrow band. Likewise, Bandyopadhyay (Bandyopadhyay, 1984) showed how severe built-up edge formation could be significantly reduced, even eliminated, during machining of Cr-alloy steel by heating the tool tip to upwards of 600 °C via electrical current, such that the tool-chip interface temperature exceeded the recrystallization temperature of the steel workpiece being cut.

Table 3 presents room temperature and elevated temperature thermal conductivity values (obtained from Martan & Benes (2012) and Jawahir & van Lutterwelt (1993)) for select tool materials with compositions similar to those used in the present study. It is evident that uncoated WC possesses the highest thermal conductivity, followed by TiN. Arguably, TiAlCrSiYN/TiAlCrN will possess a lower thermal conductivity than TiN, likely on a similar order as that of $Ti_{0.35}Al_{0.65}N$ and $Cr_{0.50}Al_{0.41}Si_{0.09}N$. Thus, the results presented in terms of lower forces and reduced BUE intensity could simply relate to the

increased heat flow into the chip, thereby softening the work material in the secondary shear zone.

Analysis of the chip characteristics becomes of great importance in discerning which of these two possible mechanisms is at work. Venkatesh et al. (1993) related the colour of the undersurface of steel chips from machining operations to the thickness of the oxide layer as well as an estimate of tool-chip interface temperature. Their work suggests that chips with a golden brown undersurface resulted from a cooler tool-chip interface than did chips exhibiting blue on their undersurface, with corresponding temperature estimates ranging from about 830 to 980 °C. Likewise, Ning et al. (2001) observed chips of a greenish colour when cutting steel at speeds higher than those which produced chips of a bluish colour, which suggests that green coloured chips result from a higher tool-chip interface temperature, cutting temperature being strongly dependent on cutting speed.

Considering the chip colour observations for cutting tests at 50 m/min (Table 1), chips from the TiN- and TiAlCrSiYN/TiAlCrN-coated inserts (gold coloured undersurface) likely encountered a cooler tool-chip interface compared with chips from the uncoated or ZrN/NbN-coated inserts (blue/purple undersurface). A lower tool-chip interface temperature would be expected for reduced sticking intensity between tool and chip, which is consistent with the friction measurements on the tribometer. At a first glance, however, the temperature associations with chip colour appear to be higher than those associated with the friction coefficient measurements obtained in this study. It is important to note that the chips studied by Venkatesh et al. (1993) were obtained from cutting tests under considerably higher cutting speed and feed conditions than those used in this study. Thus,

it is not unreasonable to expect that tool-chip interface temperatures during cutting tests in the present study were in the range of 500-700 °C, where the TiN and TiAlCrSiYN/TiAlCrN coatings exhibit a notably lower friction coefficient in contact with steel. As well, the progression of colours on an oxidized surface are known to repeat themselves as the oxide film thickness increases (McAdam, Jr. & Geil, 1939), thus, the similarity in chip undersurface colours in this study with those of Venkatesh et al. may be coincidental and arise from a thinner oxide layer, which one would anticipate from a cooler tool-chip interface.

Considering the chip colours from tests at 100 m/min (Table 2), the TiN- and TiAlCrSiYN/TiAlCrN-coated inserts produced chips with a grey/turquoise undersurface, which likely resulted from a hotter tool-chip interface than those produced by the uncoated and ZrN/NbN-coated inserts (grey/gold undersurface). Given that chips produced by all inserts at this cutting speed were of the same form (long, continuous, spiral), a tighter chip curl diameter also suggests a hotter tool-chip interface, the difference in temperature between free and sliding surfaces being proposed as a primary driving mechanism for chip curl (Jawahir & van Lutterwelt, 1993). Thus, at the higher cutting speed of 100 m/min, it is more likely that the differences in thermal conductivity of the coatings is influencing the heat flow into the chip, resulting in a drop in cutting forces and BUE intensity.

APPENDIX C: PERMISSION TO REPRODUCE/ADAPT CONTENT FROM ARTICLE BY AUTHOR

Hi Jeremy,

As long as the portions of your dissertation that are based on your published work are clearly identified, and any modifications are noted, there is no issue with adapting the work to fit your thesis requirements. I hope this helps, and good luck on completing!
Best,
Leslie

Leslie Lansman
Global Permissions Manager
SpringerNature
The Campus, 4 Crinan Street, London N1 9XW, United Kingdom
T +44 (0) 207 8432795
M + 44 (0)758 4267625
E leslie.lansman@springernature.com
http://www.nature.com
http://www.springer.com
http://www.palgrave.com
https://www.macmillanihe.com

From: J.M. Boyd < >
Sent: 10 March 2021 02:50
To: Journalpermissions <journalpermissions@springernature.com>
Subject: Requesting permission to adapt an article I authored for use in my thesis

[External - Use Caution]

Hello,

I was directed your way with regards to my inquiry, which I am copying anew below. Please advise if this request can be accommodated. If it would make it easier to accept, I can revert back to original wording (identical to what was published). However, there would still be some content/sections omitted and new content added. The green highlighted text below captures the essence of those differences.

Thank you for your consideration.

Jeremy

*****

I have prepared a draft of my PhD dissertation. I decided against a "sandwich thesis" format, instead opting for a traditional thesis. However, the content of Chapter 7 in my dissertation is largely based on a manuscript I co-authored with my graduate supervisor, Stephen Veldhuis, and published in the International Journal of Advanced Manufacturing Technology:

https://link.springer.com/article/10.1007/s00170-016-9775-x

Attached is the draft of my thesis, which I have submitted to my committee for preliminary review. The following disclaimer is present in the Declaration of Academic Achievement section (p. xxix). This can be modified as needed.

I should also add that Figure 39(a) in my dissertation (p. 98) is in essence the same as Figure 11 in the published manuscript. I can modify the above text accordingly to note this.

Chapter 7 differs in some regards to the published manuscript; I have not presented results pertaining to the ZrN/NbN coating; nor have I presented the content pertaining to long duration turning tests (tool wear studies) featured in the *Experiments and Analysis* as well as the *Results and Discussion* sections of the manuscript. As noted above, the discussion section of my dissertation differs from that of the manuscript as well. I have made efforts to modify the wording throughout; however, the flow of content is still very similar to that presented in the manuscript.

Please confirm that the intended use (somewhat of a hybrid between adaptation and reproduction) is acceptable. For the record, my thesis, once accepted, will be licenced to McMaster University and the National Archives for public posting to the web.

*****

On Tue, Mar 9, 2021 at 10:14
AM customercare@copyright.com <customercare@copyright.com> wrote:
Dear Dr. Jeremy Boyd,

Thank you for contacting Copyright Clearance Center (CCC). We act on behalf of copyright owners in providing permissions to our customers. Permission availability can vary depending on a rightsholder and also on the permission type. My name is Lex and it would be my pleasure to assist you.

I can confirm that order **5022631461051** for permission to reuse the full article

"Manifestations of reduced tool-chip friction during turning of AISI 1045 steel with PVD-coated carbide inserts" in thesis/dissertation was approved free of charge, but it is not a type of permission that would enable you to make any modifications to the portion you intend to use unless they are minor modifications (for example font/color changes).

After reading through your message explaining the intended type of use, I must inform you that if you wish to modify or adapt the portion prior to reusing it, as this is not the type of permission CCC can provide, you will have to contact **Springer Nature** directly through this email Journalpermissions@springernature.com and inquire with them if they can provide you with such a permission.

Please do not hesitate to reach out to me should you have any other questions or inconveniences.

Best regards,
Lex

Alexander Berrio
Customer Account Specialist
Copyright Clearance Center
222 Rosewood Drive
Danvers, MA 01923
www.copyright.com
Toll Free US +1.855.239.3415
International +1.978-646-2600
Facebook - Twitter - LinkedIn